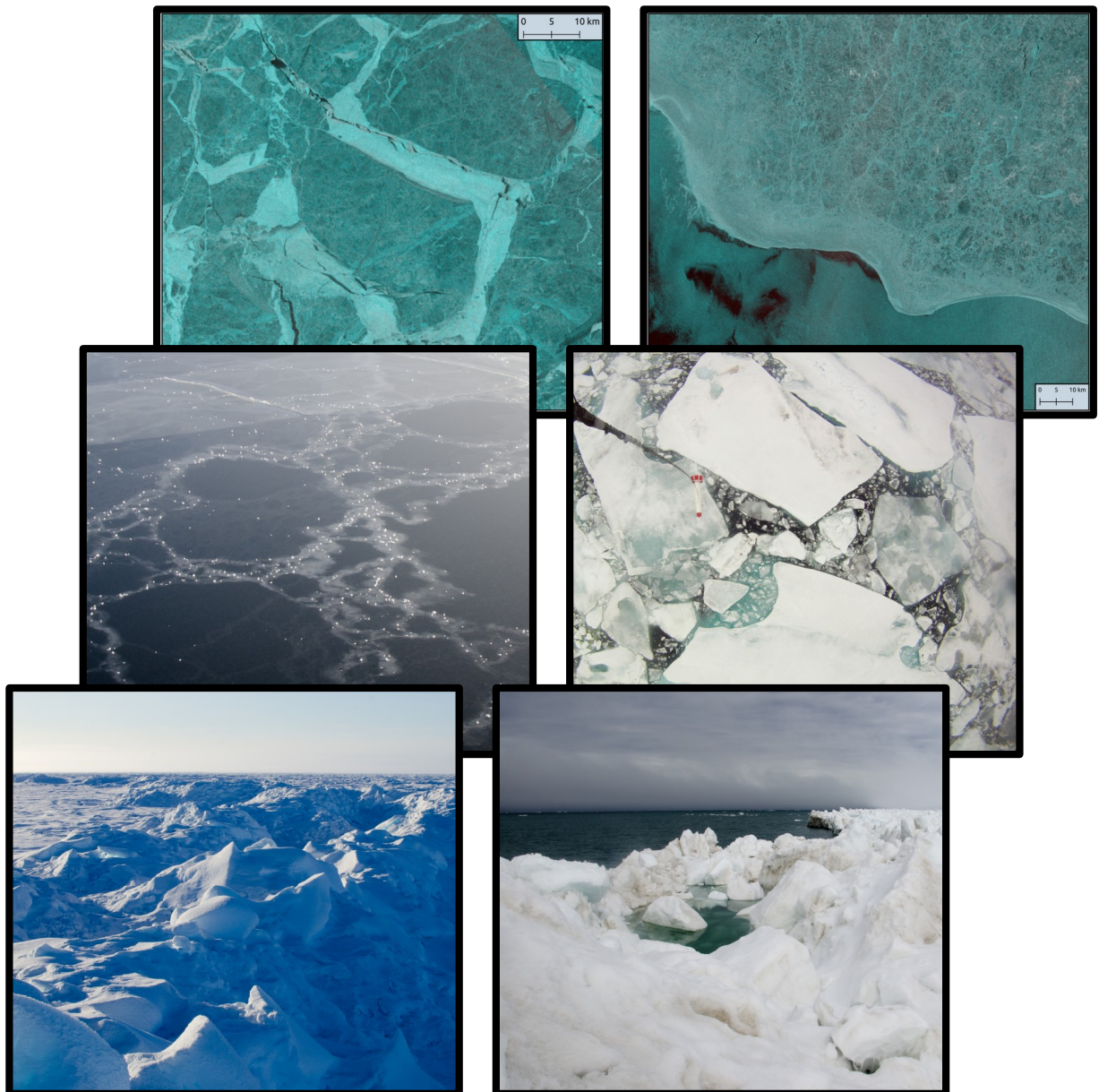


On Automated Classification of Sea Ice Types in SAR Imagery

Johannes Lohse

A dissertation of the degree of Philosophiae Doctor, December 2020



“I have had, in the course of my life, lots of encounters with lots of serious people. I have spent lots of time with grown-ups. I have seen them at close range. It hasn’t much improved my opinion of them.”
–Antoine de Saint-Exupéry

Abstract

With the Arctic sea ice continuously decreasing in both extent and thickness, the Arctic Ocean becomes more easily accessible to human activities, such as natural resource exploration, shipping, fishing, and tourism. Fast and robust production of reliable sea ice charts is essential to ensure the safety of the growing number of these Arctic operations. The main data source for ice chart production are images from spaceborne synthetic aperture radar (SAR). At present, operational sea ice charts are produced by manual analysis of these images in combination with complementary data; a process that is time-consuming and subject to the experience of the individual ice analyst. Given the increasing number of operational SAR satellites and available SAR images, methods for automated or computer-assisted mapping of sea ice will be required in the future. The work in this dissertation focuses on the development, training, and testing of such methods. Existing classification algorithms are extended and modified in order to address some of the main challenges of automated sea ice type classification from SAR data. Additionally, a new Sentinel-1 (S1) data set for training and validation of the algorithms is developed.

The first part of the thesis gives a thorough introduction into the topics of sea ice observations and ice charting, image classification and segmentation, spaceborne imaging radar, and the appearance of sea ice in radar images. The second part of the thesis presents the novel scientific contribution of the work in three research papers, each focusing on different aspects of automated classification and the ice charting process.

Paper 1 focuses on the topic of feature selection for classification. The study investigates the benefits of splitting a multi-class problem into several binary problems and selecting different feature sets specifically tailored towards these binary problems. Based on a combination of classification accuracy (CA) and sequential search algorithms, the optimal order of classes and the optimal feature set for each class are found and combined into a numerically optimized decision tree (DT). The approach is tested on a large number of synthetic images and on an airborne, multi-frequency SAR data set over sea ice. Compared to traditional all-at-once classification, the optimized DT is found to improve total CA on average between 0.5 and 4 %, albeit at the cost of increased computation time. Furthermore, the class-specific selection of individual feature sets can provide information on dominant scattering mechanisms for different ice types and on the potential of different features to distinguish between certain classes.

Paper 2 and *Paper 3* focus on the classification of S1 wide-swath images, which are important

for operational needs. Both papers use a training and validation data set for multiple sea ice types, which is based on the visual analysis and interpretation of overlapping S1 SAR data and optical images from Sentinel-2 and Landsat-8. The data set is developed as part of this thesis, specifically for the presented studies. A particular challenge for the automated analysis of wide-swath SAR images is the surface-type dependent variation of backscatter intensity with incident angle (IA). *Paper 2* develops and tests a novel method to directly incorporate this per-class IA effect into a classification algorithm. This new approach achieves improved CA compared to well established methods that apply a global IA correction during pre-processing of the data. However, when based on backscatter intensity only, several ambiguities remain and it is impossible to successfully separate all classes over the full range of the image. Therefore, *Paper 3* extends the newly developed algorithm to include textural information. The study investigates the per-class variation with IA of S1 texture features extracted from the grey level co-occurrence matrix (GLCM), and assesses their suitability to be approximated by the underlying model of the classifier developed in *Paper 2*. When extracted from intensity in the logarithmic domain, the variation is found to be linear and almost negligible. Different GLCM features and GLCM parameter settings are then analyzed for their potential to resolve the various ambiguities inherent in a classifier based on intensity only. Particular improvements are achieved for the generalized separation of sea ice and open water at different sea states, as well as for the classification of multi-year ice against young ice in refrozen leads. The improvements come at the cost of reduced spatial resolution, due to the applied texture window size.

The work in this thesis adds to the on-going research on classification of sea ice types in SAR imagery. The developed algorithms are tested and applied in various environmental and operational settings, and have the potential to contribute to better ice type mapping for safe operations in the Arctic.

Acknowledgements

Over the past years, many different people have contributed the completion of this thesis. I usually prefer to thank people in person, and so, instead of an endless series of names, I will only list a small selection here.

Most importantly, I would like to thank my supervisors, Anthony Doulgeris and Wolfgang Dierking. Thank you for your time and energy, and your continuous motivation and encouragement during my PhD studies. Tony, thanks for patiently teaching me about classification and segmentation, SAR data and image processing, and countless other technical skills. Wolfgang, thank you for always reminding me to connect these skills to the *real world*, and for never losing sight of the thing we are really interested in: the sea ice.

I would also like to thank all former and present members of the Earth observation group at UiT and the people at CIRFA. You have not only helped me through scientific and technical discussions, but more importantly made my time in the office so much more fun (and sometimes just bearable).

I would like to acknowledge CIRFA and center leader Torbjørn Eltoft, who founded this project, and gave me the opportunity to research these topics.

Finally, I thank my friends and family for always being there for me, even when far away.

Contents

Abstract	iii
Acknowledgements	v
List of Figures	ix
List of Tables	xi
List of Abbreviations	xiii
1 Introduction	1
1.1 Sea Ice in the Earth System	1
1.2 Observing Sea Ice	6
1.2.1 In-Situ Observations	7
1.2.2 Remote Sensing Observations	8
1.3 Operational Sea Ice Charting	9
1.4 Objectives of this Thesis	12
1.5 Thesis Outline	12
2 Image Classification and Segmentation	15
2.1 Objects, Features, and Classes	15
2.2 Supervised vs Unsupervised Methods	17
2.2.1 Validation	18
2.3 Linear vs Non-Linear Classifiers	20
2.4 Common Classification Algorithms	20
2.4.1 Bayesian Classifiers	21
2.4.2 Random Forests, Support Vector Machines, and Neural Networks	22
3 Spaceborne Imaging Radar	27
3.1 SAR Systems as Tools for Sea Ice Monitoring	28
3.1.1 Imaging Geometry and Spatial Resolution	28
3.1.2 Data Acquisition Modes	31
3.1.3 Temporal Resolution	32
3.1.4 Frequency and Polarimetry	33

3.2	Speckle and Noise	36
3.3	Scattering Mechanisms	37
4	Sea Ice Types and Sea Ice in SAR Imagery	41
4.1	Sea Ice Classes	41
4.2	Sea Ice in SAR Images	44
4.2.1	Surface and Volume Scattering from Sea Ice	45
4.2.2	Influence of Snow and Season	47
4.2.3	Scattering from Open Water	47
4.2.4	Complementary Information and Example Images	48
4.3	Approaches for (Semi-)automated Classification	54
5	Overview of Publications	57
5.1	Paper Summaries	57
5.2	Other Scientific Contributions	62
6	Paper I: An Optimal Decision-Tree Design Strategy and its Application to Sea Ice Classification from SAR Imagery	65
7	Paper II: Mapping Sea Ice Types from Sentinel-1 Considering the Surface-Type De- pendent Effect of Incidence Angle	83
8	Paper III: Incident Angle Dependence of Sentinel-1 Texture Features for Sea Ice Classification	97
9	Conclusion & Future Work	119
9.1	Research Conclusions	119
9.1.1	Future Work	120
9.2	Application Examples	122
	Bibliography	127

List of Figures

1.1	Arctic and Antarctic sea ice concentration	2
1.2	Evolution of Arctic and Antarctic sea ice extent	3
1.3	2017 Arctic traffic density	5
1.4	Shipping routes through the Arctic	6
1.5	Ice chart example (CIS)	10
1.6	Ice chart example (NIS)	11
2.1	Separable and non-separable training data	18
2.2	Classification accuracy and overtraining	19
2.3	Linear and non-linear decision boundaries	20
2.4	1D Bayesian classifier	22
2.5	Kernel density estimation	23
2.6	Neural network architecture	25
3.1	SAR imaging geometry	29
3.2	Synthetic aperture length	31
3.3	Sentinel-1 data acquisition modes	33
3.4	Sentinel-1 EW and Radarsat-2 FQP overlap	34
3.5	Radarsat-2 speckle and multi-looking	37
3.6	Sentinel-1 noise example	38
3.7	Common scattering mechanisms	38
3.8	Surface scattering mechanisms	39
4.1	Sea ice example photographs	43
4.2	Frost flower example photographs	46
4.3	SAR and optical overlap example 1	49
4.4	SAR and optical overlap example 2	50
4.5	SAR and optical overlap example 3	50
4.6	SAR and optical overlap example 4	51
4.7	SAR and optical overlap example 5	51
4.8	Utqiagvik overview map 2017	52
4.9	Utqiagvik clesup map 2019	52
4.10	Utqiagvik sea ice example photographs	53

5.1	Decision tree design stage	58
5.2	Per-class IA correction for open water and multi-year ice	59
5.3	Sentinel-1 texture features and classification result	61
9.1	Daily ice type map (April 1st 2020)	123
9.2	Hinlopen Strait overview map and classification result	124

List of Tables

- 1.1 Ice chart requirements 11
- 3.1 Current SAR sensors used for sea ice observation 28
- 3.2 Sentinel-1 data acquisition modes 32
- 3.3 Radar frequency and wavelength bands 35
- 4.1 WMO sea ice types 42

List of Abbreviations

AAO all-at-once

CA classification accuracy

CIRFA Center for Integrated Remote Sensing and Forecasting for Arctic Operations

CIS Canadian Ice Service

CNN convolutional neural network

DT decision tree

EM electromagnetic

ERS-1/2 European remote-sensing satellites

ESA European Space Agency

EW extra wide swath

FQP fine quad-pol

FYI first-year ice

GIS geographic information system

GLCM grey level co-occurrence matrix

GRDM ground range detected medium-resolution

HPCM high priority candidate mission

IA incident angle

- IICWG** international ice charting working group
- IW** interferometric wide swath
- J-ERS-1** Japanese Earth resource satellite
- LC-ICE** L- and C-band SAR satellites for sea ice monitoring
- MIZ** marginal ice zone
- ML** maximum likelihood
- MOSAiC** Multidisciplinary drifting Observatory for the Study of Arctic Climate
- MYI** multi-year ice
- NESZ** noise equivalent sigma zero
- NIS** Norwegian Ice Service
- NN** neural network
- NOAA** National Oceanographic and Atmospheric Association
- NPI** Norwegian Polar Institute
- PDF** probability density function
- PM** passive microwave
- RAR** real aperture radar
- RF** random forest
- RS** remote sensing
- SAR** synthetic aperture radar
- SBFS** sequential backward feature selection
- SFFS** sequential forward feature selection
- SIC** sea ice concentration

SLAR side-looking airborne radar

SM stripmap

SMMR Scanning Multichannel Microwave Radiometer

SoD stage of development

SSH sea surface height

SVM support vector machine

TOPS terrain observation by progressive scan

UiT UiT The Arctic University of Tromsø

WFQP wide fine quad-pol

WMO World Meteorological Organization

WV wave



Introduction

1.1 Sea Ice in the Earth System

The world's oceans make up approximately 71 % of the Earth surface [1]. As much as 10 % of this area is covered with sea ice during part of the year [2]. Sea ice forms by cooling and freezing of sea water and is therefore mostly encountered in the cold polar regions at high latitudes. Some areas at lower latitudes can experience sea ice in winter time, for example the Baltic Sea, the Sea of Japan, the Sea of Okhotsk, or the Bohai Sea [3].

Sea ice can grow vertically by two mechanisms: thermodynamic growth (freezing) and dynamic growth (deformation) [4–6]. Thermodynamic growth occurs as long as the atmosphere temperature is cold enough to freeze the sea water. For a constant air temperature, the thermodynamic growth rate decreases with increasing sea ice thickness, as the sea ice itself acts as an insulating layer between the ocean and the atmosphere. Thermodynamic growth is therefore usually limited to 1-2 m within one winter [6–8]. During thermodynamic growth, the salt in the sea water is partly rejected into the underlying water column and partly included in brine pockets and channels within the ice. Over time, the brine is slowly rejected from the ice volume and the sea ice becomes fresher [8, 9]. Dynamic growth occurs because of the mobility of sea ice [5]. Most sea ice occurs as drift ice which moves because of forces exerted mainly by wind and ocean currents. When ice floes collide, they can either raft on top of each other, or break and deform, building up ridges of more than 10 m [10]. Sea ice that has not experienced more than one season of growth is called first-year ice (FYI), whereas sea ice that has survived at least one melting season is called multi-year ice (MYI). As a general rule of thumb, MYI is thicker, fresher, and more deformed than FYI.

Sea ice is a highly variable medium in constant interaction with its environment. One of the most apparent variations is the seasonal change in the sea ice extent. Sea ice extent is defined as the area with at least 15 % sea ice concentration (SIC). The Arctic sea ice usually reaches its minimum extent in September and its maximum extent in March; for the Southern Seas around Antarctica, the situation is reversed (Figure 1.1).

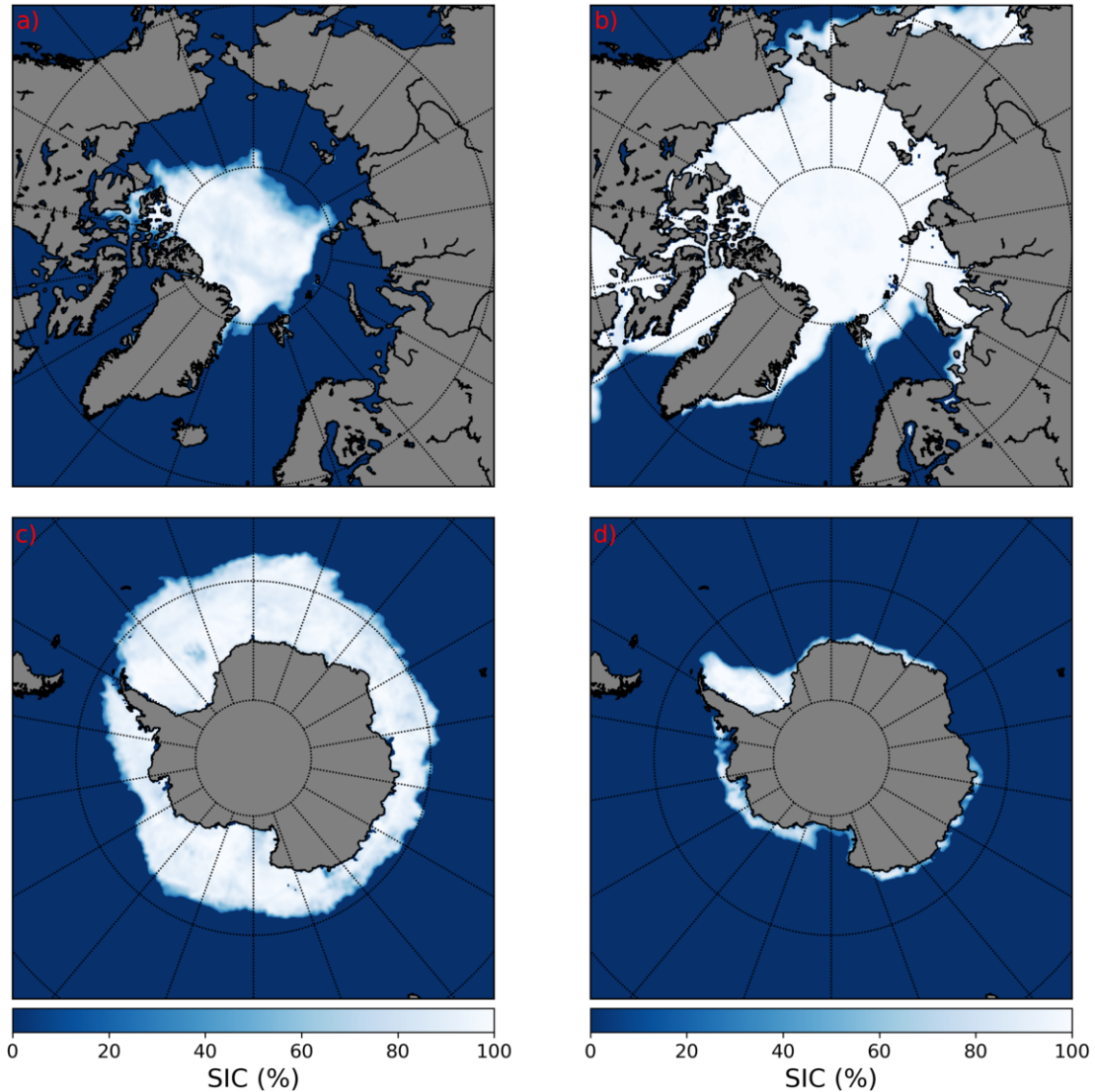


Figure 1.1: Arctic (top) and Antarctic (bottom) sea ice concentration (SIC) for selected days in the months with minimum and maximum sea ice extent. a) Arctic, September 15th 2019; b) Arctic, March 15th 2019; c) Antarctic, September 15th 2019; d) Antarctic, September 15th 2019. Sea ice extent is defined as the total area with at least 15 % SIC. Data were obtained from *osisaf.met.no: AMSR-2 Sea ice concentration product of the EUMETSAT Ocean and Sea Ice Satellite Application Facility (OSI SAF, www.osi-saf.org)* [11].

While the Antarctic minimum and maximum sea ice extent have been relatively stable over the past decades, the Arctic sea ice has declined significantly in both extent and thickness [12–16]. This decline is accompanied by a shift from a MYI-dominated ice regime to a FYI-dominated ice regime [17,18]. While the maximum Arctic sea ice extent in winter 2020 was only slightly below the maximum extent in 1980, the minimum extent in summer has decreased by almost 50 % over the last 40 years (Figure 1.2). Different climate model simulations agree that the Arctic Ocean will be ice free during summertime before the end of the 21st century [19], although the estimates are subject to uncertainty [20,21].

The loss of sea ice in the Arctic is one of the most visible signs of a changing climate and has become a subject of public awareness over the past years. Also in the research community today, sea ice is one of the most recognized topics related to climate change and continues to gain considerable attention. Scientists from different disciplines are working on an improved understanding of how the loss of sea ice will impact the Earth’s weather and climate system, polar ecosystems, and human activities in the Arctic.

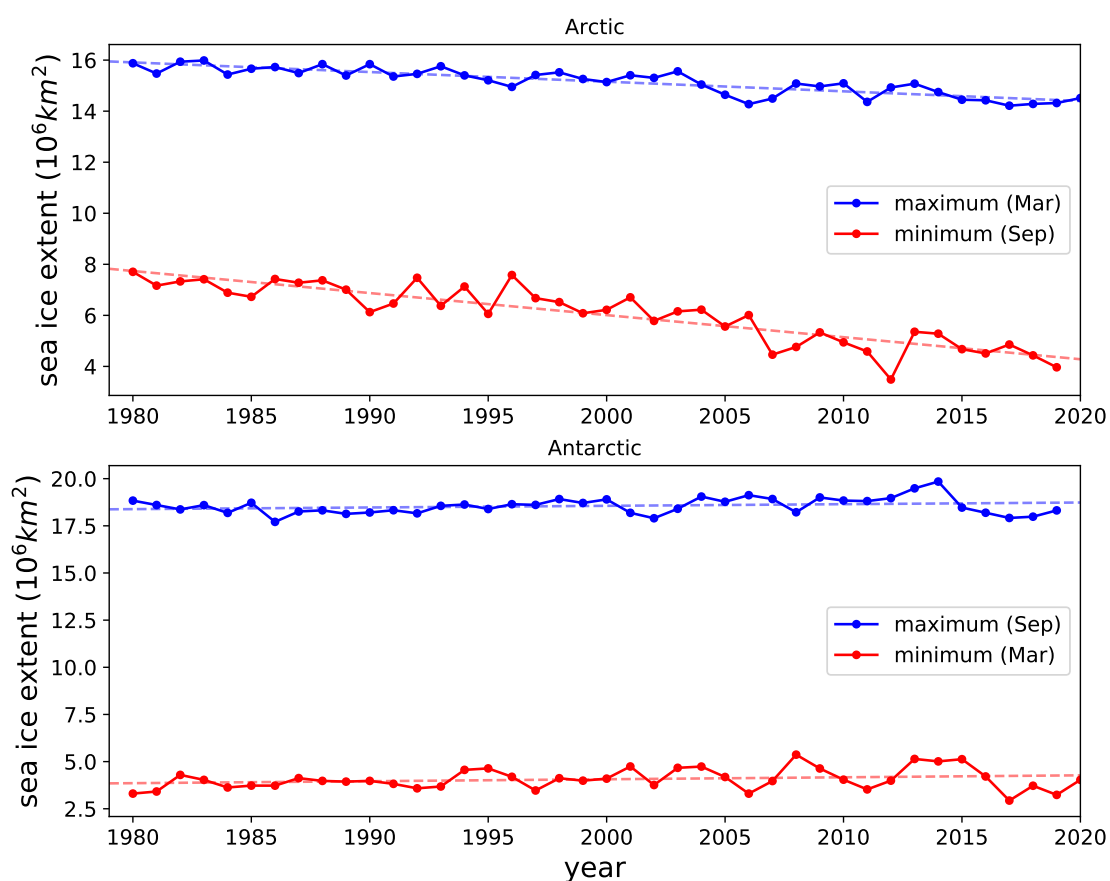


Figure 1.2: Evolution of Arctic (top) and Antarctic (bottom) sea ice extent for the months with minimum and maximum extent. Linear trends are indicated by dashed lines. Data from 1980 to 2020 were obtained from *meereisportal.de* (grant: REKLIM-2013-04) [22, 23].

Sea Ice and the Climate System

On a global scale, sea ice is a very thin layer between the ocean and the atmosphere. Despite its small vertical extent, sea ice plays an important role in the Earth's climate system [8]. It affects both the short-wave and the long-wave energy flux between the ocean and the atmosphere. The short-wave energy flux is controlled by the reflectivity (albedo) of the surface. Sea ice itself has an albedo that is much higher than that of open water and thus reflects more of the incoming radiation [24–26]. It also provides a surface on which snow can accumulate, which is even brighter than the sea ice and further intensifies the ice-albedo effect [27]. While sea ice thus increases the short-wave energy flux into the atmosphere, it reduces both the long-wave energy and the sensible heat flux. This is caused by the colder surface temperature of the sea ice compared to the open ocean, and by the insulating effect of the sea ice layer between the ocean and the atmosphere [28, 29].

Melting and freezing of sea ice redistribute brine and fresh water in the ocean. Hence, sea ice formation, drift, and melt affect global ocean circulation and stratification [30, 31], and contribute to the transformation of water masses, in particular the formation of very dense bottom water [32]. Through feedback mechanisms, these sea ice processes influence the climate of areas that are long distances away from the polar regions [33, 34].

Sea Ice and Biology

While sea ice appears to be a hostile environment for humans, it provides a habitat for a variety of other living organisms. Among the most abundant ones are bacteria, archaea, viruses, and micro-algae living inside the porous structure of the ice or directly underneath the ice [35, 36]. In particular the marginal ice zone (MIZ) and ice edge are associated with regular algae blooms and large primary production rates, which form the foundation of the Arctic food web and ecosystem [37–39]. Larger species such as birds and marine mammals also depend on the solid ice surface, its surface structure, and its snow cover for protection, hunting, and breeding [40–42]. For example, snow cover and its distribution, which are affected by the ice type and the grade of deformation, are of particular importance for seals building their lairs on the ice [43], while cracks and open leads in the ice are crucial for whales and seals to breathe [42].

Arctic Sea Ice and Human Activity

Human activities in the Arctic have always been closely tied to the presence of sea ice [2]. For large parts of recent human history, sea ice has in fact made the Arctic relatively inaccessible for humans. Only small communities, for example in Northern Canada or Alaska, lived close to and with the sea ice and adapted their way of life to it [44].

However, over the past decades, in the face of a declining Arctic sea ice extent and the

accompanying shift from thicker MYI to thinner FYI regimes, human interest and activity in the Arctic have increased. The Arctic continuously becomes more and more accessible and thus profitable to industries involved in oil and gas, mining, shipping, fishing, and tourism [45–49]. Most of the current shipping activity is concentrated along the Russian coast, the areas around Svalbard and Novaya Zemlya, the Northern Norwegian Sea, and Barents Sea (Figure 1.3). Some of the most famous shipping routes across the Arctic are the *Northwest Passage* and the *Northern Sea Route* (Figure 1.4). In 2019, they allowed for 26 and 27 transits, respectively [49].

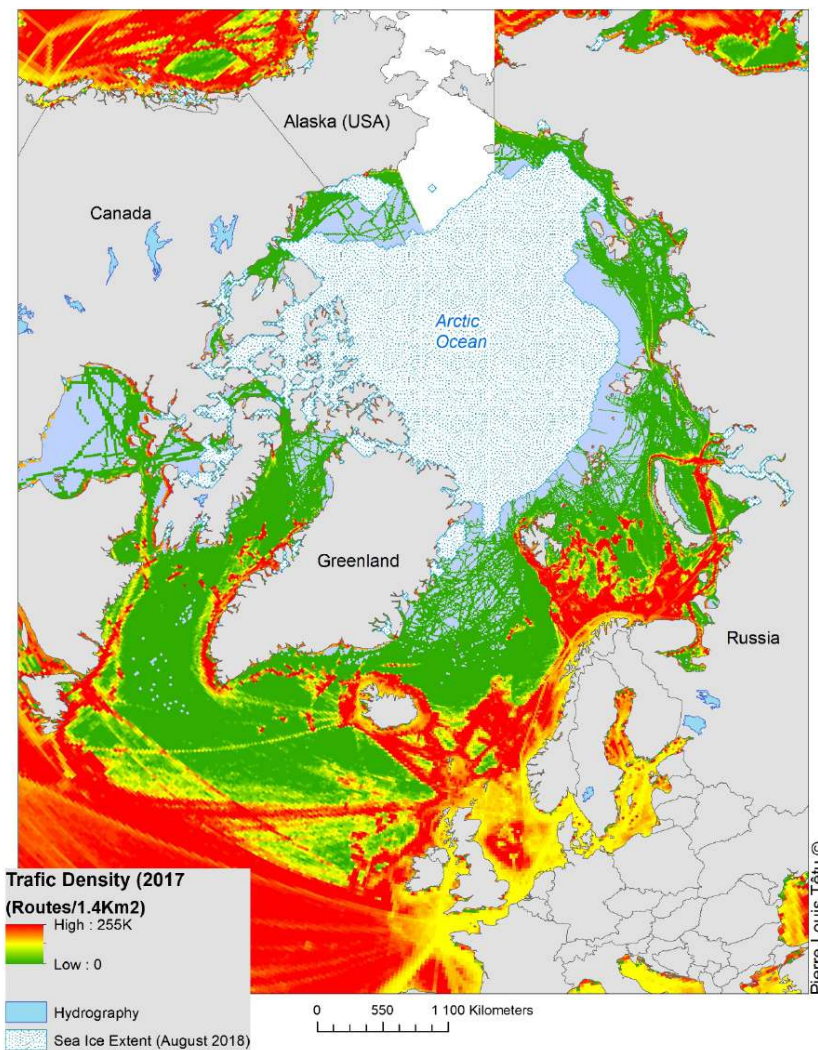


Figure 1.3: 2017 Arctic traffic density. Figure from *Lasserre and Têtu, 2020* [49].

The activities connected to the above-mentioned industries are commonly referred to as *Arctic operations*, and are expected to increase further in the near future [50, 51]. Sea ice (and icebergs) pose a significant hazard to Arctic operations. Potential accidents involving

oil production or shipping can lead to severe consequences, with sea ice impeding clean-up or rescue operations. Better observations and forecasts are therefore needed in order to ensure the

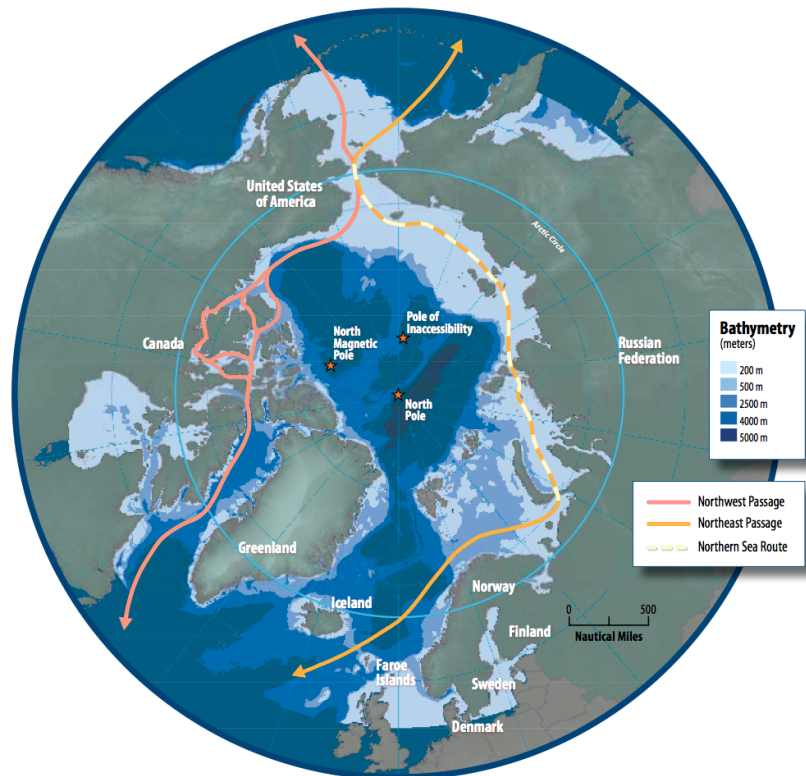


Figure 1.4: Map of main shipping routes through the Arctic. With the decreasing Arctic sea ice extent, these routes become more easily accessible and thus profitable in the summer. Figure from *National Oceanographic and Atmospheric Association (NOAA): Arctic Marine Shipping Assessment 2009 Report* [52].

1.2 Observing Sea Ice

Given the important role of sea ice in the Earth system and in Arctic operations, there is a need for regular and reliable sea ice observations. The following section summarizes how sea ice observations historically started as in-situ observations from boats and vessels, and gives an overview of today's in-situ and remote sensing (RS) methods.

1.2.1 In-Situ Observations

The first known observations of sea ice date back to the traveler Pythias of Massilia in the time between 350 to 320 B.C. While no direct records by Pythias exist, other authors have documented his journey towards the North and his reports of the frozen sea [53, 54]. The earliest confirmed first-hand records of sea ice appear in 825 A.D., written by Irish monks who encountered sea ice (the *Mare Concretum*) during voyages to Iceland [55]. Further descriptions of sea ice are found in the literature continuously throughout the following centuries. However, the goal of the mariners at the time was never to study the ice, but to avoid it [55, 56]. First scientific papers discussing physical properties of sea ice and different sea ice conditions were published in the 1870s [55]. By that time, the expansion of ocean trade routes had led to increased interest in shorter connections between Europe and the orient, in particular the Northwest and Northeast Passages (Figure 1.4). First successful crossings of the Arctic Ocean along these two routes were accomplished by Baron Adolf Erik Nordenskiöld in 1879 and Roald Amundsen in 1906, respectively [55].

It was not before the second half of the 20th century that there was a marked increase in sea ice research and in-situ observations. Today, there are multiple scientific expeditions by different nations each year. The typical and most basic in-situ measurements are regular *icewatch* observations from vessels [57, 58]. Other common in-situ observations on the ice are measurements of ice thickness and roughness, temperature and salinity profiles, as well as thickness and properties of snow cover on the sea ice [2]. Although not strictly in-situ, airborne ice thickness measurements by electromagnetic (EM) induction systems are sometimes also referred to as in-situ data when compared with satellite RS imagery [59, 60].

Despite the increasing scientific interest and large number of expeditions, in-situ observations of sea ice are still sparse and can only cover a small fraction of the polar regions. Furthermore, they are biased towards summer conditions, as the Arctic is more easily accessed in the summer compared to the colder and darker polar winter. Recent efforts that are trying to address this issue include the Norwegian N-ICE2015 expedition [61], or the Multidisciplinary drifting Observatory for the Study of Arctic Climate (MOSAIC) expedition (autumn 2019-autumn 2020), which aims at obtaining more in-situ data from the central Arctic during wintertime [62].

The fact that observations and descriptions of sea ice started as visual in-situ observations by mariners has shaped and defined our understanding and definition of different sea ice types today. Sea ice types are traditionally classified by their visual appearance and by the ice thickness, which is a critical parameter for ice-going vessels. The implications of this for sea ice classification from imaging radar data are discussed in Chapter 4.

1.2.2 Remote Sensing Observations

Since the late 1970s, spaceborne RS has revolutionized the world of sea ice observations, making regular large-scale and Arctic- and Antarctic-wide monitoring possible. Today, different sensors on multiple satellite platforms provide a vast number of observations that are frequently repeated [63]. The measurements are carried out over a wide range of the EM spectrum, at visible, infrared, and microwave wavelengths, using both active and passive sensors. Active sensors generate their own signal and are independent of a natural radiation source. Passive sensors rely either on solar illumination (optical sensors) or on radiation that is naturally emitted from the Earth surface and atmosphere (passive microwave radiometry).

Synthetic aperture radar is an active system that is widely used in sea ice monitoring today. It can achieve a high spatial resolution by utilizing the coherent nature of the transmitted radar pulse [64]. Furthermore, the data acquisition is independent of sunlight and cloud conditions. Since synthetic aperture radar (SAR) is the main data source used in this dissertation, it is introduced and discussed in detail in a separate chapter (Chapter 3). Optical images are often used as complementary data to radar images. Also in this thesis, overlapping SAR and optical images are used for the definition of ice types, the selection of training regions, and the validation of results (*Paper-2*, Chapter 4). However, optical RS in the polar regions is generally limited because of the darkness during polar winter and frequent cloud conditions in the summer.

As the Earth atmosphere is essentially regarded as transparent for wavelengths above 3 cm [65], microwave RS is generally very little influenced by clouds. Besides SAR, methods for microwave RS include radar scatterometers and passive microwave (PM) radiometers [63]. PM radiometry became available for sea ice observations with the start of the Nimbus-7 satellite carrying the Scanning Multichannel Microwave Radiometer (SMMR) in 1978. The SMMR and its successors form the basis of the sea ice extent time series. The examples of SIC in Figure 1.1 and Figure 1.2 are obtained using data from PM sensors. PM radiometers measure radiation that is naturally emitted from the Earth surface and atmosphere [66]. Power and wavelength of the radiation is controlled by the surface temperature T and the emissivity ϵ . This allows to generally distinguish open water surfaces from sea ice surfaces in the PM data. The spatial resolution of a PM radiometer depends on the size of the reflector in the antenna and the frequency of the radiation. Higher frequencies result in finer resolution (89 GHz, ~ 3 km), but are more sensitive to atmospheric disturbances. Lower frequencies are less affected by the atmosphere, but result in coarser resolution (6 GHz, ~ 40 km). Most retrieval algorithms combine different frequency and polarization channels and use empirically derived formulas to estimate SIC [67, 68]. The typically used channels have spatial resolutions between 5 and 15 km, resulting in SIC products with a km-scale grid-spacing. Sea ice extent can also be derived from radar scatterometers [63, 69, 70]. A comparison of the different methods is given in *Meier and Stroeve (2008)* [71].

SIC and sea ice area are the primary sea ice products obtained from PM radiometry

and radar scatterometry. However, the data can also be used to estimate the MYI and FYI fraction within the resolution cell [72], to calculate sea ice drift from consecutive images [73], and to estimate sea ice thickness of thin ice types (thickness < 0.2 m) [74, 75]. While PM radiometry and radar scatterometry are excellent tools for large-scale sea ice monitoring, they do not offer the spatial resolution that is required for applications in operational ice charting (Section 1.3).

Sea ice thickness is a parameter of major interest for many applications. However, except for thin ice thickness, it can not be obtained from PM radiometry or SAR [76]. Instead, estimates of sea ice thickness are inferred from spaceborne radar and laser altimeters [77]. An altimeter sends out a pulse in nadir direction and measures the signal that is reflected back to the satellite. The ice freeboard (the part of the ice above the sea surface) can be obtained from the difference in signal travel time between reflections from the ice and the water. Sea ice thickness is then calculated from the freeboard assuming hydrostatic equilibrium. The method requires re-tracking of the first return of the signal to get the travel time [78, 79], the detection of leads between the ice floes that serve as reference points for the sea surface height (SSH) [80], and an estimation of snow depth and density from climatological or airborne data [81].

1.3 Operational Sea Ice Charting

Several ice services around the world provide different types of sea ice charts on an operational basis. The requirements for the ice charts differ considerably, depending on the end user and their needs. There are operational and scientific end users. Scientific end users utilize ice charts for academic studies for example on climate, biology, or data assimilation in numerical models, whereas operational end users require timely ice charts for strategic and/or tactical information. Most efforts of the ice services are directed towards the operational end users. Strategic information refers to ice charts on a regional scale and is for example used for general route planning; tactical information requires a more local analysis in direct vicinity of a vessel, in order to support immediate operation and decision making [82]. Operational requirements on spatial and temporal resolution for different sea ice parameters are summarized in Table 1.1.

Because of its all-day and all-weather imaging capability (Chapter 3), SAR data is the primary information source for ice chart production [83]. Other RS data (Section 1.2.2) and further additional information are used whenever available. The additional information includes meteorological conditions, ship-based observations, and the temporal evolution of the sea ice. Examples of different ice charts from the Canadian Ice Service (CIS) and the Norwegian Ice Service (NIS) are shown in Figure 1.5 and Figure 1.6, respectively. The example from the CIS shows SIC and the dominant ice types within polygons. The example from the NIS shows SIC only.

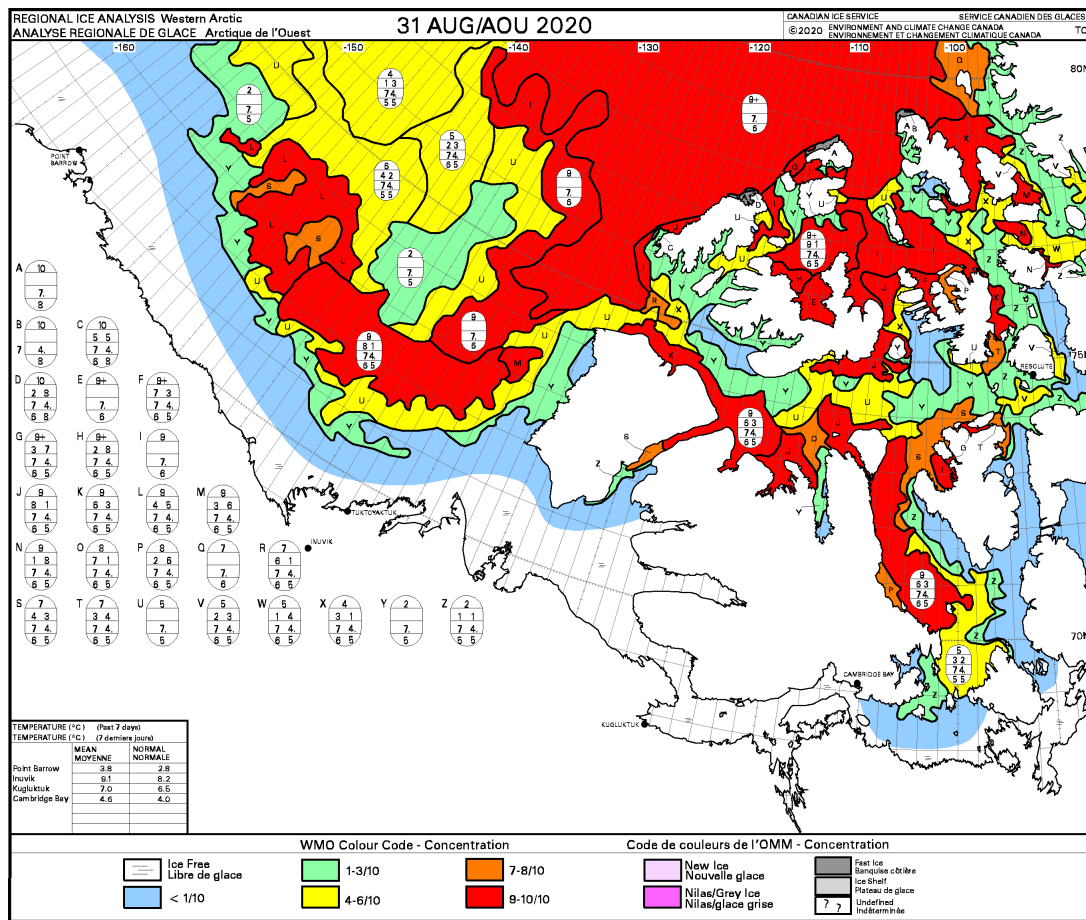


Figure 1.5: Example of an ice chart produced by the CIS. SIC is depicted by different colors. The polygons separate zones of distinct ice conditions. The dominant ice types within each polygon, their areal fractions, and relative floe size are described in the egg code. Detailed information on how to read the egg code can be found in [84].

Until today, ice charts are generated manually by trained expert sea ice analysts. With the help of a geographic information system (GIS), they combine and visually interpret all available data to draw the ice chart. This manual analysis is time-consuming and subject to the experience of the individual ice analyst. However, timeliness of the ice chart is a main requirement from the operational end users (Table 1.1); for example, the goal at the CIS is to interpret new imagery within one hour after image acquisition. Given these time constraints in combination with an increasing number of operational satellites, and consequently more available SAR data, the manual analysis of images becomes less feasible. New ways of combining and effectively exploiting all available information are needed in order to facilitate the manual work. Multiple efforts have therefore been directed towards automated or semi-automated (computer-assisted) mapping of sea ice types [83]. The main requirements for such a procedure are that it needs to be fast, reliable, and robust.

Some commonly used approaches as well as the obstacles and challenges of developing such an algorithm are discussed in more detail in Chapter 4. Despite lots of research and progress in the field of automated mapping of sea ice types, no algorithm has been developed so far that fully meets operational requirements.

Table 1.1: Requirements on spatial and temporal resolution of operational sea ice charts for strategic and tactical purposes. Adapted from [82], based on [85, 86].

Parameter	strategic		tactical	
	spatial	temporal	spatial	temporal
ice edge location	5 km	daily	< 1 km	6 hours
ice concentration	< 100 m	daily	< 25 km	6 hours
ice types	50-100 m	daily	< 20 m	6 hours
leads/polynyas	50-100 m	daily	< 20 m	6 hours
ridges	< 50 m	daily	< 10 m	6 hours
ice decay stage	20 km	weekly	< 5 km	daily
iceberg location	< 50 m	daily	< 5 m	hourly

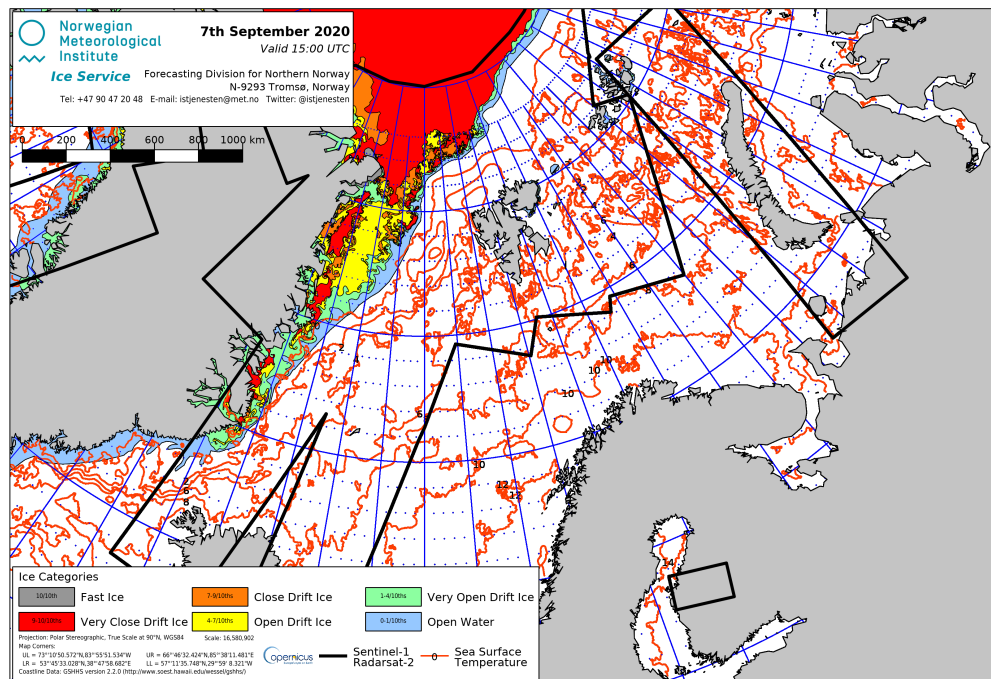


Figure 1.6: Example of an ice chart produced by the NIS. SIC is depicted by different colors. The black lines outline the SAR imagery that was used in production of the chart. The NIS does not provide ice type information on an operational basis.

1.4 Objectives of this Thesis

The previous sections have clearly outlined the need for improved algorithms for automated classification of sea ice types. The work presented in this thesis focuses on the development, training, and testing of such algorithms. For this purpose, existing methods are modified, extended, and tailored to SAR-specific challenges. Particular focus is set on the topics of feature selection (*Paper 1*, Chapter 2) and the dependence of SAR backscatter intensity on incident angle (IA) (*Paper 2*, Chapter 3). *Paper 3* investigates the possible extension of the method developed in *Paper 2* by including textural information.

For the work in *Paper 2* and *Paper 3*, a new training and validation data set for different sea ice types was generated, based on the visual analysis and interpretation of overlapping Sentinel-1 SAR and optical data. The analysis was performed in collaboration with expert sea ice analysts from the NIS, and the data set will be made publicly available in the future. A modified version intended for the application in deep-learning convolutional neural networks (Chapter 2) has already been published [87].

The research presented in this dissertation is part of the Center for Integrated Remote Sensing and Forecasting for Arctic Operations (CIRFA), which is hosted by the Department of Physics and Technology at UiT The Arctic University of Tromsø (UiT) [88].

1.5 Thesis Outline

The classification of sea ice types in SAR imagery requires knowledge from various different research fields. In the next three chapters these fields are introduced and reviewed, in order to establish the understanding of the inter-disciplinary connections inherent in the scientific work of this thesis. The individual chapters are written such that they summarize the necessary knowledge that is needed to understand the contents and assess the quality and research novelty of the journal publications. For a more detailed description of each topic please refer to the referenced literature within the text.

The three journal publications that make up the central part of this thesis deal with different aspects of image classification and algorithm development. Chapter 2 therefore introduces the basic principles of classification and segmentation. Important terminology is defined and the algorithms that form the basis of the work in this thesis are explained.

The main data source in this thesis is SAR imagery. Chapter 3 thus revises the basics of RS with imaging radar, with particular focus on SAR data processing and imaging geometry. Furthermore, it provides an overview of SAR sensor platforms, frequencies and operation modes that are commonly used for sea ice observation.

Sea ice itself is the central topic of Chapter 4. While Section 1.1 of the current chapter

provides a general introduction into the importance of sea ice and the need for constant monitoring and (semi-)automated ice charting, Chapter 4 focuses on different categories for ice type classification. It summarizes the main ice classes of the World Meteorological Organization (WMO) sea ice nomenclature and emphasizes differences and similarities between the WMO ice types and the ice types that can actually be distinguished in radar images (*radar classes*).

Chapters 5 to 8 constitute the journal publications (and their summaries) that are the main scientific novelty of this thesis.

Finally, Chapter 9 summarizes the main findings of the journal publications and outlines potential future work and research directions based on this dissertation. Furthermore, an overview of current and planned applications of the developed algorithms within other national and international projects is given.

/2

Image Classification and Segmentation

All scientific contributions in this dissertation focus on the development and testing of new or modified sea ice classification algorithms. This chapter introduces the basic terminology and mathematics needed to follow these developments and to understand how they extend pre-existing methods in order to overcome certain challenges that are specific to the classification of sea ice types. More extensive information can be found in the literature on the general field of *pattern recognition*, for example in the textbooks by *Schürmann* [89] or *Theodoridis and Koutroumbas* [90], or in online tutorials and programming toolboxes such as *scikit-learn* [91–93].

2.1 Objects, Features, and Classes

The principle goal of pattern recognition is to assign objects into a number of categories or classes [90]. The objects can be anything that can be described by some chosen criteria, usually represented by numbers. They are also referred to as patterns or samples. Throughout this dissertation, these terms will be used synonymously.

The criteria that are used to represent an object or pattern are called features. A feature is a quantity that is either directly measured, or derived from measurements. Features may be categorical, ordinal (relative), integer, real-valued, or complex-valued. The total

number of features used in a classification task is called the *dimensionality* of the problem. For a general l -dimensional problem, the individual features x_i with $i = 1, 2, \dots, l$ form the feature vector \underline{x} :

$$\underline{x} = [x_1, x_2, \dots, x_l] \quad (2.1)$$

In the case of pixel-based SAR image classification, an individual pixel constitutes one sample. Typical features are the backscatter intensity, intensity ratios from different channels, or textural and polarimetric parameters (Chapter 3). Note that the term feature is also commonly used to refer to the surface structure of the sea ice; when this is the case, it will be explicitly mentioned in the dissertation.

Finding the optimal number of features for a given classification task is a crucial step. While adding more features that allow for class separability is usually considered an improvement, there are several reasons to reduce the number of features to an optimal minimum [90]:

- Highly correlated features may carry useful information when used separately, but offer little gain when combined in the feature vector.
- Adding features increases the number of free parameters that need to be optimized in a classifier. The higher the ratio of the number of training samples N_t to the number of free classifier parameters, the better the generalization (Section 2.2) properties of the classifier.
- For a constant number of training samples N_t , increasing the dimensionality l of a classifier beyond a certain point results in an increased classification error (Hughes phenomenon) [94].
- Computation time generally increases with the number of features.

The number of features should thus be kept as large as needed, but as low as possible. This can be achieved by different methods of feature selection or feature transformation, which both lead to dimensionality reduction. A beneficial side effect of dimensionality reduction is that a meaningful visualization of a classification problem and its feature space is only feasible in two (or maybe in some cases three) dimensions. Methods for feature selection can be very simple, such as for example sequential forward feature selection (SFFS) or sequential backward feature selection (SBFS), but a variety of more advanced methods exists [95–97]. *Paper 1* addresses the problem of class-specific feature selection for a multi-class sea ice type classification problem.

2.2 Supervised vs Unsupervised Methods

In the following, the terms *segmentation* and *classification* are used in a strictly defined way:

- Segmentation is the process of assigning an index label to every data sample (pixel in an image) such that samples (pixels) with the same label share certain characteristics (are similar). It finds natural groups in the data. Segmentation is sometimes also referred to as clustering.
- Classification addresses the problem of identifying to which of a set of known categories a new sample (pixel) belongs. A classifier, or a classification algorithm, maps input data to a known category and assigns a meaningful class label.

Segmentation or clustering algorithms can be applied even when no training data is available. The process is completely automatic without manual intervention and thus called *unsupervised*. It should be emphasized here that the group labels in a segmentation result simply indicate similarity, but do not give an interpretive class name. The kind of similarity is defined by the choices of the segmentation algorithm, proximity measure, and clustering criteria. For the example of sea ice charting, the group labels of a segmentation are essentially uninformative for the end user. The different segments must be labeled either manually by an expert analyst or automatically by a classifier that works on the segments instead of individual pixels. Informative class names, which are required in the case of sea ice charting, are always a result of a classification. However, the unlabeled segmentation results can be useful in the development process of a classification algorithm, as they give an indication of the number and the kind of classes that can potentially be separated in a given data set. These radar classes are further discussed in Chapter 4.

Following the above definitions of segmentation and classification, a classification algorithm always needs training data to define the parameters of the classifier based on the trained classes. Training data are samples for which the class label is known. During a training (or fitting) phase, the classifier learns the relationships by which to map samples to a known class. These relationships define the decision boundary between the classes. For the example of a two-dimensional feature space, the decision boundary can be visualized as a line (Figure 2.1, left side). Different algorithms allow for different forms of the decision boundary (Section 2.3). The goal of the training stage is to find the optimal decision boundary within the given framework of the algorithm (Figure 2.1). The optimal decision boundary results in the best generalization properties for the classifier. This requires that the available training data are representative for each class and not biased towards particular situations. During forward classification (or prediction), the classifier uses the relationships that were learned in the training stage to predict the labels for new patterns. Because of its inherent need for user intervention and training, this is called a *supervised* method. In a strict sense, classification is always supervised. However, once an algorithm has been trained on a representative data set, it can be applied to new data without re-

training. Nevertheless, the forward classification of new samples is never possible though without the initial supervised training phase at an earlier stage.

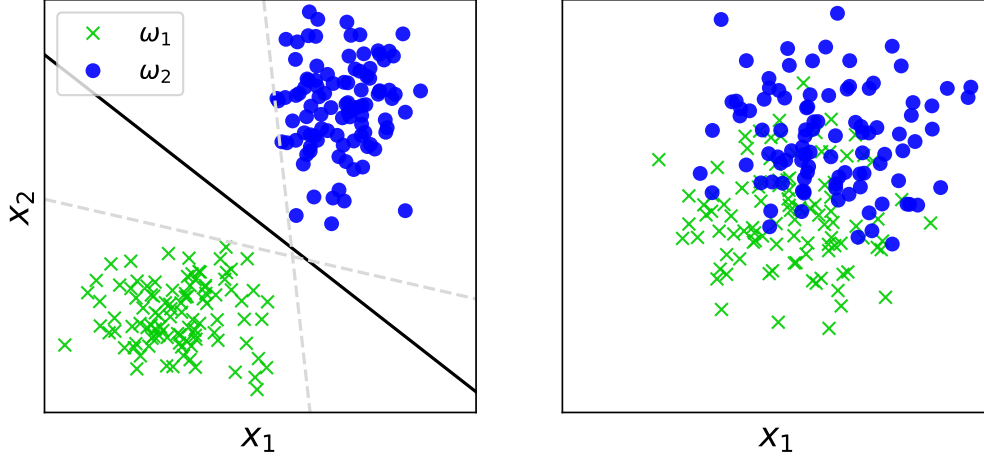


Figure 2.1: Simulated training samples for a two-dimensional two-class problem. The left side shows a separable problem with several possible linear decision boundaries. The solid line indicates the presumably optimal decision boundary with best generalization properties of the classifier. The right side shows a non-separable problem. It is still possible to define an optimal decision boundary, but some classification error will inherently occur.

2.2.1 Validation

Once a supervised classification algorithm is developed and trained, it is important to validate its performance and assess the quality of the results. The validation should be performed on an independent data set, called the *validation set*. This is usually achieved by randomly splitting the full set of available samples with known labels into a training and a validation set. While training and optimization of the classifier's free parameters is performed exclusively on the training set, the validation set can be used to estimate an independent classification accuracy (CA).

CA for a single class is given by the fraction of the number of correctly classified validation set samples from class ω_i ($N_{v,i}^{correct}$) over the total number of validation set samples from that class ($N_{v,i}$):

$$CA_i = \frac{N_{v,i}^{correct}}{N_{v,i}} \quad (2.2)$$

The average per-class CA for a problem with M total classes is then defined as:

$$\overline{CA} = \frac{1}{M} \sum_{i=1}^M CA_i \quad (2.3)$$

The total CA is the number of overall correctly classified validation samples ($N_v^{correct}$) divided by the total number of validation samples (N_v):

$$CA = \frac{N_v^{correct}}{N_v} \quad (2.4)$$

The total CA can be biased by the abundance of the different classes in the validation set and can therefore differ significantly from the average per-class CA.

Having independent training and validation sets is particularly important in order to avoid overfitting or overtraining of the classifier. Overfitting means that the free parameters that define the decision boundary adapt to peculiarities of a specific training set [98]. While the classification error on the training set continues to decrease in such a case, the generalization properties of the classifier become worse and the classification error on the independent validation set increases. Figure 2.2 conceptually shows the effect of overfitting on the classification error for an iteratively trained method such as a neural network (NN) (Section 2.4.2).

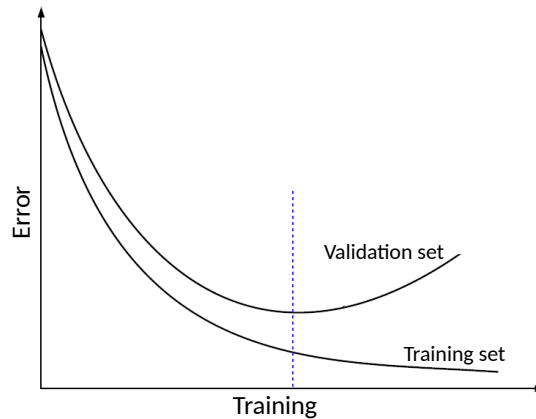


Figure 2.2: Classification error of the training set and an independent validation set during iterative training of a classifier with a large number of free parameters. At the dotted line, the classifier starts to adapt to peculiarities in the training set and the classification error of the validation set begins to increase (modified from [90]).

The validation of segmentation results is less straightforward. Different choices of algorithm, proximity measure, and clustering criteria may lead to totally different clustering results, all of which are equally valid. Neither result is objectively better or worse. The most common solution is to give the clustering results to an expert analyst and let the expert decide about the most sensible one [90]. However, the validation is always subjective and influenced by the experience of the expert.

2.3 Linear vs Non-Linear Classifiers

Depending on the distribution of the data and the available features, a classification problem can be either separable or inseparable (Figure 2.1). The decision boundary is either a point (1D), a line (2D) or a hyperplane (3D or more) that separates the different classes in the feature space. Different classification algorithms produce different forms of decision boundaries. Generally, a linear classifier defines a linear boundary, and a non-linear classifier defines a non-linear boundary (Figure 2.3). A problem can be linearly separable, non-linearly separable, or not separable at all. In the latter cases, a non-linear classifier is expected to achieve better results than a linear classifier. However, a non-linear classifier usually has more free parameters to define the decision boundary than a linear classifier, and may therefore be subject to overfitting. In the work in this thesis, both linear and non-linear classifiers are used and their advantages and drawbacks in terms of computation time and generalization properties are discussed.

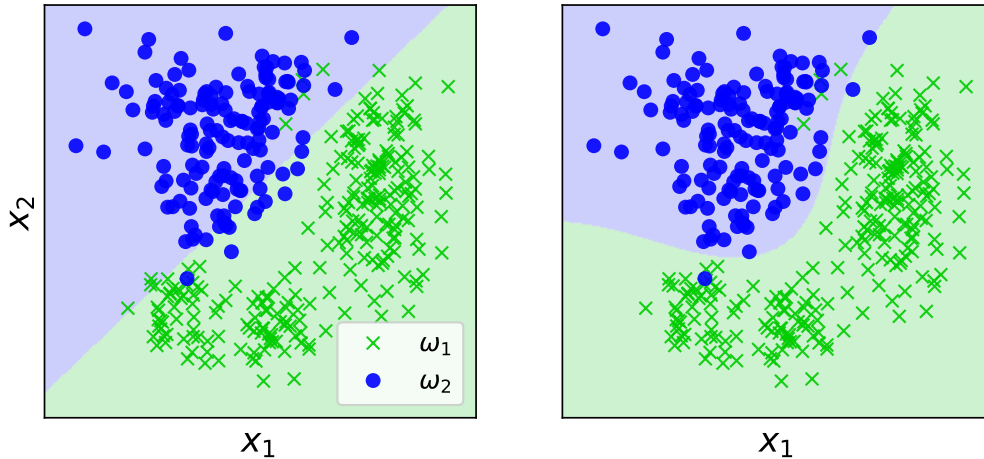


Figure 2.3: Simulated training samples for a two-dimensional two-class problem that is not linearly separable. Optimal linear and non-linear (support vector machine with radial basis function kernel, Section 2.4) decision boundaries are shown on the left and right side, respectively.

2.4 Common Classification Algorithms

There is a large variety of supervised classification algorithms, and the choice of the best algorithm for a given problem is not always clear or straightforward. Therefore, it is helpful to understand the basic principles of different algorithms in order to assess their suitability for a particular task.

Most of the algorithms developed in this dissertation are based on Bayes decision theory. Bayesian classifiers are introduced in the first part of this section. The second part reviews

the principle ideas behind three other methods that are commonly used in sea ice classification. These three methods are also used as comparison methods to the algorithms developed in the papers of this dissertation.

2.4.1 Bayesian Classifiers

A Bayesian classifier is a statistical classification method that assigns each pattern \underline{x} to the most probable class ω_i :

$$\underline{x} \rightarrow \omega_i \quad \text{if} \quad P(\omega_i|\underline{x}) > P(\omega_k|\underline{x}) \quad \forall \quad k \neq i, \quad (2.5)$$

$P(\omega_i|\underline{x})$ is the data-conditional probability (also called posterior probability) of the pattern \underline{x} belonging to class ω_i . According to equation 2.5, $P(\omega_i|\underline{x})$ needs to be calculated for all classes $i = 1, 2, \dots, M$, so that the pattern can be assigned to the class with the highest posterior probability. This can be done by exploiting Bayes rule, which is given by:

$$P(\omega_i|\underline{x}) = \frac{p(\underline{x}|\omega_i)P(\omega_i)}{p(\underline{x})} \quad (2.6)$$

Here, $p(\underline{x}|\omega_i)$ is the class-conditional probability density function (PDF) of \underline{x} , $P(\omega_i)$ is the prior probability of class ω_i , and $p(\underline{x})$ is the PDF of \underline{x} , respectively. Combining Equations 2.5 and 2.6, the decision rule for a Bayesian classifier can be written as:

$$\underline{x} \rightarrow \omega_i \quad \text{if} \quad p(\underline{x}|\omega_i)P(\omega_i) > p(\underline{x}|\omega_k)P(\omega_k) \quad \forall \quad k \neq i, \quad (2.7)$$

One now needs to know the class-conditional PDF $p(\underline{x}|\omega_i)$ and the prior probability $P(\omega_i)$ for each class ω_i . In practice, the prior probabilities are often either assumed to be equal, or can be estimated from the available training data:

$$P(\omega_i) \approx \frac{N_{t,i}}{N_t} \quad (2.8)$$

where N_t is the total number of training samples, and $N_{t,i}$ is the number of training samples for class ω_i .

The class-conditional PDF is usually estimated from the training data as well. This estimation is a crucial step in Bayesian classification, and subject to various assumptions. For a known (or assumed) parametric form of the PDF, the PDF-parameters for each class are estimated directly from the training data. The most common case is to assume a Gaussian distribution (Figure 2.4) and use a maximum likelihood (ML) approach to find the mean vector μ_i and covariance matrix Σ_i for each class. If the form of the PDF is unknown, it can be approximated through kernel density estimation [99]. The kernels are also known as Parzen windows. A typical example is the Gaussian kernel. The PDF of class ω_i is then approximated as an average of $N_{t,i}$ Gaussians, that are each centered at one point of the training set. The width of the Gaussian kernel affects the smoothness of the PDF and needs to be adjusted for the specific task and the amount of training points (Figure 2.5).

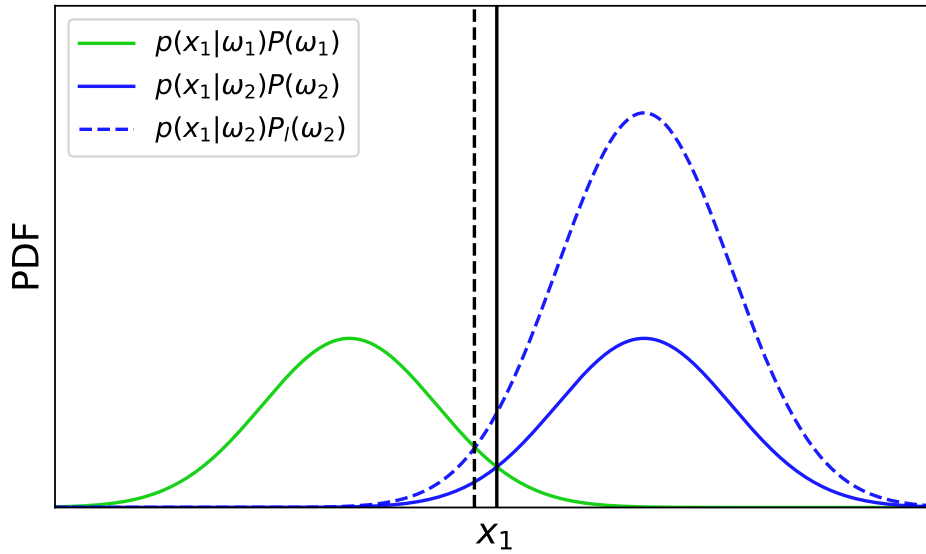


Figure 2.4: Gaussian PDFs for a simulated one-dimensional two-class problem. The solid lines show the class-conditional PDFs and the resulting decision boundary (solid black line) with equal prior probabilities $P(\omega_1) = P(\omega_2)$. The dashed blue line depicts the case of a larger prior probability for class ω_2 : $P_l(\omega_2) > P(\omega_1)$. The decision boundary (dashed black line) is shifted in that case.

While the assumption of a Gaussian PDF leads to linear or quadratic decision boundaries [90], the kernel density estimation results in a free form PDF and thus allows for more complex, nonlinear decision boundaries. However, Gaussian PDFs offer the advantage of easy computation and thus faster training and prediction times and are therefore preferable whenever appropriate for the actual underlying distribution of the data.

Paper 1 and *Paper 2* in this dissertation both develop new sea ice type classification strategies based on Bayesian decision theory. Kernel density estimation is applied in *Paper 1*, whereas *Paper 2* introduces a modified Gaussian PDF with a variable mean value to account for intensity variation with IA in the SAR data (Chapter 3).

2.4.2 Random Forests, Support Vector Machines, and Neural Networks

Random Forests

A random forest (RF) is an ensemble deep-learning classification technique [100], which is commonly used in sea ice classification [101–103]. It constructs a number of single decision tree (DT) classifiers on various sub-samples of the training set and uses averaging of the results to decide the final class label. Each individual DT in the forest is a multistage decision system that sequentially rejects classes along a path of nodes until the final

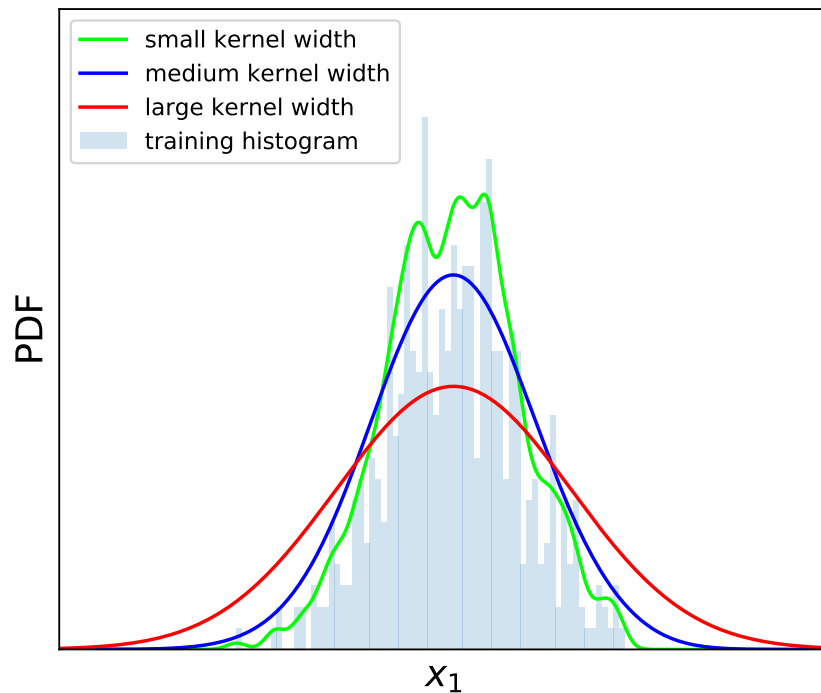


Figure 2.5: 1D Kernel density estimation for Gaussian kernel functions with different widths. A wide kernel function (red) results in a smoother PDF.

class of a pattern is found. The most common trees split the feature space linearly into hyper-rectangles with sides parallel to the axes of the feature space. However, more elaborate and complicated trees can be constructed using different methods and splitting criteria [90].

In *Paper 1*, an optimal DT with underlying non-linear Bayesian classifiers for the splits at each node is developed and tested on a multi-class sea ice type classification problem. While such an optimized DT offers several advantages (Chapter 6), its design and training is computationally expensive and time-consuming. In contrast to the single optimized tree, a typical RF uses a larger number of more simply constructed trees. The high variance that is inherent to the individual trees is then overcome by averaging. Each tree in the RF is built on a randomly sub-sampled variant of the training set and a random selection of available features [104]. The randomness of the feature and training sub-set selection has a substantial effect in the performance of the classifier, improves the final CA, and helps to control over-fitting [90, 105]. The key parameters that need to be tested and optimized with regard to CA include the total number of trees and the number of nodes in the individual trees.

Support Vector Machines

The support vector machine (SVM) is another type of classifier often used in sea ice classification [106–108]. It is a machine learning method that can model nonlinear decision boundaries through the use of kernel functions [108]. In its original form, however, the SVM is a linear classifier, that finds an optimal linear decision boundary in the training set. The optimal boundary is defined as the boundary that maximizes the margin to the closest training samples from each class. These closest training samples are called the support vectors. For classification problems that are not linearly separable, the SVM can be adapted to either allow for a certain number of misclassified samples, or to model a nonlinear decision boundary. For the latter case, a nonlinear kernel function [90] is introduced in the SVM cost function. Examples for linear and non-linear SVM decision boundaries are shown in Figure 2.3. The choice of the kernel is a key parameter that influences the classification result and needs to be tested and optimized for a specific task.

Neural Networks

Neural networks (NN) are a popular type of machine learning algorithm and have consequently been applied in sea ice classification on multiple occasions [109–112]. In its basic form, a NN used for classification combines various linear classifiers with non-linear outputs (through an activation function) to map input data to a class label. As a whole, the network consists of an input layer, one or more hidden layers with a certain number of nodes that transform the data, and an output layer that performs the final classification (Figure 2.6). The input layer simply contains the nodes where the input data, that is the different features of the input pattern, is applied. The number of nodes in the input layer is therefore equal to the dimensionality of the task. The nodes between the different layers are connected by weights $w_{i,j}$, and each node in the hidden layer transforms the output from the previous layer by a weighted linear summation followed by a nonlinear activation function [113]. This internal feature transformation lets the network find the optimal, nonlinear feature combinations for the problem. Finally, the output layer transforms the values from the last hidden layer into a class label. The weights are the free parameters of the NN. During training, they are optimized by backpropagation of errors through the network [114]. The training is performed iteratively by repeatedly running the training through the network until the classification error is minimized (Figure 2.2). The network architecture (that is the number of hidden layers and the number of nodes within each layer) is usually determined by the user and must be optimized for a given task. Due to the potentially large number of free parameters, NNs can require a long training time compared to other algorithms. However, once a network is trained, prediction time for new samples is usually fast compared to other algorithms.

In recent years, deep-learning NNs with a large number of hidden layers and convolutional neural networks have become popular in image processing and the analysis of sea ice in SAR images [115–117]. A convolutional neural network (CNN) makes use of convolution

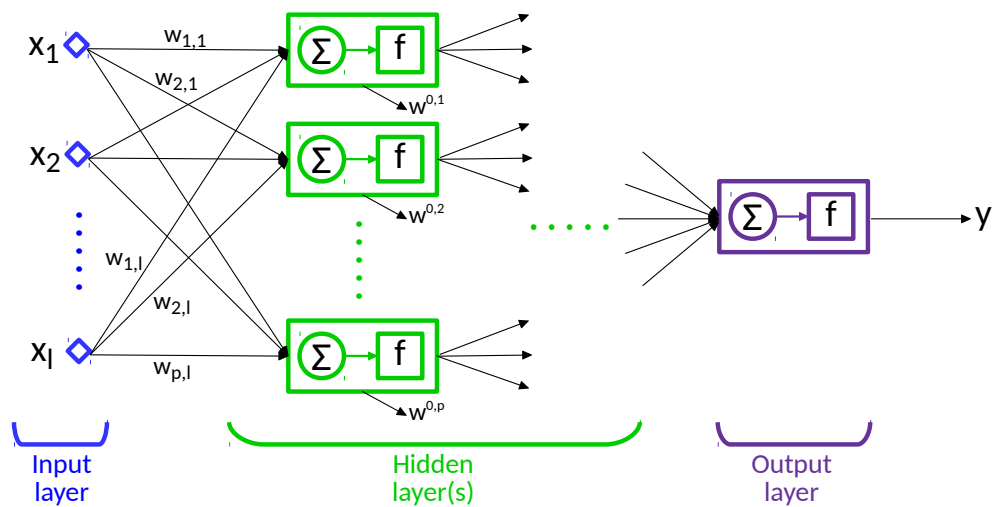


Figure 2.6: Schematic architecture of a NN for classification. Input, hidden, and output layers are connected by weights that are optimized during training. Each node in the hidden layer(s) transforms the output from the previous layer by a weighted linear summation and a nonlinear activation function. The output layer maps the values from the last hidden layer to a class label.

and pooling operations within certain window sizes in order to incorporate contextual information into the classification process. The application of CNNs in sea ice type classification is at present an ongoing research topic and investigated in various research projects [118, 119]. While CNNs are not covered directly by the papers presented in this dissertation, the data set that was generated for *Paper 2* and *Paper 3* has been adopted for deep-learning applications within the *Extreme Earth* project [87, 119].

/ 3

Spaceborne Imaging Radar

The main data source for operational ice services and for the scientific work in this dissertation is SAR. SAR is an imaging radar that can be operated from planes (airborne) or satellites (spaceborne) to produce two-dimensional images of the Earth surface. This chapter reviews the basic principles of spaceborne SAR, with particular focus on its application for RS of sea ice.

Radar (radio detection and ranging) systems are generally based on the concept of echolocation. An antenna transmits an EM signal and measures the returned echo from a specific target. Assuming that the speed of the signal is known, the distance between the antenna and the target can be calculated from the travel time of the signal.

After the first successful generation of radar waves by Heinrich Hertz in 1886 and the use of initial sensors for target detection in the early 20th century, the general development of radar instruments advanced quickly in military applications during the second world war [66]. A significant part of the groundwork on radar technology was developed in that time. The first imaging radars were introduced in the early 1950s. They were mounted on airborne platforms (planes) and the achieved image resolution was dependent on the flight altitude of the plane and limited by the antenna size (Section 3.1.1). The transition from airborne to fine-resolution spaceborne imaging radar only became feasible in the late 1950s and early 1960s, with the development of side-looking airborne radar (SLAR) and the SAR processing technique [66]. The first civilian spaceborne SAR sensor was launched in 1978 on board the oceanographic Seasat satellite, but only operated for three months. For the scientific community, spaceborne SAR became more routinely available in the early 1990s with the launches of the European remote-sensing satellites (ERS-1/2), the Japanese

Earth resource satellite (J-ERS-1), and the Canadian Radarsat-1 mission.

Today, there are several SAR instruments orbiting the Earth, operating at different frequency bands, polarization channels and spatial resolutions (Table 3.1). They provide an essential contribution to observations of remote and inaccessible areas, such as the polar regions. Since SAR is an active system generating its own signal, the observations are independent of solar illumination or any other naturally emitted radiation [120] (Section 1.2.2). Moreover, the typical SAR wavelengths penetrate through clouds without or with only weak loss of energy [121] (Section 3.1.4). SAR sensors can thus acquire images continuously, independent of sunlight and weather conditions. This is of particular importance in the Arctic, with persistent darkness during polar night and typically about 70-80 % of cloud cover [122] throughout the year. Its all-day and all-weather imaging capability has made SAR the primary data source for sea ice charting in operational ice services worldwide [83]. However, SAR images are quite different from optical images and can be challenging to interpret.

The following sections provide an overview of the fundamental principles of SAR imaging, with particular focus on the imaging geometry, spatial and temporal resolution, frequency and polarization, as well as speckle, noise artifacts and scattering mechanisms. More detailed information is available in textbooks such as *Elachi and Van Zyl* [123], *Richards* [65], or *Ulaby and Long* [66].

Table 3.1: Examples of currently operating spaceborne SAR sensors that are commonly used for sea ice observations. The bands and polarization terms are defined in Section 3.1.4. Note that the indicated polarization is the maximum polarization capability.

Sensor	Launched	Frequency Band	Polarization	Country
Radarsat-2	2007	C-band	quad	Canada
TerraSAR-X/TanDEM-X	2007/2010	X-band	quad	Germany
HJ-1C	2012	S-band	VV	China
ALOS-2	2013	L-band	quad	Japan
Kompsat-5	2013	X-band	dual	Korea
Sentinel-1A/1B	2014/2016	C-band	dual	Europe
SAOCOM-1A	2018	L-band	quad	Argentina
Radarsat Constellation	2019	C-band	dual/compact	Canada

3.1 SAR Systems as Tools for Sea Ice Monitoring

3.1.1 Imaging Geometry and Spatial Resolution

The geometry of a side-looking imaging radar system is sketched in Figure 3.1. As the sensor platform moves in the azimuth (along-track) direction, the side-looking antenna sends an

EM pulse in the slant-range (across-track) direction. The antenna dimensions determine the size of the illuminated area on the ground. The swath width is the coverage of the image in range direction [124]. While slant range is measured along the radar's line of sight, the measurements can be re-sampled to ground range, which is measured along the Earth surface as distance from nadir (the point directly below the sensor platform). Ground range detected images are still in the radar geometry. For visualization on a map or combination with other data sources, they can be geo-located to a map projection [121].

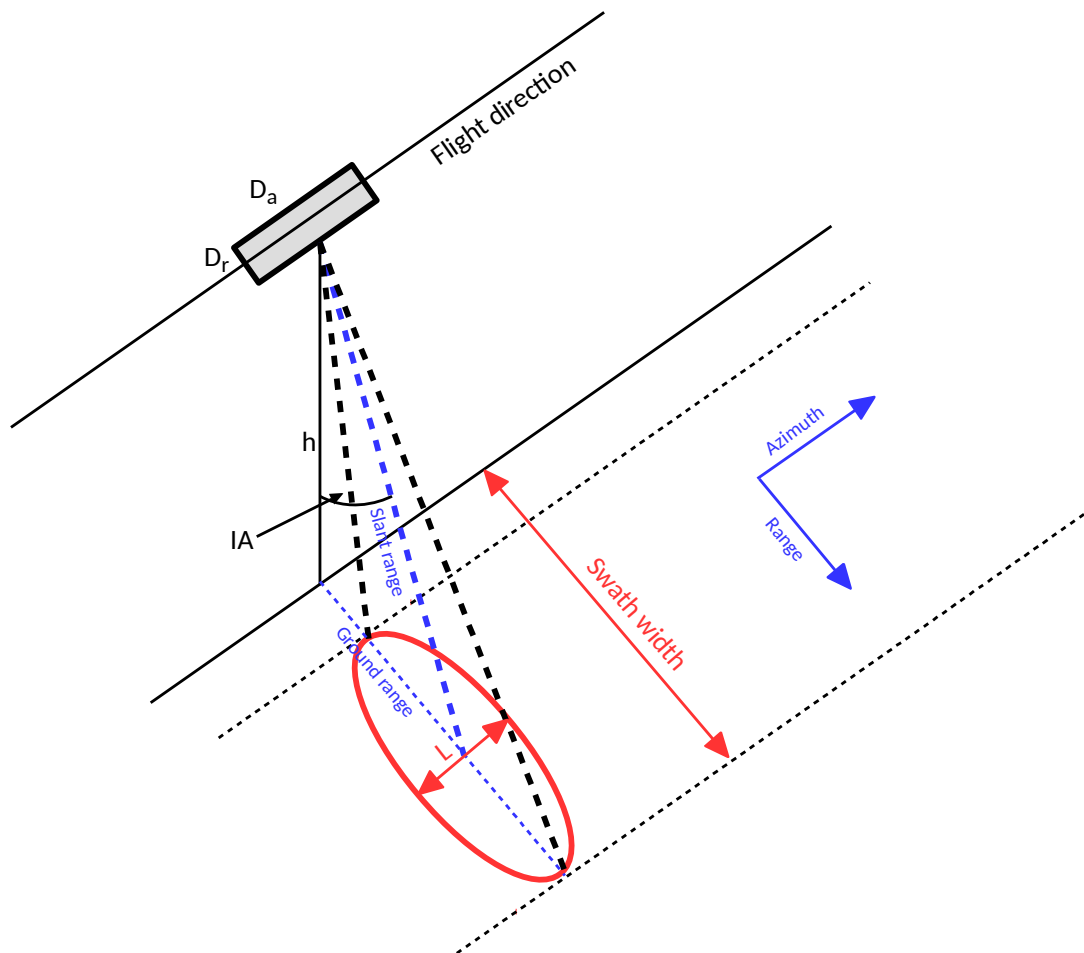


Figure 3.1: Simplified SAR imaging geometry (modified from [125]). ($D_r \times D_a$): antenna dimensions, h : platform flight altitude, L : Synthetic aperture length.

The illumination geometry is often given in terms of the IA , which is the angle between the radar beam and the normal to the surface. The IA increases across the swath from near range (close to the satellite track, low IA) to far range (far from the satellite track, high IA). The geometry can also be described in terms of the elevation angle, which is the angle between the radar beam and the vertical direction at the Earth surface.

The image that is acquired by a radar system as sketched in Figure 3.1 consists of pixels that are associated with a given area on the Earth surface. The spatial resolution of that image is defined as the minimum distance between the two closest points on the ground that can still be distinguished [126]. For a real aperture radar (RAR), the resolution in both range and azimuth direction depends on the physical size of the antenna ($D_r \times D_a$), the pulse duration τ , the signal wavelength λ , and the flight altitude h of the sensor platform:

$$\begin{aligned} r_{gr} &= \frac{c\tau}{2\sin\theta} \\ r_{az} &= \frac{\lambda}{D_a}R_0 \end{aligned} \quad (3.1)$$

Here, r_{gr} is the ground range resolution, r_{az} is the azimuth resolution, c is the speed of light, θ is the IA, and R_0 is the slant distance from the platform to the point at the ground where the azimuth resolution is considered.

Assuming typical values for the radar system parameters ($\tau=10 \mu\text{s}$, $\theta=30^\circ$ [65]) yields a ground range resolution of 3000 m. This is insufficient for operational sea ice observations and ice charting, as well as many other SAR applications (Table 1.1, Section 1.3). Given Equation 3.1, the obvious way to improve range resolution would be to narrow the transmitted pulse. However, a shorter pulse carries less energy and thus limits the sensitivity of the radar. This problem is solved by transmitting a frequency modulated pulse, called a chirp, in which the frequency is linearly changed during the duration of the signal. On reception of the returned signal, the chirp is correlated with a replica of itself, resulting in a very short, compressed pulse. This technique, called pulse compression, is applied in both RAR and SAR [123]. The resulting resolution in range direction depends on the bandwidth B_c of the transmitted chirp and is given by:

$$r_{gr} = \frac{c}{2B_c\sin\theta} \quad (3.2)$$

Typical ground range resolution for imaging radars using pulse compression is on the order of tens of meters (Section 3.1.2, Table 3.2).

The azimuth resolution depends on the antenna size and the distance to the surface. Assuming typical values for an airborne system ($\lambda=0.03 \text{ m}$, $D_a=3 \text{ m}$, $R_0=2000 \text{ m}$) yields an along-track resolution of 20 m [65]. However, placing the same system in space, at an altitude of around 1000 km, results in much coarser azimuth resolution (no better than 10 km). According to Equation 3.1, the easiest way to improve azimuth resolution would be to physically increase the antenna size, which is not feasible for spaceborne instruments. The actual solution uses sophisticated data processing that makes use of the forward motion of the sensor platform and the phase and Doppler shift of the signal, that is caused by the movement of the sensor platform. This SAR processing synthesizes an apparently long antenna, which is several orders of magnitude larger than the physical antenna on board the satellite. The length of the synthetic aperture is determined by the time that a particular target on the ground is illuminated by the radar (Figure 3.2). The mathematical

basis for SAR processing can be found in several of the textbooks mentioned above. It leads to the remarkably simple result, that the along-track resolution is given by:

$$r_{az} = \frac{D_a}{2} \quad (3.3)$$

SAR azimuth resolution does not depend on the flight altitude of the sensor platform. The imaging system can therefore be transferred to spaceborne satellites without loss of detail in the images. Furthermore, Equation 3.3 shows that a shorter antenna will actually result in improved resolution, albeit at the expense of sensitivity. In practice azimuth resolution is limited by the desired area coverage and observation geometry (Section 3.1.2), as well as technological factors, such as the data collection rate and volume, the pulse power, phase control, and calibration [126].

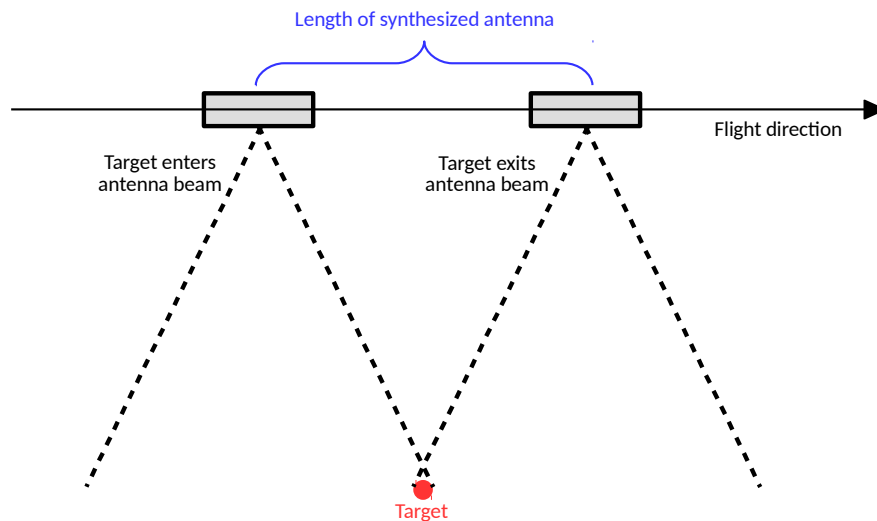


Figure 3.2: Forward movement of the SAR platform over a target on the surface. The length of the synthesized antenna is determined by the time that the target is illuminated by the radar.

3.1.2 Data Acquisition Modes

Most spaceborne SAR sensors can operate in different acquisition modes. These modes differ in spatial coverage, resolution, and availability of polarimetric channels (Section 3.1.4). The best acquisition mode and respective image product for a particular application must therefore be chosen based on its specific goals and requirements, as well as overall data availability.

The most common acquisition modes are the stripmap (SM) and the ScanSAR mode. In SM mode, the antenna footprint is fixed to one swath and a continuous strip on the Earth surface is imaged. The ScanSAR mode achieves wider spatial coverage by steering the antenna to different elevation angles and combining multiple subswaths. This improved

Table 3.2: Sentinel-1 acquisition modes and key parameters. (stripmap (SM), interferometric wide swath (IW), extra wide swath (EW), wave (WV))

Mode	Swath Width (km)	Resolution	IA Range (deg)
SM	80	5 x 5 m	18.3 - 46.8
IW	250	5 x 20 m	29.1 - 46.0
EW	400	20 x 40 m	18.9 - 47.0
WV	20	5 x 5 m	21.6 - 25.1; 34.8 - 38.0

spatial coverage comes at the cost of coarser spatial resolution. Individual SAR sensors offer further acquisition modes, such as the Radarsat-2 fine quad-pol (FQP) and wide fine quad-pol (WFQP) modes or the Sentinel-1 wave (WV) mode. The extra wide swath (EW) and interferometric wide swath (IW) modes available for Sentinel-1 are essentially an improved version of the traditional ScanSAR mode, called terrain observation by progressive scan (TOPS) [127]. Table 3.2 shows an overview of Sentinel-1 acquisition modes and key parameters. The different modes are illustrated in Figure 3.3.

The Sentinel-1 EW mode is aimed primarily for use over sea ice, polar zones and certain maritime areas, in particular for ice, oil spill monitoring and security services [127]. It offers wide coverage at a resolution that is acceptable for at least some requirements of operational sea ice charting (Tables 1.1 and 3.2). *Paper 2* and *Paper 3* of this dissertation both focus on the development of operational algorithms and therefore use Sentinel-1 EW mode data as the primary data source. Higher resolution modes, such as the Radarsat-2 FQP mode, offer more detail about individual structures on the ice surface and can be very useful for particular applications and academic studies. However, their spatial coverage is usually not sufficient for operational ice services (Figure 3.4).

3.1.3 Temporal Resolution

The temporal resolution of a spaceborne SAR sensor is given by the satellite revisit cycle. The revisit cycle is the time between two observations of the same target on the Earth surface. Depending on the satellite orbit, these observations can occur at different IAs. The revisit cycle is not to be confused with the repeat cycle, which is defined as the time between two passes of a satellite along the exact same orbit [128]. While the repeat cycle only depends on the satellite orbit configuration, the revisit time is also dependent on the target location and the swath width. Most spaceborne SAR sensors are on Polar orbiting satellites. The orbit track spacing on the Earth surface for these satellites is closer at higher latitudes, which results in a significantly greater revisit rate in the Polar regions compared to the equator.

For example, the repeat cycle for Sentinel-1 is twelve days, with 175 full orbits per cycle. Since Sentinel-1a and Sentinel-1b share the same orbit plane with a 180° orbital phasing

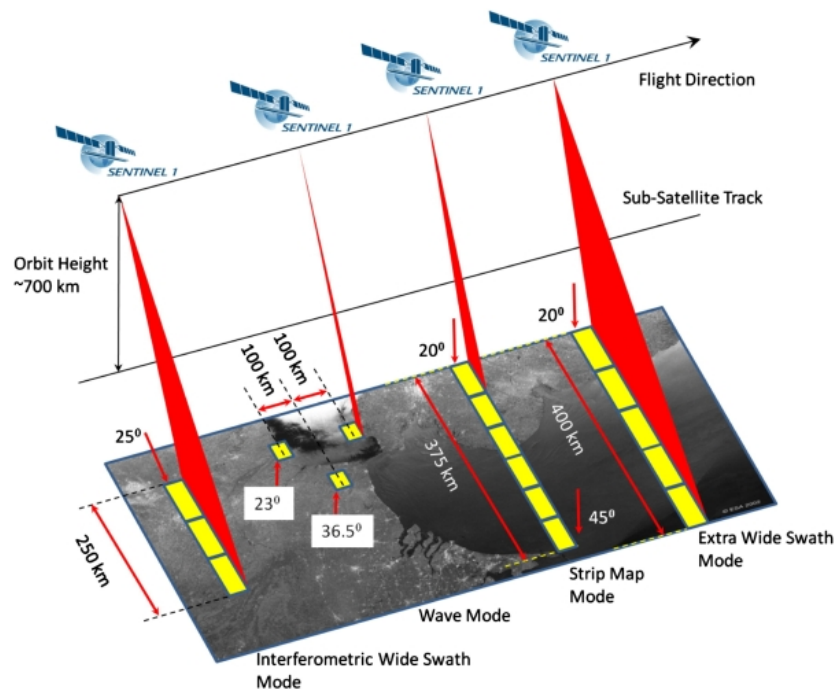


Figure 3.3: Illustration of Sentinel-1 acquisition modes. Figure from European Space Agency (ESA) [127].

difference, the effective repeat cycle of the constellation is reduced to six days. While the combined revisit interval at the equator is about three days, the Polar regions are imaged more than once a day [129]. Combining different sensors and satellites can improve temporal resolution even further.

3.1.4 Frequency and Polarimetry

Frequency

Most spaceborne SAR systems operate at wavelengths between 0.5 and 75 cm [130]. The main benefit of using this spectral region is that the atmosphere can essentially be regarded as transparent for wavelengths larger than 3 cm (Section 1.2.2). Table 3.3 gives an overview of the specific microwave wavelength and frequency bands.

The choice of wavelength should match the size of surface structures of the targeted object, because the backscattered energy depends on the surface roughness relative to the wavelength. Furthermore, in the case of sea ice, longer wavelengths are more likely to penetrate through the snow cover and deeper into the ice, which results in a stronger contribution of volume scattering (Section 3.3). The most commonly used frequency bands for spaceborne SAR observations of sea ice are L-, C-, and X-band [82].

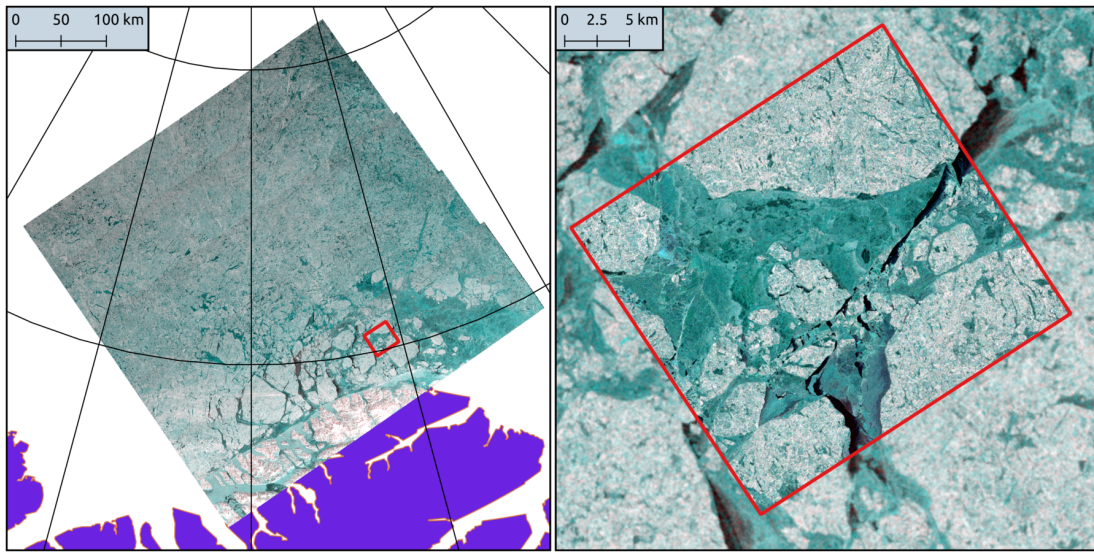


Figure 3.4: Spatially overlapping Sentinel-1 EW and Radarsat-2 FQP mode images, acquired north of Greenland on March 18th 2018 with a time difference of 23 minutes. Both images are displayed in false-color representation, with green=HV, red=HH, blue=HH for Sentinel-1 and green=HV, red=HH, blue=VV for Radarsat-2, respectively.

The use of different frequencies can give complementary information about the surface. This can be particularly helpful for classification of sea ice types, where multi-frequency observations can significantly increase CA [133–135]. The main challenge in using multi-frequency data is the data acquisition and co-location. Images with different frequencies must be acquired overlapping closely in space and time, which can be difficult to achieve with the individual acquisition plans of different satellites. Co-location of the images usually requires a correction for sea ice drift [136]. *Paper 1* of this dissertation uses an airborne multi-frequency data set and develops a method to assess and exploit the particular advantages of certain frequencies for the classification of individual sea ice classes.

Polarimetry

An EM wave consists of an electric and a magnetic field. These fields are perpendicular to each other and to the direction of wave propagation. The polarization of the signal is defined as the orientation of the electric field and can be described in terms of two orthogonal basis vectors [123]. EM waves are generally elliptically polarized, with linear or circular polarization as special cases [120].

Most SAR satellites use linear polarization on both the transmitter and the receiver. The polarization direction is either horizontal (H) or vertical (V) to the plane of wave propagation. An individual SAR channel can then be described with a two-letter combination,

Table 3.3: Wavelength and frequency bands of radar remote sensing (based on IEEE standards [131,132]).

Band	Frequency (GHz)	Wavelength (cm)
VHF	0.03–0.3	100–1000
UHF	0.3–1	30–100
L	1–2	15–30
S	2–4	7.5–15.0
C	4–8	3.75–7.5
X	8–12	2.5–3.75
Ku	12–18	1.67–2.5
K	18–27	1.11–1.67
Ka	27–40	0.75–1.11

where the first letter indicates the polarization of the transmitted signal and the second letter the polarization of the received signal. For example, the HV channel transmits at horizontal polarization and measures at vertical polarization, respectively.

The information about a target's scattering signature can be summarized in the scattering matrix S [120]:

$$E^r = \begin{bmatrix} S_{HH} & S_{VH} \\ S_{HV} & S_{VV} \end{bmatrix} E^t = SE^t \quad (3.4)$$

Here, E^t and E^r are the transmitted and received electric field vectors, respectively, and S_{pq} with $p, q \in \{H, V\}$ are the complex scattering coefficients within the scattering matrix. The reciprocity theorem states that $S_{HV} = S_{VH}$ [65, 120]. This holds for typical conditions of radar remote sensing from space, and the scattering matrix S can be written as:

$$S = \begin{bmatrix} S_{HH} & S_{HV} \\ S_{HV} & S_{VV} \end{bmatrix} \in \mathbb{C}^{2 \times 2} \quad (3.5)$$

The full scattering coefficients contain both amplitude and phase information. SAR images are often displayed as intensity images, where the intensity is equal to the amplitude squared. The phase information is then lost. The intensity of single SAR channels is usually shown as a gray-scale image. Multiple channels can be displayed as false-color representations, where individual channels or combinations of channels are assigned to the R,G,B channels of the color image (Figure 3.4). In order to relate the pixel values to the actual radar backscatter value and allow for comparison between different images and sensors, the data must be calibrated. The intensity is therefore often given in terms of the normalized radar cross section σ^0 , which is proportional to the ratio of received power P^r over transmitted power P^t [137]:

$$\frac{P^r}{P^t} = \sigma^0 \frac{\lambda^2 G^2 A}{(4\pi)^3 R^4 \sin\theta} \quad (3.6)$$

This known as the *radar equation*, where λ is the wavelength, G is the antenna gain pattern, A is the area on the ground, R is the distance to the target, and θ is the IA.

While a fully polarimetric (quad-pol) SAR system measures all four components of the scattering matrix S [138], single- and dual-pol systems only measure one or two of the components, respectively. In the field of SAR polarimetry, the full scattering matrix can be used to calculate the covariance and coherency matrix. These matrices are frequently used in decomposition methods, form the basis for the extraction of polarimetric features, and are input to physical scattering models [120, 139].

In operational sea ice classification, fully polarimetric data play only a minor role. The spatial coverage that is achieved by most quad-pol acquisition modes is usually on the order of tens of kilometers (for example 25 km for Radarsat-2 FQP), compared to hundreds of kilometers for ScanSAR modes (for example 400 km for Sentinel-1 EW). Furthermore, most available studies agree that the first step for a major improvement of operational sea ice mapping is achieved by combining different frequency bands rather than different polarizations [140]. However, fully polarimetric data are helpful and needed for certain sea ice applications, such as the possible retrieval of thin ice thickness and the improvement of our understanding of the interaction between radar waves and sea ice [140].

3.2 Speckle and Noise

One characteristic property of SAR images is their grainy appearance (Figure 3.5). This is called speckle, and sometimes also referred to as "salt-and-pepper" noise. Speckle is an inherent property in all coherent imaging systems. It is the result of constructive and destructive interference of the energy reflected from the many elemental scatterers that are located within a resolution cell (or pixel) [65]. Although often referred to as noise, speckle is in fact a deterministic and repeatable phenomenon, and thus strictly speaking not noise [137]. Speckle degrades the SAR image quality and complicates both manual and automated interpretation and classification. Several techniques for speckle reduction exist, all of which ultimately have a trade-off between radiometric and spatial resolution [120].

One of the most straightforward speckle filters is multi-looking. Multi-looking can be performed incoherently during image formation by dividing the full aperture into sub-apertures that are then averaged, or in the spatial image domain by averaging over a set of neighbouring pixels within a defined window. The standard deviation of the speckle is reduced proportionally to the square root of the number of independent looks [141]. Multi-looking consequently reduces the grainy appearance of the image, but at the cost of a decreased spatial resolution (Figure 3.5).

There are several other noise artifacts present in SAR images [142]. The noise sources

include cross-talk between different polarization channels [126], aliasing, antenna sidelobe effects, and system thermal noise [143]. Automation of sea ice classification is particularly affected by the thermal system noise.

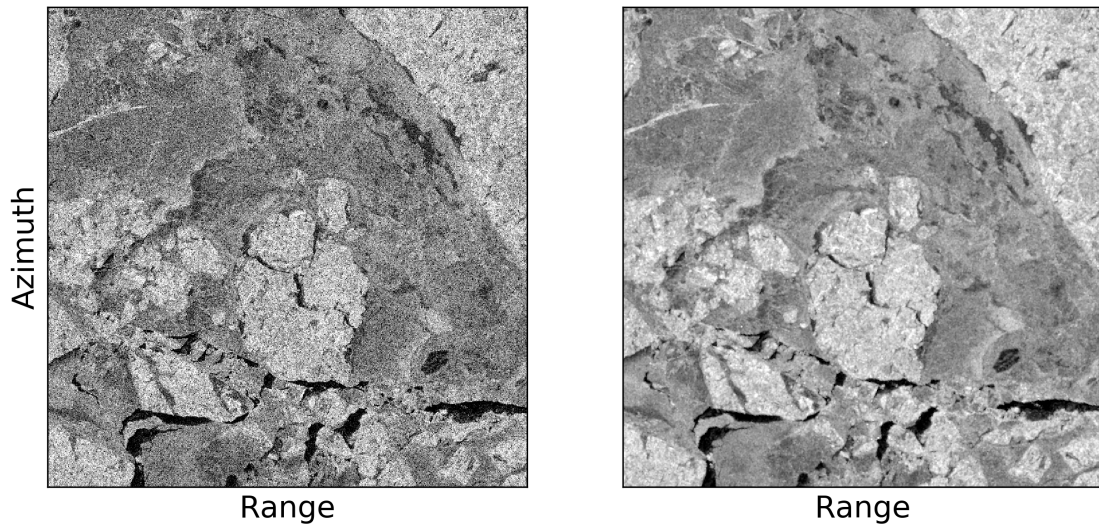


Figure 3.5: Radarsat-2 FQP image acquired north of Greenland on March 12th 2018. VV single-look intensity (in dB) is shown on the left side, VV multi-look (36 looks) intensity (in dB) on the right. Multi-looking reduces speckle at the cost of spatial resolution.

Thermal noise is an additive background noise that defines the sensor's noise floor [144]. The intensity value of the thermal noise is called the noise equivalent sigma zero (NESZ) and varies across the image. It is usually corrected for during pre-processing by applying the calibrated noise vectors provided with the product in order to subtract the NESZ. However, this noise correction is sometimes insufficient. For the Sentinel-1 EW mode, for example, the standard correction with the noise profiles provided by ESA leads to significant remaining residual artifacts [103, 145, 146]. These are particularly strong close to sub-swath boundaries in the images and in areas with low backscatter values (more often present in the HV channel) (Figure 3.6). Several studies have developed and tested improved methods for thermal noise correction for Sentinel-1 data [145, 147, 148]. Until today, none of these methods have been implemented and accepted as a publicly available standard processing. Robust noise correction thus remains an urgent research topic in order to improve visual and automated interpretation of SAR data.

3.3 Scattering Mechanisms

A SAR sensor measures the energy that is backscattered from the illuminated surface. The strength of the backscattered signal depends on the radar parameters (Section 3.1) and on the surface parameters. The latter can be described by the surface roughness, the

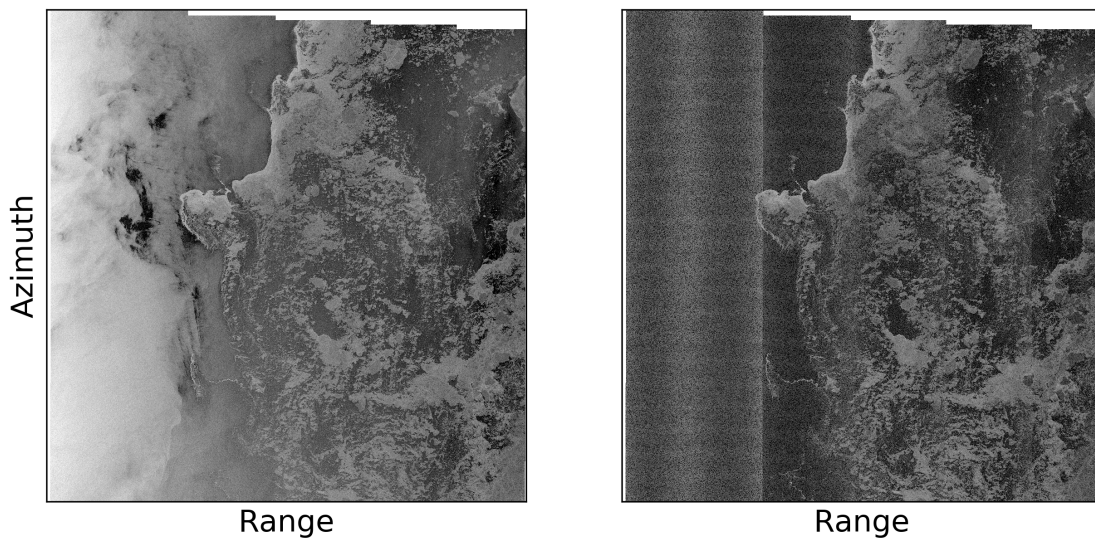


Figure 3.6: Sentinel-1 EW image acquired over Fram Strait on August 21st 2020. HH and HV intensity (in dB) are shown on the left side and on the right side, respectively. The open water area in the left part of the image has generally low backscatter in the HV channel and appears particularly noisy in the first swath and around swath boundaries.

large-scale surface geometry, the dielectric constant of the surface, and the existence of dielectric discontinuities or discrete scatterers in the subsurface medium [149]. There are three basic groups of scattering mechanisms that can contribute to the returned signal: surface scattering, volume scattering, and hard target scattering [65] (Figure 3.7).

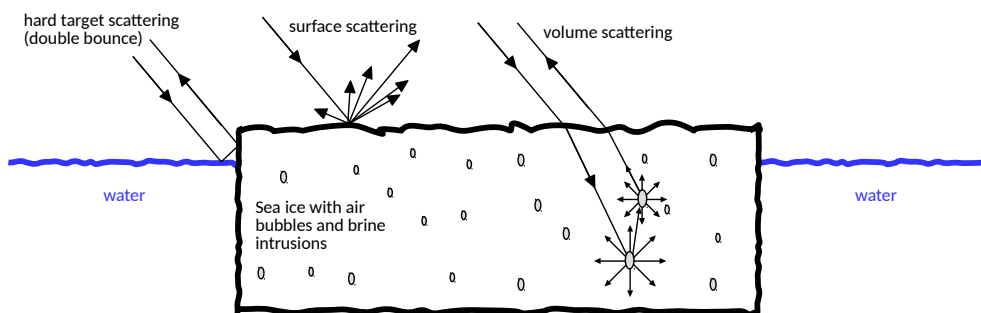


Figure 3.7: Simplified scattering mechanisms for sea ice.

The dominant scattering mechanism for sea ice is surface scattering [150]. Its strength is controlled by the surface roughness and the dielectric constant of the medium. A perfectly smooth surface (Figure 3.8, left side) acts like a mirror and will appear dark in the image. This is called a specular surface. Generally, the rougher the surface, the stronger the backscatter component and the brighter it will appear in the image (Figure 3.8).

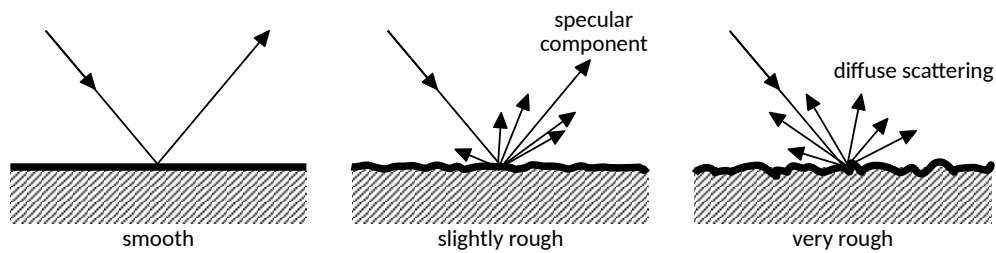


Figure 3.8: Specular and diffuse surface scattering, depending on surface roughness (modified from [65]).

A common criterion to quantify surface roughness is the Rayleigh criterion. If h is the vertical height variation on the surface, then the surface is regarded as specular when:

$$h < \frac{\lambda}{8\cos\theta} \quad (3.7)$$

The definition of surface roughness in Equation 3.7 depends on the signal wavelength λ and the IA θ . Surface roughness can only be assessed in a meaningful way with respect to these parameters.

While frequency (or wavelength) is fixed for a given SAR sensor, the IA on the surface varies across the image. This has important implications for the surface scattering component, as the backscatter intensity from a homogeneous surface decreases with increasing IA. Thus, intensity generally decreases across the image from near range to far range. The decrease rate depends on the surface type, which makes a correction of the IA effect during pre-processing difficult. *Paper 2* of this dissertation introduces a new classification method to overcome this issue and include the per-class variation of backscatter intensity with IA directly into the classifier. *Paper 3* lays the groundwork for the inclusion of texture into that classification scheme.

Besides surface scattering, hard target scattering and volume scattering can also play a role in sea ice RS. Hard target scattering may occur for example at ice floe edges or ice ridges that are oriented perpendicular to the radar's line of sight. Volume scattering increases with the penetration depth of the signal, which in turn increases with decreasing bulk salinity of the sea ice. Furthermore, longer wavelengths generally penetrate deeper into the ice volume. The amount of volume scattering will therefore usually be larger for L-band sensors compared to C-band sensors [64].

Understanding these interactions between the radar waves and the sea ice is important for the analysis and interpretation of the SAR images. This is discussed in more detail in Chapter 4, with particular emphasis on different ice types.

/4

Sea Ice Types and Sea Ice in SAR Imagery

The previous chapters have provided a general introduction into the role of sea ice in the Earth system, sea ice observations, and operational ice charting (Chapter 1), and have revised important concepts of image classification (Chapter 2) and spaceborne imaging radar systems (Chapter 3). This chapter outlines the connections between these topics. Different criteria for ice type classification are described and the different ice types are linked to the appearance of sea ice in SAR images (*radar classes*). Various examples of sea ice SAR imagery are given, and the challenges of automated classification are discussed, reviewing the main approaches and algorithms found in the literature.

4.1 Sea Ice Classes

Sea ice can be classified based on a number of different criteria [5]. Different applications require different ice class definitions, and the choice of any automated algorithm needs to take into account which particular information is required. The most commonly used classification criterion is based on ice thickness and associates each ice type with a particular thickness range. Ice thickness is generally related to ice age, and thus this criterion can also be considered as age-based [5]. The different thickness-/age-based classes are also referred to as the sea ice stage of development (SOD). This classification scheme has been adopted by the WMO and is often used in operational ice charts [151]. The thickness-based

ice types are also referred to as *WMO ice types* throughout this chapter. An overview of the main WMO sea ice types is given in Table 4.1, Figure 4.1 shows example photographs of several ice types.

Table 4.1: Overview of WMO sea ice types (stage of development) [151]. The classification scheme is primarily based on sea ice thickness/age. It is the most commonly used scheme and adopted in several ice charts by different ice services.

Stage of development	Properties	Thickness
New ice	general term for recently frozen sea water; not solid ice yet	
<i>Frazil ice</i>	fine spicules or plates of ice, suspended in sea water	
<i>Grease ice</i>	thin soupy layer of ice crystals on the water surface	
<i>Slush</i> <i>Shuga</i>	slushy mixture of water-saturated snow accumulation of spongy white ice with a diameter of a few cm	
Nilas	thin elastic crust of consolidated ice, bending on waves and swells	< 10 cm
<i>Dark nilas</i>	dark in color	< 5 cm
<i>Light nilas</i>	brighter in color	5-10 cm
Young ice	transition stage between nilas and FYI	10-30 cm
<i>Grey ice</i>	less elastic than nilas; breaks on swell; usually rafts under pressure	10-15 cm
<i>Grey-white ice</i>	more likely to ridge than to raft under pressure	15-30 cm
First-year ice (FYI)	not more than one winter of age	> 30 cm
<i>thin FYI</i>		> 30-70 cm
<i>medium FYI</i>		70-120 cm
<i>thick FYI</i>		> 120 cm
Old ice	ice that has survived at least one melt season	~2 m or more
<i>Second-year ice</i>	ice that has survived only one melt season	
<i>Multi-year ice</i>	ice that has survived at least two melt seasons	

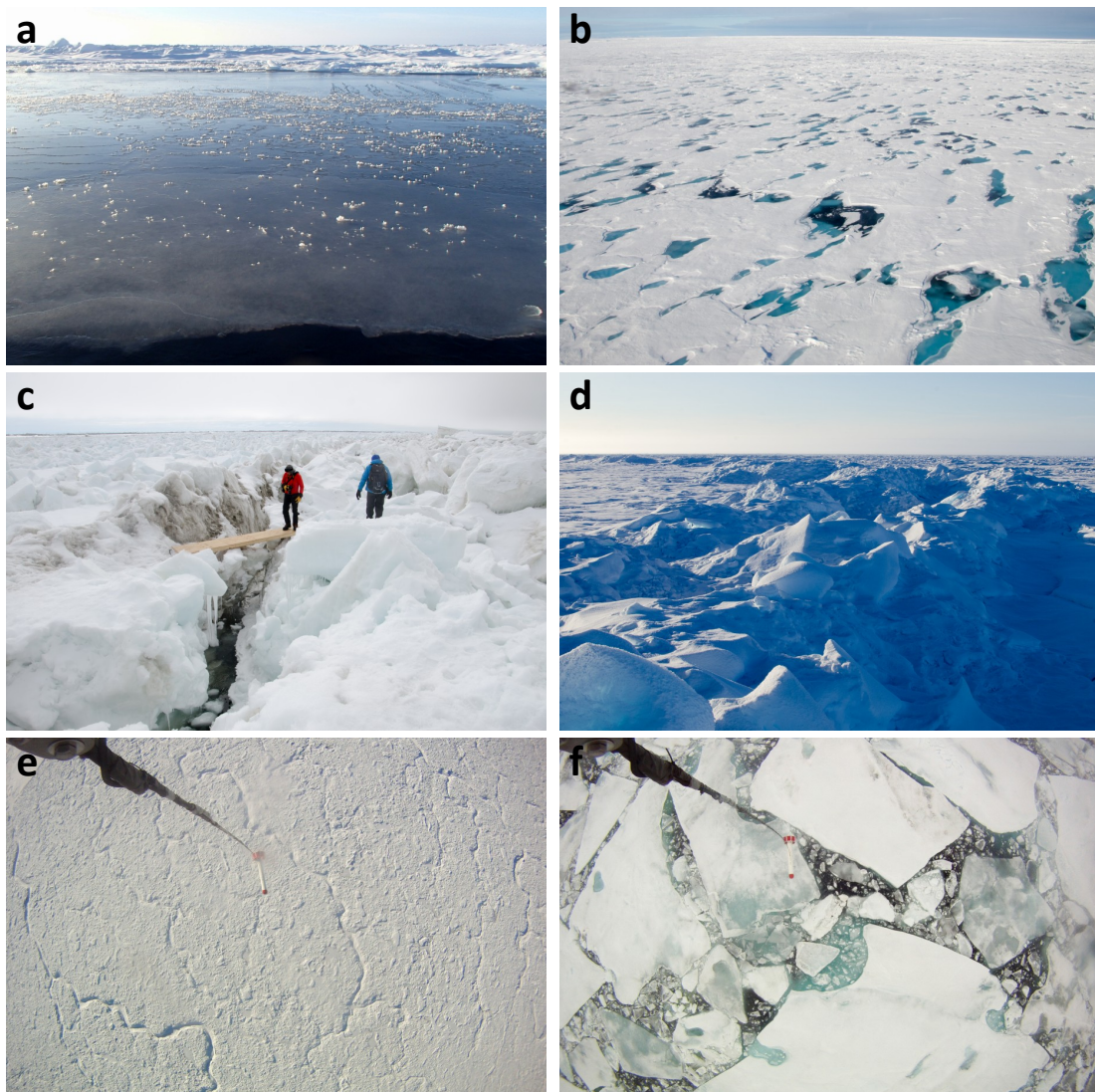


Figure 4.1: Example photos of different sea ice conditions. **a:** Nilas, partly covered with frost flowers, thicker snow-covered FYI in the background; **b:** Snow-covered FYI with melt ponds in the late summer; **c:** Strongly deformed rubble field with ice thickness of several meters; **d:** Sea ice ridge on landfast MYI ice; **e:** Snow-covered, ridged FYI; **f:** Broken ice floes with a mix of brash ice and open water between them. Sea ice photographs **e** and **f** were taken from the helicopter during the Norwegian Polar Institute (NPI) monitoring cruise to the Fram Strait in 2016; images also show the airborne electromagnetic ice thickness sensor used during ice survey flights.

In addition to the WMO ice types, there are a variety of binary classification categories:

- Seasonal vs perennial ice (FYI vs MYI)
- Level ice vs deformed ice
- Fast ice vs drift ice

The term *fast ice* refers to ice that is fastened to the shore (landfast), or for some cases in shallow waters grounded to the sea floor (bottomfast) [152, 153]. *Drift ice*, in contrast, is driven by forces from wind and ocean currents and moves continuously. Sea ice can furthermore be categorized by the ice form (for example pancake ice, ice floes, ice breccias, or brash ice), or by SIC. Note that the ice types from the different categories are not exclusive, but can overlap. For example, an area could be classified as seasonal, level, landfast ice. SIC can always directly be derived from any product that has classified ice and water in a previous step, although with a reduction in spatial resolution.

4.2 Sea Ice in SAR Images

The WMO ice types are the most common classification scheme for sea ice and SAR is the main data source for operational ice services. It is therefore a desirable goal to obtain these ice types from SAR images. However, SAR sensors can not directly measure ice thickness (with the exception of very thin sea ice in some cases [154]). WMO ice types can therefore only indirectly be inferred from the radar images.

The classes/ice types that can be separated in SAR images will be referred to as *radar classes*. For the interpretation of the imagery and a useful definition of the radar classes, it is important to understand the interaction of the radar signal with the sea ice. As discussed in Chapter 3, the backscattered signal depends on the radar parameters (mainly frequency, polarization, IA) and the surface parameters (roughness, dielectric constant, subsurface volume structure). For sea ice, the most important surface (and subsurface volume) parameters are given by [155]:

- Small-scale surface roughness (mm to cm, for example frost flowers, snow crusts, or general small-scale structures on the ice surface)
- Large-scale surface roughness and sea ice conditions: deformation structures (for example brash, ridges, leads, or lead edges)
- Sea ice volume structure (for example layers, brine inclusions, air bubbles)

- Sea ice temperature and salinity profile
- Snow cover (density, grain size, moisture)

The following sections discuss how the interplay of these different parameters determines the appearance of sea ice in radar images.

4.2.1 Surface and Volume Scattering from Sea Ice

The penetration depth of the radar signal into the ice, and thus the amount of volume scattering, is mainly controlled by the complex dielectric constant ϵ of sea ice and by the wavelength of the signal. The most commonly used SAR sensors in operational ice charting are operating at C-band frequency (Sentinel-1, Radarsat-2), and the following considerations therefore focus mostly on scattering mechanisms at C-band. The dielectric constant ϵ is mostly a function of salinity, temperature, and porosity of the ice [63]. Total brine content and bulk salinity are largest for newly formed ice and decrease over time (Chapter 1); hence, the loss factor (which is the imaginary part of ϵ) is higher for young, saline ice and lower for old, fresh ice [82]. The penetration depth of the radar signal can therefore differ significantly for different ice types. Longer wavelengths generally penetrate deeper into the ice volume. At temperatures of -10° and salinities between 5 and 12 psu (practical salinity units), the typical penetration depth of the radar signal into Arctic FYI is approximately 3-15 cm at X-band, 7-30 cm at C-band, and 15-100 cm at L-band [82]. Deeper penetration of the signal into the ice volume allows for more scattering at inclusions within the ice, such as air bubbles, interstices, interfaces between layers, and brine pockets. This increased volume scattering results in a stronger returned signal in both co- and cross-polarization channels. For example, MYI is usually less saline than young ice or FYI. At higher frequencies (C-, X-, Ku-band), the difference in penetration depth into FYI and MYI is significant and can help to separate these ice types in SAR images.

Surface scattering is mostly controlled by the surface roughness with respect to the signal wavelength [64]. Large-scale surface roughness, which is defined as roughness on scales of decimeters to meters, is often associated with mechanical deformation structures and thus, for example, with areas of sea ice ridges or rubble fields. The large-scale deformation creates facets that are oriented at random angles (Figure 4.1 c and d) and can cause specular reflections or double-bounce reflections, resulting in a strong backscattered signal from such areas. However, small-scale surface roughness elements that have sizes on the order of the radar wavelength also play a major role in controlling the backscatter intensity. The small-scale roughness strongly affects the signal both from areas that are smooth/level and from areas that are rough on the large scale. It is important to understand that this small-scale roughness does not necessarily correlate with large-scale deformation and ice thickness. The superimposed effects of small-scale and large-scale surface roughness therefore considerably complicate the manual and automated interpretation of radar images and the identification of WMO ice types. For example, a lead that is covered with

smooth young ice will have a weak backscatter signal and appear dark in a SAR image. If the young ice is covered with frost flowers or a snow crust, however, the small-scale surface roughness is dramatically increased and the lead will appear bright in the image [156,157]. Figure 4.2 shows example photos of frost flowers on an otherwise very smooth nilas surface.

Further challenges for the interpretation of SAR images are caused by structures on the ice surface that are of a size which is below the pixel resolution of the radar image and by pixels containing mixed classes. For example, for the Sentinel-1 EW mode, the commonly used ground range detected medium-resolution (GRDM) product comes at a pixel spacing of 40 m with an effective resolution of approximately 90 m. Individual sea ice ridges can therefore be too small to be visible in the image. Despite being of sub-pixel size, sea ice ridges can through specular reflection nevertheless contribute to the sum of all individual scattering elements within one resolution cell on the ground. This effect, which is dependent on the orientation of the ice ridge with respect to the radar look direction, will cause a stronger backscattered signal from resolution cells containing sea ice ridges. Areas with deformation are therefore expected to appear generally brighter in the images, making it possible to distinguish between level and deformed ice, and to potentially infer parameters related to large-scale deformation such as ridge density.

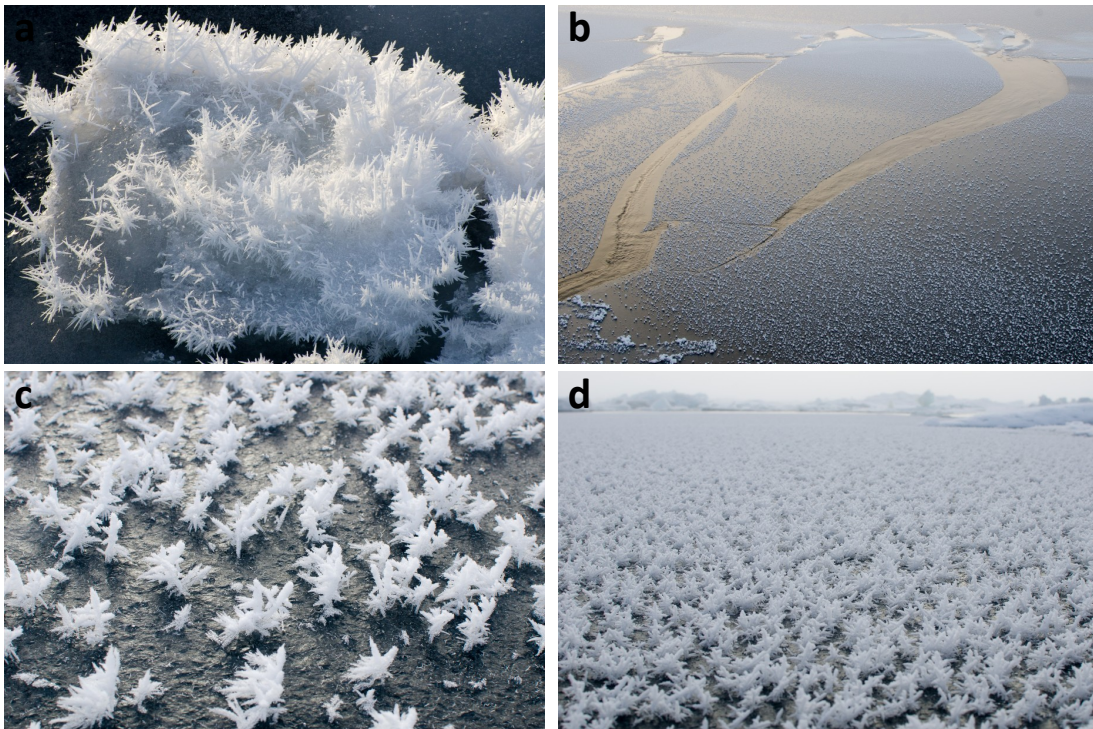


Figure 4.2: Example photos of nilas and young ice, covered with frost flowers. The frost flowers significantly change the small-scale roughness of the otherwise smooth ice surface, which will in return result in a much stronger backscattered radar signal.

4.2.2 Influence of Snow and Season

The above considerations are based on the assumption that the dominant scattering processes take place at the sea ice surface or within the sea ice volume. However, sea ice is often covered by snow. During freezing conditions, the snow is dry and consists of a mixture of ice crystals and air. Because the difference of the dielectric constants of ice and air is small, surface scattering from the dry snow surface can be neglected. Volume scattering in dry snow is generally assumed to be negligible too, because the ice crystal structures within the snow pack are small compared to the typical radar wavelengths at C-band frequencies [82].

For temperatures close to or above the freezing point, the situation is very different. The snow is then wet and consists of ice crystals, air, and liquid water. Depending on the liquid water content, the penetration depth of the radar signal can be significantly reduced. Hence, the backscattered signal will be largely or entirely dominated by the snow layer, making it difficult or even impossible to distinguish ice types underneath the snow. It should be noted that shorter wavelengths are generally more affected by the snow pack than longer wavelengths, because of the difference in penetration depth.

The most straightforward approach to solve the issue of varying snow conditions is to train a classification algorithm for different seasons. The type and number of classes that can be separated will differ between melting and freezing conditions, as the wet snow masks the ice underneath. The algorithms developed in this thesis are tested on data acquired under freezing conditions. However, the working principle of the methods can be readily transferred to melting conditions, given a representative training data set.

4.2.3 Scattering from Open Water

The separation of sea ice and open water is one of the most essential tasks in sea ice charting and classification. It provides important information to end users who want to avoid any contact with sea ice at all, and it allows to infer the SIC, which is an important parameter. While this binary classification problem may appear simple at first glance, it can, in fact, be greatly complicated by different wind states, which influence the surface roughness of the water. Sea water has a large dielectric constant, hence the radar signal does not penetrate into the water. The surface roughness is thus the critical factor that determines the radar signature of open water [124]. Typically, the backscatter from the ocean surface is modelled as Bragg scattering [158]. A smooth water surface will act almost like a mirror and cause a specular reflection. This surface appears dark in a SAR image. A wind-roughened water surface will scatter the signal more strongly, and appear brighter in a SAR image. The use of multiple polarization channels can help to overcome this problem, as rough water does not usually display a strong cross-polarization signal. However, the cross-pol channel can also have a weak signal for smooth ice types, so some ambiguities remain. Furthermore, a weak signal in the cross-pol channel will often be close

to or below the noise floor of the sensor, and thus impede useful interpretation. Possible solutions to this problem include the training of several open water classes for different wind conditions, or the use of textural information (Section 4.3) [159].

4.2.4 Complementary Information and Example Images

When available, overlapping SAR and optical images can offer complementary information on the sea ice situation and facilitate the identification of individual ice types. Generally, the analysis of such image pairs can help to gain a better understanding for the interpretation of sea ice SAR imagery. A large set of such overlapping SAR and optical data was analyzed in detail for the generation of the training and validation data set used in *Paper 2* and *Paper 3*. Several examples are presented and discussed in Figure 4.3 to 4.6. It should be noted that an exhaustive visual analysis of these examples requires continuous adjustment of zoom levels and dynamic ranges, in order to combine the general overview with detailed small-scale information. This kind of analysis is not possible to reproduce in the form of this written dissertation. Nevertheless, the examples give an introduction into the general idea of the interpretation of sea ice in SAR imagery.

In-situ observations on the ice can also assist in the interpretation of the radar images. However, in the field it can be difficult to time the observations such that the time difference between the in-situ measurement and the SAR image acquisition is sufficiently small to allow for precise co-registration of the data. Drift corrections may need to be applied, which can be challenging depending on the time difference and the general ice situation. This challenge can be circumvented by using imagery of landfast ice. Examples of SAR images showing the land- and bottomfast sea ice outside of Utqiagvik, Alaska, are shown in Figure 4.8 and 4.9. Photographs of the sea ice conditions on the ground at three different locations are presented and discussed in Figure 4.10.

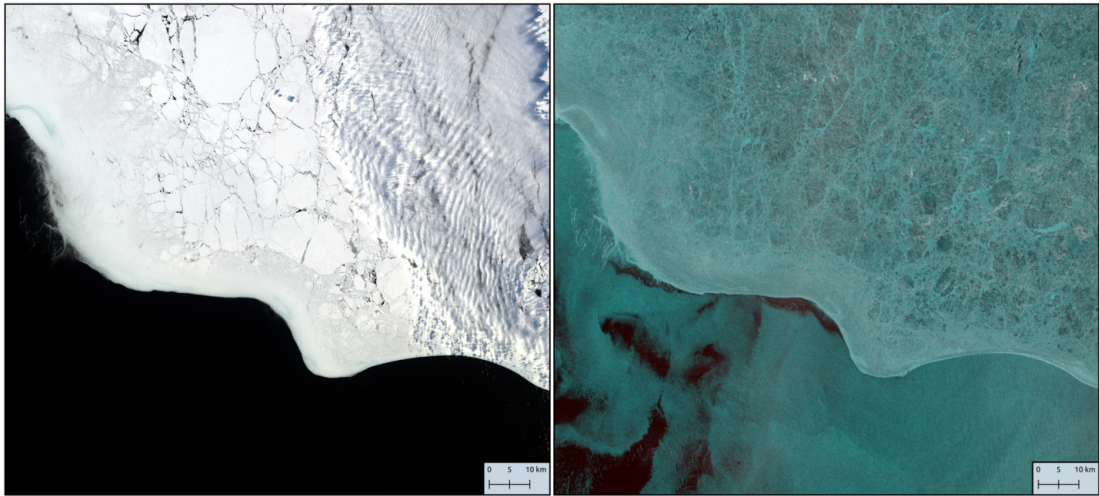


Figure 4.3: Overlapping optical (left; RGB channels) and SAR (right; red=HV, green=HH, blue=HH) data, acquired on April 6th 2015. Time difference: 1h 53min.

Sea ice (upper right) and open water (lower left), separated by a clearly defined ice edge. The sea ice close to the ice edge is most likely brash or pancake ice. The surface structure of this ice is below the spatial resolution of both sensors. Further inside the ice pack, low-backscatter areas are intersected by areas with stronger backscatter. While the low-backscatter areas are associated with rather smooth FYI floes, areas in between the larger ice floes appears to be covered with brash ice, resulting in a stronger backscattered signal. Ripping clouds partly obscure the right-hand side of the optical image.

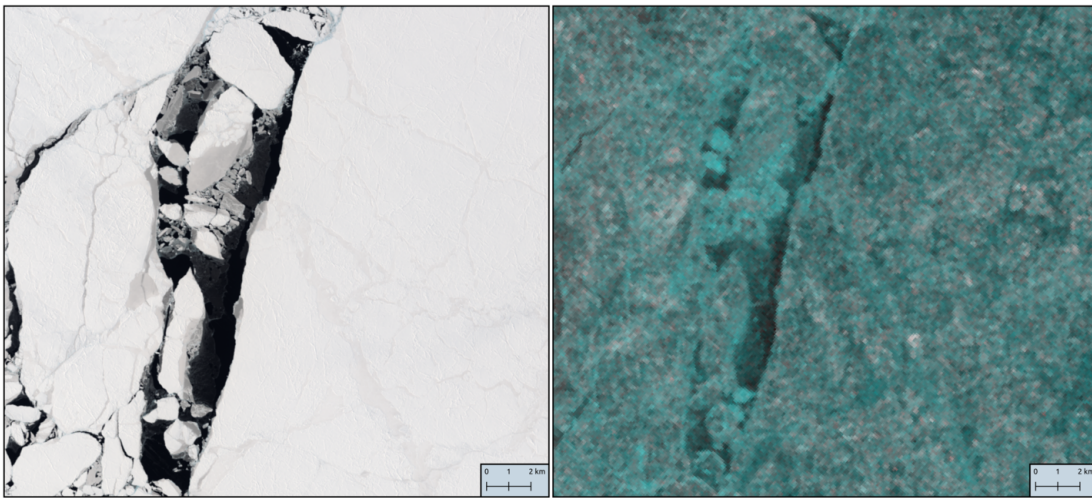


Figure 4.4: Overlapping optical (left; RGB channels) and SAR (right; red=HV, green=HH, blue=HH) data, acquired on April 6th 2015. Time difference: 1h 53min.

The optical image shows mostly snow-covered sea ice, intersected by a lead with open water or newly formed sea ice and smaller areas of young ice. The snow-covered sea ice reveals differences in the backscatter signature in the SAR image. The combination of optical and SAR data allows to distinguish between smooth/level FYI and more deformed FYI in the snow-covered areas.

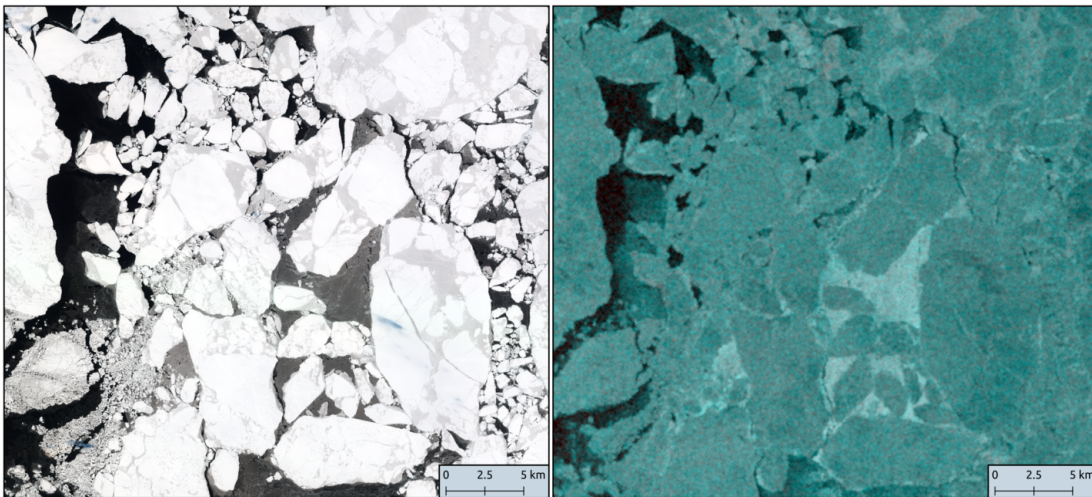


Figure 4.5: Overlapping optical (left; RGB channels) and SAR (right; red=HV, green=HH, blue=HH) data, acquired on April 2nd 2016. Time difference: 5h 59min.

Individual ice floes with a size of several kilometers are clearly visible in both images. Between the floes is either open water (left-hand side of the images) or young ice (grey/grey-white ice, center part of the images). The young ice areas in the center part of the image show a strong backscatter signature, probably caused by small-scale surface roughness. In the upper part of the image, young ice with a much weaker backscatter signal is visible.

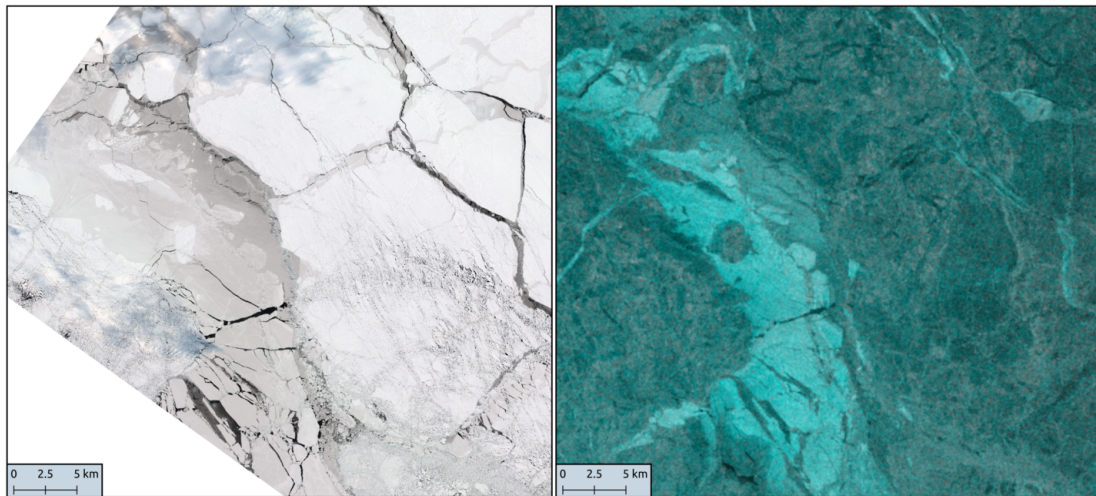


Figure 4.6: Overlapping optical (left; RGB channels) and SAR (right; red=HV, green=HH, blue=HH) data, acquired on April 5th 2016. Time difference: 3h 55min.

Mostly snow-covered FYI in the upper right part of the images. Differences between level and deformed FYI can be inferred from changes in the SAR backscatter. Zooming into the snow-covered regions of the optical images and adjusting the dynamic range (not shown here) can, in fact, also reveal these differences in the optical data. The central part of the image shows a refrozen lead that is covered with young ice with a strong backscatter signal. Some grey clouds are visible in the left part of the optical image.

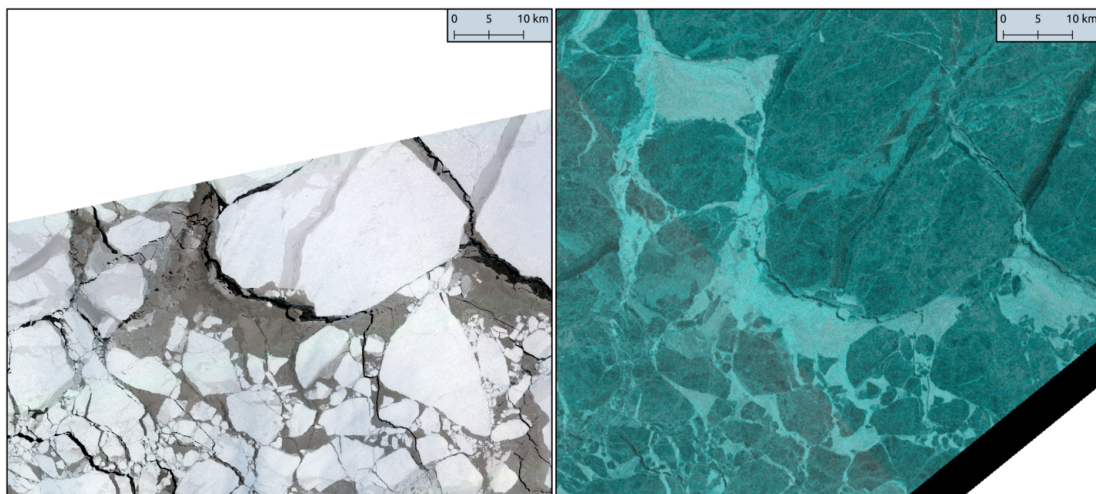


Figure 4.7: Overlapping optical (left; RGB channels) and SAR (right; red=HV, green=HH, blue=HH) data, acquired on April 3rd 2018. Time difference: 12min.

Individual ice floes with small open water areas and young ice in between. The young ice displays variable backscatter signatures, which makes it difficult to classify this ice type using an automated algorithm. Level and deformed areas in the snow-covered FYI can again be distinguished by backscatter differences in the SAR image.

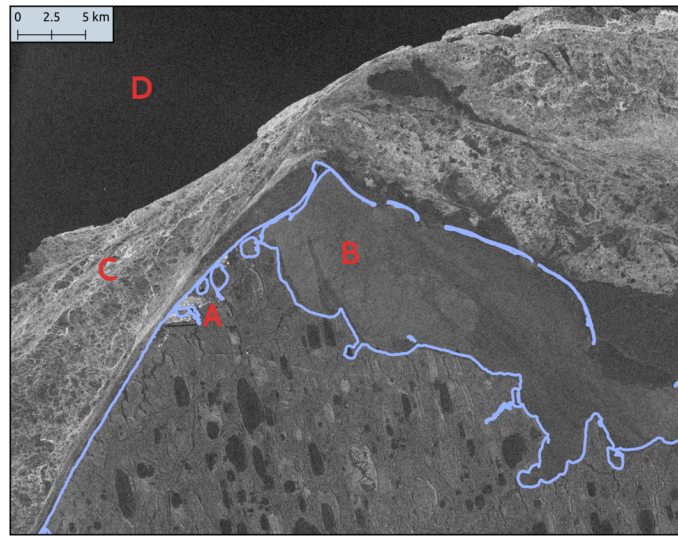


Figure 4.8: Sentinel-1 image (VH channel, June 6th 2017) over the coastal area around Utqiagvik, Alaska. The blue line marks the coastline. A: Utqiagvik settlement; B: Elson Lagoon, covered by smooth sea ice (partly bottomfast) with a weak backscatter signal; C: Heavily deformed landfast ice with a strong backscatter signal due to large-scale deformation; D: Open water with a weak backscatter signal in the shown cross-polarization channel.

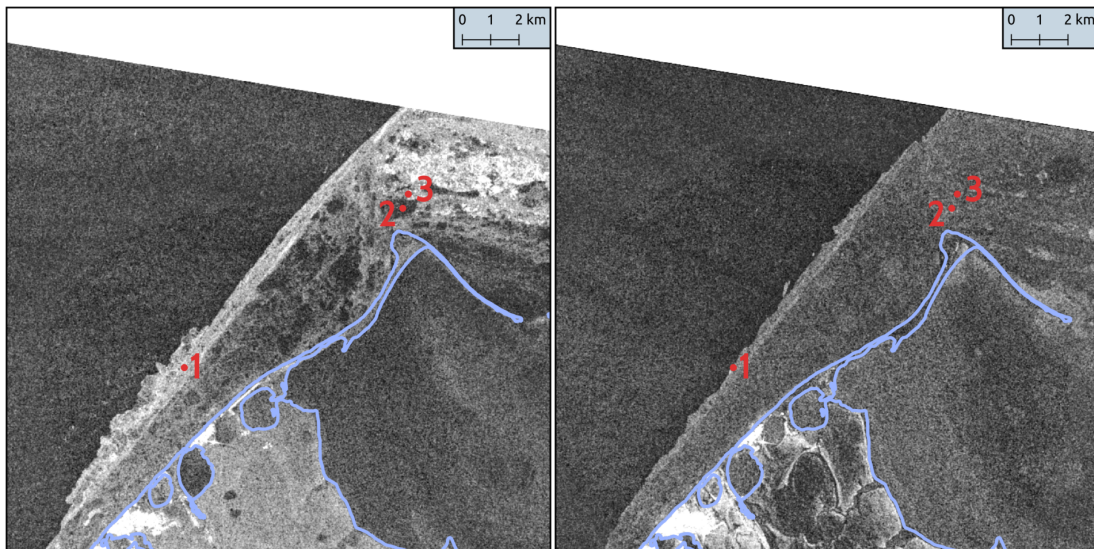


Figure 4.9: Sentinel-1 images (VH channel, left: May 17th 2019, right: May 29th 2019) over Elson Lagoon and the coastal area outside Utqiagvik, Alaska. Photographs taken at locations 1, 2, and 3 are shown in Figure 4.10. The overall sea ice conditions of the landfast ice did not change significantly between the two repeat-pass acquisitions. Rising temperatures and the melt onset at the end of May cause de-correlation between the images. While different ice conditions can clearly be distinguished in the earlier image (left), most of this information is masked by the wet snow in the later image (right).

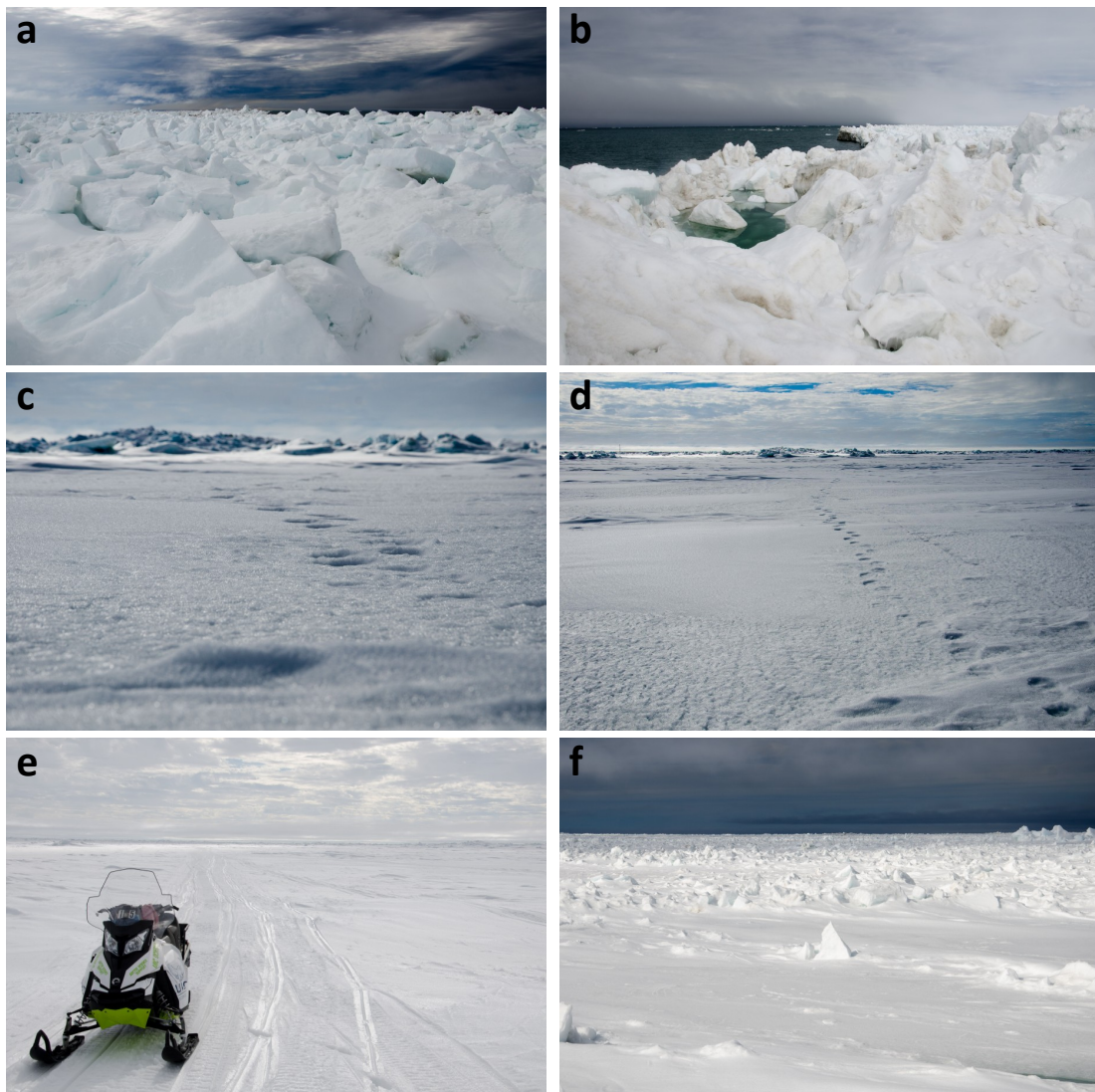


Figure 4.10: Example photographs of sea ice conditions taken on the landfast ice outside Utqiagvik, Alaska. All photographs were taken on May 23rd 2019. Locations are indicated on the map in Figure 4.9: **a**, **b** on location 1; **c**, **d**, **e** on location 2; **f** on location 3. The large-scale deformation that causes the strong backscatter at location 1 is clearly visible in photographs **a** and **b**. Photographs **c**, **d**, and **e** show a much smoother surface, which results in the area with low backscatter at location 2. Photograph **f** shows how heavily deformed and smooth areas alternate in the area viewed from location 3.

4.3 Approaches for (Semi-)automated Classification

The need for automated or semi-automated (computer-assisted) classification of sea ice in SAR imagery has been established in Chapter 1. However, the automated interpretation of the images is very challenging [83], because of a variety of factors:

- Ambiguity of sea ice backscatter from different ice types
- Varying surface roughness of open water caused by different wind states
- Variation of backscatter intensity with IA
- Noise and speckle in the images

Numerous studies have been published that propose different strategies for automated classification. Applied algorithms include Bayesian classifiers [150, 160], SVMs [106, 108], DTs [161], NNs and CNNs [107, 109–112], and RFs [162]. The amount of publications on the topic is too large to give a comprehensive summary here. Instead, the following section provides an overview of the most common approaches and outlines some remaining challenges. More details and further references can for example be found in the book chapter by *Dierking* [82] or the review paper on satellite SAR data-based sea ice classification by *Zakhvatkina et al* [83].

According to *Zakhvatkina et al* [83], "the most common approach to detect sea ice types is the use of the SAR image characteristic - tone or brightness - determined by the sea ice backscatter". Ambiguities in backscatter in one polarization channel can partly be resolved by the use of dual- or quad-pol data. In particular fully polarimetric data and the use of polarimetric features have proven to significantly improve classification results [139, 163, 164]. As discussed in Chapter 3, however, fully polarimetric data do not offer the swath width and spatial coverage that is required for operational monitoring. The needed wide-swath data (Sentinel-1 EW mode and Radarsat-2 ScanSAR mode) is mostly available in dual-polarization. A common way to overcome ambiguities in backscatter intensity of these images is the use of textural information. Image texture refers to the spatial variation of backscatter intensity as a function of scale [165, 166]. Multiple studies have shown that textural information can help to resolve ambiguities in sea ice classification, both for the binary problem of ice-water classification and for the multi-class separation of different ice types [112, 159, 166–172]. While there are different ways of extracting texture features [170], the most commonly used features are based on the grey level co-occurrence matrix (GLCM), that was first proposed by *Haralick et al* [165]. The GLCM is a measure of the probability that a pixel of a particular grey tone occurs at a specified distance and direction from the reference pixel [82]. The probabilities for all grey levels are summarized in the GLCM, and multiple scalar features can be extracted from the matrix.

All texture extraction requires parameter choices for the calculation of the features. The most straightforward parameter is the window size in which the intensity variation is investigated. For the GLCM, additional parameters are the number of quantization levels, the displacement distance, and the displacement direction. Various studies have investigated the parameter settings for GLCM feature extraction, but the optimal parameter choices differ between the studies. A more detailed overview of the parameters found in different studies and a further discussion of GLCM features is given in *Paper 3*. The paper furthermore investigates the IA dependency of SAR image texture.

While texture features can contribute useful information to the classification problem, the calculation of the features within a user-defined spatial window reduces the effective resolution of the image. Several studies suggest large window sizes (for example 25 pixels [166] or 64 pixels [159]), which results in a final product with much coarser resolution than the original image. Furthermore, texture calculation is computationally expensive. This needs to be considered when using texture in automated classification, as speed is an essential requirement for operational applications.

Besides the ambiguities in backscatter, the automated classification of SAR images is complicated by the influence of IA on the backscattered signal. In the wide-swath images mostly used by the ice services, IA varies between approximately 19° in near range and 45 to 49° in far range. The IA sensitivity of the backscatter intensity depends on the ice surface roughness spectrum at scales from centimetres to metres. With intensity given in decibel, the relationship between intensity and IA in wide-swath SAR images can often be approximated by a linear function. The sensitivity is largest for scattering from smooth surfaces, and moderate to low for scattering from rough surfaces [173]. In practice this means that different surface types (that is different ice classes) have different IA dependencies, which has been confirmed by multiple studies [173–176]. As it is not known a priori to which class a specific pixel belongs, it is not possible to apply the appropriate per-class correction during pre-processing of the data. The classification task is complicated by this issue. Most studies apply a global IA correction, that uses one constant slope to project all backscatter intensities to a reference IA [107, 108, 145, 159, 177]. *Paper 2* in this dissertation introduces a method to directly incorporate per-class IA variation of backscatter intensity into the classification algorithm. *Paper 3* assesses the potential to extend this new algorithm to include texture features.

Several studies have investigated the multi-frequency approaches to sea ice classification [133–135]. However, until today multi-frequency SAR data is not routinely available for operational services. Other multi-sensor approaches combine SAR and PM observations [177, 178]. While this introduces the challenge of combining data products with considerably different spatial resolution, the approaches show promising results for automated ice charts.

The combination of multiple polarization channels, co-registered multi-frequency or multi-sensor data, polarimetric features, and texture features offers a potentially large number

of features for classification. As described in Chapter 2, the number of features used in an algorithm should be as large as necessary, but as small as possible. Thus, many studies apply some method of feature selection to choose the optimal (or at least a good) combination of all available features. This is often done by visual/manual analysis of feature distributions [159], evaluation of separability measures for different classes, or sequential feature selection [139, 150]. Usually, a common feature set is selected for the entire classification problem. *Paper 1* in this dissertation introduces a method that allows to select different features for different classes in a multi-class problem, and assesses the potential improvement of classification results.

/5

Overview of Publications

This chapter gives a summary of the three papers presented in Chapter 6 to 8, and lists an overview of the author's other scientific contributions.

5.1 Paper Summaries

Paper I

J. Lohse, A. P. Doulgeris, W. Dierking (2019). "An Optimal Decision-Tree Design Strategy and Its Application to Sea Ice Classification from SAR Imagery". *Remote Sensing*, 11(13):1574

This study introduces the fully automatic design of a numerically optimized DT algorithm and demonstrates its application on sea ice classification in SAR imagery. The DT splits an initial multi-class problem with m classes into a sequence of $m - 1$ binary problems. Each branch of the tree separates one single class from all other remaining classes, using a feature set that is specifically selected for that single class. The order of the single classes and the different feature sets for each branch are optimized during the design stage of the tree: For every branch, each of the remaining classes is tested as a single class against the combination of all other remaining classes, and the optimal feature set is found by SFFS with respect to CA. The highest scoring class with the best feature set is chosen for each branch. The strategy can be adapted to other class separability measures instead of CA and adopt different internal classifiers for the two-class problems within

each branch. In this study, the binary classifier within each branch is a Bayesian classifier with a non-parametric PDF. The PDF is estimated from the training data using kernel density estimation (Parzen windows) with a Gaussian kernel. Whenever several classes are combined to one mixed class in the tree, this choice of classifier requires careful balancing of the prior probabilities in order to ensure maximum likelihood for the final classification result and thus maximize the final CA. Once the design stage is finished for a given problem, the algorithm can be used to forward classify given samples along the chosen path through the tree (Figure 5.1).

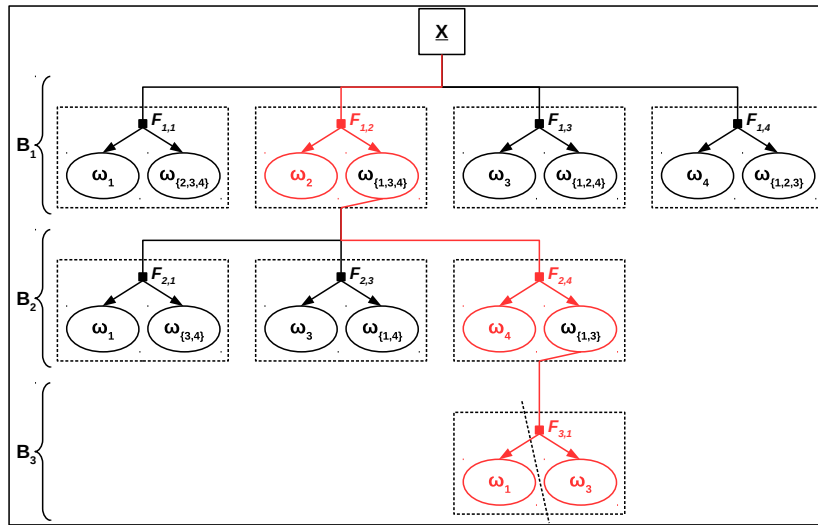


Figure 5.1: Design stage of the optimized DT for a four-class problem. The optimal path through the tree is highlighted in red. Within each of the black squares, a SFFS is performed to determine the feature set F_{ij} for the branch B_i and the class ω_j .

The algorithm is tested on a variety of simulated training and validation sets to ensure that the order of selected classes and individual feature sets is correct, and to demonstrate the basic working principle and possible advantages of the method. Comparison to results from an all-at-once (AAO) method, where one commonly selected feature set is used to separate all classes in a single step, shows that the optimized DT with feature sets specifically tailored towards individual classes can improve average per-class CA up to 4%. Tests on an airborne multi-frequency SAR data set show an improvement of 2.5%. Besides improved CA, the individually selected feature sets can also provide information on dominant scattering mechanisms for different ice types and on the potential of different features or frequencies to distinguish between specific classes. For the airborne SAR data set, for example, the higher sensitivity of L-band compared to C-band for the detection of large-scale deformation is confirmed by the selected feature sets. The improved CA comes at the cost of longer computation time, in particular during the design stage of the DT. The final choice of algorithm must therefore be a trade-off between required accuracy and time constraints.

Paper II

J. Lohse, A. P. Doulgeris, W. Dierking (2020). "Mapping Sea Ice Types from Sentinel-1 Considering the Surface-Type Dependent Effect of Incidence Angle". *Annals of Glaciology*, 1-11. doi:10.1017/aog.2020.45

Classification of sea ice types in SAR images is complicated by the dependence of backscatter intensity on IA. In a typical wide-swath SAR image, this IA effect is visible as a general decrease in image brightness (backscatter intensity) across range, with generally higher backscatter values in near range and lower backscatter values in far range. In most studies, the IA effect is treated as an image property and corrected globally during pre-processing of the data. Such a global correction of the entire image neglects the fact that different classes show different rates of decrease. With intensity given in dB, the decrease can be approximated by a linear function over the typical IA range of spaceborne wide-swath SAR images, and the slopes of these linear functions are class-dependent. However, a class-dependent correction during pre-processing is not possible, because the class labels are not known a priori.

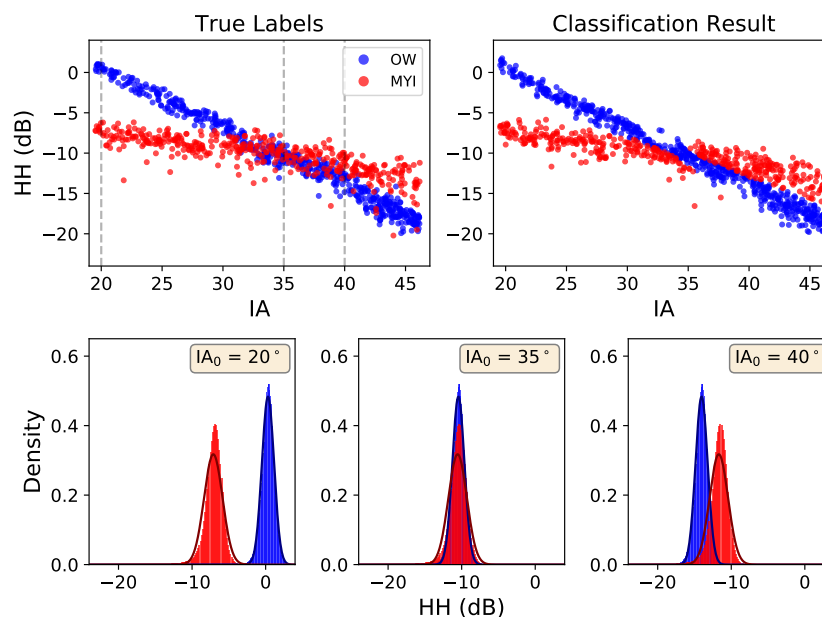


Figure 5.2: Intensity (in dB) for open water and MYI shown against IA, with true class labels indicated on the top left and predicted class labels indicated on the top right. The lower panel shows histograms and slices through the class-conditional PDFs with variable mean at different IA locations.

This study introduces a novel classification method for wide-swath SAR data that accounts for per-class variation of backscatter intensity with IA. This is achieved by replacing the constant mean vector in a multi-variate Gaussian PDF with a variable mean vector that

depends linearly on IA. The covariance is then calculated as the mean squared deviation relative to the linear function describing the variable mean value. Once slope and intercept of the linear function and the covariance matrix for each class are known, the PDFs can be readily evaluated for new input data and each pixel is assigned to the most probable class.

The algorithm is trained and tested on a data set generated manually from overlapping SAR and optical data. The identification of different sea ice types in these image pairs was done in collaboration with expert sea ice analysts from the NIS and takes into account the appearance of the ice in both the optical and the SAR image, as well as geographic location, time of year, and history of the ice pack. Different simplified case studies (Figure 5.2) demonstrate how including the per-class variation of backscatter intensity with IA can successfully improve CA compared to different approaches using a global IA correction during pre-processing. Additionally, the introduced algorithm is fast and performs at an operationally feasible speed.

While some ambiguities for particular ice types remain (for example confusion of MYI and young ice with frost flowers), the major limitation of a method based on backscatter intensity only is the selection and training of open water classes. For a given radar frequency and polarization channel, the open water backscatter intensity and slope depends on the wind speed as well as the angle between the radar look and the wind direction. Possible solutions to this challenge are the inclusion of texture features into the algorithm, training and selection of several open water classes based on wind conditions, or data fusion with data from other sensors.

Paper III

J. Lohse, A. P. Doulgeris, W. Dierking (2020). "**Incident Angle Dependence of Sentinel-1 Texture Features for Sea Ice Classification**". Submitted to some journal.

This study investigates the per-class IA dependence of texture features that are commonly used in sea ice type classification from SAR imagery. The purpose of this investigation is to extend the IA-sensitive algorithm developed in *Paper 2* to include textural information, in order to resolve some of the inherent ambiguities found with classifiers based on intensity only. Several previous studies have confirmed that in particular GLCM texture features can be helpful to solve such ambiguities; however, all of these studies either apply a global IA correction before texture feature extraction, or no IA correction at all. A systematic investigation of the dependence of common texture features on IA for different classes had not been performed prior to this study.

In the first part of the study, the relationship of texture features and IA is investigated. The analysis is based on the same Sentinel-1 training and validation data set that was developed in *Paper 2*. Seven commonly used GLCM texture features are computed from

both HH and HV intensity, testing a variety of typical GLCM parameter settings. Initially, all texture features are calculated from both the linear and the logarithmic intensities (that is, intensities in dB). While the tested GLCM texture features from the linear intensity show considerable and partly non-linear variation with IA, the texture features from the logarithmic intensity show no significant IA dependence. A slight linear trend can be observed, in particular for large window sizes. The trend is either negligible or can be readily modelled by the existing IA-sensitive classifier. To avoid IA effects in the texture features, it is thus recommended to compute the GLCM from the logarithmic intensity domain. For all tested texture features and parameter settings, the different number of looks between sub-swath EW1 and sub-swath EW2 of the Sentinel-1 EW GRDM product causes a significant offset in numerical texture values between both sub-swaths. The offset must be considered whenever using texture directly computed from this product. A possible correction is demonstrated for the example of GLCM contrast.

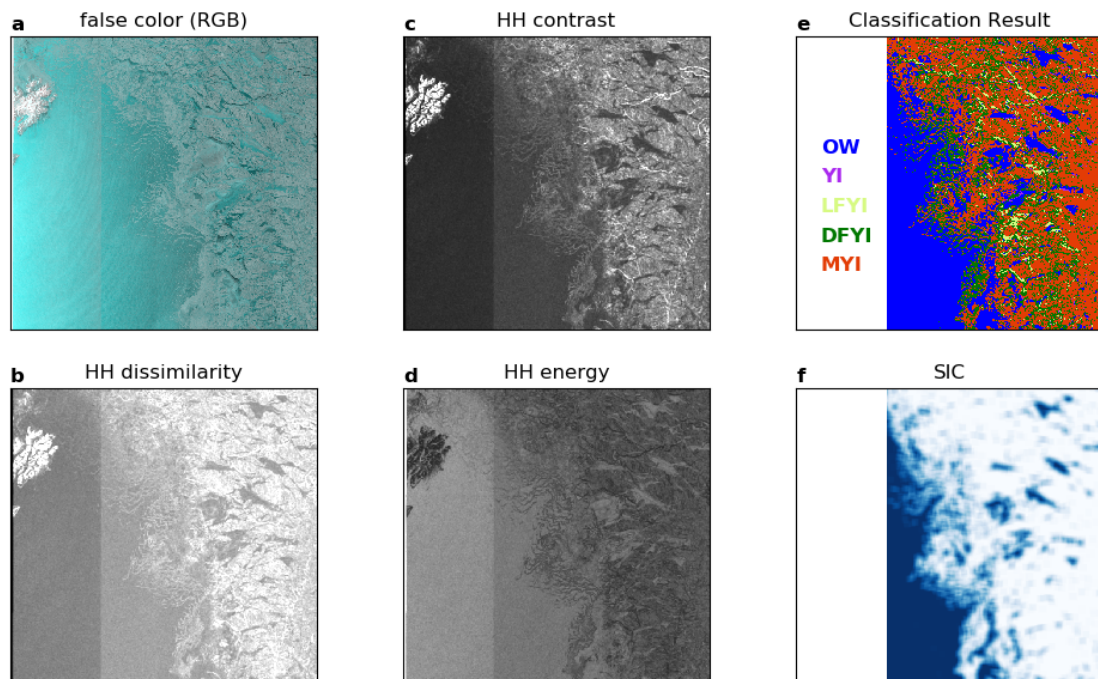


Figure 5.3: Input features and classification result for image ID F2FE. The used features are HH and HV intensity (a, false-color intensity image [R:HV, G:HH, B:HH]), HH dissimilarity (b), HH contrast (c), and HH energy (d). Sea ice concentration (f) can be calculated directly from the classification result (e). Because of the distinct offset between sub-swaths EW1 and EW2 in the GLCM features (b, c, d), EW1 is masked out in the classification result.

In the second part of the study, the tested GLCM texture features and parameter settings are analyzed for their potential to improve the classification of open water and different sea ice types. For the given data set and class definitions, larger window sizes for texture

calculation result in better class separability, albeit at the cost of reduced spatial resolution. Based on this analysis, a meaningful feature set is selected to train a classifier and process multiple test images. Several classification examples are presented to illustrate the improvements in separation of open water and FYI/MYI (Figure 5.3), and in separation of MYI and young ice in refrozen leads. As the texture signature of open water is not significantly influenced by different wind conditions, training of one windy open water class is sufficient for a classifier that can generalize well between sea ice and open water. The separation of other classes, such as for example FYI and MYI, is found to be challenging based on texture only, and backscatter intensity remains an important feature. Thus, the final classifier uses both texture and intensity.

5.2 Other Scientific Contributions

As first author:

- J. Lohse, A. P. Doulgeris, W. Dierking (2018). "**Sea ice classification from SAR on varying scales**", EGU General Assembly Abstracts 2018-04-08 - 2018-04-13
- J. Lohse (2018). "**Sea ice in the Arctic: Remote sensing and ice charting**", Science and Advanced Technology in the Arctic PhD Course 2018-09-23 - 2018-09-30
- J. Lohse, S. M. Fritzner (2018). "**Assimilation of sea ice information in numerical models**", CIRFA Annual Conference 2018-10-17 - 2018-10-18
- J. Lohse, A. P. Doulgeris, W. Dierking (2019). "**New strategies for automated sea ice classification at CIRFA**", International Ice Charting Working Group Meeting 2019-09-23 - 2019-09-27.
- J. Lohse, A. P. Doulgeris, W. Dierking (2019). "**Ice type mapping from Sentinel-1 considering surface-type dependent effect of incidence angle**", IGS Sea Ice Symposium 2019-08-19 - 2019-08-23.
Winner of best poster presentation award in "Technical Science".

As co-author:

- J. Negrel, S. Gerland, A. P. Doulgeris, A. Rösel, J. Lohse, M. Johansson (2017). "**In situ validation of Arctic sea ice classification based on remote sensing**", Arctic Frontiers 2017-01-22 - 2017-01-27
- V. Akbari, J. Lohse, W. Dierking, T. Eltoft (2018). "**Characterization and detection of icebergs in open water and sea ice using spaceborne fully polarimetric SAR**", SEASAR 2018-05-07 - 2018-05-11

- S. Khaleghian, J. Lohse, T. Kræmer (2020). "**Synthetic-Aperture Radar (SAR) based Ice types/Ice edge dataset for deep learning analysis**", DataverseNO, V1
- W. Guo, P. Itkin, J. Lohse (2020). "**Sea ice classification using wide-swath SAR data considering incidence angle dependency of backscatter intensity and surface texture**", EGU General Assembly Conference Abstracts 2020-05-04 - 2020-05-08.
- W. Guo, P. Itkin, J. Lohse (2020). "**Cross-platform application of a sea ice classification method considering incidence angle dependency of backscatter intensity and its use in detecting ice deformation**", AGU Fall Meeting Abstracts 2020-12-01 - 2020-12-17.

/6



Paper I:

An Optimal Decision-Tree Design Strategy and its Application to Sea Ice Classification from SAR Imagery

Lohse J, Doulgeris AP and Dierking W (2019). Remote Sensing,11(13), ISSN 2072-4292 (doi: 10.3390/rs11131574)

Article

An Optimal Decision-Tree Design Strategy and Its Application to Sea Ice Classification from SAR Imagery

Johannes Lohse ^{1,*}, Anthony P. Doulgeris ¹  and Wolfgang Dierking ^{1,2} 

¹ Department of Physics and Technology, UiT The Arctic University of Norway, 9019 Tromsø, Norway

² Alfred Wegener Institute, Helmholtz Center for Polar and Marine Research, Bussestr. 24, 27570 Bremerhaven, Germany

* Correspondence: johannes.p.lohse@uit.no

Received: 10 May 2019; Accepted: 1 July 2019; Published: 3 July 2019



Abstract: We introduce the fully automatic design of a numerically optimized decision-tree algorithm and demonstrate its application to sea ice classification from SAR data. In the decision tree, an initial multi-class classification problem is split up into a sequence of binary problems. Each branch of the tree separates one single class from all other remaining classes, using a class-specific selected feature set. We optimize the order of classification steps and the feature sets by combining classification accuracy and sequential search algorithms, looping over all remaining features in each branch. The proposed strategy can be adapted to different types of classifiers and measures for the class separability. In this study, we use a Bayesian classifier with non-parametric kernel density estimation of the probability density functions. We test our algorithm on simulated data as well as airborne and spaceborne SAR data over sea ice. For the simulated cases, average per-class classification accuracy is improved between 0.5% and 4% compared to traditional all-at-once classification. Classification accuracy for the airborne and spaceborne SAR datasets was improved by 2.5% and 1%, respectively. In all cases, individual classes can show larger improvements up to 8%. Furthermore, the selection of individual feature sets for each single class can provide additional insights into physical interpretation of different features. The improvement in classification results comes at the cost of longer computation time, in particular during the design and training stage. The final choice of the optimal algorithm therefore depends on time constraints and application purpose.

Keywords: classification; decision tree; feature selection; SAR; sea ice; ice types

1. Introduction

The focus of this study is the development of a strategy for automatic optimization of a decision tree for classification problems. While the proposed algorithm is generic and can be applied to any given classification problem, we demonstrate its potential on the example of sea ice type classification in Synthetic Aperture Radar (SAR) data.

There is a strong interest in ice type classification in particular from an operational perspective. As, in particular, the summer sea ice extent declines [1–3], the Arctic Ocean becomes more accessible to marine traffic and offshore operations [4], to which sea ice and icebergs can pose a significant danger [5–7]. Fast, robust and reliable methods for mapping of sea ice types are therefore needed to ensure the safety of shipping and offshore operations in the Arctic.

There are several ice services worldwide that produce sea ice charts on a regular daily basis. Usually, the charts show total ice concentration or a combination of ice concentration and ice type. Because of its independence of daylight and weather conditions, SAR provides an excellent tool for

year-round sea ice observations. It is therefore one of the main data sources for mapping of ice types and ice chart production. For now, however, analysis of the images is mostly performed manually. With new satellite missions being launched and an increasing number of images available, this manual approach needs to be supplemented by reliable methods for automatic or semi-automatic mapping of sea ice conditions.

There are already a substantial number of studies that investigate automatic or semi-automatic sea ice classification using SAR imagery. Many approaches use traditional classification strategies, that separate all classes in one step and assign a class label to each pixel. Common algorithms are Bayesian classifiers [8,9], support vector machines [10,11] or neural networks [12–16]. All of these methods require training data with known class labels in order to determine the decision boundaries between classes. In segmentation-based approaches, on the other hand, no training data is needed. The image is simply segmented into regions [17,18] with statistically similar backscatter. However, the actual class labels, i.e., the ice type of each segment, are initially unknown and have to be determined after the segmentation [19,20].

Both classification and segmentation methods need a set of features that allows to distinguish between different surface types. There are numerous studies investigating the potential of various features for ice type classification. Commonly used features are simple backscatter intensities [21], texture features [22–24] or polarimetric features [9,25]. The performance of features for separation of ice types can furthermore differ depending on the ice situation (winter or melt season) and the wavelength of the radar system [26–28]. Prior to classification or segmentation, a set of suitable features needs to be generated. There are various established methods to do so, including feature transformations such as Principal Component Analysis (PCA) or feature selection methods such as Sequential Forward/Backward Feature Selection (SFFS, SBFS) [29]. In the methods described so far, one common feature set is selected for the entire classification or segmentation problem. This constitutes the main conceptual difference compared to decision trees.

Decision trees (DT) are a particular type of supervised forward classifier that requires training data with known class labels. In contrast to the classification methods mentioned earlier, where all classes are separated in one step (all-at-once), a DT splits the multi-class decision into a series of binary decisions. It uses these binary splits to extract patterns or rules in a dataset [30]. DTs have been used for sea ice classification in various studies. For example, the authors of [31] employ a DT for discrimination of sea ice types and open water from dual co-polarized SAR, while the authors of [32] use it to classify multi-sensor satellite observations of a polynya region in the Ross Sea. In both of these studies, as in many other cases, the DTs are designed manually, based on local knowledge or manual interpretation of data. Automated trees, on the other hand, can be designed by applying splitting criteria and stop-splitting rules. However, single trees tend to show large variance, and in practice it is not uncommon for a small change in training data to result in a very different tree [29]. Random-forest (RF) classifiers are one established way to overcome this overfitting issue. As implied by the name, an RF classifier uses a large number of individual trees, each of which is designed from a randomly selected subset of the entire training set (Bootstrap Aggregation, Bagging) and a randomly selected subset of features. Each tree gives an individual class label as output and the final class is decided by a majority vote from all trees in the forest. Generalization of the method is achieved through the randomization of the different training subsets and thus overfitting to the training data is avoided. Single DTs as well as RFs are used by, e.g., Refs. [30,33] for monitoring of landfast ice and retrieval of melt ponds on multi-year ice, respectively.

The objective of our study is to develop the automatic design of a numerically optimized DT with regard to classification accuracy (CA). In contrast to the RF, our algorithm designs and uses only one single tree. Each branch of this tree classifies one single class and takes it out of the dataset. The order of classification steps and the chosen feature sets are selected by combining CA and sequential search algorithms. Depending on the available features and the balancing of the training data, we expect this optimized DT classifier to perform better than a traditional classifier. While the RF achieves

generalization through random selection of training and feature subsets and a subsequent majority vote of a large number of independent trees, our algorithm generalizes through cross-validation over the entire training set during the design stage. The algorithm specifically tailors the feature set in each branch of the tree to the class that will be separated in that respective branch. Besides improved CA, these individually selected feature sets can also provide information on dominant scattering mechanisms for different ice types and on the potential of different features to distinguish between certain classes. This information is more difficult to obtain from an RF, which uses the majority vote of a large number of different trees with random feature sets.

We test our proposed method on a variety of simulated and real data and compare the results with those from all-at-once (AAO) classifiers. The remainder of this article is structured as follows: The fully automatic design of the DT is described in detail in Section 2. In Section 3, we introduce the datasets used for testing the algorithm performance. Section 4 presents the optimized tree designs and all classification results, followed by discussion and conclusion in Sections 5 and 6, respectively.

2. Method

2.1. DT Design Strategy

Separation of sea ice types is a typical multi-class problem. A traditional AAO classification algorithm uses one set F of input features (e.g., radar intensities at different frequencies, polarimetric or texture parameters) to separate all classes ω_i in a single step (Figure 1). In a DT, this multi-class decision is replaced by several binary decisions with distinct feature sets F_i (Figure 2). Both approaches are supervised and require training data for each class.

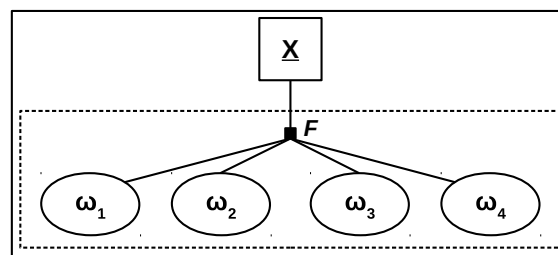


Figure 1. Traditional multi-class classification for a four-class problem. A feature vector x is assigned to one of the four classes ω_j in a single decision, using the feature set F .

In the DT example, sketched in Figure 2, the order of separating single classes is given. The DT architecture is usually determined manually, based on expert knowledge of regional ice conditions at the given point in time. Class ω_1 is classified in branch B_1 , class ω_2 in branch B_2 and a final binary decision separates ω_3 and ω_4 in branch B_3 . Furthermore, feature sets F_i are given, which are different in each branch B_i . In the final branch, the two remaining classes are classified simultaneously. The architecture of the tree, i.e., the order of classes and the chosen feature sets, needs to be determined in some way. We refer to this as the DT design stage. After the design stage, the finished tree can be used for forward classification of new samples, i.e., images acquired at similar ice and temperature ranges.

In this work, we present an automated design strategy for an optimal DT in terms of CA. The basic concept of our proposed DT design stage is sketched in Figure 3. In every branch, we test each of the remaining classes as a single class against the combination of all other remaining classes and calculate the average per-class CA. To ensure that the CA is independent of the training data, we use 100-fold cross validation, i.e., we randomly split all training data over the two step-specific classes into 100 sub-groups. Looping over these sub-groups, each of them is once retained for determining the CA, while the remaining sub-groups serve as training data. The results from all sub-groups are averaged to obtain the final score for the current step. The highest scoring class is selected as the single class ω_j for the current branch B_i . All samples from this class are taken out of the training data

before the next branch. Note that other class-separability criteria than average per-class CA may be used at this stage without altering the proposed strategy for the DT design. To obtain the best CA for every single-class test within each branch, we run a Sequential Forward Feature Selection (SFFS) to determine the optimal feature set. The procedure of the SFFS is as follows:

- Compute the CA for each of the features individually. Select the feature with the highest score.
- Compute the CA for all possible pairs of features that contain the winner from the previous step. Select the best two-feature combination.
- Continue sequentially to add remaining features to the previously selected set, always choosing the highest scoring combination.
- Stop if the CA of the currently best feature set is lower than the CA of the best feature set from the previous step, or when all available features are selected.
- Select the feature set from the step with the maximum CA as the optimal one.

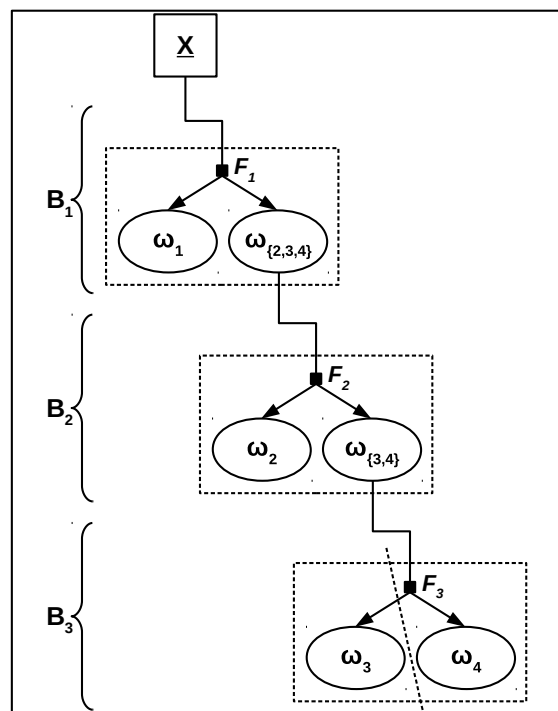


Figure 2. Decision-tree classification for a four-class problem. A feature vector x is assigned to one of the four classes ω_j after a maximum of three binary decisions, using separate feature sets F_i for each individual decision.

During the DT design stage, sketched in Figure 3, SFFS is performed in total eight times: Four times in branch B_1 , three times in branch B_2 and once in the final branch B_3 . As mentioned in many textbooks, the SFFS is in fact a sub-optimal method of feature selection, as there is no guarantee that the optimal two-dimensional feature set originates from the optimal one-dimensional one (or similar at higher levels). However, if many features are available, forming all possible combinations quickly results in a very large number of feature sets to test, which is impractical [29]. Nevertheless, the choice of feature selection can be adjusted depending on the available time and computational power. As long as a logical selection criterion is applied that results in an optimal choice of features in terms of this metric, the exact selection process does not alter the concept of the optimized DT design that we propose here.

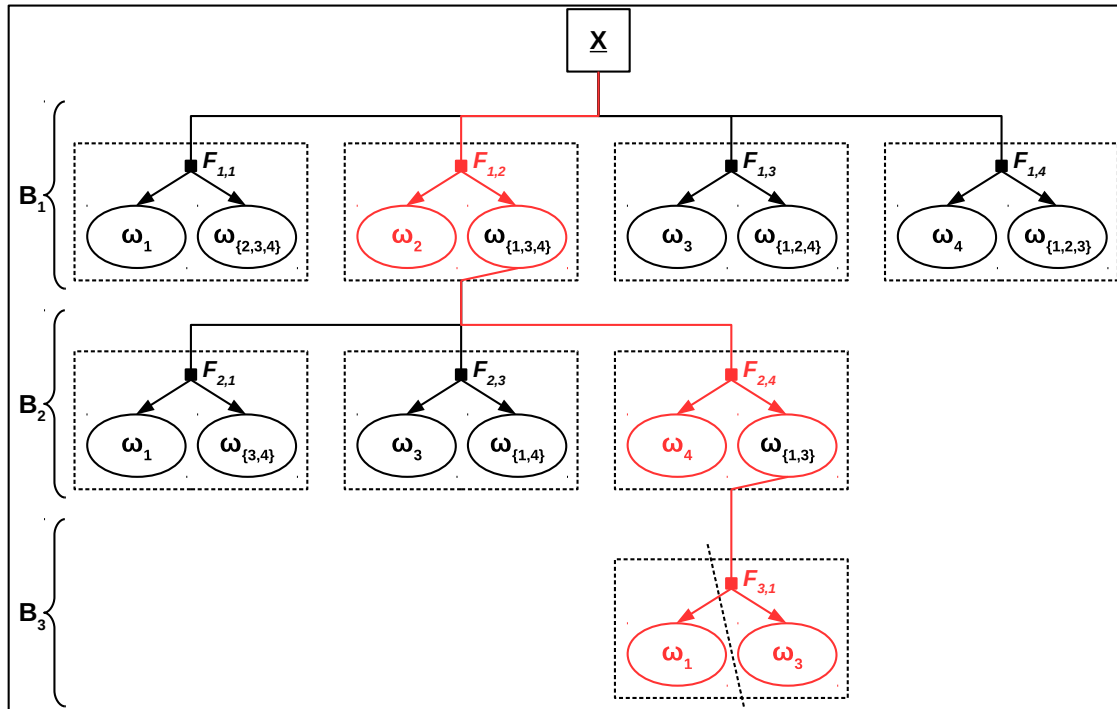


Figure 3. Design stage of decision tree for a four-class problem. The optimal path through the tree is highlighted in red and may differ from the decision-tree (DT) architecture shown in Figure 2. Sequential Forward Feature Selection (SFFS) is run at each black square to determine the feature set F_{ij} during the design stage.

2.2. Choice of Classifier

The concept of the DT design strategy can generally be applied to any classification algorithm. In this study, we use an algorithm based on Bayesian decision theory, which assigns the feature vector \underline{x} for each pixel in the image to the most probable class ω_i :

$$\underline{x} \rightarrow \omega_i \quad \text{if} \quad P(\omega_i|\underline{x}) > P(\omega_k|\underline{x}) \quad \forall \quad k \neq i, \quad (1)$$

where $P(\omega_i|\underline{x})$ is the posterior probability of class ω_i , given pixel \underline{x} . Employing Bayes rule, the decision rule can be expressed through the likelihood ratio:

$$\underline{x} \rightarrow \omega_i \quad \text{if} \quad \frac{p(\underline{x}|\omega_i)}{p(\underline{x}|\omega_k)} > \frac{P(\omega_k)}{P(\omega_i)} \quad \forall \quad k \neq i, \quad (2)$$

with the prior probabilities $P(\omega_i)$ and the class-specific probability density functions (PDF) $p(\underline{x}|\omega_i)$. The prior probabilities reflect total abundances of different classes and can be estimated from training data or set equal for Maximum-Likelihood (ML) classification. The decision then depends entirely on the class-specific probability density functions (PDFs) $p(\underline{x}|\omega_i)$, which must be estimated from the data. For known parametric forms of class distributions, the parameters for each class can be estimated from the training data. If the form of the PDFs is unknown, it can be approximated through kernel density estimation (also known as Parzen windows [34]). Since we do not want to include assumptions about the PDFs in our algorithm, we have implemented Parzen windows with a multi-variate Gaussian kernel function to approximate the PDFs directly from the training data. The width of the Gaussian kernel function is estimated using Silverman's rule of thumb [35] and the number of used kernels is controlled by the number of available training points.

2.3. Balancing of Probabilities

At various steps during the DT design stage, several single classes are combined to one mixed class ω_{mix} . Each of these combinations requires a choice for the balancing of the prior probabilities, with the two basic options being an ML decision for the final result or an ML decision in every single branch. We choose to balance the prior probabilities for ML of the final result. Without prior knowledge about the data, this is the most natural approach to take. Furthermore, it corresponds to the balancing of an ML AAO classifier, and we score our results accordingly.

In practice, prior influence of single individual classes is removed when estimating class-specific PDFs and choosing equal prior probabilities. (Remember that the PDF by definition integrates to one). The prior probability $P(\omega_{mix})$ for a mixed class consisting of N individual classes must therefore be weighted by the factor N . The PDF $p(\underline{x}|\omega_{mix})$ of the mixed class can either be estimated by summing up and scaling the PDFs from the individual classes, or by a single kernel density estimation using all training samples from the combined classes. For the latter option, however, the number of training samples per class will be embedded in the resulting PDF and thus influence the balance of individual classes. We therefore compute the mixed PDF by summing up and scaling individual PDFs:

$$p(\underline{x}|\omega_{mix}) = \frac{1}{N} \cdot \sum_{i=1}^N p(\underline{x}|\omega_i) \quad (3)$$

The decision rule is now given by:

$$\underline{x} \rightarrow \omega_{single} \quad \text{if} \quad \frac{p(\underline{x}|\omega_{single})}{p(\underline{x}|\omega_{mix})} > \frac{P(\omega_{mix})}{P(\omega_{single})} \quad (4)$$

With prior probabilities according to:

$$P(\omega_{mix}) = \frac{N}{N+1} \quad \text{and} \quad P(\omega_{single}) = \frac{1}{N+1} \quad (5)$$

This results in:

$$\underline{x} \rightarrow \omega_{single} \quad \text{if} \quad \frac{p(\underline{x}|\omega_{single})}{p(\underline{x}|\omega_{mix})} > N \quad (6)$$

Equation (6) is now the decision rule for a single-vs.-mixed-class decision where we assume that all individual classes appear with the same probability.

2.4. Experiment Design

We have implemented the DT design strategy with a Bayesian classifier as described in Sections 2.1–2.3 and tested it on different simulated and real examples. For each example, we designed the numerically optimized DT and employed it for classification of the full image. Since we desire ML for the final result, we adjusted the balancing of prior probabilities according to Equations (5) and (6). For comparison, we also tested the numerically optimized DT with ML in each individual branch.

Furthermore, we performed an SFFS for traditional AAO classification and separated all classes in one step using the single selected feature set. To be able to compare results in terms of the AAO vs. DT approach, the AAO classifier is designed in exactly the same way as the DT, i.e., a multi-dimensional Bayesian classifier with Parzen density estimation using Gaussian kernel functions. It should be noted that any other classification method (support vector machine, neural network, etc.) could potentially be chosen. However, the same method should be employed for both AAO and DT to allow a comparison of the two approaches, which is independent of the underlying classifier.

To assess the final performance of a classifier in terms of classification accuracy, an independent validation set is needed. For the simulated images, we know all class labels by definition. We can therefore use all image pixels for validation that were not selected for the DT design and training.

For the real datasets, we have split the selected ROIs for the different classes into training and validation set. During the DT design stage, cross-validation as described in Section 2.1 is performed within the training set, such that the performance of the final classifier can be assessed from a completely independent validation set.

3. Datasets

We have tested the numerically optimized DT on a variety of simulated and real datasets. The simulated data are used to demonstrate the robustness of the proposed method under controlled conditions with perfect validation data. For testing on real data we have used images from the spaceborne Sentinel-1 mission and an airborne, multi-channel SAR dataset with overlapping optical data. In the following, we present two representative examples. Since validation on the real datasets is much more reliable in the high-resolution airborne case with overlapping optical data, we choose to present this example as a detailed case study.

3.1. Simulated Test Dataset

To test the functionality and performance of the algorithm, we have generated several simulated examples with varying numbers of classes and features. In these simulated examples, the samples are simply drawn from class-dependent, multi-variate distributions and do not have a particular physical interpretation. In the case of SAR data, the different dimensions (features) could, e.g., represent intensities, polarimetric parameters, texture or other features. The test case presented here is an image with 1000×1000 pixels, 25 features and four classes separated in the four quadrant corners. We therefore refer to it as the C4-F25 dataset. The samples for each class are drawn from multi-variate Gaussian distributions. Mean values and variances of the distributions are designed such that the classes are partly separable in some of the features, while completely overlapping in other features. Furthermore, some features allow only to distinguish between two classes, while the remaining classes overlap.

We have randomly selected training data from the image with a varying number of training samples for each class. To ascertain that the training data is representative for the classes, we have run several tests using different training set sizes. We found the minimum required number of training samples per class to be approximately 400, with the exact number depending on the design of the distributions, i.e., the mean values and covariance matrices and the chosen dimensionality of the problem. The results shown in the next section were obtained with 1989, 1768, 1968 and 2139 training samples for classes C_1 to C_4 , respectively. Remember that the different abundances of training samples are taken care of by correct balancing of probabilities, such that we achieve an ML classification (Section 2.3). Figure 4 shows one-dimensional histograms for some selected features of the training data set.

3.2. Airborne SAR Dataset: ICESAR

As a test case for airborne SAR data, we have chosen the ICESAR dataset acquired by AWI and DLR over sea ice in Fram Strait in March 2007. The dataset is described in detail in [26,36].

During the campaign, joint flights of AWI and DLR airplanes were carried out acquiring both radar (ESAR) and optical data. The ESAR measurements were recorded at C-band (dual-polarization, VH and VV) and at L-band (quad-polarization, HV, HH and VV) at incidence angles ranging from 26 to 55°. At a flight altitude of 3000 m, the resulting swath width is approximately 3 km.

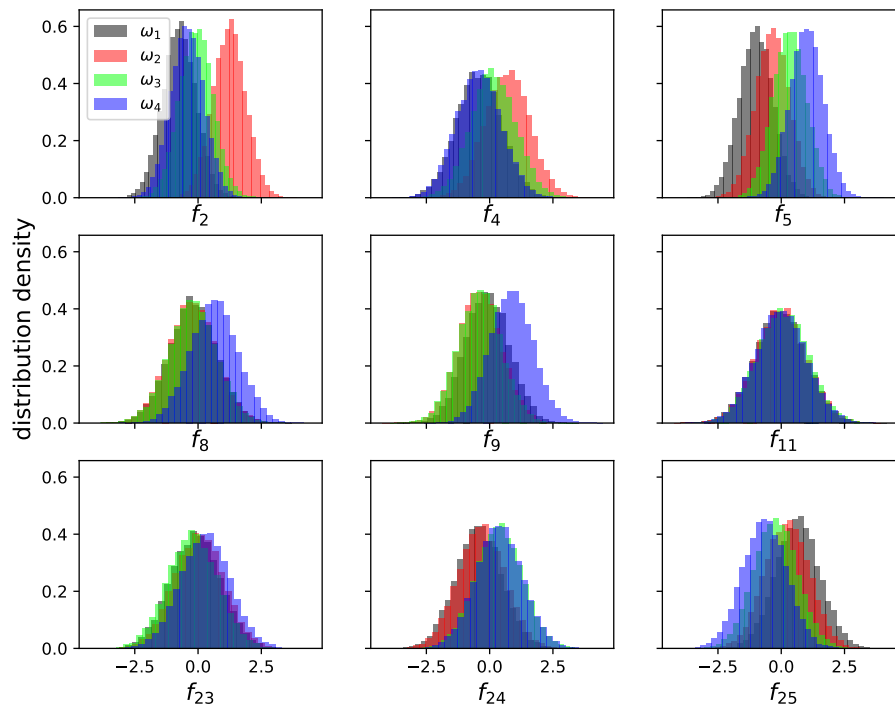


Figure 4. Single-feature histograms for selected example features of the training data from the simulated test image C4-F25.

The original ESAR images are delivered in single-look-complex (SLC) format and the measured reflectivity is given as radar brightness β^0 . For the classification, we used final products in a ground-range multilook format with a pixel size of 1.5 m. To decrease the incidence angle sensitivity of the ground reflectivity, we converted the β^0 -values to γ^0 -values. Relationships between β^0 , γ^0 and the backscattering coefficient σ^0 are given by

$$\beta^0 = \frac{\sigma^0}{\sin(\theta_1)} \quad (7)$$

and

$$\gamma^0 = \frac{\sigma^0}{\cos(\theta_1)}, \quad (8)$$

where θ_1 is the local incidence angle.

Optical images were recorded while repeating the flight track from the ESAR data at low altitudes. The RGB-layers in the visual representation of the optical data correspond to wavelength ranges 410 to 470 nm, 500 to 570 nm and 580 to 680 nm, respectively. The spatial resolution of the optical data is dependent on flight altitude and speed. It varies between 0.2 and 0.5 m across-track and 0.9 and 1.3 m along-track.

The maximum time lag between radar and optical measurements during the campaign was less than two hours and only minor variations of the ice cover characteristics can be recognized in the images, due to ice drift and deformation (Figure 5). However, the main ice situation during optical and SAR measurements was the same. We could therefore use a combination of optical data, SAR data and handheld photos taken during the flights to manually determine training regions for different ice classes. Only areas that appeared homogeneous were taken into account for these regions of interest (ROI). In total, we have defined six distinct classes (Table 1). The acquired images and the manually defined ROIs for all classes are shown in Figure 5.

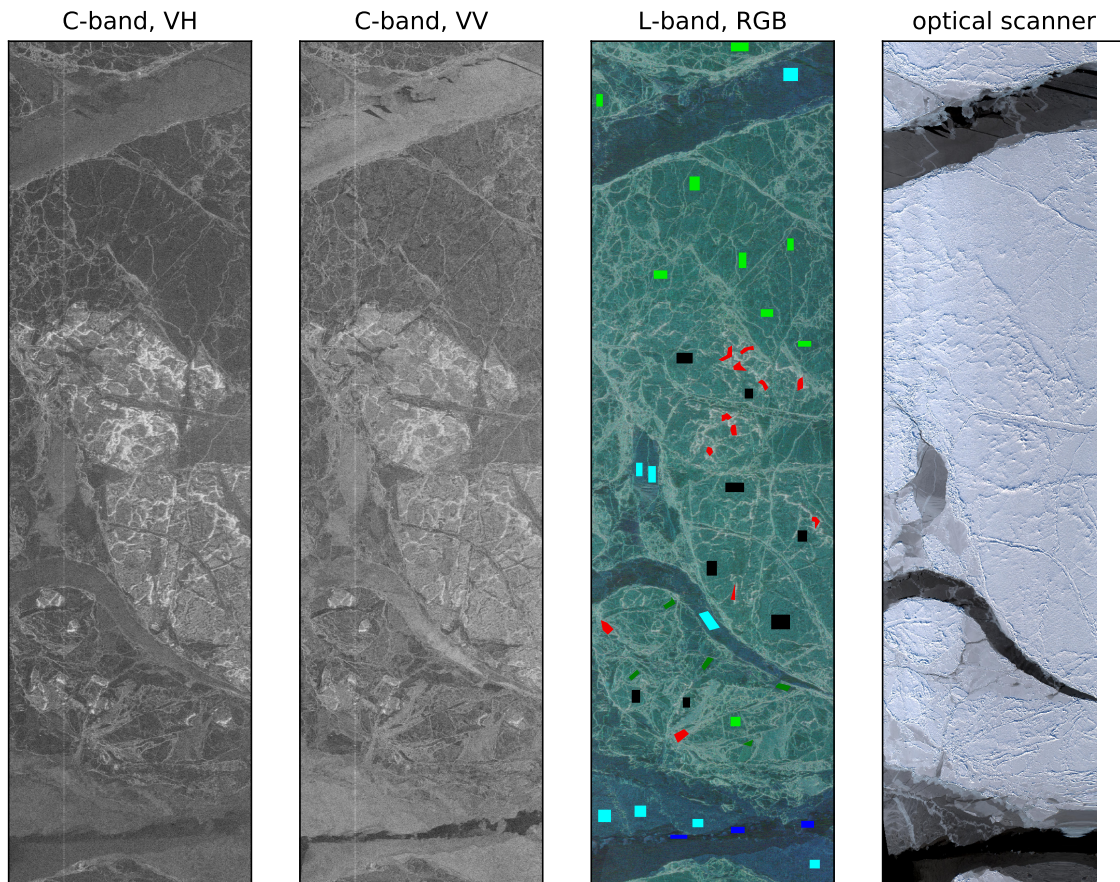


Figure 5. ICESAR dataset. From left to right: C-band VH, C-band VV, L-band false-color (R-HV, G-HH, B-VV), optical scanner. Colored boxes in the L-band image indicate training regions for different classes.

Table 1. Classes defined from visual inspection of the ICESAR dataset, with corresponding color codes and number of samples.

	Description	Color Code	# Training Samples	# ROIs
Class ω_1	Open water	dark blue	2398	3
Class ω_2	Grey-white ice	light green	10,640	9
Class ω_3	Level ice	black	14,233	8
Class ω_4	Deformed ice	red	6356	12
Class ω_5	Nilas	cyan	12,946	8
Class ω_6	Grey ice	dark green	2342	5

4. Results

In this section, we present the results obtained from our proposed algorithm and the comparison methods. We first give a general comment on computation times and then list the detailed classification accuracies, order of classes in the DT and selected feature sets for the previously introduced datasets.

Generally, the DT approach is more time consuming than the AAO approach, since it requires more operations. This is in particular true for the design stage. In the AAO approach, a six-class problem requires one single SFFS with six classes during the design stage. In the DT approach however, the design stage of the same six-class problem requires six SFFSs with two classes each in the first branch, five in the second branch, four in the third, three in the fourth and one in the fifth. Besides the dimensionality of the feature vector, the number of operations within a SFFS is proportional to the number of training samples and trained classes. In the DT, the number of training samples decreases with every branch, but the decrease is not known a priori and differs from case to case. For a six-class

problem, the upper limit of the design stage computation time ratio for DT versus AAO is therefore $\frac{6 \times 2 + 5 \times 2 + 4 \times 2 + 3 \times 2 + 1 \times 2}{1 \times 6} = 6.33$, meaning that the DT design and feature selection takes up to six times longer than the AAO feature selection. Once designed and trained, the forward classification for the DT approach is still more time consuming than the AAO approach, but with smaller difference. In the AAO approach, the forward classification stage of a six-class problem requires the evaluation of 6 PDFs for all patterns that are to be classified. In the DT approach, forward classification of the same six-class problem requires the evaluation of two PDFs in each branch. Again, we do not know a priori how many patterns will be removed from the data in each branch, so the upper limit for the ratio of forward classification times is $\frac{5 \times 2}{6} = 1.67$.

4.1. Results for Simulated Test Dataset

For the simulated example, all pixels that were not selected for training can be used as a validation set to estimate the final CA. The results for the C4-F25 dataset are summarized in Table 2. Our numerically optimized DT performs 3.5% better overall than a traditional AAO classifier, increasing total CA and average per-class CA from 75.21% to 78.78%. For individual classes, the improvement can be significantly larger (Table 2, class ω_3). Table 3 shows the order of selected classes and the corresponding feature sets. The single feature set selected for AAO classification is $\{f_5, f_2, f_9, f_4, f_{13}\}$. Note that the class-specific feature sets can either be subsets of the AAO feature set (Table 3, Branch 1), or may contain features which are not in the AAO feature set at all (Table 3, Branch 2).

The total CA for the DT with ML in each individual branch is 76.60%, which is 2% lower than the total CA for our proposed approach of ML for the final result.

Table 2. Classification accuracy (%) for simulated test dataset C4-F25 for all-at-once (AAO) and decision-tree (DT) classifier.

	Total	Per-Class CA				Average
	CA	ω_1	ω_2	ω_3	ω_4	Per-Class CA
AAO	75.21	81.70	80.38	60.12	78.62	75.21
DT	78.78	84.50	82.61	68.84	79.16	78.78

We show here only one representative example for the simulated datasets. Naturally, the exact scores and improvements in classification results differ, depending on dimensionality and design of the feature space as well as number and separability of the classes. However, in all 100 simulated cases, the optimized DT performs better than the traditional AAO classification. In all tested cases, improvements in average per-class CA range from 0.5% to 4%.

The DT with ML in each individual branch always performs worse than the final ML DT. In many cases, it also results in a lower CA than the traditional AAO classification, and hence correct balancing of the prior probabilities is important. After tuning of basic input parameters, the RF classifier performs similar to our optimized single DT. The best result was found with 100 trees and a maximum depth of 10, and achieved a total CA of 79.29% for the presented example.

Table 3. Single classes and selected features for each branch of the numerically optimized DT for simulated test dataset C4-F25.

DT Branch	Single Class	Selected Features
B_1	ω_2	f_2, f_5, f_4
B_2	ω_1	f_5, f_{25}, f_{24}, f_2
B_3	ω_4	f_9, f_5, f_8, f_2
AAO	—	$f_5, f_2, f_9, f_4, f_{13}$

4.2. Results for ICESAR Dataset

To estimate an independent CA for the ICESAR dataset, we split the pixels from the ROIs evenly into training and validation pixels. While the training set is used for kernel density estimation of the PDFs (see Section 2.2), the validation set is used for calculation of CA. The estimated CA and the order of selected classes with corresponding feature sets are summarized in Tables 4 and 5, respectively. Figure 6 shows the classification result from the DT classification.

Again, the DT performs better in terms of total CA as well as average per-class CA, with an improvement of about 2.5%. We also note that all individual classes score higher in the DT than in the AAO method. A particularly large improvement is achieved for grey-white and grey ice, with per-class CA increased by 7% and 4%, respectively (Table 4). Note also, that these are the lowest scoring classes overall, which are separated in the last branch of the DT.

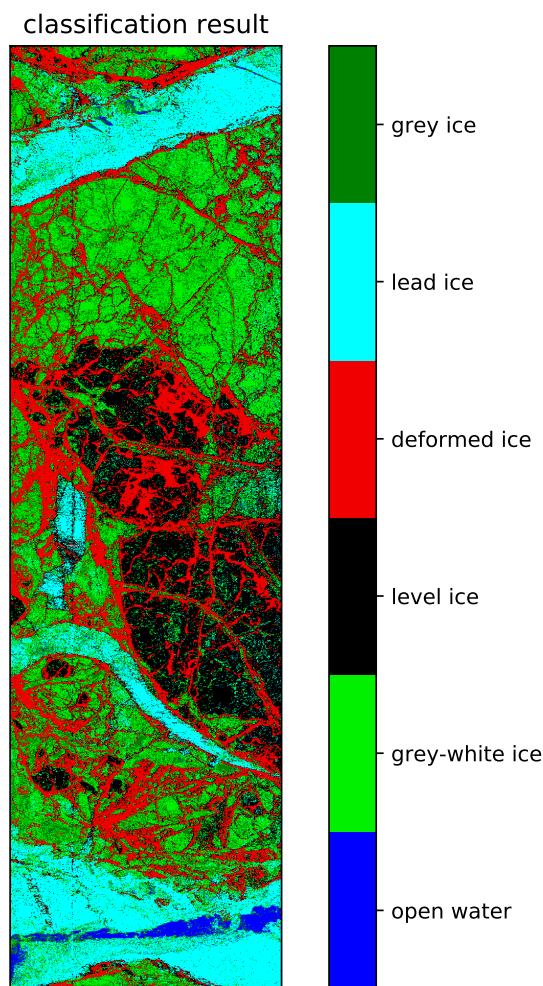


Figure 6. Result of ICESAR ice type classification from numerically optimized DT.

Table 4. Classification Accuracy (%) for ICESAR dataset for all-at-once (AAO) and decision-tree (DT) classifier.

	Total		Per-Class CA					Average
	CA	ω_1	ω_2	ω_3	ω_4	ω_5	ω_6	Per-Class CA
AAO	85.12	97.25	68.24	86.75	98.21	92.81	61.36	84.10
DT	87.48	99.75	75.43	87.40	98.57	93.69	65.76	86.77

Table 5. Single classes and selected features for each branch of the numerically optimized DT for ICESAR dataset.

DT Branch	Single Class	Feature Set
B_1	ω_4 : deformed ice	L_{HV}, L_{HH}
B_2	ω_1 : open water	$L_{HH}, C_{VV}, L_{VV}, L_{HV}$
B_3	ω_5 : nilas	$C_{VV}, L_{HH}, L_{VV}, C_{VH}$
B_4	ω_3 : level ice	C_{VH}, C_{VV}, L_{HV}
B_5	ω_6 : grey ice	$C_{VV}, L_{HH}, L_{HV}, L_{VV}$
AAO	—	$L_{HH}, C_{VV}, L_{VV}, L_{HV}, C_{VH}$

We use five features in this example, and they all contain relevant information on some of the trained classes. Consequently, the single feature set for AAO classification contains all available features in order selected by the SFFS: $\{L_{HH}, C_{VV}, L_{VV}, L_{HV}, C_{VH}\}$. The class-specific feature sets of the individual DT branches are subsets of the single AAO feature set (Table 5).

5. Discussion

The tests on the simulated datasets show that the DT design works as expected. Class ω_2 is selected as the individual class in the first branch, starting with feature f_2 , followed by f_5 and f_4 . This is in agreement with our design of the class distributions and can be confirmed by visual inspection of the histograms in Figure 4: In the 1D histograms, the most separable single class is clearly class ω_2 in feature f_2 .

Once the samples of class ω_2 are removed from the dataset, class ω_1 becomes the most separable, starting with feature f_5 , followed by f_{25} and f_{24} . Interestingly, the latter two features are not part of the commonly selected feature set in the traditional AAO classifier. This is due to different reasons: For feature f_{24} , there is large overlap between classes ω_1 and ω_2 , and classes ω_3 and ω_4 , respectively. Therefore, this feature does not contribute enough information to be selected in an AAO approach, where all classes are supposed to be separated simultaneously. For feature f_{25} , there seems to be too much overlap between the classes, although all distributions are slightly offset. However, after removing all samples from class ω_2 in the first branch of the DT, class ω_1 suddenly becomes significantly more separable in both features f_{24} and f_{25} . This example demonstrates how the optimized DT allows us to make efficient use of features, which are not considered at all in a traditional multi-class classification.

Furthermore, we find that the numerically optimized DT performs about 3% better in terms of total CA than a corresponding AAO classifier. As shown earlier, this improvement comes at the cost of significantly longer computation times for classifier design and slightly longer times for forward classification. However, once an optimal design for a given problem such as ice type classification for a certain ice condition and from a particular sensor or combination of sensors has been decided, the most time consuming design stage does not need to be performed repeatedly for new images. As expected, demanding ML in each individual branch of the DT leads to reduced classification accuracy. This emphasizes the importance of proper balancing of the single and mixed-class prior probabilities according to Equation (5).

The tuned RF classifier achieves results comparable to those of the optimized single DT. While the total CA is slightly higher in the presented example, it is slightly lower for other simulated cases. However, the final class label of the RF is determined by a majority vote from a large number of trees in the forest. Our method uses only one single, multi-variate tree, with feature sets tailored towards individual classes. These class-specific feature sets of the single tree make the interpretation of individual features easier compared to the statistical interpretation of an RF. The direct connection between a particular set of features and class distinction is obvious.

An improved overall classification result for DT compared to AAO is also achieved for ice type classification from the airborne ICESAR dataset. As in the simulated cases, demanding ML in every

single branch leads to lower total CA. The order of selected individual classes confirms that, at the relatively fine spatial resolution of 1.5 m, deformed ice is the individually best separable of the six classes given in Table 1. Furthermore, the selected features verify that L-band is superior to C-band measurements in the detection of deformed ice zones (Table 5, Branch 1). This is in agreement with results from earlier studies on the use of L-band for sea ice type classification, e.g., [26,28,36]. For open water we expect changing feature vectors, dependent on wind speed and direction relative to the open water leads in the ice cover. Visually, level ice and grey-white ice can be much better distinguished at C-band than at L-band, and level ice appears more inhomogeneous in the cross-polarized intensity channels than grey and grey-white ice (here we refer to intensity variations between the bright narrow deformation features). Both observations are reflected in the selected features (Table 5, B_4). This may be a consequence of beginning brine drainage, increasing volume of air bubbles and continued metamorphism processes in the snow layer.

A particularly large improvement in per-class CA was achieved for grey-white (7.2%) and grey ice (4.4%). Note that these are the classes with the overall lowest per-class CA, and thus the classes that are separated in the last branch of the DT (Table 5, B_5). Usually one expects that higher frequencies are more suitable to distinguish new and young ice. It is hence interesting to note that—although C-band VV-polarization is the first choice for distinguishing grey and grey-white ice—the additional use of L-band improves their separation. A more detailed analysis of the optimal choice of single features in the DT approach is beyond the scope of this study. We emphasize, however, that the selected features are related both to the characteristics of the single selected class and the remaining mixture of classes in each branch. In our example, this is valid for B_1 – B_4 .

6. Conclusions

We have introduced the fully automatic design of a numerically optimized DT classification algorithm that splits a multi-class classification problem with m classes into $m-1$ binary problems. In each branch of the DT, one class is separated from the other still remaining classes with an optimal set of features.

Tests on simulated datasets have demonstrated the capability of our algorithm to increase the total CA by 3.5% compared to traditional AAO classification. Improvement of 2.5% was achieved for classification of sea ice types from an airborne SAR dataset. Depending on class distributions and separability, individual classes may show larger improvement. In the presented sea ice example, CA for grey-white and for grey ice was improved by 7.2 and 4.4%. Since the absolute numbers of actual CA scores are highly dependent on the scene contents, we can only meaningfully compare to other methods using the same scenes. In our simulation and real world ICESAR examples, our proposed algorithm performs better than the more traditional AAO feature selection and Bayesian classification, and performs equivalently to the commonly used RF machine learning approach. At the same time our algorithm offers more direct interpretation of features and their potential to distinguish between particular classes.

The improved CA of the DT compared to the AAO approach comes at the cost of longer computation time. This is in particular true for the design and training stage, but to a lesser extent also for the forward classification stage. When time constraints are an essential part of the problem, as is the case in operational sea ice charting, the final choice of the classification strategy must be a trade-off between desired CA for single ice types and time constraints.

Author Contributions: Conceptualization, J.L. and A.P.D.; data curation, J.L. and W.D.; formal analysis, J.L.; investigation, J.L., A.P.D. and W.D.; methodology, J.L. and A.P.D.; supervision, A.P.D. and W.D.; validation, J.L., A.P.D. and W.D.; visualization, J.L.; writing—original draft, J.L., A.P.D. and W.D.; writing—review and editing, J.L., A.P.D. and W.D.

Funding: This research was funded by CIRFA partners and the Research Council of Norway (RCN) (grant number 237906).

Conflicts of Interest: The authors declare no conflict of interest.

Data Availability: Data as well as Python and Matlab scripts for data processing, analysis and classification can be achieved by contacting the first author.

Abbreviations

The following abbreviations are used in this manuscript:

AAO	All-At-Once
CA	Classification Accuracy
DT	Decision Tree
ML	Maximum Likelihood
PDF	Probability Density Function
ROI	Region Of Interest
RF	Random Forest
SAR	Synthetic Aperture Radar
SBFS	Sequential Backward Feature Selection
SFFS	Sequential Forward Feature Selection

References

1. Comiso, J.C.; Parkinson, C.L.; Gersten, R.; Stock, L. Accelerated decline in the Arctic sea ice cover. *Geophys. Res. Lett.* **2008**, *35*. [[CrossRef](#)]
2. Comiso, J.C. Large Decadal Decline of the Arctic Multiyear Ice Cover. *J. Clim.* **2012**, *25*, 1176–1193. [[CrossRef](#)]
3. Maslanik, J.; Stroeve, J.; Fowler, C.; Emery, W. Distribution and trends in Arctic sea ice age through spring 2011. *Geophys. Res. Lett.* **2011**, *38*. [[CrossRef](#)]
4. Lasserre, F.; Pelletier, S. Polar super seaways? Maritime transport in the Arctic: An analysis of shipowners' intentions. *J. Transp. Geogr.* **2011**, *19*, 1465–1473. [[CrossRef](#)]
5. National Research Council. *Seasonal-to-Decadal Predictions of Arctic Sea Ice: Challenges and Strategies*; The National Academies Press: Washington, DC, USA, 2012.
6. Eicken, H. Arctic sea ice needs better forecast. *Nature* **2013**, *497*, 431–433. [[CrossRef](#)]
7. Mussells, O.; Dawson, J.; Howell, S. Navigating pressured ice: Risks and hazards for winter resource-based shipping in the Canadian Arctic. *Ocean Coast. Manag.* **2017**, *137*, 57–67. [[CrossRef](#)]
8. Scheuchl, B.; Caves, R.; Cumming, I.; Staples, G. Automated sea ice classification using spaceborne polarimetric SAR data. In Proceedings of the Scanning the Present and Resolving the Future, IEEE 2001 International Geoscience and Remote Sensing Symposium (Cat. No.01CH37217), Sydney, Australia, 9–13 July 2001; Volume 7, pp. 3117–3119. [[CrossRef](#)]
9. Moen, M.A.N.; Doulgeris, A.P.; Anfinsen, S.N.; Renner, A.H.H.; Hughes, N.; Gerland, S.; Eltoft, T. Comparison of feature based segmentation of full polarimetric SAR satellite sea ice images with manually drawn ice charts. *Cryosphere* **2013**, *7*, 1693–1705. [[CrossRef](#)]
10. Leigh, S.; Wang, Z.; Clausi, D.A. Automated Ice-Water Classification Using Dual Polarization SAR Satellite Imagery. *IEEE Trans. Geosci. Remote Sens.* **2014**, *52*, 5529–5539. [[CrossRef](#)]
11. Liu, H.; Guo, H.; Zhang, L. SVM-Based Sea Ice Classification Using Textural Features and Concentration From RADARSAT-2 Dual-Pol ScanSAR Data. *IEEE J. Sel. Top. Appl. Earth Obs. Remote Sens.* **2015**, *8*, 1601–1613. [[CrossRef](#)]
12. Kwok, R.; Hara, Y.; Atkins, R.G.; Yueh, S.H.; Shin, R.T.; Kong, J.A. Application of Neural Networks to Sea Ice Classification Using Polarimetric SAR Images. In Proceedings of the Remote Sensing: Global Monitoring for Earth Management, IGARSS'91, Espoo, Finland, 3–6 June 1991; Volume 1, pp. 85–88. [[CrossRef](#)]
13. Hara, Y.; Atkins, R.G.; Shin, R.T.; Kong, J.A.; Yueh, S.H.; Kwok, R. Application of neural networks for sea ice classification in polarimetric SAR images. *IEEE Trans. Geosci. Remote Sens.* **1995**, *33*, 740–748. [[CrossRef](#)]
14. Karvonen, J.A. Baltic Sea ice SAR segmentation and classification using modified pulse-coupled neural networks. *IEEE Trans. Geosci. Remote Sens.* **2004**, *42*, 1566–1574. [[CrossRef](#)]
15. Zakhvatkina, N.Y.; Alexandrov, V.Y.; Johannessen, O.M.; Sandven, S.; Frolov, I.Y. Classification of Sea Ice Types in ENVISAT Synthetic Aperture Radar Images. *IEEE Trans. Geosci. Remote Sens.* **2013**, *51*, 2587–2600. [[CrossRef](#)]

16. Ressel, R.; Frost, A.; Lehner, S. A Neural Network-Based Classification for Sea Ice Types on X-Band SAR Images. *IEEE J. Sel. Top. Appl. Earth Obs. Remote Sens.* **2015**, *8*, 3672–3680. [[CrossRef](#)]
17. Remund, Q.P.; Long, D.G.; Drinkwater, M.R. An iterative approach to multisensor sea ice classification. *IEEE Trans. Geosci. Remote Sens.* **2000**, *38*, 1843–1856. [[CrossRef](#)]
18. Deng, H.; Clausi, D.A. Unsupervised segmentation of synthetic aperture Radar sea ice imagery using a novel Markov random field model. *IEEE Trans. Geosci. Remote Sens.* **2005**, *43*, 528–538. [[CrossRef](#)]
19. Ochilov, S.; Clausi, D.A. Operational SAR Sea-Ice Image Classification. *IEEE Trans. Geosci. Remote Sens.* **2012**, *50*, 4397–4408. [[CrossRef](#)]
20. Moen, M.A.M.; Anfinsen, S.N.; Doulgeris, A.P.; Renner, A.H.; Gerland, S. Assessing polarimetric SAR sea-ice classifications using consecutive day images. *Ann. Glaciol.* **2015**, *56*, 285–294. [[CrossRef](#)]
21. Shokr, M.E. Evaluation of second-order texture parameters for sea ice classification from radar images. *J. Geophys. Res. Ocean.* **1991**, *96*, 10625–10640. [[CrossRef](#)]
22. Barber, D.G.; LeDrew, E. SAR Sea Ice Discrimination Using Texture Statistics: A Multivariate Approach. *Photogramm. Eng. Remote Sens.* **1991**, *57*, 385–395.
23. Soh, L.K.; Tsatsoulis, C. Texture Analysis of SAR Sea Ice Imagery Using Gray Level Co-Occurance Matrices. *IEEE Trans. Geosci. Remote Sens.* **1999**, *37*, 780–795. [[CrossRef](#)]
24. Clausi, D.A. Comparison and fusion of co-occurrence, Gabor and MRF texture features for classification of SAR sea-ice imagery. *Atmosphere–Ocean* **2001**, *39*, 183–194. [[CrossRef](#)]
25. Ressel, R.; Singha, S. Comparing Near Coincident Space Borne C and X Band Fully Polarimetric SAR Data for Arctic Sea Ice Classification. *Remote Sens.* **2016**, *8*, 198. [[CrossRef](#)]
26. Dierking, W. Mapping of Different Sea Ice Regimes Using Images From Sentinel-1 and ALOS Synthetic Aperture Radar. *IEEE Trans. Geosci. Remote Sens.* **2010**, *48*, 1045–1058. [[CrossRef](#)]
27. Eriksson, L.E.; Borenäs, K.; Dierking, W.; Berg, A.; Santoro, M.; Pemberton, P.; Lindh, H.; Karlson, B. Evaluation of new spaceborne SAR sensors for sea-ice monitoring in the Baltic Sea. *Can. J. Remote Sens.* **2010**, *36*, S56–S73. [[CrossRef](#)]
28. Dierking, W. Sea Ice Monitoring by Synthetic Aperture Radar. *Oceanography* **2013**, *26*, 100–111. [[CrossRef](#)]
29. Theodoridis, S.; Koutroumbas, K. *Pattern Recognition*, 4th ed.; Academic Press, Inc.: Orlando, FL, USA, 2008.
30. Kim, M.; Im, J.; Han, H.; Kim, J.; Lee, S.; Shin, M.; Kim, H. Landfast sea ice monitoring using multisensor fusion in the Antarctic. *Gisci. Remote Sens.* **2015**, *52*, 239–256. [[CrossRef](#)]
31. Geldsetzer, T.; Yackel, J.J. Sea ice type and open water discrimination using dual co-polarized C-band SAR. *Can. J. Remote Sens.* **2009**, *35*, 73–84. [[CrossRef](#)]
32. Hollands, T.; Dierking, W. Dynamics of the Terra Nova Bay Polynya: The potential of multi-sensor satellite observations. *Remote Sens. Environ.* **2016**, *187*, 30–48. [[CrossRef](#)]
33. Han, H.; Im, J.; Kim, M.; Sim, S.; Kim, J.; Kim, D.; Kang, S. Retrieval of Melt Ponds on Arctic Multiyear Sea Ice in Summer from TerraSAR-X Dual-Polarization Data Using Machine Learning Approaches: A Case Study in the Chukchi Sea with Mid-Incidence Angle Data. *Remote Sens.* **2016**, *8*, 57. [[CrossRef](#)]
34. Parzen, E. On Estimation of a Probability Density Function and Mode. *Ann. Math. Stat.* **1962**, *33*, 1065–1076. [[CrossRef](#)]
35. Silverman, B. *Density Estimation for Statistics and Data Analysis*, 1st ed.; Routledge: New York, NY, USA, 1986.
36. Dierking, W. *Technical Assistance for the Deployment of Airborne SAR and Geophysical Measurements during the ICESAR 2007; Final Report—Part 2: Sea Ice*; ESA-ESTEC: Noordwijk, The Netherlands, 2008.





Paper II:

**Mapping Sea Ice Types from
Sentinel-1 Considering the
Surface-Type Dependent Effect
of Incidence Angle**

Lohse J, Doulgeris AP and Dierking W (2020). *Annals of Glaciology*



Paper

Cite this article: Lohse J, Doulgeris AP, Dierking W (2020). Mapping sea-ice types from Sentinel-1 considering the surface-type dependent effect of incidence angle. *Annals of Glaciology* 1–11. <https://doi.org/10.1017/aog.2020.45>

Received: 6 December 2019

Revised: 29 May 2020

Accepted: 1 June 2020

Key words:

classification; remote sensing; sea ice

Author for correspondence:

Johannes Lohse,

E-mail: johannes.p.lohse@uit.no

Mapping sea-ice types from Sentinel-1 considering the surface-type dependent effect of incidence angle

Johannes Lohse¹, Anthony P. Doulgeris¹ and Wolfgang Dierking^{1,2}

¹Department of Physics and Technology, UiT The Arctic University of Norway, 9019 Tromsø, Norway and ²Alfred Wegener Institute, Helmholtz Center for Polar and Marine Research, Bussestr. 24, 27570 Bremerhaven, Germany

Abstract

Automated classification of sea-ice types in Synthetic Aperture Radar (SAR) imagery is complicated by the class-dependent decrease of backscatter intensity with Incidence Angle (IA). In the log-domain, this decrease is approximately linear over the typical range of space-borne SAR instruments. A global correction does not consider that different surface types show different rates of decrease in backscatter intensity. Here, we introduce a supervised classification algorithm that directly incorporates the surface-type dependent effect of IA. We replace the constant mean vector of a Gaussian probability density function in a Bayesian classifier with a linearly variable mean. During training, the classifier first retrieves the slope and intercept of the linear function describing the mean value and then calculates the covariance matrix as the mean squared deviation relative to this function. The IA dependence is no longer treated as an image property but as a class property. Based on training and validation data selected from overlapping SAR and optical images, we evaluate the proposed method in several case studies and compare to other classification algorithms for which a global IA correction is applied during pre-processing. Our results show that the inclusion of the per-class IA sensitivity can significantly improve the performance of the classifier.

Introduction

Continuous monitoring and mapping of sea ice are important for a variety of reasons. Besides usage in environmental and climatological studies, timely and accurate high-resolution ice charts are needed to (a) support offshore operations as well as marine traffic and navigation, (b) generate long-term statistics of sea-ice conditions in particular regions of interest and (c) assimilate high-resolution sea-ice information into numerical models. Currently, the main and often only source on sea-ice conditions is remote-sensing data (Zakhvatkina and others, 2019). National ice services worldwide rely, in particular, on Synthetic Aperture Radar (SAR) observations, because of the radar's continuous imaging capability during darkness and its independence of cloud conditions (Scheuchl and others, 2004; Dierking, 2010, 2013). At present, analysis of the images and production of ice charts is performed manually by ice analysts (Zakhvatkina and others, 2019). Ice chart production thus involves subjective decisions and is a time-consuming process. Yet many of the applications mentioned above require the processing of large numbers of images in near-real-time. Hence, robust and reliable automation of sea-ice type mapping is required to assist in operational ice charting.

A lot of effort has been put into research on the automated or semi-automated classification of sea ice in SAR images during the last decades. Different classification methods have been tested, including Bayesian classifiers (Scheuchl and others, 2001; Moen and others, 2013), Support Vector Machines (SVM) (Leigh and others, 2014; Liu and others, 2015), Decision Trees (DT) (Geldsetzer and Yackel, 2009; Lohse and others, 2019), Neural Networks and Convolutional Neural Networks (NN and CNN) (Kwok and others, 1991; Hara and others, 1995; Karvonen, 2004; Zakhvatkina and others, 2013; Ressel and others, 2015) or Random Forests (RF) (Han and others, 2016). Advantages and disadvantages of different radar frequencies (Dierking, 2010; Eriksson and others, 2010) have been investigated as well as combinations of sensors (Hollands and Dierking, 2016) and the use of textural information (Barber and LeDrew, 1991; Clausi, 2001), different polarizations and polarimetric features (Moen and others, 2015). Generic, automated analysis of ice types in SAR images, however, remains difficult. The main challenges include the general ambiguity of radar backscatter from different sea-ice types, varying wind states and thus changing surface roughness of open water, sensor-dependent noise in the data and, in particular, the Incidence Angle (IA) dependency of the backscattered signal. While we consider and discuss all of these factors within this study, our major focus will be the issue of IA dependency.

It is known that the IA of a radar signal onto a surface influences the intensity of the signal backscattered from that surface (Onstott and Carsey, 1992). In a typical SAR image, this effect is visible as a global trend of image brightness in range direction, with generally higher backscatter values in near-range (low IA) and lower backscatter values in far-range (high IA). The IA effect is usually treated as a single image property and accounted for globally during

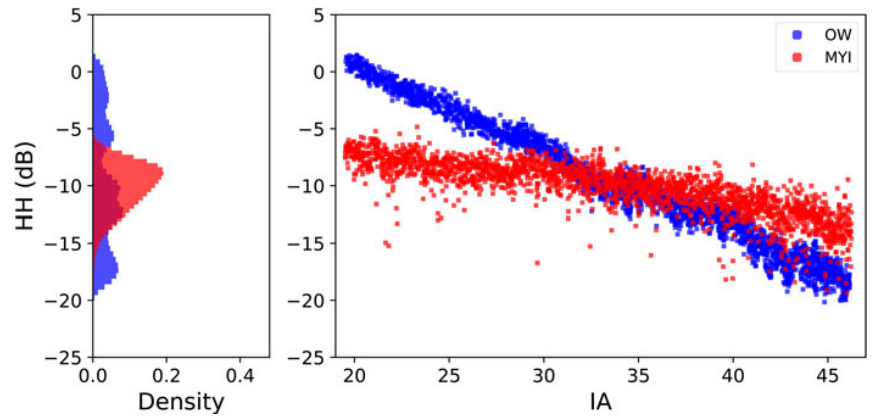


Fig. 1. Right panel: Linear dependency of HH backscatter intensity in dB with IA for two different surface types: OW and MYI. The two classes show considerable differences in the decrease of the backscatter intensity at HH-polarization as a function of IA. Left panel: distribution of backscatter intensity for both classes over the full IA range. Both distributions are highly affected and broadened by the IA effect.

pre-processing of the data before automatic classification. A range-dependent correction can be applied to normalize the backscatter across the image to a reference IA (Zakhvatkina and others, 2013, 2017; Karvonen, 2014, 2017; Liu and others, 2015) or to convert the normalized radar cross section from σ^0 values to γ^0 values, with $\gamma^0 (\sigma^0 / \cos^2 \theta)$.

Although such a pre-processing correction improves the result of automatic classification, a global correction of the entire image neglects the fact that different surface types show varying rates of decrease in backscatter with IA. The more the rates differ for distinct classes, the more the classification is affected. The surface-type dependent rates for various sea-ice types and different radar frequencies have been investigated in several studies, such as Mäkynen and others (2002), Mäkynen and Karvonen (2017) or Mahmud and others (2018). Over the typical range of most spaceborne SAR sensors, i.e. roughly between 20° and 45° , backscatter intensity in decibel (dB) decreases approximately linear with IA (Fig. 1).

The slopes of the linear functions, however, show large variations (Mäkynen and Karvonen, 2017). Reasons for this are different definitions of ice classes (that usually comprise different ‘pure’ ice types), regional differences of ice and snow conditions (Gill and others, 2015), seasonal variations of meteorological conditions (in particular effects of melt-freeze cycles) and also differences in methodological approaches.

A straightforward surface-type dependent IA correction during pre-processing is not possible. As the surface type at a given position in the image is not known before classification, it is not possible to decide a priori which rate of decrease to apply. In this study, we demonstrate how to incorporate surface-type dependent IA effect into a supervised, probabilistic classification algorithm. We use overlapping SAR and optical images acquired under freezing conditions over several years to identify different ice types and select training and validation sets with the help of expert sea-ice analysts from the Norwegian Ice Service. We then assess the benefits and drawbacks of our developed method in comparison with other classification algorithms applied to the same dataset.

The remainder of this paper is structured as follows: in the following section we describe the dataset and the applied pre-processing steps. We provide definitions of the different ice classes and explain how we selected suitable training and validation sets for the algorithm, based on overlapping optical and SAR images from different locations distributed all over the Arctic. Next, we give a detailed explanation of the algorithm framework, followed by an outline of the study design. After presenting the results, we evaluate and discuss our findings and then summarize our main conclusions in the final section.

Data

Sentinel-1 SAR data

For the SAR imagery, we use Sentinel-1 (S1) Extra Wide swath (EW) data. S1 operates at C-band (5.4 GHz) in either single or dual-polarization mode. All S1 imagery is freely available and can be obtained for example from the Copernicus Open Access Hub. The EW data are typically provided in Single-Look Complex (SLC) or Ground Range Detected (GRD) format. The Level-1 GRD product is multi-looked and projected to ground range using an Earth ellipsoid model (Aulard-Macler, 2011). Its resulting spatial resolution depends on the number of looks. The Medium resolution product (GRDM) is provided at a pixel spacing of $40 \text{ m} \times 40 \text{ m}$ with an actual resolution of $\sim 93 \text{ m} \times 87 \text{ m}$ and an estimated number of looks of 10.7.

In this study, we use only GRDM data at dual-polarization (HH and HV). To obtain a broad, Arctic-wide definition of sea-ice classes, we use data from different years (2015–19) and from many different locations all over the Arctic (Fig. 2). However, as surface melt affects the radar backscatter signature of sea ice, we restrict our current demonstration study of the algorithm principle to data acquired under freezing conditions in winter and early spring months.

SAR data processing

During processing, we apply ESA’s thermal noise correction implemented in the Sentinel Application Platform (SNAP) and calibrate the data to obtain the normalized radar cross section σ^0 . To further reduce speckle, we perform additional multi-look with a sliding window. After testing different window sizes of 3×3 , 5×5 , 7×7 and 9×9 pixels, we chose 3×3 as the default window size for our processing. This proved to reduce speckle sufficiently, while at the same time keeping the spatial resolution at better than 200 m in each direction. Finally, we convert the backscatter intensities into dB. All S1 data presented in this study has been processed accordingly.

Overlapping SAR and optical data

For identification of different sea-ice types as well as the initial selection of training and validation regions we use overlapping SAR and optical data. We utilize the ‘sentinelAPI’ from the Python ‘sentinelapi’ module to search for spatially overlapping S1 and optical data (Sentinel-2 (S2) and LandSat-8 (L8)) across the entire Arctic, with a difference in an acquisition time of $< 3 \text{ h}$ and a cloud cover of $< 30\%$. Different examples of overlapping SAR and optical scenes are shown in Figure 3.

With the assistance of expert sea-ice analysts from the Norwegian Ice Service we have manually analyzed 80 such pairs

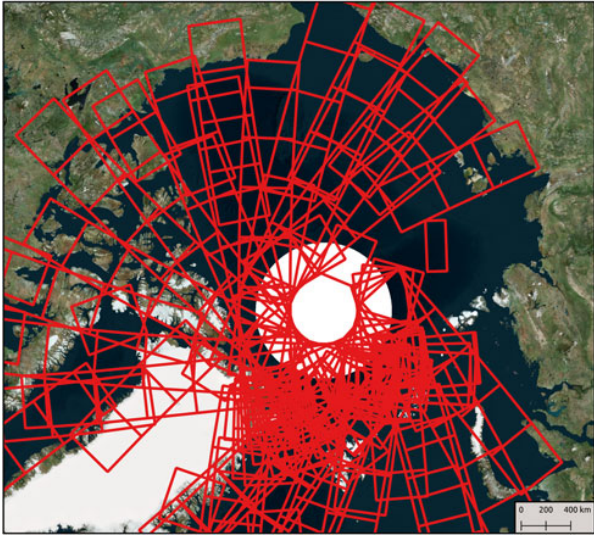


Fig. 2. Locations of all S1 images used for manual identification of ice types and selection and verification of training and validation data. All images are acquired in winter or early springtime between 2015 and 2019.

of overlapping optical and SAR images to identify different sea-ice types and select Regions Of Interest (ROIs) with training and validation data in the S1 data. All identified ice types are listed in Table 1. The identification of many of these ice types is only possible from the combination of SAR and optical imagery, with the addition of expert experience. In particular, Level First-Year Ice (LFYI), Deformed First-Year Ice (DFYI) and Multi-Year Ice (MYI) are difficult to distinguish in optical images, depending on spatial resolution, light conditions, snow coverage and ice concentration.

However, based on differences in radar backscatter in combination with information on the location and the ice history (which the ice analysts usually take into account), reliable ROIs can be defined. Areas with example ROIs are indicated in Figure 3.

As we explain in detail in the next section, our developed algorithm relies on an accurate estimation of the linear rate in backscatter intensity given in logarithmic scale with IA for each class. This estimation requires training data over a wide enough IA range, preferably over the entire swath width. Since the overlapping data with cloud-free conditions in the optical image often only cover a small range of the SAR image, we have investigated additional S1 images searching for homogeneous areas with a particular ice type covering a wide distance in range. The second column in Table 1 indicates for which ice types we could identify such homogeneous areas over a wider distance in range. In total, we used more than 100 S1 images for our definition of sea-ice types and the selection of training and validation regions. The spatial distribution of all these images is shown in Figure 2.

For the work presented in this study, we focus only on homogeneous ice classes. Pixels covering a mixture of different ice types or ice and water are not included in analyzing the IA sensitivity of different ice types. During classification, such mixed pixels will be assigned to the ice type that is dominant in the pixel or to another ice type with similar backscatter at the given IA. This, however, is not specific to our method but a general problem for all classification algorithms.

One particularly challenging class is Open Water (OW). Its overall backscatter values, as well as the slopes of backscatter intensity with IA, depend on radar parameters (frequency, polarization and look-direction) and environmental factors (wind

speed and direction). In a first attempt, we have tried to train several OW classes for different wind conditions. However, in the presented case studies, we restrict ourselves to data acquired under similar wind conditions, which reveal a constant and steep slope.

Method

The major novelty of the presented work is the development of an algorithm framework that can directly incorporate per-class variation of backscatter intensity with IA into supervised classification. This method section, therefore, starts with the detailed explanation of the design of the algorithm, followed by a description of the study design to test and validate the method and compare it to approaches used in the past.

Algorithm design

The per-class incorporation of the IA effect into supervised classification can be implemented most straightforwardly in a Bayesian classifier. We thus give a short review of Bayesian classification before explaining our modifications to the traditional algorithm.

Bayesian classification

A Bayesian classifier is a well-known probabilistic classification method. Every sample \underline{x} , i.e. image pixel in our case, is assigned to the most probable class ω_i (Theodoridis and Koutroumbas, 2008). For Maximum Likelihood, the decision rule of a Bayesian classifier can be expressed as:

$$\underline{x} \rightarrow \omega_i \quad \text{if} \quad p(\underline{x}|\omega_i) > p(\underline{x}|\omega_k) \quad \forall k \neq i. \quad (1)$$

Here, $p(\underline{x}|\omega_i)$ is the multi-variate class-conditional Probability Density Function (PDF) of class ω_i . The PDFs must be known in order to assign an individual sample to a particular class and are usually estimated from training data with known class labels. For an unknown shape, the PDF can be approximated by kernel density estimation (Parzen, 1962). If we know the general shape of the PDF, we can directly estimate the shape parameters from the training data. Since we work with backscatter intensities in the log-domain (i.e. in dB) we can use the common assumption of a multi-variate Gaussian distribution. The PDF for class ω_i is then fully described by its mean vector $\underline{\mu}_i$ and covariance matrix Σ_i :

$$p_i(\underline{x}|\omega_i) = \frac{1}{(2\pi)^{\frac{d}{2}} |\Sigma_i|^{\frac{1}{2}}} e^{-\frac{1}{2}(\underline{x}-\underline{\mu}_i)^T \Sigma_i^{-1} (\underline{x}-\underline{\mu}_i)} \quad (2)$$

Once the mean vector and covariance matrix have been determined for each class, Eqns (1) and (2) can be combined to classify any given test sample \underline{x} . We later use this traditional Bayesian classifier with a Gaussian PDF with constant mean value and an image-wide correction of IA as one comparison method to our proposed algorithm.

The Gaussian IA classifier

In the case of SAR data, both the mean vector and the covariance matrix of an individual class can be affected by the distribution of the available training data over IA for that particular class. The spatial abundance distribution of training in the range direction is being translated through the IA relation (Fig. 1) into the spreading of the distributions in intensity. If most training data are available at near-range, the mean backscatter values will be higher compared to a case where most training data

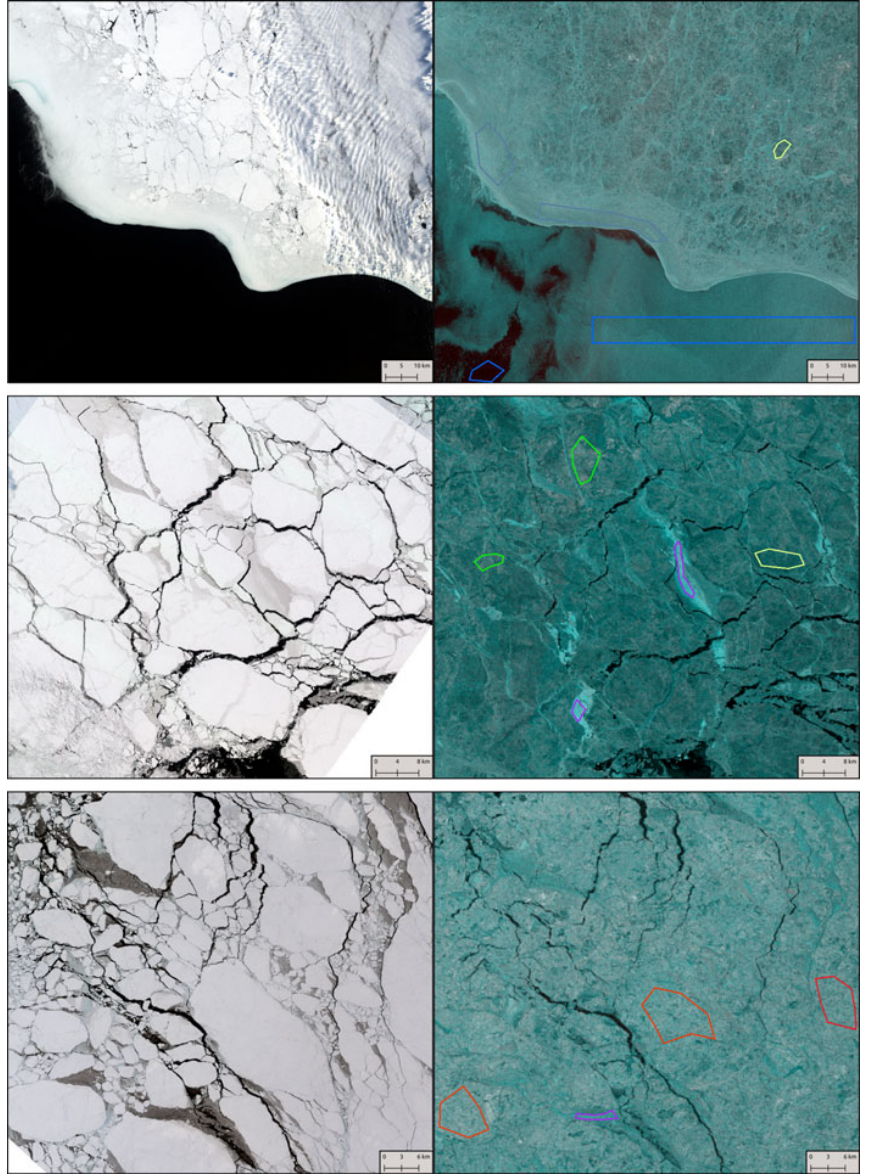


Fig. 3. Examples of overlapping SAR (right, R = HV, G = HH and B = HH) and optical (left, RGB channels) data for the selection of training data. Example ROIs for different surface types, selected with the assistance of experienced ice analysts from the Norwegian Ice Service, are indicated with different colours (OW (blue), Brash/Pancake Ice (gray-blue), YI (purple), LFYI (yellow), DFYI (green), MYI (red)).

Table 1. List of ice types identified from overlapping SAR and optical images

Ice-type	Found in homogeneous area over wide range
Open water (OW), calm	No
Open water (OW), windy	Yes
Leads	No
Brash/Pancake Ice	No
Young ice (YI)	No
Level first-year ice (LFYI)	Yes
Deformed first-year ice (DFYI)	No
Multi-year ice (MYI)	Yes

are available at far-range. If training data are available over a large range of IAs, the mean value will be somewhere in between, but the variance will be high due to the spread over the IA range. Although a global IA correction during pre-processing reduces these effects, incorrect slopes will still result in increased variances and insufficiently corrected means. Figure 4 shows an example of training data for two classes with clearly distinct IA dependency and the resulting histograms for global corrections along different slopes. Note that the distribution of an

individual class becomes almost Gaussian when the class is corrected along the right slope.

Instead of using a pre-processing correction, we suggest treating the IA sensitivity as an ice-class property. For the Bayesian approach, this means to make use of the approximately linear relationship between mean vector and IA and replace the constant mean vector $\underline{\mu}_i$ with a linearly variable mean vector $\underline{\mu}_i(\Theta)$:

$$\underline{\mu}_i(\Theta) = \underline{a}_i + \underline{b}_i \cdot \Theta \quad (3)$$

The class-conditional PDF can then be written as a PDF with linearly variable mean:

$$p_i(\underline{x}|\omega_i) = \frac{1}{(2\pi)^{\frac{d}{2}}|\Sigma_i|^{\frac{1}{2}}} e^{-\frac{1}{2}(\underline{x}-(\underline{a}_i+\underline{b}_i\Theta))^T \Sigma_i^{-1}(\underline{x}-(\underline{a}_i+\underline{b}_i\Theta))} \quad (4)$$

Instead of the mean vector $\underline{\mu}_i$ the algorithm retrieves the intercept \underline{a}_i and slope \underline{b}_i (Eqn 3) for each class during the learning phase. The covariance is now calculated as the mean squared deviation relative to a mean value that depends on the IA. Its magnitude is lower since the spread due to the IA sensitivity that occurs

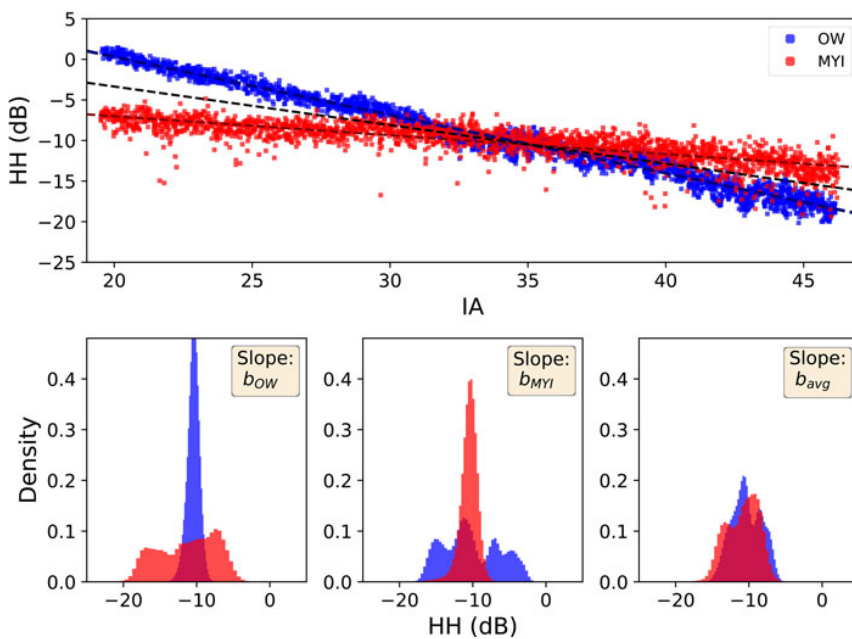


Fig. 4. HH intensity in dB of training data for OW and MYI, with per-class and average linear slopes indicated by dashed lines (top panel). Per-class histograms of HH intensity are shown after global correction to 35° along each of the three individual slopes (bottom panel).

when assuming a constant mean is reduced. Note that a remnant in sensitivity to IA may remain if nonlinear terms in the variation of the mean cannot be neglected. Finally, Eqns (1) and (4) can again be combined to classify any given test sample \underline{x} . In the following, we refer to this classification method as the Gaussian IA (GIA) classifier.

Study design

We have implemented the GIA classifier according to the equations given above and investigate its performance on a variety of case studies for sea-ice type classification. For comparison, we apply other well-established classification methods that use a traditional, global IA correction with a constant slope for all classes. In the following section, we summarize the implementation details of the GIA classifier and give an overview of the various case studies, validation procedure and the selected comparison methods.

Implementation

We have coded the implementation of the GIA classifier in python in the same style as other supervised classifiers in the scikit-learn module (Pedregosa and others, 2011). During training, a classifier object `clf` is created, then the classification parameters (for the GIA classifier i.e. class-dependent slope, intercept and covariance matrix) are estimated by calling the object method `clf.fit()`. Afterwards, new samples can be classified by calling the object method `clf.predict()`. This implementation makes it very easy to switch between different classification methods and compare the GIA classifier to other approaches by simply changing how the classifier object is created.

During training in default mode, the GIA classifier retrieves the class-dependent slopes for each dimension from the available training data. However, we have added the possibility to manually prescribe slopes when initializing the classifier. This allows the user to set reasonable slopes if the training data for an individual class is not sufficient for accurate slope estimation, or to test slopes for certain ice types that have been reported in previous studies.

Case studies

To test and demonstrate the principle functionality of the GIA classifier, we start our analysis by investigating various two-class case studies. For this purpose, we select two classes out of the entire multi-class training and validation set. These simple two-class tests are most suitable to demonstrate and visualize the underlying concept of our developed method and to point out particular benefits and drawbacks of the method under well-defined conditions.

Since the HH polarization reveals a stronger IA sensitivity than the HV polarization, we first focus on testing our method using the HH channel only, which we denote ‘1D case’. HV polarization is less sensitive to IA but provides complementary information to improve Classification Accuracy (CA). In the next step, we therefore extend the classifier to include the HV channel as well. The resulting classifier uses both HH and HV intensity and we refer to it as a ‘2D case’.

Different 2-class case studies with both 1-D and 2-D instances of the GIA classifier offer the easiest way to gain insights into the newly introduced method for class-dependent IA correction during classification and we, therefore, regard them as instructive for the demonstration of the novel concept. However, ice type classification is typically a multi-class problem. Following the 2-class case studies, we thus extend the classifier to multiple classes and finally demonstrate its potential for automated ice chart production.

Validation

We calculate CA from a broad and independent validation set, which we obtain by randomly splitting the data points from all selected ROIs into training and validation sets. This means in practice that the validation is not carried out for individual images, but for various ice conditions found in the collection of different images with our ROIs. While the training sets are used for fitting the coefficients of the classifiers to the data, the validation sets are used to independently evaluate the classifiers’ performance based on CA. Varying the randomized train-test split of the ROIs allows us to estimate standard deviations for CA based on the selected dataset.

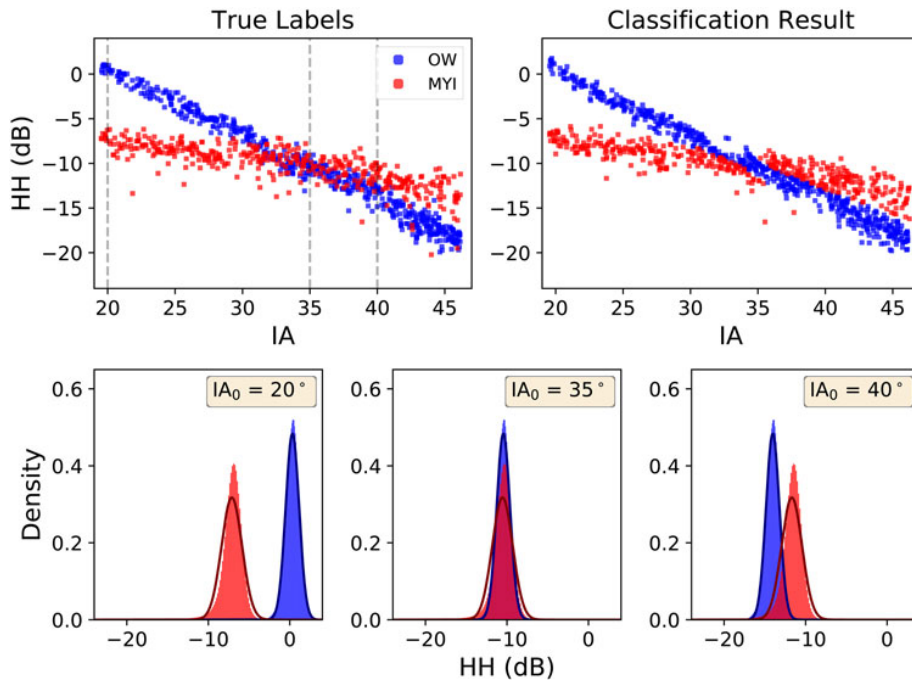


Fig. 5. 1D Example of the two-class case study (2), OW vs (MYI). The top panel shows HH intensity over IA, with true class labels (training) indicated on the left and predicted class labels (validation) indicated on the right, respectively. The bottom panel shows histograms and slices through the class-conditional PDFs with variable mean at three different IA locations. The IA locations are indicated with grey dashed lines in the training data.

Comparison classifiers

In order to assess improvements in CA, we compare the GIA classifier to other commonly used classification methods. In particular, we test a RF classifier, a SVM and a traditional Bayesian Classifier with Gaussian PDF (denoted as BCG). All of these comparison algorithms have previously been shown to be useful for classification of sea-ice types. For all the comparison methods, we apply a global IA correction with a constant slope during pre-processing. For the global correction, we always choose the average slope of the involved classes. Furthermore, we optimize the comparison classifiers in terms of CA by performing a grid-search over the number of trees and the maximum depth of the RF and by testing different kernels for the SVM.

Results

Two-class case studies

We present the results of the algorithm performance on three different case studies with simplified two-class problems. The individual classes in these case studies are the classes with training data from large homogeneous areas (Table 1). Note that training and validation data are collected from numerous images and not from a single individual scene. The individual two-class problems presented here are:

- (1) OW vs LFYI
- (2) OW vs MYI
- (3) LFYI vs MYI

The results for a 1-D GIA classifier applied to the case study (2) using only HH intensity are illustrated in Figure 5. The classes OW and MYI have clearly distinct slopes of -0.72 dB/1° and -0.23 dB/1° , respectively. The GIA classifier can successfully handle the case for most IA ranges. Some misclassification occurs in the IA range where the backscatter coefficients of MYI and OW overlap (-7 dB to -13 dB). The slices of the histograms and class-

conditional PDFs at different IAs (Fig. 5, bottom panel) illustrate the locally narrow Gaussian distributions and can furthermore indicate whether or not the data are well separable for a particular IA range. Figure 6 shows the improved results when extending the classifier to two dimensions, including HV intensity. Note that the HV intensity also shows a considerable slope for both classes with -0.33 dB/1° for OW and -0.23 dB/1° for MYI, respectively.

The corresponding per-class CA and mean per-class CA is given in Table 2. We compare 1-D (using only HH intensity) and 2-D classifiers (using intensities at HH and HV) and give results for all three case studies and all tested classifiers. CA standard deviation estimated by bootstrapping is in the range of 0.1 and 0.25% for all individual CA values. For the cases including the OW class, the GIA classifier achieves the best CA, while the results are very similar for the LFYI-vs-MYI case. Note that the slopes for these two ice types are quite similar with -0.27 dB/1° at HH and -0.26 dB/1° at HV for LFYI and -0.23 dB/1° at both HH and HV for MYI, respectively. We observe a general improvement in CA when adding the HV intensity for all classifiers and all case. In the 1-D examples, the classifiers using a global IA correction can favour one individual class in some cases. For case study (2), this results in a high score for one particular class (CA_{MYI}) and a low score for another class (CA_{OW}). Overall, the GIA classifier clearly performs best with the highest average per-class CA.

Average processing time for training and prediction is also presented in Table 2. Since absolute timing always depends on hardware and software components as well as the implementation of the algorithm itself, we present processing times relative to each other. All times are given normalized to the processing time of the GIA classifier. Training of the traditional BCG is more than twice as fast as training of the GIA classifier, and prediction of new sample labels is slightly faster. Both RF and SVM take one to two orders of magnitude longer for both training and prediction compared to the GIA classifier.

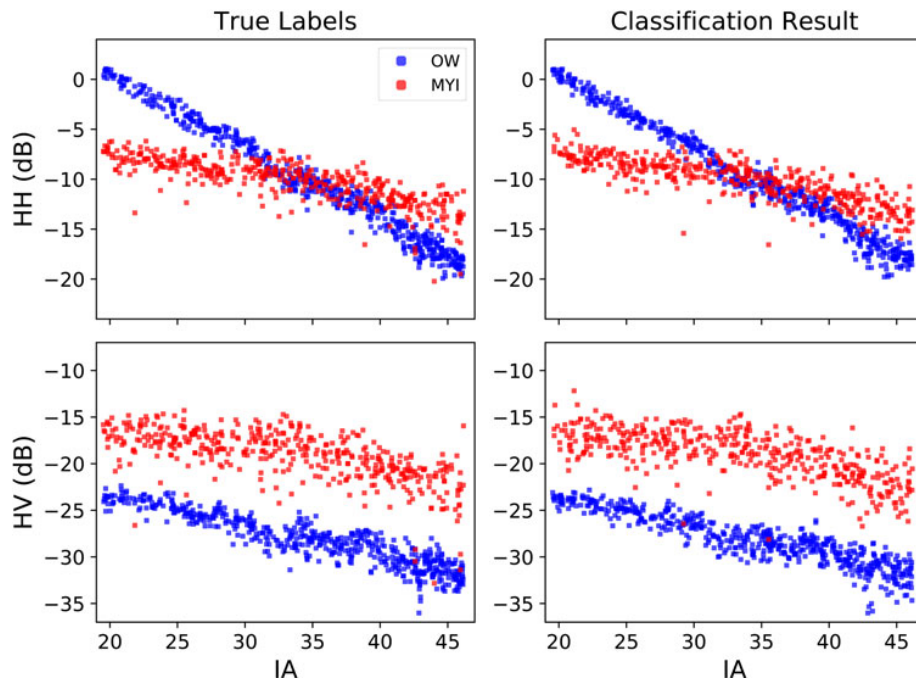


Fig. 6. 2D Example of the two-class case study (2), OW vs MYI. HH intensity (top) and HV intensity (bottom) are shown over IA, with true class labels (training) indicated on the left and predicted class labels (validation) indicated on the right, respectively.

Table 2. Classification Accuracy (CA) for different classifiers tested on three individual two-class problems

Classifier	OW vs LFYI			OW vs MYI			LFYI vs MYI			Normalized timing	
	CA_{OW}	CA_{LFYI}	..	CA_{OW}	CA_{MYI}	\bar{CA}	CA_{LFYI}	CA_{MYI}	\bar{CA}	Train	Predict
BCG (1D)	88.72	95.07	91.90	56.86	86.70	71.78	96.66	98.41	97.53	0.37	0.95
GIA (1D)	94.84	93.33	94.08	85.93	75.92	80.93	96.78	98.35	97.56	1.00	1.00
RF (1D)	90.71	91.89	91.30	62.88	80.17	71.52	95.84	98.34	97.09	99.09	44.32
SVM (1D)	91.45	92.81	92.13	62.81	81.89	72.35	96.28	98.78	97.53	186.22	103.59
BCG (2D)	89.73	95.92	92.82	97.15	98.95	98.05	97.30	99.43	98.36	0.41	0.91
GIA (2D)	96.45	94.55	95.50	98.11	99.60	98.85	97.33	99.41	98.37	1.00	1.00
RF (2D)	91.77	93.94	92.85	96.96	99.18	98.07	97.56	99.27	98.41	83.31	22.72
SVM (2D)	91.45	94.68	93.06	96.95	99.34	98.14	97.56	99.35	98.45	108.27	68.71

All classifiers are tested in 1D (HH intensity only) and 2D (both HH and HV intensity). Global IA correction with a constant slope has been applied before BCG, RF and SVM classification to compare with per-class IA correction within the GIA classifier. Standard deviation for all the above values given is between 0.1 and 0.25.

Three-class case studies

Based on the results for the two-class case studies presented so far, we extend our analysis to a three-class problem. Following the three different two-class case studies, the three-class example is enumerated as a case study (4):

(1) OW vs. LFYI vs MYI

The results for all tested classifiers are presented in Table 3. Again, the GIA classifier achieves the highest overall CA. Individual classes can occasionally score higher in other classifiers (e.g. CA_{MYI} for the BCG, Table 3), but again this comes at the expense of lower scores for the other classes. Compared to the different two-class case studies, the average per-class CA of the 2D GIA classifier for the three-class case is $\sim 3\%$ lower than the CA of case studies (2) and (3), and almost equal to the CA of the case study (1).

Ice charts

Results for mosaic ice type maps from two randomly selected dates are presented in Figure 7. Both examples show the

Table 3. Classification Accuracy (CA) for different classifiers tested on a three-class problem OW-vs-LFYI-vs-MYI (case study (4))

Classifier	CA_{OW}	CA_{LFYI}	CA_{MYI}	\bar{CA}
BCG (1D)	85.23	44.46	96.84	75.51
GIA (1D)	74.37	82.72	94.10	83.73
RF (1D)	79.88	53.42	93.83	75.71
SVM (1D)	80.39	53.35	94.72	76.16
BCG (2D)	89.47	96.69	95.51	93.89
GIA (2D)	96.22	96.74	94.27	95.74
RF (2D)	92.51	96.58	92.46	93.85
SVM (2D)	91.91	96.60	93.63	94.04

All classifiers are tested in 1D (HH intensity only) and 2D (both HH and HV intensity). Global IA correction with a constant slope has been applied before BCG, RF and SVM classification to compare with per-class IA correction within the GIA classifier. Standard deviation for all the above values given is between 0.1 and 0.25 for individual values.

underlying S1 data on the left side and the classification result on the right side. The example in the top panel covers nearly the entire Arctic and is based on 72 S1 images acquired on 3 and 4 March 2019. The example in the bottom panel covers a smaller region north of Svalbard and is based on three overlapping S1 images acquired on 5 April 2018. We regard the

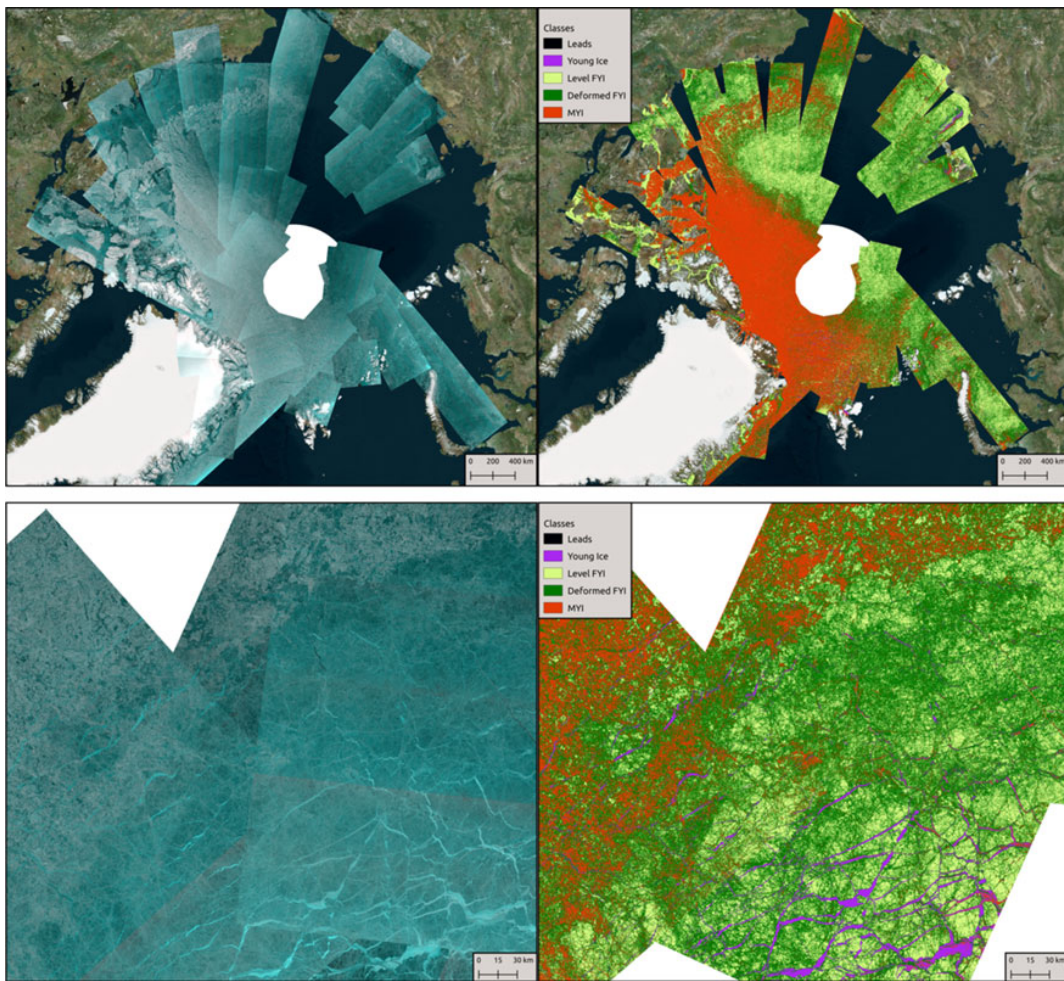


Fig. 7. Examples of mosaic classification results for the entire Arctic (top panel, based on 72 S1 images acquired on 3 and 4 March 2019) and a smaller region north of Svalbard (bottom panel, based on 3 S1 images acquired on 5 April 2018). S1 data are shown on the left (R = HV, G = HH and B = HH) and classification results on the right. The classified regions seamlessly overlap at image boundaries, indicating a successful per-class correction of IA effect.

presentation of a combination of three images as useful, as it allows for inspection of classification results across image boundaries, which is potentially strongly influenced by IA effect. [Figure 7](#) shows that the classification results connect consistently across image boundaries.

Discussion

Algorithm behaviour

Overall, the proposed inclusion of the per-class IA sensitivity directly in the classification process performs very well for the test cases and improves the CA significantly. The underlying concept and the effect of the method is best visualized in a 1-D case for two classes ([Fig. 5](#)). The classes in the shown example for the case study (2), OW and MYI, have significantly different slopes and the GIA classifier clearly improves the classification result. Furthermore, histograms and slices of the PDF with variable mean at different base values IA_0 give an indication of how well separable the data are in a particular IA range. In the presented case, OW and MYI are well separable at HH-polarization in near range. As we move towards far range, the overlap between the PDFs increases, resulting in a decreased separability. At an IA of $\sim 35^\circ$, the linear functions describing the variable mean value for each class intersect. The local mean values of both classes are thus identical at this range and the distributions

have maximum overlap; hence the two classes have worst separability ([Fig. 5](#), bottom panel). Since the OW class has a smaller covariance than the MYI class, the maximum probability from the OW PDF is larger than the maximum probability from the MYI PDF. Hence, when local mean values are identical, pixels with a backscatter value close to this local mean will be classified as OW, and pixels with a backscatter value far from the local mean will be classified as MYI, resulting in a narrow band of pixels classified as OW overlying the broader band of pixels classified as MYI ([Fig. 5](#), top panel, right). This ambiguity can only be solved by adding additional information (e.g. HV intensity or texture parameters) and thus extending the classifier to more dimensions (see [Table 2](#), 1-D and 2-D classifier results). The extension of the GIA classifier to multiple dimensions is straightforward, given that Eqn (4) describes a multi-variate Gaussian with variable mean vector. For the two-class case study (2), [Figure 6](#) illustrates a clear improvement that is achieved by adding the HV component to the GIA classifier.

Algorithm performance

The comparison of the GIA classifier to BCG, SVM and RF classifiers is summarized in [Tables 2](#) and [3](#). Note again that the selected classifiers for comparison are applied after a global IA correction was carried out in the pre-processing. When the slopes

of the individual classes differ (2-class case studies (1) and (2)), the GIA classifier achieves the highest CA. For classes with very similar slopes (2-class case study (3)), the methods perform almost equally well. This is expected since in such a case the per-class IA correction inherent in the GIA classifier is almost identical to the global IA correction during pre-processing. When we extend the case studies to three classes, however, we note that the presence of one surface type with a significantly different slope, i.e. OW, affects the overall classification result (Table 3). Again, the GIA classifier performs better than the comparison methods. The improvement is particularly strong in the 1D case (~8%) and still almost 2% in the 2-D case. This is due to the variation in slope values of the individual classes. The largest difference in slope occurs between OW and MYI, where it is 0.49 dB/1° in the HH channel. In the HV channel, however, it is only 0.1 dB/1°. Hence, a global correction will achieve better results for HV than for HH.

Furthermore, it is interesting to compare the GIA classifier's average per-class CA of the three-class case against the different two-class cases. For the 1-D examples, the two-class case studies (1) and (3) achieve the highest scores, with 94.08% and 97.56%, respectively. Case study (2) scores considerably lower at 80.93%, while the three-class example score is at 83.73% (Tables 2 and 3). Generally, a lower score for the three-class problem can be expected, since the classification error of a Bayesian classifier corresponds to the overlap of the class-specific PDFs, and adding more PDFs may lead to more overlap. Two-class case study (2) however scores low in 1-D due to large overlap of the distributions, so that the average per-class score is increased when adding another, better separable class.

Processing time

For the presented case studies and the given implementations of the different classifiers, both Bayesian classifiers (BCG and GIA) are clearly superior to RF and SVM in processing time for both training and prediction. Considering a possible future application in operational ice charting, the timing for prediction of labels for new samples is particularly critical. Here, the BCG classifier is slightly faster than the GIA classifier, as it does not require the linear operation to estimate the local mean value from the class-dependent slope. However, both BCG and GIA classifiers are considerably faster than the RF or the SVM. As the computation time for prediction of class labels increases approximately linear with the number of trained classes for a Bayesian classifier, we expect this advantage to slightly decrease with the extension to more classes. Nevertheless, the GIA classifier is certainly suitable for fast processing of images and near-real-time classification, and in our investigated case studies it is clearly superior to SVM and RF in terms of computation time.

Current limitations and future work

We have so far shown how to incorporate the per-class correction of IA effect into a classifier and demonstrated that this direct incorporation can generally improve CA while operating at an operationally acceptable speed. Besides the classification of wide-swath images such as S1 EW, the GIA classification framework could also be applied to transfer training data across images acquired in quad-pol mode at different IA. In the following part of this section, we discuss the current limitations of the method and possible future development and improvement of the algorithm.

One of these limitations is the present definition and selection of the OW class. For the shown case studies, we have restricted

ourselves to OW conditions with a steep and constant slope. However, in reality, OW is more challenging. For a given radar frequency and polarization, the OW slope and brightness depends on wind speed as well as the angle between radar look and wind direction. While one simple OW class may be useful in particular cases and for demonstrating the principle algorithm, it will not be sufficient for operational ice charting. Possible ways to deal with this issue may be the inclusion of texture features or the definition of several OW classes for varying environmental and acquisition conditions. However, both alternatives require thorough investigation and are beyond the scope of the present demonstration study.

Furthermore, in the presented case studies we have focused only on the ice types that we could observe over large homogeneous areas covering a wide distance in range (Table 1). Hence, the training and validation data are well defined for these cases, offering optimal conditions for the demonstration of how to incorporate the class-dependent IA effect directly into the classification process, and for the evaluation of the method in comparison to global IA correction during pre-processing. The slope values that we obtain represent a generalized, Arctic-wide class property for the particular classes as we have defined them based on the available input data. Comparison to literature values reveals slight differences between our values and the ones from previous studies, which are most likely caused by intra-class variability or slightly different class definitions. While the slopes given in this study are optimal for use over the entire Arctic (and may only have to be slightly adjusted when the input dataset is extended), a new estimation of slopes and thus re-training of the classifier may be valuable for more locally constrained studies.

In future work, we will focus on the extension of the algorithm to all identified classes and different seasons, as well as the improvement and validation of automated production of ice charts. Two examples of ice type maps and the underlying S1 data are shown in Figure 7. Rigorous validation of several such examples in terms of absolute CA is currently carried out in collaboration with the Norwegian Ice Service. The detailed evaluation of the results is, however, beyond the scope of the present demonstration study. Visual inspection of the examples presented in Figure 7, however, reveals additional capabilities and limitations of the current algorithm: The overall pan-Arctic distribution of ice types (Fig. 7, top panel) shows a reasonable pattern, with MYI dominating in the Canadian Arctic and starting to circulate in the Beaufort Gyre, and FYI (level and deformed) dominating in the Russian Arctic. The closeup ice chart located north of Svalbard (Fig. 7, bottom panel) shows the separation of MYI, deformed and level FYI and refrozen leads with young ice. The algorithm successfully finds distinct regions for each class. Note that the classification result is consistent across image boundaries. As the effect of IA angle is clearly visible across image boundaries in the SAR imagery and no pre-processing IA correction is applied, this indicates that the per-class correction of the IA effect within the GIA classifier is successful. Classification results overlap seamlessly. However, on visual inspection, we also find some misclassification in the ice charts, in particular in areas with low signal, where the noise in the HV channel influences results. Furthermore, we observe occasional confusion of young ice and MYI due to ambiguities in backscatter intensity. These ambiguities are not new issues, however, and have been described for example, in Zakhvatkina and others (2017). They are not inherent to the algorithm framework presented in this study.

One common way to overcome such remaining ambiguities in the mapping of sea-ice types is the use of textural information. Texture features can for example be extracted from all channels in the data via the Gray-Level Co-Occurrence Matrix (GLCM). However, computation of the GLCM is time extensive and will

significantly increase the processing time of any operational workflow. Furthermore, texture features are calculated within a window around the individual pixel, leading to an effectively reduced resolution of the result. Nevertheless, including textural information into the GIA classifier may be necessary for successful separation of all identified ice types. Texture features are commonly assumed to be less sensitive to IA, although to our best knowledge there is no systematic study yet that provides a detailed investigation of the variation of texture features with IA. In any case, the extension of the GIA classifier to other features is straightforward, as long as their IA dependence can be described by a simple function. Even if there is no IA dependence, the GIA classifier can be applied as-is, simply estimating a slope of zero for the individual features.

Conclusion

We have introduced a supervised classification algorithm for sea-ice types that directly incorporates class-dependent variation of backscatter intensity with IA. This is achieved by replacing the constant mean vector in a multi-variate Gaussian PDF of a Bayesian classifier with a linearly variable mean vector. The IA effect is thus no longer treated as a global image property and corrected during pre-processing, but as an ice type property. We have shown in several case studies that our proposed GIA classifier improves CA when the slopes for individual classes are significantly different. The simplicity and fast processing time of the GIA classifier allow for easy interpretation of results over the entire swath and enables processing of images in near-real-time, which is required for operational ice charting.

Although classification results are improved, some ambiguities and misclassified regions remain. In future work, we will focus on resolving these ambiguities by including further training and textural information into the GIA algorithm to further improve our automated mapping of sea-ice types.

Acknowledgements. This research was funded by CIRFA partners and the Research Council of Norway (RCN) (grant number 237906). The presented work contains primary and altered Sentinel data products (@Copernicus data). We thank the Norwegian Ice Service for their help in analyzing overlapping SAR and optical data to identify different ice types in the images. Furthermore, we also thank the anonymous reviewers for their constructive comments and feedback.

Data. The code for the GIA classifier framework selected training data and lists of image IDs can be obtained by contacting the first author.

References

- Aulard-Macler M** (2011) Sentinel-1 product definition s1-rs-mda-52-7440. Technical report, MacDonald, Dettwiler and Associates Ltd.
- Barber DG and LeDrew E** (1991) Sar sea ice discrimination using texture statistics: a multivariate approach. *Photogrammetric Engineering and Remote Sensing* 57(4), 385–395.
- Clausi DA** (2001) Comparison and fusion of co-occurrence, gabor and mrf texture features for classification of sar sea-ice imagery. *Atmosphere-Ocean* 39(3), 183–194. doi: [10.1080/07055900.2001.9649675](https://doi.org/10.1080/07055900.2001.9649675).
- Dierking W** (2010) Mapping of different sea ice regimes using images from sentinel-1 and alos synthetic aperture radar. *IEEE Transactions on Geoscience and Remote Sensing* 48(3), 1045–1058. ISSN 0196-2892. doi: [10.1109/TGRS.2009.2031806](https://doi.org/10.1109/TGRS.2009.2031806).
- Dierking W** (2013) Sea ice monitoring by synthetic aperture radar. *Oceanography* 26(2), 100–111. ISSN 10428275, 2377617X.
- Eriksson LE and 7 others** (2010) Evaluation of new spaceborne sar sensors for sea-ice monitoring in the baltic sea. *Canadian Journal of Remote Sensing* 36 (sup1), S56–S73. doi: [10.5589/m10-020](https://doi.org/10.5589/m10-020).
- Geldsetzer T and Yackel JJ** (2009) Sea ice type and open water discrimination using dual co-polarized c-band sar. *Canadian Journal of Remote Sensing* 35 (1), 73–84. doi: [10.5589/m08-075](https://doi.org/10.5589/m08-075).
- Gill JPS, Yackel J, Geldsetzer T and Fuller MC** (2015) Sensitivity of c-band synthetic aperture radar polarimetric parameters to snow thickness over landfast smooth first-year sea ice. *Remote Sensing of Environment* 166, 34–49.
- Han H and 6 others** (2016) Retrieval of melt ponds on arctic multiyear sea ice in summer from terrasars-x dual-polarization data using machine learning approaches: a case study in the Chukchi sea with mid-incidence angle data. *Remote Sensing* 8(1), 1–23. doi: [10.3390/rs8010057](https://doi.org/10.3390/rs8010057).
- Hara Y and 5 others** (1995) Application of neural networks for sea ice classification in polarimetric sar images. *IEEE Transactions on Geoscience and Remote Sensing* 33(3), 740–748. ISSN 0196-2892. doi: [10.1109/36.387589](https://doi.org/10.1109/36.387589).
- Hollands T and Dierking W** (2016) Dynamics of the terra nova bay polynya: the potential of multi-sensor satellite observations. *Remote Sensing of Environment* 187, 30–48. ISSN 0034-4257. doi: <https://doi.org/10.1016/j.rse.2016.10.003>.
- Karvonen JA** (2004) Baltic sea ice sar segmentation and classification using modified pulse-coupled neural networks. *IEEE Transactions on Geoscience and Remote Sensing* 42(7), 1566–1574. ISSN 0196-2892. doi: [10.1109/TGRS.2004.828179](https://doi.org/10.1109/TGRS.2004.828179).
- Karvonen J** (2014) A sea ice concentration estimation algorithm utilizing radiometer and sar data. *The Cryosphere* 8(5), 1639–1650. doi: [10.5194/tc-8-1639-2014](https://doi.org/10.5194/tc-8-1639-2014).
- Karvonen J** (2017) Baltic sea ice concentration estimation using sentinel-1 sar and amsr2 microwave radiometer data. *IEEE Transactions on Geoscience and Remote Sensing* 55(5), 2871–2883. doi: [10.1109/TGRS.2017.2655567](https://doi.org/10.1109/TGRS.2017.2655567).
- Kwok R and 5 others** (1991) Application of neural networks to sea ice classification using polarimetric sar images. In *[Proceedings] IGARSS'91 Remote Sensing: Global Monitoring for Earth Management, I*, 85–88. doi: [10.1109/IGARSS.1991.577672](https://doi.org/10.1109/IGARSS.1991.577672).
- Leigh S, Wang Z and Clausi DA** (2014) Automated ice-water classification using dual polarization sar satellite imagery. *IEEE Transactions on Geoscience and Remote Sensing* 52(9), 5529–5539. ISSN 0196-2892. doi: [10.1109/TGRS.2013.2290231](https://doi.org/10.1109/TGRS.2013.2290231).
- Liu H, Guo H and Zhang L** (2015) Svm-based sea ice classification using textural features and concentration from radarsat-2 dual-pol scansar data. *IEEE Journal of Selected Topics in Applied Earth Observations and Remote Sensing* 8(4), 1601–1613. ISSN 1939-1404. doi: [10.1109/JSTARS.2014.2365215](https://doi.org/10.1109/JSTARS.2014.2365215).
- Lohse J, Doulgeris AP and Dierking W** (2019) An optimal decision-tree design strategy and its application to sea ice classification from sar imagery. *Remote Sensing* 11(13), 1–15. doi: [10.3390/rs11131574](https://doi.org/10.3390/rs11131574).
- Mahmud MS and 5 others** (2018) Incidence angle dependence of hh-polarized c- and l-band wintertime backscatter over Arctic sea ice. *IEEE Transactions on Geoscience and Remote Sensing* 56, 1–13. ISSN 0196-2892. doi: [10.1109/TGRS.2018.2841343](https://doi.org/10.1109/TGRS.2018.2841343).
- Mäkynen M and Karvonen J** (2017) Incidence angle dependence of first-year sea ice backscattering coefficient in sentinel-1 sar imagery over the kara sea. *IEEE Transactions on Geoscience and Remote Sensing* 55(11), 6170–6181. doi: [10.1109/TGRS.2017.2721981](https://doi.org/10.1109/TGRS.2017.2721981).
- Mäkynen MP, Manninen AT, Similä MH, Karvonen JA and Hallikainen MT** (2002) Incidence angle dependence of the statistical properties of c-band hh-polarization backscattering signatures of the baltic sea ice. *IEEE Transactions on Geoscience and Remote Sensing* 40(12), 2593–2605. doi: [10.1109/TGRS.2002.806991](https://doi.org/10.1109/TGRS.2002.806991).
- Moen MAN and 6 others** (2013) Comparison of feature based segmentation of full polarimetric sar satellite sea ice images with manually drawn ice charts. *The Cryosphere* 7(6), 1693–1705. doi: [10.5194/tc-7-1693-2013](https://doi.org/10.5194/tc-7-1693-2013).
- Moen MAM, Anfinson SN, Doulgeris AP, Renner AHH and Gerland S** (2015) Assessing polarimetric sar sea-ice classifications using consecutive day images. *Annals of Glaciology* 56(69), 285–294. doi: [10.3189/2015AoG69A802](https://doi.org/10.3189/2015AoG69A802).
- Onstott RG and Carsey FD** (1992) Sar and scatterometer signatures of sea ice. *Microwave Remote Sensing of Sea Ice* 68, 73–104.
- Parzen E** (1962) On estimation of a probability density function and mode. *The Annals of Mathematical Statistics* 33(3), 1065–1076. ISSN 00034851.
- Pedregosa F and 15 others** (2011) Scikit-learn: machine learning in python. *Journal of Machine Learning Research* 12, 2825–2830.
- Ressel R, Frost A and Lehner S** (2015) A neural network-based classification for sea ice types on x-band sar images. *IEEE Journal of Selected Topics in Applied Earth Observations and Remote Sensing* 8(7), 3672–3680. ISSN 1939-1404. doi: [10.1109/JSTARS.2015.2436993](https://doi.org/10.1109/JSTARS.2015.2436993).

- Scheuchl B, Caves R, Cumming I and Staples G** (2001) Automated sea ice classification using spaceborne polarimetric sar data. In *IGARSS 2001. Scanning the Present and Resolving the Future. Proceedings. IEEE 2001 International Geoscience and Remote Sensing Symposium (Cat. No.01CH37217)* 7, 3117–3119. doi: [10.1109/IGARSS.2001.978275](https://doi.org/10.1109/IGARSS.2001.978275).
- Scheuchl B, Flett D, Caves R and Cumming I** (2004) Potential of radarsat-2 data for operational sea ice monitoring. *Canadian Journal of Remote Sensing* 30(3), 448–461. doi: [10.5589/m04-011](https://doi.org/10.5589/m04-011).
- Theodoridis S and Koutroumbas K** (2008) *Pattern Recognition*, 4th Edn. Orlando, FL, USA: Academic Press, Inc., ISBN 9781597492720.
- Zakhvatkina NY, Alexandrov VY, Johannessen OM, Sandven S and Frolov IY** (2013) Classification of sea ice types in envisat synthetic aperture radar images. *IEEE Transactions on Geoscience and Remote Sensing* 51(5), 2587–2600. ISSN 0196-2892. doi: [10.1109/TGRS.2012.2212445](https://doi.org/10.1109/TGRS.2012.2212445).
- Zakhvatkina N, Korosov A, Muckenhuber S, Sandven S and Babiker M** (2017) Operational algorithm for ice–water classification on dual-polarized radarsat-2 images. *The Cryosphere* 11(1), 33–46. doi: [10.5194/tc-11-33-2017](https://doi.org/10.5194/tc-11-33-2017).
- Zakhvatkina N, Smirnov V and Bychkova I** (2019) Satellite sar data-based sea ice classification: an overview. *Geosciences* 9(4), 1–15. doi: [10.3390/geosciences9040152](https://doi.org/10.3390/geosciences9040152).

/ 8

Paper III:

Incident Angle Dependence of Sentinel-1 Texture Features for Sea Ice Classification

Lohse J, Doulgeris AP and Dierking W (2020). Submitted to *Remote Sensing*, special issue *Remote Sensing of Sea Ice and Icebergs*, on December 24th, 2020

Article

Incident Angle Dependence of Sentinel-1 Texture Features for Sea Ice Classification

Johannes Lohse ^{1*} , Anthony P. Doulgeris ¹ and Wolfgang Dierking ^{1,2}

¹ Department of Physics and Technology, UiT The Arctic University of Norway, 9019 Tromsø, Norway

² Alfred Wegener Institute, Helmholtz Center for Polar and Marine Research, Bussestr. 24, 27570 Bremerhaven, Germany

* Correspondence: johannes.p.lohse@uit.no

Version December 24, 2020 submitted to Remote Sens.

Abstract: Robust and reliable classification of sea ice types in synthetic aperture radar (SAR) images is needed for various operational and environmental applications. Previous studies have investigated the class-dependent decrease of SAR backscatter intensity with incident angle (IA), others have shown the potential of textural information to improve automated image classification. In this work, we investigate the inclusion of Sentinel-1 (S1) texture features into a Bayesian classifier that accounts for linear per-class variation of its features with IA. We use the S1 EW GRDM product and compute seven GLCM texture features from the HH and the HV backscatter intensity in the linear and logarithmic domain. While GLCM texture features computed from the linear domain vary significantly with IA, the features computed from the logarithmic intensity do not depend on IA or reveal only a weak, approximately linear dependency. They can therefore be directly included in the IA-sensitive classifier that assumes a linear variation. The different number of looks in the first sub-swath EW1 of the product causes a distinct offset in texture at the sub-swath boundary between EW1 and EW2. This offset must be considered when using texture in classification; we demonstrate a manual correction for the example of GLCM contrast. Based on the Jeffries-Matusita distance between class histograms, we perform a separability analysis for 57 different GLCM parameter settings. We select a suitable combination of features for the ice classes in our data set and classify several test images using a combination of intensity and texture features. We compare the results to a classifier using only intensity. Particular improvements are achieved for the generalized separation of ice and water, as well as the classification of young ice and multi-year ice.

Keywords: classification; sea ice; ice types; SAR; Sentinel-1; texture; GLCM; incident angle

21 1. Introduction

22 Synthetic aperture radar (SAR) is a primary tool for monitoring of sea ice conditions in the polar
23 regions. A radar system is an active device that both transmits and receives electromagnetic radiation
24 in the microwave region, and is thus independent of sunlight and cloud conditions. The resulting
25 continuous imaging capability of the SAR is important for operational ice services worldwide [1]. The
26 analysis and interpretation of the SAR images and the production of ice charts is at present carried out
27 manually and therefore subject to the expertise of the individual ice analyst [2,3]. Furthermore, while
28 timeliness of ice charts is a critical requirement, the manual image analysis is a time-consuming process.
29 In combination with an increasing volume of available SAR imagery, this underlines the need for
30 automated or computer-assisted classification of sea ice. The backscatter signature of sea ice in radar
31 images, however, depends on a variety of different factors, including both sea ice, environmental, and
32 radar parameters. Despite multiple efforts and various approaches, robust and automated classification
33 of ice types therefore remains a challenging task [1].

34 The important radar parameters that influence the signal include radar frequency, polarization,
35 and incident angle (IA) [4]. While frequency and polarization are fixed for a given sensor and
36 operation mode, IA varies across the image. The backscatter intensity (also referred to as image
37 brightness or tone) from a homogeneous surface varies with IA and decreases across a SAR image from
38 near-range (low IA) to far-range (high IA). In the logarithmic domain, i.e., with the intensity given in
39 dB, the decrease is approximately linear with a constant slope per surface class [5–8]. Despite many
40 studies showing that the rate of decrease differs between different surface types, most classification
41 approaches apply a global IA correction during pre-processing, using a constant slope for the entire
42 SAR image [9–13]. Although such approaches can achieve good results, they neglect the known
43 physical differences in backscatter behaviour with IA for different surface types. Lohse et al. [14]
44 recently introduced a method to directly incorporate the class-dependent effect of IA into a supervised
45 algorithm. The method is based on a Bayesian classifier with multi-variate Gaussian probability
46 density functions (PDF), where the constant mean value is replaced with a linearly varying mean value.
47 The linear slopes are class-dependent and thus directly included in the classifier. Since it is based on
48 underlying Gaussian PDFs and accounts for a per-class IA effect, the classification method is referred
49 to as the GIA (Gaussian incident angle) classifier. The approach achieves improved classification
50 results compared to intensity-based methods with a global IA correction. However, ambiguities in
51 backscatter intensity remain for individual classes at some IA ranges. In particular, changes in the
52 sea surface roughness (the sea surface state), caused for example by varying wind conditions, ocean
53 currents, or natural and oil slicks, can complicate the reliable classification of open water (OW).

54 Previous studies have shown that in many cases textural information can help to resolve
55 ambiguities in sea ice classification, both for the binary problem of ice-water classification and for
56 the multi-class separation of different ice types [13,15–22]. Texture generally refers to the local spatial
57 variation of tone or brightness within an image at a given scale [23]. While many different ways of
58 extracting texture features exist [19], the most common texture features used for sea ice classification
59 are based on the grey level co-occurrence matrix (GLCM) [23]. A straightforward way to directly
60 utilize information from the GLCM in a pixel-based classifier is to extract scalar features from the
61 matrix. Such GLCM-based texture features have been used in a variety of studies and algorithms
62 and improved overall classification accuracy (CA) of OW areas vs. sea ice [9,13,16–20,22,24]. Texture
63 extraction, and in particular computation of the GLCM, requires several input parameters such as
64 window size, quantization levels, displacement distance, and displacement direction (see Section 3 for
65 details). Many of these parameters have been investigated in previous studies. The optimal choice,
66 however, differs between studies (Table 1) and depends on class definitions and data properties. To
67 our best knowledge, a systematic investigation of the dependence of common GLCM texture features
68 on IA for different classes has not been performed prior to this study. All approaches presented in the
69 literature that use the GLCM for the analysis of sea ice imagery either apply a global IA correction or
70 no correction.

71 In this study, we therefore investigate the per-class IA dependence of different texture features.
 72 We do so with the intention of incorporating texture directly into the GIA classifier, which accounts for
 73 per-class IA effects. The main prerequisite for this incorporation is that there must be a clearly defined
 74 relationship between texture parameters and IA. Ideally, for the linear GIA, this relationship should
 75 be constant or linear and the distribution of the individual features around the linear function can be
 76 approximated as Gaussian. These ideal conditions allow for the direct use of the texture features in the
 77 existing algorithm, while a more complicated IA relationship or a clearly non-Gaussian distribution
 78 would require changing the underlying model of the GIA classifier. After we confirm that common
 79 texture features fulfill these conditions, we select a useful set of features and demonstrate the benefits
 80 of including them in the classification process.

81 This paper is organized as follows. Section 2 gives an overview of the data set, including the
 82 standard pre-processing steps that were applied. The outline of the investigations in this study
 83 is presented in Section 3, followed by a detailed description of the computation and selection of
 84 the texture features as well as the tested parameter settings. Section 4 presents the results of these
 85 investigations. We discuss our findings in Section 5, pointing out implications and limitations for the
 86 usage of texture in sea ice type classification from SAR data, and in particular in the GIA classifier. In
 87 Section 6, we summarize the main findings and conclusions.

Table 1. Overview of GLCM computation parameters from selected studies that investigate GLCM texture features for sea ice classification. The parameters are window size w , co-occurrence distance d , angle α , and number of grey level quantization intervals k . Bold type indicates the preferred choice selected by these studies, where applicable. Information on the intensity domain (linear or dB) and quantization method is not explicitly mentioned in many studies.

Authors	dB	w	d	α	k	Features
Holmes et al. (1984)	?	5	2	average	8	Con, Ent
Barber and LeDrew (1991)	?	25	1, 5, 10	0, 45, 90	16	Con, Cor, Dis, Ent, Uni
Shokr (1991)	?	5, 7, 9	1, 2, 3	average	16, 32	Con, Ent, Idm, Uni, Max
Soh and Tsatsoulis (1999)	?	64	1, 2, ..., 32	average	64	Con, Cor, Ent, Idm, Uni, Aut
Leigh et al.(2014)	?	5, 11, 25, 51, 101	1, 5, 10, 20	average	?	ASM, Con, Cor, Dis, Ent, Hom, Inv, Mu, Std
Ressel et al. (2015)	no	11, 31, 65	1	average	16, 32, 64	Con, Dis, Ene, Ent, Hom
Karvonen (2017)	yes	5	1	average	256	Ent, Aut
Zakhvatkina et al. (2017)	yes	32, 64, 128	4, 8, 16, 32, 64	average	16, 25, 32	Ene, Ine, Clu, Ent, Cor, Hom

88 2. Data

89 2.1. Sentinel-1 Data

90 All SAR imagery in this study is Sentinel-1 (S1) data acquired in extra wide swath (EW) operation
 91 mode [25]. S1 operates at C-band (5.4 GHz) providing either single- or dual-polarization data. As part
 92 of the European Copernicus Earth observation program, all S1 data are freely available (e.g. through
 93 the Copernicus Open Access Hub). The data used in this study are acquired at dual-polarization (HH
 94 and HV), and downloaded in ground-range detected format at medium resolution (GRDM). The EW
 95 GRDM product comes at a pixel spacing of 40x40 m with an actual spatial resolution of approximately
 96 93x87 m; its values are multi-looked intensities with 18 looks in the first sub-swath EW1 and 12 looks

97 in the remaining sub-swaths EW2 to EW5. As standard pre-processing, we apply the thermal noise
 98 correction implemented in ESA's Sentinel Application Platform (SNAP) and calibrate the data to obtain
 99 the normalized radar cross-section σ^0 . All processing is performed in the ground-range detected image
 100 geometry.

101 2.2. Training and Validation Data

102 We use the training and validation data set introduced by Lohse et al. [14] in 2020. This data
 103 set is based on the visual inspection and expert analysis of overlapping SAR (S1) and optical remote
 104 sensing data acquired during winter conditions between 2015 and 2019. The main identified classes in
 105 the data set are open water (OW), leads with OW or newly formed ice (NFI), brash or pancake ice,
 106 young ice (YI), level first-year ice (LFYI), deformed first-year ice (DFYI) and multi-year ice (MYI). A
 107 detailed description of the data set, image locations and acquisition times, and the selection of classes
 108 and training polygons is given in Lohse et al. [14]. For parts of this study, we have added new images
 109 and test polygons to the existing data set. Generally, the training data for individual classes used in
 110 this study are collected from a large number of scenes. In some cases we show training data from a
 111 single image for a particular class. The image IDs (product unique IDs) are given in the respective
 112 subsections of this article.

113 3. Method

114 3.1. Outline of This Study

After pre-processing, we extract various texture features from both the HH and the HV channel of
 the S1 images. Initially, we compute all texture features from both the backscatter intensity in the linear
 domain (normalized radar cross-section σ^0) and the backscatter intensity in the logarithmic domain.
 In the logarithmic domain, the intensities are given in decibel (dB):

$$\begin{aligned} HH_{dB} &= 10 \cdot \log_{10}(\sigma_{HH}^0) \\ HV_{dB} &= 10 \cdot \log_{10}(\sigma_{HV}^0) \end{aligned} \quad (1)$$

115 The relationship of intensity with IA is approximately exponential in the linear domain, and thus in
 116 turn approximately linear in the logarithmic domain (Figure 1). These differences in IA dependence,
 117 in combination with the change of variance with IA in the linear domain, are expected to translate into
 118 differences in IA dependence of the texture features extracted from the respective intensity domains.

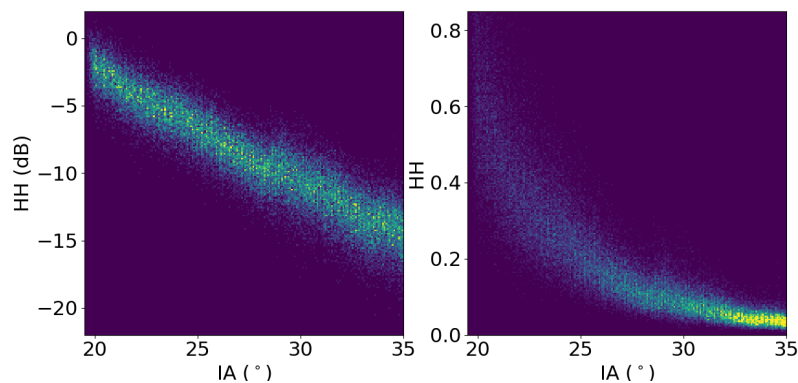


Figure 1. Distribution of HH intensity with IA for OW training data selected over the first two sub-swaths of a single image (Image ID: F2FE). Intensity is shown in the logarithmic domain (in dB) on the left side, and in the linear domain on the right side.

119 The initial extraction of texture from both linear and logarithmic intensity allows us to find the
 120 preferred domain to compute the texture features. For the preferred domain, we test a variety of

parameter settings (see Sections 3.2.1 and 3.2.2 for details), and investigate the variation of the extracted features with IA for these different settings. We adjust the borders of the training regions according to the size of the texture windows, such that little or no mixing of ice classes occurs within the texture windows. We then use the Jeffries-Matusita (JM) distance [26] to evaluate all features and parameter settings in terms of class separability for various two-class cases. Based on this evaluation, we finally select a suitable feature set and demonstrate the benefits of incorporating textural information into the GIA classifier. In particular, we present examples for the classification of sea ice against OW, as well as YI against MYI, and compare against results obtained from a classifier based on intensities only.

3.2. Calculation of Texture Features

Since many previous studies suggest that the GLCM provides a useful method to generate texture features that can improve sea ice classification results [19,21], we focus on this method (Section 3.2.1). However, calculation of the GLCM is computationally expensive and time-consuming, which can impede its use in operational applications. As an example for a simpler and more easily calculated texture feature, we therefore also extract the variance (Section 3.2.2) and assess its usability compared to the GLCM features.

3.2.1. GLCM Texture Features

The GLCM provides a second-order statistic for extraction of texture features [20,23]. It calculates the probability of a pixel with grey level value i occurring at a certain distance and angle from another pixel with grey level j within a given window. The key parameters that must be set are the window size w for which to calculate the GLCM, the co-occurrence distance d , the angle α , and the number of grey level quantization intervals k . Algebraically, the GLCM can be expressed as:

$$S_{w,d,\alpha,k}(i,j) = \frac{P_{w,d,\alpha,k}(i,j)}{\sum_{i=1}^k \sum_{j=1}^k P_{w,d,\alpha,k}(i,j)} \quad (2)$$

where $S_{w,d,\alpha,k}$ is an element of the GLCM for a given window size, direction, co-occurrence distance and grey level quantization, $P_{w,d,\alpha,k}$ is the frequency of occurrence of grey levels i and j , and k is the number of quantized grey levels. The size of the GLCM depends on the number of grey levels. In order to neglect effects from ice floe rotation and changes in the angle between the radar-look direction and the physical structures on the ice, the GLCM is often calculated for different directions (0° , 45° , 90° , 135°) and then averaged before feature extraction [9,20]:

$$S(i,j) = \frac{1}{4} \sum_{\alpha} S_{w,d,\alpha,k}(i,j) \quad \text{for } \alpha = 0, 45, 90, 135 \quad (3)$$

The resulting averaged GLCM S still includes the effects of directional structures, but the effects are diluted by the averaging. The specific orientation of the structures is not reflected any more in the averaged GLCM. The remaining parameters are usually chosen manually or optimized for a particular study and then kept fixed. Individual scalar texture features can be calculated from the GLCM according to Equations 4 to 10:

$$\text{Angular second moment : } ASM = \sum_{i=1}^k \sum_{j=1}^k S(i,j)^2 \quad (4)$$

$$\text{Contrast : } Con = \sum_{i=1}^k \sum_{j=1}^k (i-j)^2 S(i,j) \quad (5)$$

$$\text{Correlation : } Cor = \frac{\sum_{i=1}^k \sum_{j=1}^k (i-\mu_x)(j-\mu_y) S(i,j)}{\sigma_x \sigma_y} \quad (6)$$

$$\text{Dissimilarity : } Dis = \sum_{i=1}^k \sum_{j=1}^k |i - j| S(i, j) \quad (7)$$

$$\text{Energy : } Ene = \sqrt{ASM} \quad (8)$$

$$\text{Entropy : } Ent = - \sum_{i=1}^k \sum_{j=1}^k S(i, j) \log_{10}[S(i, j)] \quad (9)$$

$$\text{Homogeneity : } Hom = \sum_{i=1}^k \sum_{j=1}^k \frac{S(i, j)}{1 + (i - j)^2} \quad (10)$$

153 Different parameter settings and feature choices from selected studies that use GLCM texture
 154 features for the interpretation of sea ice SAR imagery are summarized in Table 1. It is evident that there
 155 is no consensus in the literature on an optimal set of features and parameters. The preferred choices that
 156 lead to the best classification results for the individual studies differ from window sizes between 5 and
 157 64 pixels, co-occurrence distances between 1 and 8, and grey level quantization levels between 8 and
 158 64. The optimal features and parameter set depend on the class definitions, the image pre-processing
 159 steps (in particular multi-looking and re-sampling), and the data properties (in particular frequency,
 160 spatial resolution, polarization). In this study, we therefore test a variety of GLCM parameter settings
 161 (Table 2), covering a reasonable range of settings that is based on the literature values in Table 1. Our
 162 goal is to assess the effect of different settings on potential IA dependence of the features, and to find a
 163 suitable set of features and parameters for the specific data set that we use.

164 To be consistent and to ensure identical quantization for all images, we choose a uniform
 165 quantization with equally spaced grey level intervals. We clip the minimum and maximum grey
 166 levels at -35 and +5 dB for HH and -40 and 0 dB for HV, respectively. To avoid directional effects, we
 167 average the GLCMs obtained for four directions (0° , 45° , 90° , 135°) before computation of individual
 168 scalar features.

Table 2. Summary of GLCM computation parameters tested in this study (w: window size, d: GLCM co-occurrence distance, k: GLCM grey levels). The window is applied on the original 40x40 m pixel spacing of the S1 EW GRDM product. Quantization is performed with equally spaced intervals between -35 and +5 dB for HH and -40 and 0 dB for HV, respectively. The GLCM is calculated for four different directions (0° , 45° , 90° , 135°) and then averaged before feature extraction.

w	d	k
5	1/2	16/32/64
7	1/2/4	16/32/64
9	1/2/4/8	16/32/64
11	1/2/4/8	16/32/64
21	2/4/8	16/32/64
51	2/4/8	16/32/64

169 3.2.2. Simple Texture Features

170 Computation of the GLCM is time-consuming and depends on multiple different parameters.
 171 Hence, it is interesting to also test other texture features that can be calculated faster and more easily,
 172 and investigate if they can be used instead of GLCM features. In this study, we investigate the
 173 variance (Var) as an example for such simpler texture features. The only required input parameter is
 174 the window size. We calculate variance from the logarithmic intensity for the same window sizes as
 175 the GLCM features (Table 2). Unlike the GLCM, variance does not depend on a distance parameter
 176 inside the defined texture window. Additionally, it is not sensitive to the spatial orientation of physical
 177 structures on the ice. However, many of the physical structures that we are interested in, for example
 178 leads or pressure ridges, have some specific spatial orientation. Even though we are not interested in
 179 this specific orientation itself, looking in different directions can be necessary to detect the physical

180 structures' presence. Hence, the larger computational effort of the GLCM can be beneficial to detect
 181 certain structures that the variance may miss, depending on the applied window size and the physical
 182 size of the structures on the ground. A comparison between the different approaches to quantify
 183 texture in terms of class separability is therefore useful.

184 4. Results

185 In this section, we present the results of our study. As we have tested a large number of different
 186 texture parameter settings and individual features, it is not feasible to show a full overview of all tested
 187 combinations. We therefore present and discuss representative examples for the various experiments
 188 performed in this study.

189 4.1. Texture and IA

190 We begin by comparing the influence of IA on GLCM texture features computed from intensity
 191 in dB against GLCM texture features computed from linear intensity. An example including both
 192 intensity domains and three selected GLCM features is shown in Figure 2. When computed from the
 193 logarithmic intensity, the GLCM features show no significant per-class variation with IA (Figure 2,
 194 upper panel); when computed from the linear intensity, there is an evident variation (Figure 2, lower
 195 panel). For some features (for example entropy and homogeneity) the relationship appears to be
 196 approximately linear over part of the shown IA range. Overall, however, the IA dependence of
 197 the GLCM texture features is significantly more complicated when computed from linear intensity
 198 compared to logarithmic intensity. Furthermore, the OW class in the example of Figure 2 shows some
 199 internal variability in intensity, caused by changes in the sea surface state across the image. The GLCM
 200 texture from the logarithmic intensity appears to be less sensitive to such internal class variation than
 201 the GLCM texture from the linear intensity.

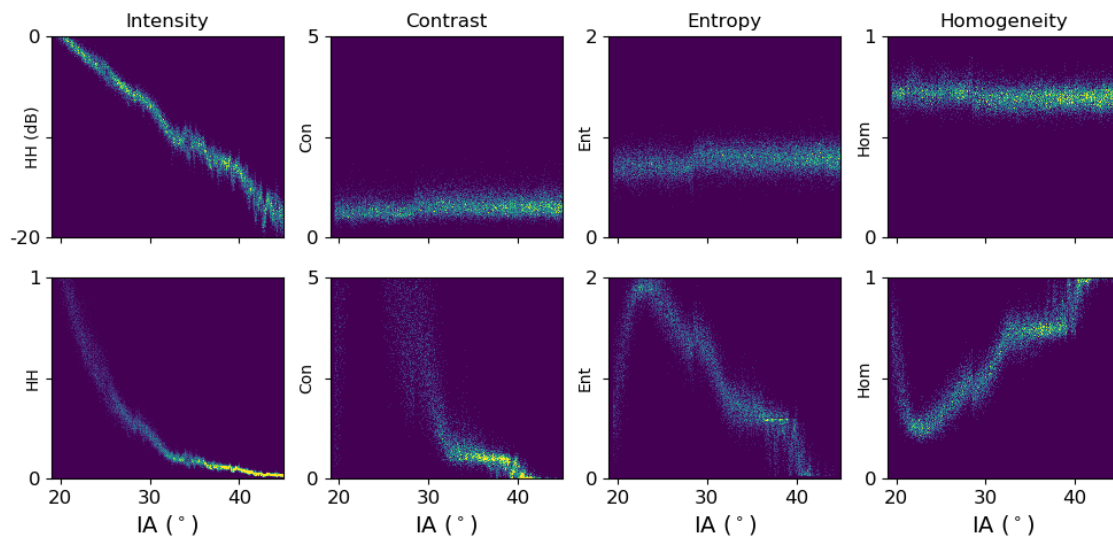


Figure 2. Density distribution of HH intensity and three selected GLCM texture features with IA for OW training data selected over the full range of a single S1 image (Image ID: 77BA). The upper panel shows HH intensity in the logarithmic domain (in dB) and the GLCM features extracted from it; the lower panel shows intensity in the linear domain with its respective GLCM features. Note that the OW class displays some internal class variation in intensity due to varying sea surface state across the image. GLCM parameter settings: $w=11$, $d=4$, $k=16$.

202 All tested texture features reveal a significant offset at the boundary between the first and the
 203 second sub-swath of the image, which is located at an IA of approximately 28.5° . This offset is observed
 204 for all tested parameter settings, and it occurs independently of the intensity metric. Since the offset

205 will affect the performance of the texture features in any classifier, it requires further investigation. It
 206 is reasonable to assume that the offset in texture values at the sub-swath boundary is at least partly
 207 caused by the different number of looks in the respective sub-swaths of the S1 EW GRDM product.
 208 The image contrast, for example, is directly linked with the variance of the image brightness within
 209 a given window. A change in the number of looks causes a corresponding change in the magnitude
 210 of variance. Therefore, we can presumably correct the contrast values in sub-swath EW1 manually
 211 by multiplying with the square root of the ratio of number of looks between EW1 and EW2. Figure 3
 212 shows the distribution of HH contrast with IA before and after the correction. The proposed correction
 213 successfully removes the offset. Note that the correction may be less straightforward for other texture
 214 features, depending on the formula for their computation.

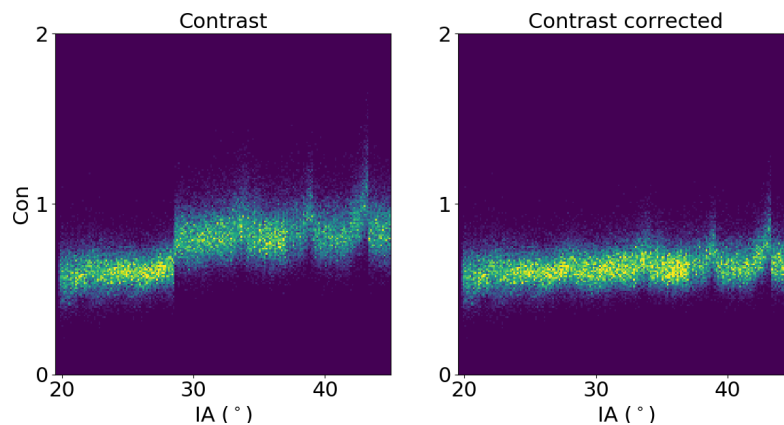


Figure 3. Density distribution of GLCM contrast (computed from HH intensity in dB) with IA for OW training data selected over the full range of a single S1 image (Image ID: F2FE). The left side shows contrast computed directly from the GRDM product; the right side shows contrast manually corrected by multiplying with the square root of the ratio of number of looks in the sub-swaths. GLCM parameter settings: $w=21$, $d=4$, $k=16$.

215 Based on the findings from the comparison of texture from linear intensity against texture from
 216 logarithmic intensity, all of the following calculations are performed with intensity given in dB. Further
 217 tests with different GLCM parameter settings (57 different settings in total, Table 2) confirm that the
 218 selected GLCM features are not or only weakly dependent on the IA.

219 Figure 4 shows examples for two selected features and four representative parameter settings
 220 for the MYI training data. The changes in the different parameters (w , d , and k) clearly affect the
 221 numerical values of the texture features. The variance of the distributions around the mean value
 222 decreases with increasing window size w (Figure 4 from left to right). Therefore, the linear trend
 223 in the feature distribution with IA is more easily visible for larger window sizes ($> \sim 21$ pixels). The
 224 dependency of texture with IA is linear (and almost constant) for all the tested parameter settings;
 225 hence, the parameter settings do not affect the general inclusion of GLCM texture into the concept of
 226 the GIA classifier.

227 All texture features shown so far have been extracted from the HH channel of the data. Figure 5
 228 shows an example of three selected texture features extracted from both HH and HV channel for
 229 LFYI training data. For a weak signal close to or below the nominal noise floor of the sensor, the
 230 distribution of texture with IA is strongly affected by the noise profile. This problem is of particular
 231 importance in the HV channel, as the signal at HV polarization is generally weaker than the signal
 232 at HH polarization. These noise floor artifacts in the texture features will complicate the inclusion of
 233 the HV texture features in the GIA classifier. Additionally, texture profiles for both channels display
 234 artifacts at the sub-swath boundaries between EW2 and EW5. The stronger these artifacts are, the
 235 more they will affect the use of texture across sub-swath boundaries in the classification. Note that we
 236 have only applied the calibration and nominal noise-floor corrections provided by ESA in the SNAP

237 software. Improved noise-floor corrections and more accurate data calibration between the sub-swaths
 238 may remedy this problem in the future.

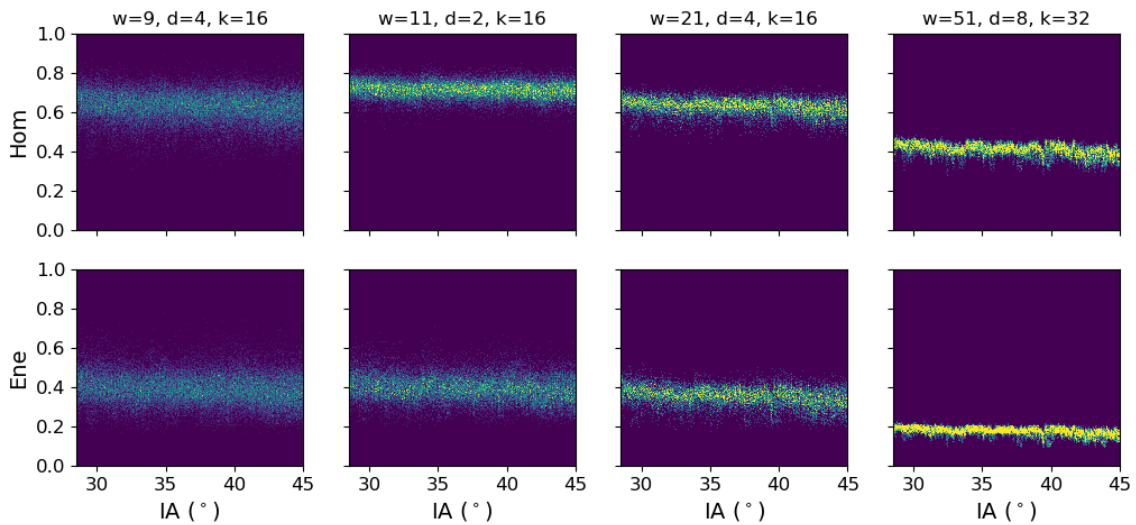


Figure 4. Density distribution of two selected GLCM texture features with IA for MYI training data selected from multiple S1 images. The texture features are computed from HH intensity in dB for different GLCM parameter settings. The first sub-swath EW1 is excluded because of the different number of looks in the GRDM product.

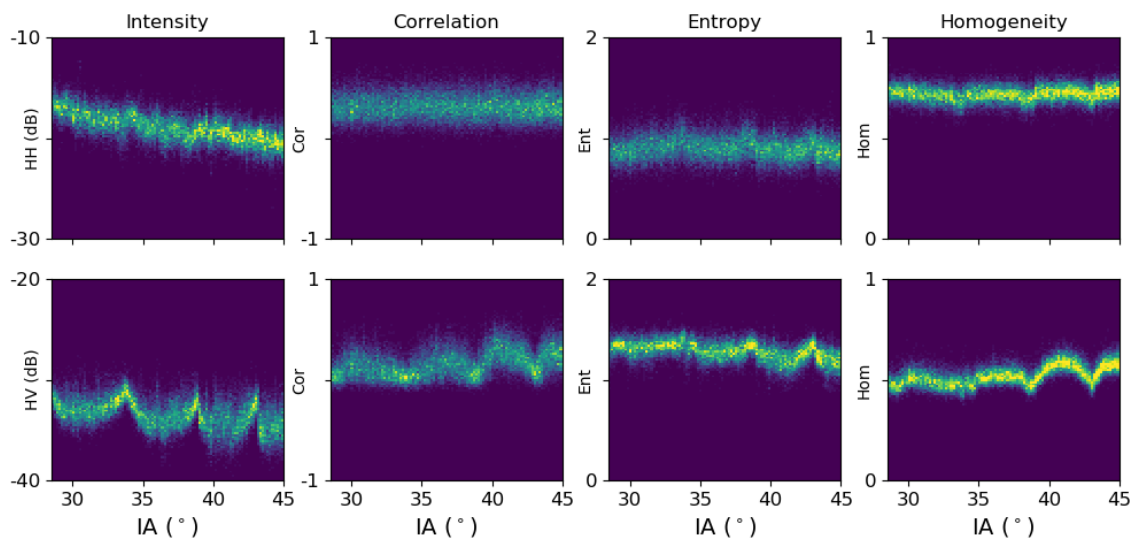


Figure 5. Density distribution of intensity and three selected GLCM texture features with IA for LFYI training data collected from multiple images. The upper panel shows HH intensity in dB and the corresponding HH texture features, the lower panel shows HV intensity in dB and the corresponding texture features. GLCM parameter settings: $w=11, d=2, k=16$.

239 Our tests for the variance as an example of a more simply calculated texture feature give similar
 240 results (not shown). When computed from the HH channel in dB, variance is approximately constant
 241 over the full range of the image, except for a significant offset between sub-swaths EW1 and EW2.
 242 When extracted from the HV channel, which often has a signal strength close to the nominal noise
 243 floor, the noise profile is clearly visible in the IA relationship of the variance. The assumptions needed
 244 for the GIA classifier (linear IA dependence, approximately Gaussian distribution) are then violated.

245 4.2. Texture and Different Sea Surface States

246 One of the main challenges in sea ice classification is to automatically separate sea ice and OW. As
 247 spatial and temporal variations in sea surface state affect the backscatter intensity from OW, a purely
 248 intensity-based classifier will often struggle with a generalized separation of sea ice and water, unless
 249 additional information is included. We now confirm that texture can help to overcome the issue of
 250 different backscatter intensity for varying sea surface states. Figure 6 shows training data of OW areas
 251 collected from multiple S1 images. The left column shows the density distributions of HH intensity in
 252 dB with IA. Clearly, the intensity levels differ between the images; assuming that the intensity level
 253 can be explained by Bragg scattering, its variations can be explained by differences in OW surface
 254 roughness. The numerical values of the texture features are consistent over the selected images and
 255 wind states (Figure 6, column 2,3,4). In agreement with previous results (Figure 4), the numerical
 256 texture values and the width of the distributions differ between different GLCM parameter settings
 257 (not shown here). Furthermore, the distributions of the texture features remain constant over the IA
 258 range, except for the offset between EW1 and EW2.

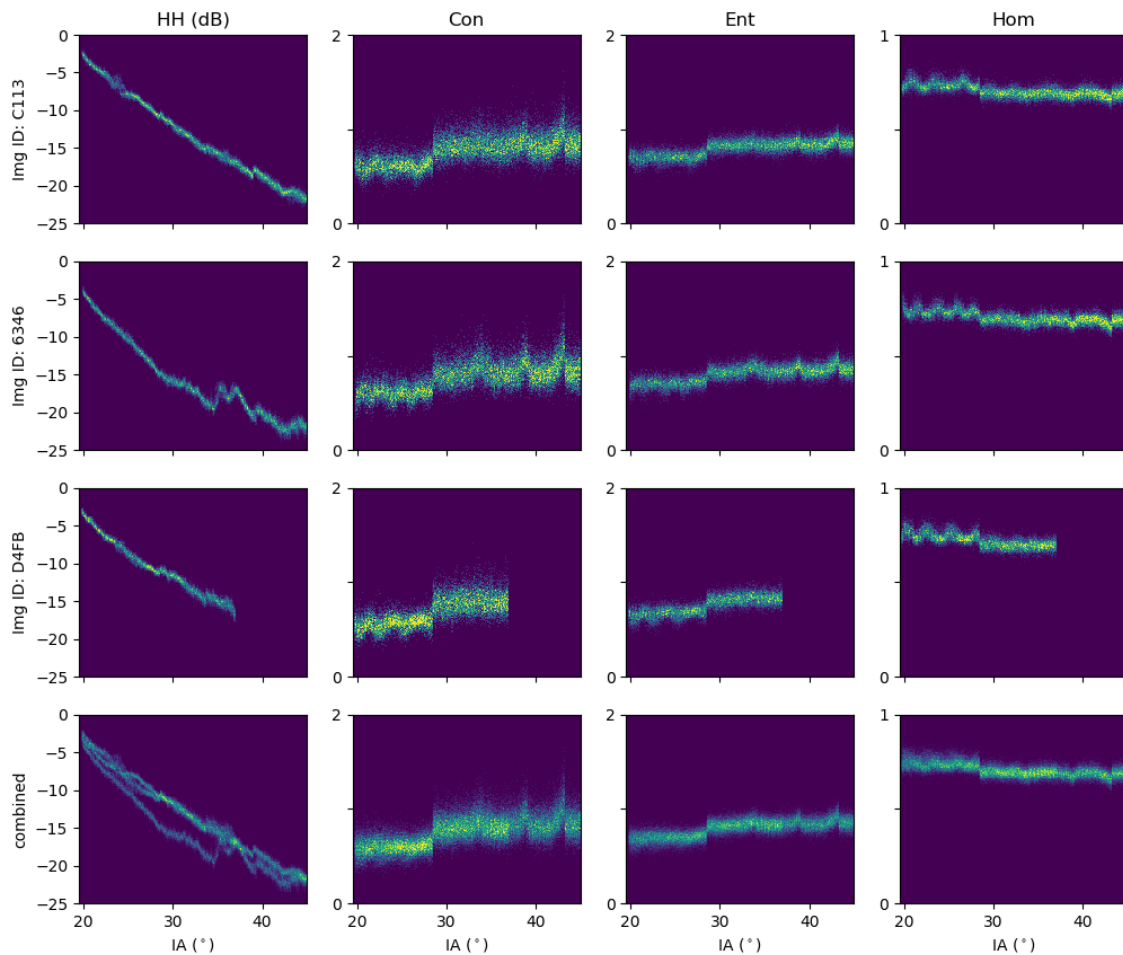


Figure 6. Density distribution of HH intensity in dB and three selected GLCM texture features with IA for OW training data selected from three different images (Image IDs: C113, 6346, D4FB). The lowest panel shows the data from all three images combined. The intensity values clearly differ between the images, the texture values are consistent. The offset in texture between sub-swaths EW1 and EW2 is caused by the different number of looks in the respective sub-swaths. The texture artifacts at the remaining sub-swath boundaries are caused by errors in the calibration and noise correction between the sub-swaths. GLCM parameter settings: $w=21$, $d=4$, $k=16$.

259 *4.3. Separability of Different Classes*

260 The results presented so far show that the tested GLCM texture features can be directly
 261 incorporated into the concept of the GIA classifier, given that the signal is strong enough to avoid
 262 noise floor artifacts. The GIA classifier assumes a linear relationship of its features with IA, and
 263 an approximately Gaussian feature distribution; thus the incorporation of GLCM texture features
 264 calculated from intensity in dB is straightforward. For the S1 EW GRDM product, the first sub-swath
 265 should be ignored or corrected according to the number of looks. However, for the inclusion of the
 266 texture features to be useful in terms of improving classification results, we need to investigate the
 267 separability of different classes for individual features and varying parameter settings.

Table 3. Jeffries-Matusita (JM) distance between class distributions for multiple combinations of texture features, two-class cases, and parameter settings. Blue and green colors indicate strong JM values above 0.7 and 1.0, respectively. The parameter settings are:

Set 1: w=07, d=2, k=16; Set 2: w=11, d=2, k=16; Set 3: w=11, d=4, k=16; Set 4: w=11, d=4, k=32;

Set 5: w=21, d=4, k=16; Set 6: w=21, d=4, k=32; Set 7: w=51, d=4, k=16; Set 8: w=51, d=4, k=32.

		HH ASM	HH Con	HH Cor	HH Dis	HH Ene	HH Ent	HH Hom	HH Var
	Set 1	0.08	0.16	0.03	0.10	0.08	0.12	0.09	0.29
	Set 2	0.20	0.29	0.11	0.22	0.21	0.29	0.19	0.49
OW	Set 3	0.20	0.36	0.01	0.27	0.22	0.30	0.23	0.49
vs.	Set 4	0.22	0.39	0.01	0.30	0.24	0.30	0.22	0.49
LFYI	Set 5	0.61	0.70	0.16	0.64	0.63	0.75	0.59	0.85
	Set 6	0.66	0.73	0.14	0.68	0.68	0.77	0.61	0.85
	Set 7	1.37	1.28	0.45	1.30	1.35	1.40	1.30	1.27
	Set 8	1.44	1.29	0.42	1.33	1.41	1.43	1.35	1.27
	Set 1	0.11	0.21	0.09	0.13	0.12	0.18	0.11	0.48
	Set 2	0.28	0.36	0.26	0.27	0.31	0.41	0.24	0.75
OW	Set 3	0.30	0.58	0.04	0.43	0.33	0.43	0.36	0.75
vs.	Set 4	0.33	0.61	0.03	0.48	0.36	0.44	0.35	0.75
MYI	Set 5	0.79	0.91	0.29	0.84	0.81	0.90	0.81	1.06
	Set 6	0.86	0.94	0.26	0.89	0.87	0.93	0.84	1.06
	Set 7	1.46	1.42	0.59	1.49	1.41	1.43	1.53	1.30
	Set 8	1.56	1.43	0.54	1.51	1.49	1.45	1.59	1.30
	Set 1	0.00	0.01	0.00	0.01	0.00	0.00	0.00	0.00
	Set 2	0.01	0.01	0.01	0.01	0.01	0.01	0.01	0.01
OW	Set 3	0.01	0.01	0.00	0.01	0.01	0.01	0.01	0.01
vs.	Set 4	0.01	0.01	0.00	0.01	0.01	0.01	0.01	0.01
YI	Set 5	0.03	0.02	0.05	0.02	0.03	0.04	0.02	0.12
	Set 6	0.03	0.02	0.05	0.02	0.03	0.04	0.02	0.12
	Set 7	0.16	0.18	0.54	0.11	0.20	0.36	0.08	0.95
	Set 8	0.18	0.19	0.51	0.12	0.22	0.34	0.07	0.95
	Set 1	0.00	0.01	0.01	0.00	0.00	0.01	0.00	0.07
	Set 2	0.01	0.01	0.04	0.01	0.02	0.03	0.01	0.15
LFYI	Set 3	0.01	0.08	0.01	0.05	0.02	0.03	0.03	0.15
vs.	Set 4	0.91	0.09	0.01	0.05	0.02	0.03	0.03	0.15
MYI	Set 5	0.04	0.13	0.04	0.09	0.05	0.08	0.07	0.27
	Set 6	0.04	0.14	0.04	0.10	0.05	0.08	0.06	0.27
	Set 7	0.08	0.21	0.12	0.18	0.10	0.16	0.16	0.38
	Set 8	0.08	0.21	0.10	0.18	0.09	0.15	0.15	0.38
	Set 1	0.15	0.27	0.08	0.18	0.15	0.22	0.15	0.51
	Set 2	0.34	0.44	0.20	0.36	0.36	0.45	0.33	0.68
MYI	Set 3	0.35	0.58	0.02	0.46	0.37	0.45	0.40	0.68
vs.	Set 4	0.39	0.61	0.02	0.50	0.40	0.47	0.40	0.68
YI	Set 5	0.76	0.88	0.12	0.86	0.75	0.80	0.85	0.81
	Set 6	0.84	0.90	0.09	0.90	0.82	0.84	0.90	0.81
	Set 7	0.92	1.16	0.03	1.32	0.86	0.78	1.40	0.23
	Set 8	1.00	1.17	0.03	1.34	0.94	0.83	1.50	0.23

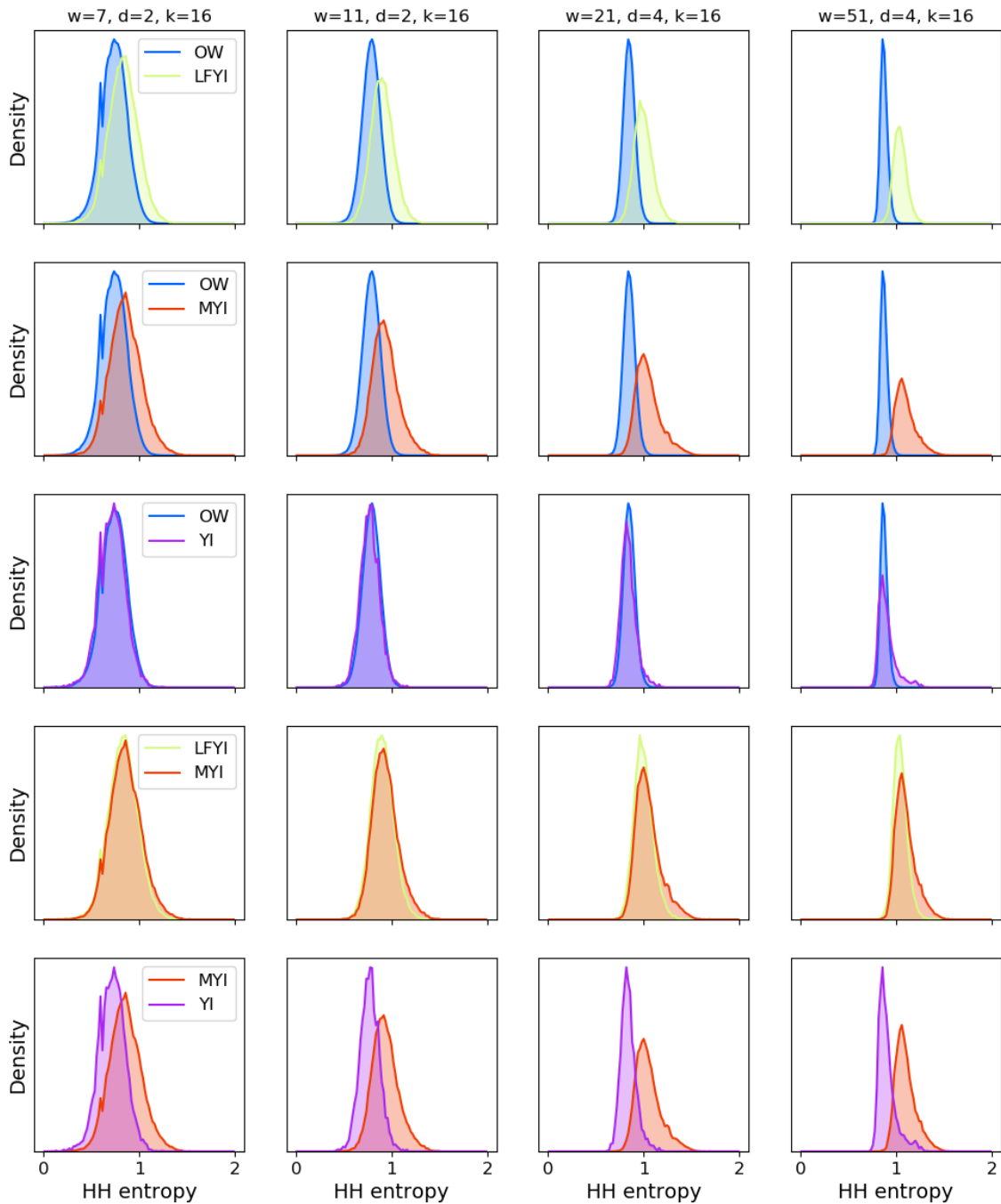


Figure 7. Histograms of HH entropy distribution for four selected GLCM parameter settings (one setting per column). For easier interpretation, each row shows only two classes compared against each other. Increasing window size (from left to right) generally leads to narrower distributions and better class separability.

268 We perform this analysis by computing the JM distance between the different feature distributions
 269 for all settings. The JM distance is an established separability measure between class distributions that
 270 returns values between zero (no separability) and two (perfect separability). Features with a JM value
 271 above one are commonly considered useful for classification [26]. Since the HV texture is strongly
 272 affected by the noise, we only evaluate texture features extracted from the HH channel at this point. In
 273 total, we have analyzed 57 different parameter settings (Table 2) for 8 separate features (seven GLCM

274 features (Equations 4 to 10) and variance). Table 3 presents the JM distance for eight selected parameter
 275 settings. Corresponding class distributions for four of these settings are shown in Figure 7.

276 For the given data set and the parameter settings tested in this study, we find that window size is
 277 the parameter with the largest influence on class separability. If a feature offers any separability at
 278 all between two tested classes, the separability improves with increasing window size (Table 3 and
 279 Figure 7, rows 1, 2, and 5). In agreement with previous studies, we find that many of the tested GLCM
 280 features allow for partial separation of OW from thicker ice types (that is LFYI, DFYI, and MYI). In
 281 particular, HH ASM, HH contrast, HH dissimilarity, HH energy, HH entropy, and HH homogeneity all
 282 display distinct class distributions that reveal at least some separability of LFYI/DFYI/MYI and OW,
 283 with JM distance values close to one (for $w=21$) and significantly above one (for $w=51$).

284 Figure 8 presents more histogram examples of HH dissimilarity and HH energy for the classes
 285 OW and MYI. Again, significant improvement of separability with increasing window size is clearly
 286 visible. Separation between the aforementioned thicker ice types (LFYI, DFYI, MYI) is not possible
 287 based on the investigated texture features only. This can be seen by the overlapping histograms for
 288 LFYI and MYI in Figure 7 (row 4) and is confirmed by the low JM distances between the distributions
 289 for all parameter settings and features (Table 3). Partial separation of LFYI and MYI may be possible
 290 using the GLCM correlation from the HV channel (Figure 9, right-hand side); however, the HV signal
 291 is often close to the nominal noise floor and the channel must be treated cautiously.

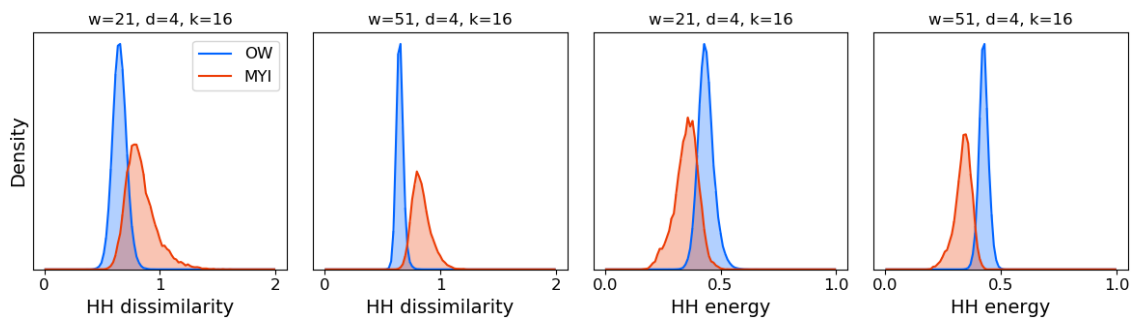


Figure 8. Histograms of HH dissimilarity and HH energy from two different window sizes ($w=21$ and $w=51$) for OW and MYI. Both features show improved class separability with larger window size.

292 None of the tested features separate well between YI and OW. The distributions of these two
 293 classes overlap significantly for all features and all parameter settings (Figure 7, row 3), resulting in
 294 low JM distances. However, HH texture shows the potential to improve the classification of MYI
 295 against YI in refrozen leads. For several features, JM distances between these two classes are close to
 296 and exceeding one at large window sizes ($w=21,51$). Histogram examples of HH dissimilarity and HH
 297 energy for YI and MYI are shown on the left-hand side of Figure 9.

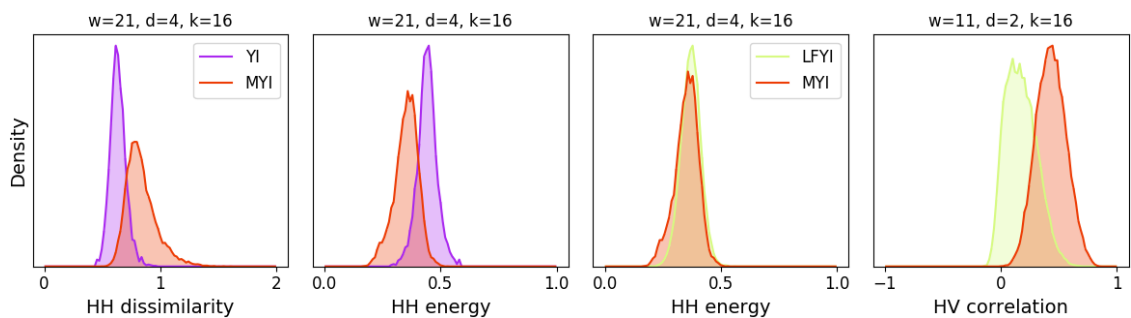


Figure 9. Histograms of HH dissimilarity, HH energy, and HV correlation for YI against MYI (left) and LFYI against MYI (right). YI and MYI can be partly separated using HH texture. LFYI and MYI are inseparable in HH texture, but can be partly separated in HV correlation, although significant overlap of the distributions remains.

298 *4.4. Classification Result Examples*

299 Finally, we demonstrate the potential of including useful texture features in the GIA classifier to
 300 improve classification results. Based on the class separability indicated by the JM distances, we choose
 301 different feature combinations and train the GIA algorithm to classify various test images. Three
 302 examples are shown in Figures 10 and 11. The features used for the classification of the presented
 303 images are HH intensity, HV intensity, HH contrast, HH dissimilarity, and HH energy. Because of the
 304 offset in numerical texture values between sub-swaths EW1 and EW2, we mask out the results for the
 305 first sub-swath.

306 Figure 10 shows all used features (a, b, c, and d) together with the classification result (e) and a map
 307 of sea ice concentration (SIC) (f), which can be directly obtained from the classification result. OW and
 308 sea ice are well separated in the image, and the ice edge can be successfully detected in both the ice type
 309 map as well as the SIC. Some areas within the pack ice are classified as OW; without complementary
 310 information, it is difficult to assess whether these areas are in fact OW or YI. Classification of an image
 311 containing large OW areas (such as the example in Figure 10) is challenging based on intensity only, as
 312 one would need to know the sea surface state to select the correct intensity level and training data for
 313 the OW class. Without that additional information, it is only the inclusion of textural information that
 314 makes the classification of the image with a generalized classifier feasible. We therefore do not present
 315 a result based on intensity only for this case.

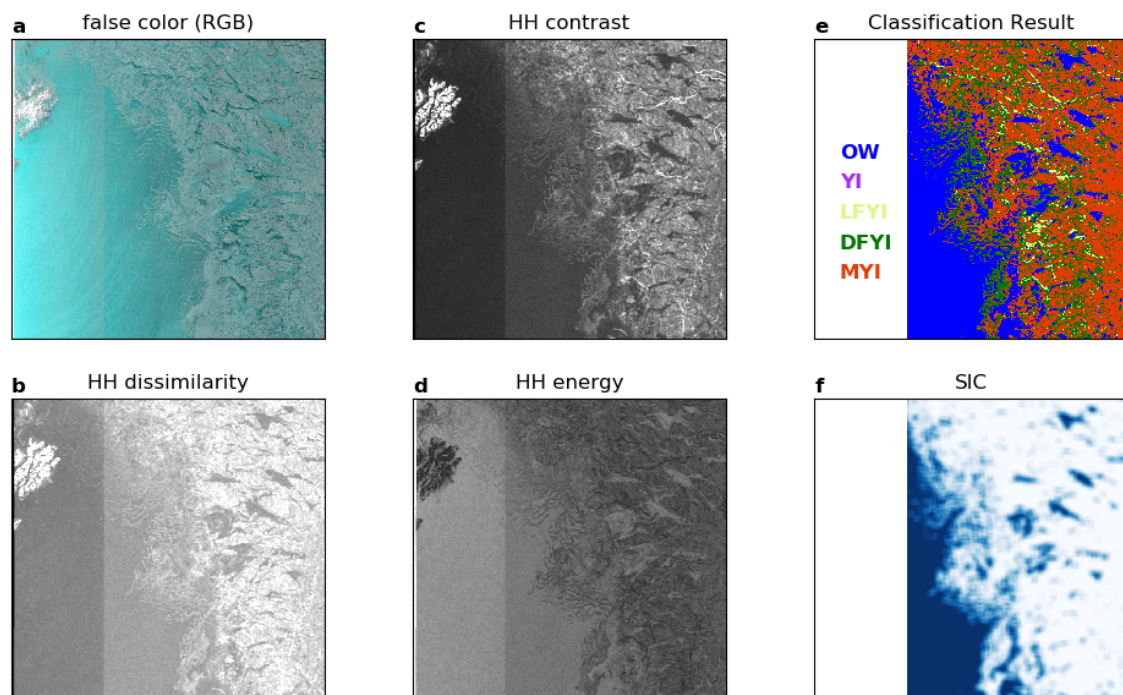


Figure 10. Input features and classification result for image ID F2FE. The used features are HH and HV intensity (a, false-color intensity image [R:HV, G:HH, B:HH]), HH dissimilarity (b), HH contrast (c), and HH energy (d). Sea ice concentration (f) can be calculated directly from the classification result (e). Because of the offset between sub-swaths EW1 and EW2 in the GLCM features (b, c, d), EW1 is masked out in the classification result. GLCM parameter settings: $w=51$, $d=4$, $k=32$.

316 Figure 11 shows false-color images (a and b) and classification results (c, d, e, and f) for two
 317 different images that are almost entirely covered by sea ice. The classification results in the middle
 318 column (Figure 11, c and d) are obtained with a GIA classifier that is based on intensities only. The
 319 same generalized classifier is used for both images. While the classifier captures the YI areas in the
 320 lower image correctly (ID B7A9), there is significant mis-classification of YI areas as MYI in the upper

321 image (ID 89A6). This mis-classification occurs despite the fact the YI areas appear visually similar in
 322 both images. A minor change in the properties of the YI areas and thus in the backscatter intensity
 323 from the surface can result in the confusion of YI and MYI. The texture signatures of the two classes
 324 can help to solve this problem. When the classification is performed including the textural information
 325 (Figure 11, e and f), the YI areas are classified correctly in both images. The examples demonstrate the
 326 superior capability of the GIA classifier using both intensity and texture to separate YI and MYI in
 327 situations where the purely intensity-based classifier fails.

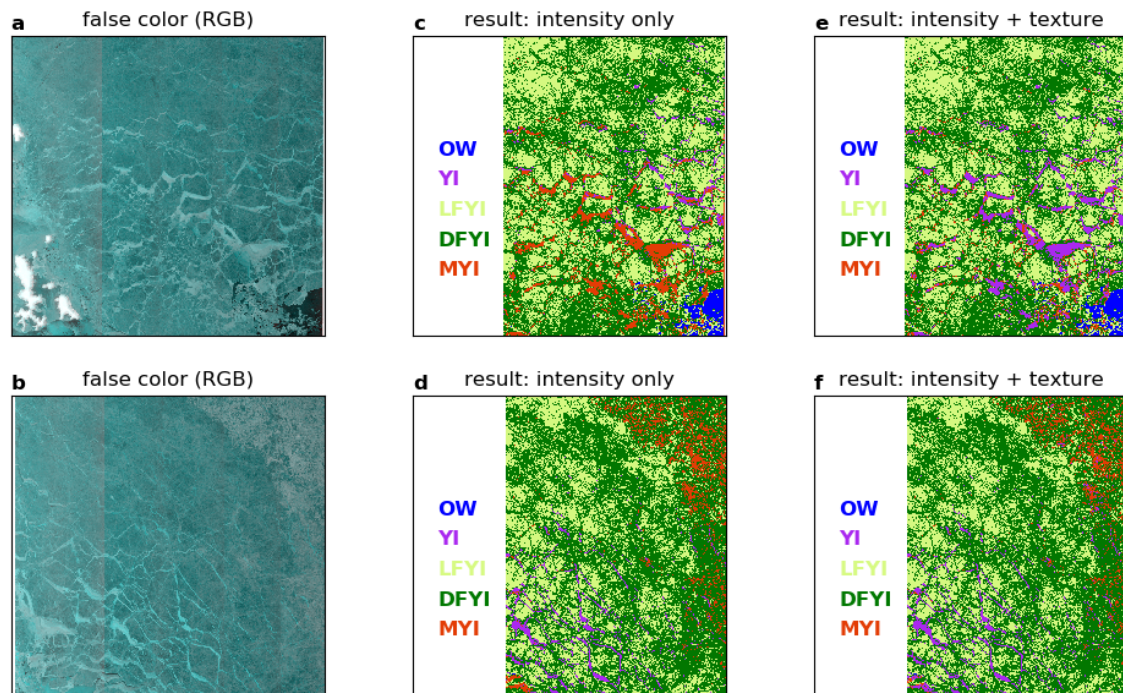


Figure 11. False-color intensity images (a and b, [R:HV, G:HH, B:HH]) and classification results using intensities only (c and d) and using intensities in combination with HH dissimilarity, HH contrast, and HH energy (e and f). The top row (a, c, e) shows image ID 89A6, the bottom row (b, d, f) shows image ID B7A9. For image ID 89A6, the purely intensity-based classifier mis-classifies many YI areas as MYI (c). The inclusion of texture improves the classification of YI (e). For image ID B7A9, the purely intensity-based classifier captures most of the YI areas correctly (d). The difference to the classification results based on intensities and texture is negligible. Because of the distinct offset between sub-swaths EW1 and EW2 in the GLCM features, EW1 is masked out in the classification result.

328 5. Discussion

329 We have investigated the class-dependent variation of different texture features with IA, in order
 330 to include them into the GIA classifier. The GIA classifier accounts for per-class variation of its features
 331 with IA, and requires approximately linear relationships and Gaussian distributions. Our results
 332 show that it is possible to directly incorporate GLCM texture into the GIA classifier. When computed
 333 from intensity in the logarithmic domain (that is in dB), the tested GLCM features do not depend
 334 on IA or reveal only a weak, approximately linear dependency. When computed from intensity in
 335 the linear domain, the tested GLCM features show considerable variation with IA. For some features
 336 the variation is approximately linear over part of the IA range, while for other features it is more
 337 complicated. Generally, we therefore recommend to compute texture from the logarithmic intensity;
 338 the slope of texture with IA is then constant (approximately zero) and the features can be used in the
 339 GIA classifier that assumes a linear relationship. Furthermore, for any other application in a different
 340 classification algorithm, as long as texture features are computed from logarithmic intensity, no global

341 correction of the IA effect during pre-processing is needed. We have tested a variety of different
342 GLCM parameter settings and find that the results regarding the IA dependence of the features are
343 independent of the parameter choice. They hold for all tested window sizes, grey levels, and distances.
344 For classes with a weak intensity signal, the S1 noise profile is clearly visible in the distribution of
345 texture features as a function of IA. While this noise pattern will cause problems for any classification
346 algorithm, it is particularly challenging for the GIA classifier, as the basic assumptions of linear IA
347 dependence and Gaussian distributions are violated. The HV channel is more problematic than the HH
348 channel in this regard, because the signal at HV polarization is often weak and close to the nominal
349 noise floor. HV texture should thus be used carefully, and will benefit from an improved thermal noise
350 correction of the S1 data.

351 Furthermore, we find that there is a distinct offset in all texture features at the sub-swath boundary
352 between EW1 and EW2 of the S1 EW GRDM product. This offset is caused by the different number
353 of looks applied to the individual sub-swaths; the GRDM product is delivered with 18 looks in EW1
354 and 12 looks in EW2 to EW5. We demonstrate how to correct this offset for the example of GLCM
355 contrast, by multiplying with the square root of the ratio of number of looks in the different EW GRDM
356 sub-swaths. Corrections can also be applied for other GLCM features, but will depend on the formula
357 for the texture computation. The exact correction factors for all individual features require further
358 investigation and are not part of this study. However, the offset must be considered whenever using
359 texture features extracted from S1 wide-swath products in GRDM format across the full range of the
360 image. Generally, it must be kept in mind that texture is dependent on the speckle contribution in the
361 intensity, and thus on the number of looks in the data.

362 When integrated into the GIA classifier, GLCM texture features help to resolve some of the
363 inherent ambiguities found with intensity-only classifiers. For example, the general separation of OW
364 and thicker sea ice types, such as LFYI, DFYI and MYI, is significantly improved by the inclusion
365 of texture. While the backscatter intensity from OW is dependent on the sea surface state and may
366 require the training of several OW classes for different sea surface conditions, the texture signature
367 of OW is nearly independent of the sea state. It suffices to train one OW class for a smooth water
368 surface (where the signal will be close to the nominal noise floor), and one OW class for all rough
369 surface conditions (Figure 6). Another challenge of a classifier based on intensity only is the separation
370 of YI and MYI. Especially for YI with frost flowers or a snow crust, which increases the small-scale
371 roughness and causes strong backscatter from the YI surface, mis-classification of YI as MYI can occur
372 [9,27]. We demonstrate in this study that the inclusion of texture features can significantly improve the
373 separation of YI and MYI.

374 While some ambiguities of the sea ice type classification can be improved or solved by adding
375 texture features, other classes are not separable in the texture feature space alone. Their per-class texture
376 distributions overlap significantly for all tested features and parameter settings. Hence, backscatter
377 intensity remains an important feature for the classification of these ice types. In particular, this is true
378 for the separation between the thicker ice types (LFYI, DFYI, and MYI), and for the separation of YI and
379 OW. FYI and MYI can be distinguished quite well based on their intensity, as the less saline MYI will
380 cause more volume scattering [28], which results in a stronger signal at both HH and HV polarization.
381 We therefore recommend to always include intensity as a feature in ice type classification. YI and OW,
382 on the other hand, can be more challenging. When the sea surface state, and thus the intensity level of
383 OW, is known, backscatter intensity can be used to overcome this ambiguity. However, since the sea
384 surface conditions are not usually known a priori, the separation of YI and OW remains difficult at
385 this point. We will explore possible solutions such as the inclusion of SIC from passive microwave
386 observations [29] or the results of SAR wind retrieval algorithms [30] in our future work.

387 The evaluation of features and parameter settings in this study is based on JM distances between
388 different class distributions. Generally, we find that larger window sizes improve the separability
389 between the classes in the used data set. It must be kept in mind, however, that large texture windows

390 result in smoothing and thus in a coarser effective resolution of the results. Hence, there is a trade-off
391 between spatial resolution of the results and separability of sea ice and OW, as well as YI and MYI.

392 The main focus of our analysis has been on the use of GLCM texture features, as the GLCM
393 method has been widely used for sea ice image analysis [13,15–22]. However, the calculation of
394 the GLCM requires substantial computational resources and is time consuming. For operational ice
395 charting, where timeliness of the results is a main requirement, this can be problematic. We have
396 therefore also tested variance as an example of a more simply calculated texture feature. We find that
397 variance from intensity in dB is roughly independent of IA and can potentially be used as a faster and
398 alternative to GLCM texture. Further investigation of other computationally cheap texture features,
399 such as for example the coefficient of variation or wavelets, is needed in future work and may help to
400 speed up the process of automated sea ice classification, making application of the algorithms feasible
401 in operational ice charting.

402 6. Conclusion

403 In this study, we have investigated the IA dependence of seven commonly used GLCM texture
404 features extracted from the S1 EW GRDM product, and assessed their potential to be included in
405 IA-sensitive sea ice classification (the GIA classifier). When calculated from intensity in dB, the GLCM
406 features are found to be almost independent of IA and can thus be directly included in the GIA
407 classifier, with the estimated slope being approximately zero. Particular attention must be paid to
408 classes with a weak signal, which will lead to noise artifacts in the texture parameters, and to the first
409 sub-swath of the EW GRDM product, as the different number of looks in the sub-swaths results in an
410 offset of texture at the sub-swath boundary. We have shown how this offset can be corrected for the
411 example of GLCM contrast.

412 We have tested a large number of GLCM parameters and evaluated the resulting features in terms
413 of class separability. Using per-class histograms of feature distributions in combination with the JM
414 distance, we have selected meaningful combinations of texture features and backscatter intensities to
415 train a classifier and demonstrate the improvement in ice-water classification as well as the separation
416 of YI and MYI on various examples compared to classification based on intensity only. Our analysis
417 shows that larger texture windows (up to 51x51 pixels) generally result in better class separability,
418 albeit at the cost of reduced spatial resolution of the image.

419 Code and Data Availability

420 Enquiries regarding python code and training data should be made by contacting the first author.

421 **Author Contributions:** Conceptualization, J.L. and A.P.D; Data curation, J.L. and W.D.; Formal analysis, J.L.;
 422 Investigation, J.L., A.P.D. and W.D.; Methodology, J.L. and A.P.D.; Supervision, A.P.D. and W.D.; Validation, J.L.,
 423 A.P.D. and W.D.; Visualization, J.L.; Writing - original draft, J.L., A.P.D. and W.D.; Writing - review & editing, J.L.,
 424 A.P.D. and W.D.

425 **Acknowledgments:** This research was funded by CIRFA partners and the Research Council of Norway (grant
 426 number 237906). The presented work contains primary and altered Sentinel data products (@Copernicus data).

427 **Conflicts of Interest:** The authors declare no conflict of interest.

428 Abbreviations

429 The following abbreviations are used in this manuscript:

430	CA	classification accuracy
	dB	decibel
	DFYI	deformed first-year ice
	ESA	European Space Agency
	EW	extra wide
	GIA	gaussian incident angle classifier
	GLCM	grey level co-occurrence Matrix
	GRDM	ground range detected medium
	IA	incident angle
	JM	Jeffries-Matusita
431	LFYI	level first-year ice
	MYI	multi-year ice
	NFI	newly formed ice
	OW	open water
	PDF	probability density function
	ROI	region of interest
	S1	Sentinel-1
	SAR	synthetic aperture radar
	SIC	sea ice concentration
	SNAP	Sentinel Application Platform
	YI	young ice

432 References

- 433 1. Zakhvatkina, N.; Smirnov, V.; Bychkova, I. Satellite SAR Data-based Sea Ice Classification: An Overview.
 434 *Geosciences* **2019**, *9*. doi:10.3390/geosciences9040152.
- 435 2. Moen, M.A.N.; Dougeris, A.P.; Anfinsen, S.N.; Renner, A.H.H.; Hughes, N.; Gerland, S.; Eltoft, T.
 436 Comparison of feature based segmentation of full polarimetric SAR satellite sea ice images with manually
 437 drawn ice charts. *The Cryosphere* **2013**, *7*, 1693–1705. doi:10.5194/tc-7-1693-2013.
- 438 3. Cheng, A.; Casati, B.; Tivy, A.; Zagon, T.; Lemieux, J.F.; Tremblay, L.B. Accuracy and inter-analyst agreement
 439 of visually estimated sea ice concentrations in Canadian Ice Service ice charts using single-polarization
 440 RADARSAT-2. *Cryosphere* **2020**, *14*.
- 441 4. Onstott, R.G.; Carsey, F.D. SAR and scatterometer signatures of sea ice. *Microwave remote sensing of sea ice*
 442 **1992**, *68*, 73–104.
- 443 5. Mäkynen, M.P.; Manninen, A.T.; Similä, M.H.; Karvonen, J.A.; Hallikainen, M.T. Incidence
 444 angle dependence of the statistical properties of C-band HH-polarization backscattering signatures
 445 of the Baltic Sea ice. *IEEE Transactions on Geoscience and Remote Sensing* **2002**, *40*, 2593–2605.
 446 doi:10.1109/TGRS.2002.806991.

- 447 6. Gill, J.P.S.; Yackel, J.; Geldsetzer, T.; Fuller, M.C. Sensitivity of C-band synthetic aperture radar polarimetric
448 parameters to snow thickness over landfast smooth first-year sea ice. *Remote Sensing of Environment* **2015**,
449 *166*, 34–49.
- 450 7. Mäkynen, M.; Karvonen, J. Incidence Angle Dependence of First-Year Sea Ice Backscattering Coefficient
451 in Sentinel-1 SAR Imagery Over the Kara Sea. *IEEE Transactions on Geoscience and Remote Sensing* **2017**,
452 *55*, 6170–6181. doi:10.1109/TGRS.2017.2721981.
- 453 8. Mahmud, M.S.; Geldsetzer, T.; Howell, S.E.L.; Yackel, J.J.; Nandan, V.; Scharien, R.K. Incidence Angle
454 Dependence of HH-Polarized C- and L-Band Wintertime Backscatter Over Arctic Sea Ice. *IEEE Transactions*
455 *on Geoscience and Remote Sensing* **2018**, pp. 1–13. doi:10.1109/TGRS.2018.2841343.
- 456 9. Zakhvatkina, N.; Alexandrov, V.Y.; Johannessen, O.M.; Sandven, S.; Frolov, I.Y. Classification of Sea Ice
457 Types in ENVISAT Synthetic Aperture Radar Images. *IEEE Transactions on Geoscience and Remote Sensing*
458 **2013**, *51*, 2587–2600. doi:10.1109/TGRS.2012.2212445.
- 459 10. Karvonen, J. A sea ice concentration estimation algorithm utilizing radiometer and SAR data. *The*
460 *Cryosphere* **2014**, *8*, 1639–1650. doi:10.5194/tc-8-1639-2014.
- 461 11. Liu, H.; Guo, H.; Zhang, L. SVM-Based Sea Ice Classification Using Textural Features and Concentration
462 From RADARSAT-2 Dual-Pol ScanSAR Data. *IEEE Journal of Selected Topics in Applied Earth Observations*
463 *and Remote Sensing* **2015**, *8*, 1601–1613. doi:10.1109/JSTARS.2014.2365215.
- 464 12. Karvonen, J. Baltic Sea Ice Concentration Estimation Using SENTINEL-1 SAR and AMSR2
465 Microwave Radiometer Data. *IEEE Transactions on Geoscience and Remote Sensing* **2017**, *55*, 2871–2883.
466 doi:10.1109/TGRS.2017.2655567.
- 467 13. Zakhvatkina, N.; Korosov, A.; Muckenhuber, S.; Sandven, S.; Babiker, M. Operational algorithm
468 for ice–water classification on dual-polarized RADARSAT-2 images. *The Cryosphere* **2017**, *11*, 33–46.
469 doi:10.5194/tc-11-33-2017.
- 470 14. Lohse, J.; Doulgeris, A.P.; Dierking, W. Mapping Sea Ice Types from Sentinel-1 Considering the Surface-Type
471 Dependent Effect of Incidence Angle. *Annals of Glaciology* **2020**, pp. 1–14. doi:10.1017/aog.2020.45.
- 472 15. Holmes, Q.A.; Nuesch, D.R.; Shuchman, R.A. Textural Analysis And Real-Time Classification of Sea-Ice
473 Types Using Digital SAR Data. *IEEE Transactions on Geoscience and Remote Sensing* **1984**, *GE-22*, 113–120.
474 doi:10.1109/TGRS.1984.350602.
- 475 16. Barber, D.G.; LeDrew, E. SAR Sea Ice Discrimination Using Texture Statistics: A Multivariate Approach.
476 *Photogrammetric Engineering and Remote Sensing* **1991**, *57*, 385–395.
- 477 17. Shokr, M.E. Evaluation of second-order texture parameters for sea ice classification
478 from radar images. *Journal of Geophysical Research: Oceans* **1991**, *96*, 10625–10640,
479 [<https://agupubs.onlinelibrary.wiley.com/doi/pdf/10.1029/91JC00693>]. doi:10.1029/91JC00693.
- 480 18. Soh, L.K.; Tsatsoulis, C. Texture Analysis of SAR Sea Ice Imagery Using Gray Level Co-Occurrence Matrices.
481 *IEEE Transactions on Geoscience and Remote Sensing* **1999**, *37*, 780–795. doi:10.1109/36.752194.
- 482 19. Clausi, D.A. Comparison and fusion of co-occurrence, Gabor and MRF texture
483 features for classification of SAR sea-ice imagery. *Atmosphere-Ocean* **2001**, *39*, 183–194,
484 [<https://doi.org/10.1080/07055900.2001.9649675>]. doi:10.1080/07055900.2001.9649675.
- 485 20. Clausi, D.A. An analysis of co-occurrence texture statistics as a function of grey level quantization. *Canadian*
486 *Journal of remote sensing* **2002**, *28*, 45–62.
- 487 21. Deng, H.; Clausi, D.A. Unsupervised segmentation of synthetic aperture Radar sea ice imagery using a
488 novel Markov random field model. *IEEE Transactions on Geoscience and Remote Sensing* **2005**, *43*, 528–538.
489 doi:10.1109/TGRS.2004.839589.
- 490 22. Ressel, R.; Frost, A.; Lehner, S. A Neural Network-Based Classification for Sea Ice Types on X-Band SAR
491 Images. *IEEE Journal of Selected Topics in Applied Earth Observations and Remote Sensing* **2015**, *8*, 3672–3680.
492 doi:10.1109/JSTARS.2015.2436993.
- 493 23. Haralick, R.M.; Shanmugan, K.; Dinstein, I. Textural features for image classification. *IEEE Transactions on*
494 *Systems, Man and Cybernetics* **1973**, pp. 610–621.
- 495 24. Clausi, D.A.; Deng, H. Operational segmentation and classification of SAR sea ice imagery. *IEEE*
496 *Workshop on Advances in Techniques for Analysis of Remotely Sensed Data*, 2003, 2004, pp. 268–275.
497 doi:10.1109/WARSD.2003.1295204.
- 498 25. Aulard-Macler, M. Sentinel-1 Product Definition S1-RS-MDA-52-7440. Technical report, MacDonald,
499 Dettwiler and Associates Ltd., 2011.

- 500 26. Sen, R.; Goswami, S.; Chakraborty, B. Jeffries-Matusita distance as a tool for feature selection. 2019
501 International Conference on Data Science and Engineering (ICDSE). IEEE, 2019, pp. 15–20.
- 502 27. Isleifson, D.; Hwang, B.; Barber, D.; Scharien, R.; Shafai, L. C-band polarimetric backscattering signatures
503 of newly formed sea ice during fall freeze-up. *IEEE Transactions on Geoscience and Remote Sensing* **2010**,
504 *48*, 3256–3267.
- 505 28. Komarov, A.; Buehner, M. Detection of first-year and multi-year sea ice from dual-polarization SAR images
506 under cold conditions. *IEEE Transactions on Geoscience and Remote Sensing* **2019**, *57*, 9109–9123.
- 507 29. Ivanova, N.; Johannessen, O.; Pedersen, L.; Tonboe, R. Retrieval of Arctic sea ice parameters by satellite
508 passive microwave sensors: A comparison of eleven sea ice concentration algorithms. *IEEE Transactions on*
509 *Geoscience and Remote Sensing* **2014**, *52*, 7233–7246.
- 510 30. Komarov, A.; Zabeline, V.; Barber, D. Ocean surface wind speed retrieval from C-band SAR images without
511 wind direction input. *IEEE Transactions on Geoscience and Remote Sensing* **2013**, *52*, 980–990.

512 © 2020 by the authors. Submitted to *Remote Sens.* for possible open access publication
513 under the terms and conditions of the Creative Commons Attribution (CC BY) license
514 (<http://creativecommons.org/licenses/by/4.0/>).

/9

Conclusion & Future Work

The work presented in Chapters 6 to 8 of this dissertation adds to the on-going research on automated mapping of sea ice types in SAR imagery. It has drawn interest from several ice services around the world and has been presented at the annual international ice charting working group (IICWG) meeting in 2019. This chapter summarizes the main conclusions and points out remaining challenges that need to be addressed in the future. Furthermore, this chapter presents past, presently ongoing, and planned applications of the developed algorithms in different fields. These applications underline the interest of the sea ice community in automated sea ice mapping in general, and point out possibilities for both operational and environmental applications of the work in this thesis in particular.

9.1 Research Conclusions

In this dissertation, existing classification algorithms are modified and extended to address specific challenges of sea ice type classification in SAR imagery. The main focus is on exploring the advantages of class-specific feature selection in a numerically optimized DT (*Paper 1*) and on incorporating the per-class IA effect into a supervised classifier for both intensity (*Paper 2*) and texture (*Paper 3*).

Paper 1 introduces the fully automated design of an optimal DT that splits a multi-class problem into several binary problems. The method determines the best order of classification steps and selects an individually optimized feature set for each branch of the tree (that is, for each individual class). Evaluation of simulated test data and an airborne multi-

frequency SAR data set shows that this variable and class-dependent feature selection can significantly improve the total CA. Additionally, the specifically selected feature sets provide information on which features are dominant in the separation of certain ice classes. This information can for example be used to assess dominant scattering mechanism or to investigate the contributions of different sensors and frequencies in a multi-sensor data set. The improved CA and the additional information gained from the optimal feature sets come at the cost of longer computation time.

Paper 2 and *Paper 3* focus on the classification of Sentinel-1 wide-swath images. These images are essential for operational ice charting in national ice services worldwide. Their automated analysis is complicated by the class-dependent decrease of backscatter intensity with IA across the images. *Paper 2* introduces a novel classification approach that can account for the class-dependent variation of intensity with IA. The IA effect is no longer treated as a global image property and corrected during pre-processing, but as an ice type property. Case studies in the paper demonstrate the advantages of the new algorithm compared to methods that use a global IA correction. *Paper 3* investigates the IA dependence of commonly used GLCM texture features and assesses their potential to be included in the IA-sensitive sea ice classification. When calculated from the logarithmic intensity, the GLCM features do not depend on IA or reveal only a weak, approximately linear dependency. A separability analysis and classification examples show significant improvements in the separation of ice and water, as well as young ice and MYI. The final classifier therefore uses both intensity features and texture features and accounts for linear per-class variation of its features with IA.

For the work in *Paper 2* and *Paper 3*, a new training and validation set for sea ice types from Sentinel-1 has been developed. All images in the data set are acquired during the winter and early spring months from 2015 to 2019 and thus represent freezing conditions. The regions of interest for the different classes are based on the visual analysis of overlapping SAR and optical images, with assistance from expert sea ice analysts of the NIS.

9.1.1 Future Work

The developed algorithms have been tested and applied in various environmental and operational settings (Section 9.2), and have the potential to contribute to better ice type mapping for safe operations in the Arctic. However, despite extensive research on the topic, including the work in this dissertation, automated classification of sea ice types and computer-assisted generation of ice charts remains a challenging task. The following list summarizes potential research ideas that should be addressed in the future:

- **Combination of the algorithms developed in *Paper 1* and in *Paper 2/Paper 3*:** The IA-sensitive algorithm including texture features can be integrated into the framework for the optimal DT design. *Paper 3* has shown that certain classes can be well separated by texture features, while other classes rely largely on backscatter

intensity. The class-specific feature selection of the optimized DT will allow to separate all classes with the highest possible CA.

- **Data-fusion with other sensors (PM and multi-frequency SAR):**
Even when using both intensity and texture features in combination with optimized feature selection, some ambiguities are expected to remain. Multi-sensor analysis can contribute to solving these ambiguities. For operational purposes, the additional sensors should be independent of sunlight and weather conditions. For example, SIC from PM observations can be used in a Bayesian classifier to set prior probabilities for ice and water classes. Alternatively, overlapping SAR images acquired at different frequencies can offer complementary information and improve the results of automated classification approaches (Section 9.2: *L-band for sea ice monitoring*).
- **Extension of the IA-sensitive algorithm to other acquisition modes, frequencies, and sensors:**
In this dissertation, the IA-sensitive classifier is developed and tested on Sentinel-1 data acquired in EW mode. The concept of how to include the class-specific IA effect into a forward classifier is directly transferable to different acquisition modes, radar frequencies, and sensors.
- **Adjustment of the algorithms to regional-specific tasks:** Depending on the application, the requirements for a classification algorithm differ in terms of needed accuracy, computational speed, spatial resolution, or number of ice classes. Particular regional applications require adjustment and re-training of the algorithms and implementation of a task-specific workflow (Section 9.2: *Operational Support for the Norwegian Coastal Administration*). Foremost, this includes a trade-off between spatial resolution and class separability, in particular when the application requires the use of texture features. The latter will also significantly increase processing time, which must be considered.
- **Extension of the training set to different seasons:**
The training set developed in this dissertation considers only winter/freezing conditions. As the backscatter signature from sea ice changes when temperatures approach the freezing point and there is liquid water in the snow pack on the ice, summer/melting conditions require a different training set. The concepts of the developed algorithms are directly transferable to such a new training set. Fully automated classification will then require an additional decision module (for example using meteorological information) to determine which training set to use in which conditions.

9.2 Application Examples

Development of a sea ice classification algorithm is in itself a technical task. The quality of this technical work can be assessed by splitting the set of samples with known class labels into a training and a validation set, and evaluating the classification result for the validation set. To be useful, the algorithm must also be tested, validated, and applied in actual operational and environmental settings. The following examples give an overview of past, presently ongoing, and planned applications of the algorithms developed in this dissertation.

Arctic-Wide Mapping of Sea Ice Types

The IA-sensitive algorithm developed in *Paper 2* and *Paper 3* has been set up at CIRFA to routinely map Arctic-wide sea ice conditions during winter and produce daily maps of sea ice type distribution. The resulting maps will be made publicly available in the future. The algorithm can be run using both intensity and texture or using intensity only. While the inclusion of texture is necessary to avoid significant errors in the detection of large open water areas, its computation is time-consuming. To provide a faster result while at the same time avoiding extensive mis-classification of open water, the classification result based on intensity-only is merged with SIC data from PM sensors. For that purpose, a simple data fusion approach has been implemented, which needs to be tested and refined in future studies. Figure 9.1 shows examples for the routinely produced classification results for the entire Arctic (top panel) and a smaller region in the Northern Barents Sea (lower panel).

L-band SAR for Sea Ice Monitoring (ROSE-L)

The algorithms developed in this dissertation will be utilized in the L- and C-band SAR satellites for sea ice monitoring (LC-ICE) project that will investigate the advantages of using combinations of C- and L-band SAR images for operational ice charting. The project is designed in support of the advisory group for ESA's high priority candidate mission (HPCM) ROSE-L. It will use ALOS-2 PALSAR-2 L-band images and Sentinel-1 or Radarsat-2 C-band data acquired over the same area with the shortest possible time difference. The classification part of the project will test (semi-)automated algorithms for classification of sea ice and detection of icebergs, using L-band and C-band as stand-alone, respectively, and C- and L-band combined.

Mapping of Seal Habitats

Application of the algorithms developed in this dissertation is proposed in a collaborative project with multiple international partners to integrate SAR data into habitat and

movement analyses of ice seals in the Pacific Arctic. The project suggests to link satellite locations of ice seals (i.e., biotelemetry data) with sea ice observations collected at multiple scales, including PM data, SAR data, and ice thickness data from ICESat-2. SAR data will be available from multiple sensors and in different acquisition modes (Sentinel-1 IW mode, ALOS PALSAR (dual- and quad-pol mode), Radarsat-1, and ERS-1/2). This will require re-training of the algorithm for the specific cases. Once training of the classifiers is completed, the available images will be classified according to ice age (multi-year, first-year, new, open water) and roughness. Similar studies have been performed using only PM data. The inclusion of SAR imagery will increase spatial resolution of the RS data by several orders of magnitude and add information on ice type.

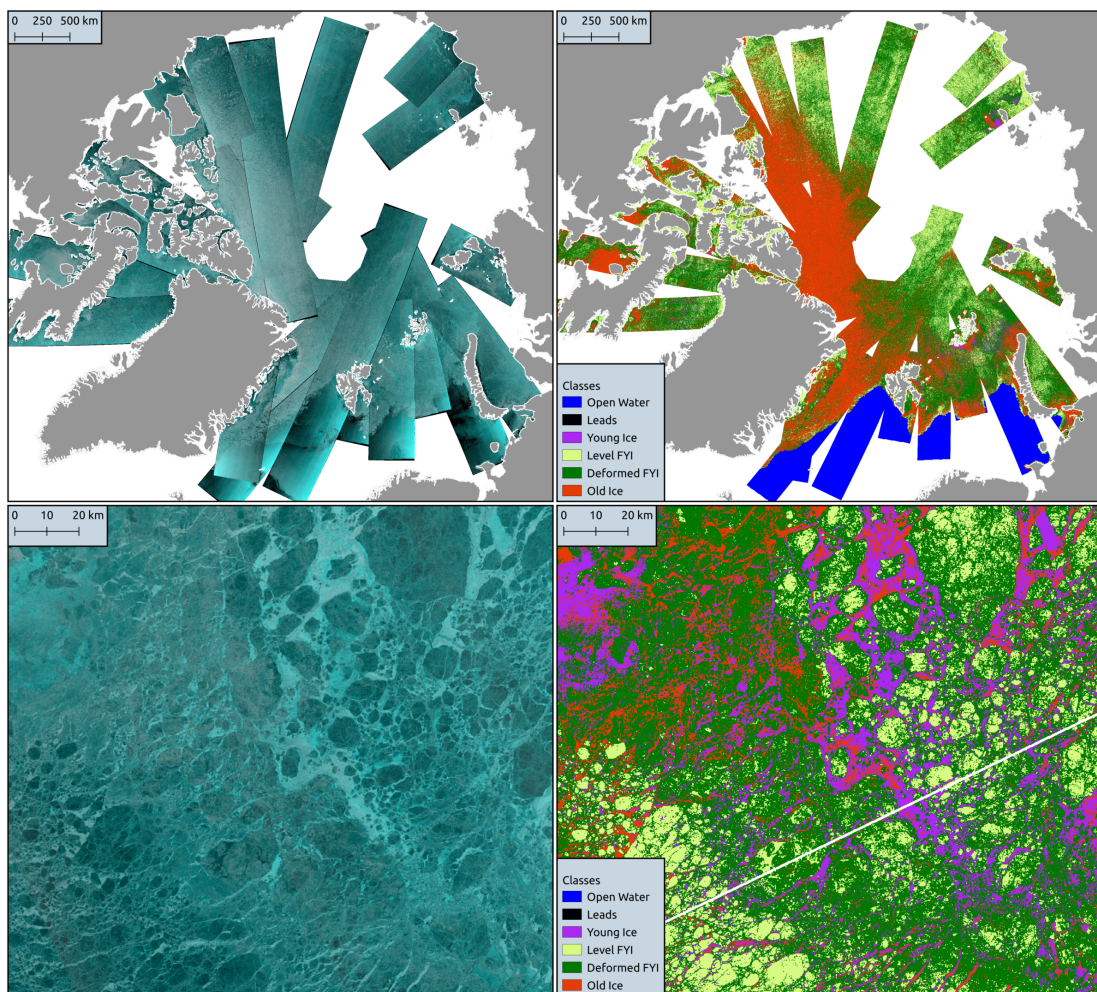


Figure 9.1: Routinely produced maps of sea ice type distribution for the entire Arctic (top panel) and a smaller region in the Northern Barents Sea (lower panel) on April 1st 2020. SAR imagery is shown on the left (red=HV, green=HH, blue=HH) and classification results are shown on the right. The classification is based on intensities only and the result is combined with SIC from PM observations.

Operational Support for the Norwegian Coastal Administration

In September 2019, the Norwegian Coastal Administration (Kystverket) tried to recover the damaged vessel *Northguider* that had run aground in the Hinlopen Strait between Spitsbergen and Nordaustland in December 2018 (Figure 9.2). Sea ice conditions in the strait can be challenging for marine traffic, as they can change quickly with the wind conditions. A simplified version of the classifier developed in *Paper 2* was re-trained to map sea ice and open water in the strait. The results were evaluated together with the Norwegian Coastal Administration during their recovery operation.

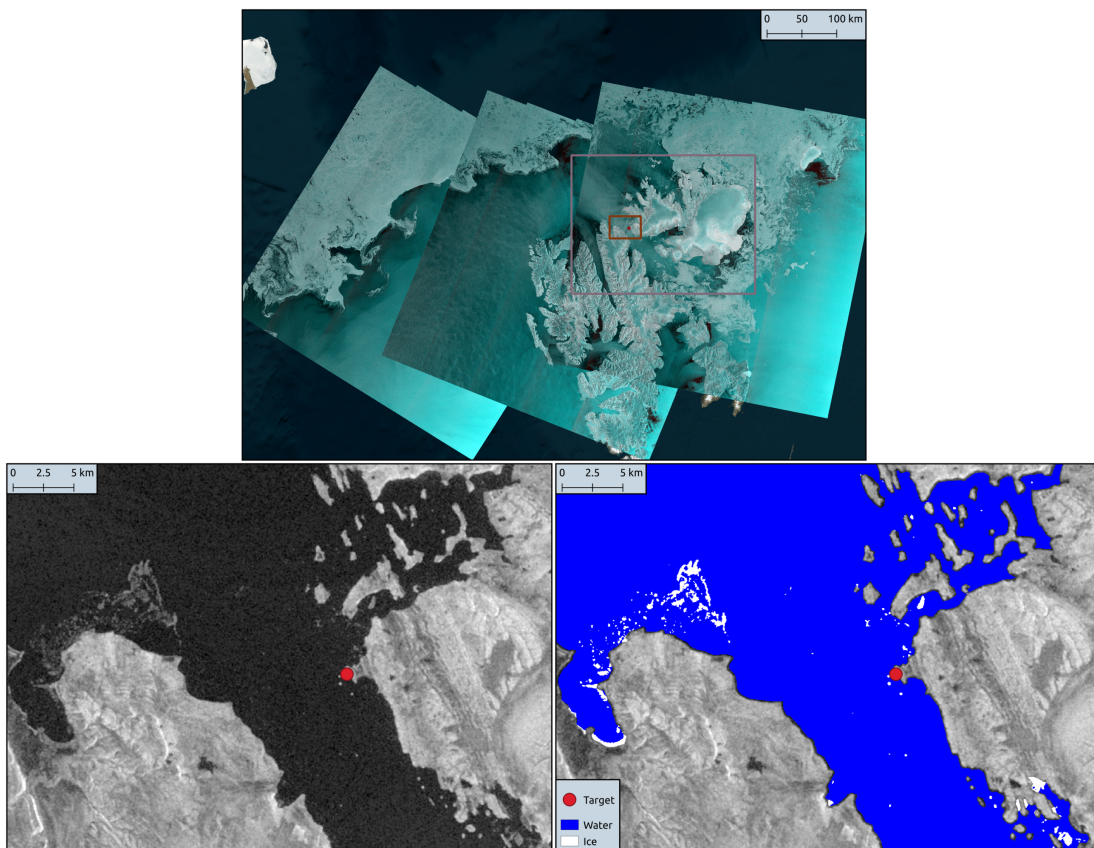


Figure 9.2: The top panel shows three Sentinel-1 images (red=HV, green=HH, blue=HH) acquired over the Svalbard archipelago in September 2019. The large square box indicates the area of interest with the Hinlopen Strait between Spitsbergen and Nordaustland. The small square box outlines the region shown in the lower panel, where HV intensity is shown on the left and the ice-water classification result on the right. The red circle (*Target*) marks the position of the grounded vessel.

The selected application examples above highlight the utility of the algorithms developed throughout this dissertation. The algorithms lay necessary groundwork for future developments in operational ice charting and robust and reliable mapping of sea ice types for the Arctic Ocean.

Bibliography

- [1] C. M. R. Fowler, *The solid earth: an introduction to global geophysics*. Cambridge University Press, 2nd ed., 2005.
- [2] H. Eicken, R. Gradinger, M. Salganek, K. Shirasawa, D. Perovich and M. Leppäranta, *Field techniques for Sea-ice Research*. University of Alaska Press, 2010.
- [3] H. Kaartokallio, M. Granskog, H. Kuosa and J. Vainio, “Ice in subarctic seas,” in *Sea Ice, 3rd Edition*, pp. 630–644, John Wiley & Sons, 2017.
- [4] W. F. Weeks and S. F. Ackley, “The growth, structure, and properties of sea ice,” in *The geophysics of sea ice*, pp. 9–164, Springer, 1986.
- [5] M. Shokr and N. Sinha, *Sea ice: physics and remote sensing*. John Wiley & Sons, 2015.
- [6] C. Petrich and H. Eicken, “Overview of sea ice growth and properties,” in *Sea Ice, 3rd Edition*, pp. 1–41, John Wiley & Sons, Ltd Chichester, UK, 2017.
- [7] M. Leppäranta, “A review of analytical models of sea-ice growth,” *Atmosphere-Ocean*, vol. 31, no. 1, pp. 123–138, 1993.
- [8] D. Notz, *Thermodynamic and fluid-dynamical processes of sea ice*. PhD thesis, Trinity College, 2005.
- [9] D. Notz and M. G. Worster, “In situ measurements of the evolution of young sea ice,” *Journal of Geophysical Research: Oceans*, vol. 113, no. C3, 2008.
- [10] M. Leppäranta, *The drift of sea ice*. Springer Science & Business Media, 2011.
- [11] “<http://osisaf.met.no/p/ice/>,” last accessed 18th September 2020.
- [12] J. C. Comiso, C. L. Parkinson, R. Gersten and L. Stock, “Accelerated decline in the Arctic sea ice cover,” *Geophysical Research Letters*, vol. 35, no. 1, 2008.

- [13] L. Polyak, R. B. Alley, J. T. Andrews, J. Brigham-Grette, T. M. Cronin, D. A. Darby, A. S. Dyke, J. J. Fitzpatrick, S. Funder, M. Holland, A. E. Jennings, G. H. Miller, M. O'Regan, J. Saville, M. Serreze, K. St. John, J. W. C. White and E. Wolff, "History of sea ice in the Arctic," *Quaternary Science Reviews*, vol. 29, no. 15, pp. 1757–1778, 2010. Special Theme: Arctic Palaeoclimate Synthesis (PP. 1674-1790).
- [14] J. Maslanik, J. Stroeve, C. Fowler and W. Emery, "Distribution and trends in Arctic sea ice age through spring 2011," *Geophysical Research Letters*, vol. 38, no. 13, 2011.
- [15] J. C. Comiso, "Large Decadal Decline of the Arctic Multiyear Ice Cover," *Journal of Climate*, vol. 25, no. 4, pp. 1176–1193, 2012.
- [16] J. C. Stroeve, M. C. Serreze, M. M. Holland, J. E. Kay, J. Malanik and A. P. Barrett, "The Arctic's rapidly shrinking sea ice cover: a research synthesis," *Climatic change*, vol. 110, no. 3-4, pp. 1005–1027, 2012.
- [17] J. Maslanik, C. Fowler, J. Stroeve, S. Drobot, J. Zwally, D. Yi and W. Emery, "A younger, thinner Arctic ice cover: Increased potential for rapid, extensive sea-ice loss," *Geophysical Research Letters*, vol. 34, no. 24, 2007.
- [18] R. Kwok, "Arctic sea ice thickness, volume, and multiyear ice coverage: losses and coupled variability (1958–2018)," *Environmental Research Letters*, vol. 13, no. 10, p. 105005, 2018.
- [19] L. H. Smedsrud, A. Sorteberg and K. Kloster, "Recent and future changes of the Arctic sea-ice cover," *Geophysical Research Letters*, vol. 35, no. 20, 2008.
- [20] M. C. Serreze, M. M. Holland and J. Stroeve, "Perspectives on the Arctic's shrinking sea-ice cover," *science*, vol. 315, no. 5818, pp. 1533–1536, 2007.
- [21] A. Jahn, J. E. Kay, M. M. Holland and D. M. Hall, "How predictable is the timing of a summer ice-free Arctic?," *Geophysical Research Letters*, vol. 43, no. 17, pp. 9113–9120, 2011.
- [22] "<https://www.meereisportal.de/en/>," last accessed 30th August 2020.
- [23] K. Grosfeld, R. Treffeisen, J. Asseng, A. Bartsch, B. Bräuer, B. Fritsch, S. Hendricks, W. Hiller, G. Heygster, T. Krumpfen, C. Melsheimer, M. Nicolaus, R. Ricker and M. Weigelt, "Online sea ice knowledge and data platform: www.meereisportal.de," *Polarforschung*, vol. 85, no. 2, pp. 143–155, 2015.
- [24] D. K. Perovich, B. Light, H. Eicken, K. F. Jones, K. Runciman and S. V. Nghiem, "Increasing solar heating of the Arctic Ocean and adjacent seas, 1979–2005: Attribution and role in the ice-albedo feedback," *Geophysical Research Letters*, vol. 34, no. 19,

2007.

- [25] A. S. Gardner and M. J. Sharp, "A review of snow and ice albedo and the development of a new physically based broadband albedo parameterization," *Journal of Geophysical Research: Earth Surface*, vol. 115, no. F1, 2010.
- [26] Y. Cao, S. Liang, X. Chen and T. He, "Assessment of sea ice albedo radiative forcing and feedback over the Northern Hemisphere from 1982 to 2009 using satellite and reanalysis data," *Journal of Climate*, vol. 28, no. 3, pp. 1248–1259, 2015.
- [27] J. A. Curry, J. L. Schramm and E. E. Ebert, "Sea Ice-Albedo Climate Feedback Mechanism," *Journal of Climate*, vol. 8, no. 2, pp. 240–247, 1995.
- [28] G. A. Maykut, "Energy exchange over young sea ice in the central Arctic," *Journal of Geophysical Research: Oceans*, vol. 83, no. C7, pp. 3646–3658, 1978.
- [29] M. G. McPhee and N. Untersteiner, "Using sea ice to measure vertical heat flux in the ocean," *Journal of Geophysical Research: Oceans*, vol. 87, no. C3, pp. 2071–2074, 1982.
- [30] K. Aagaard and E. C. Carmack, "The role of sea ice, other fresh water in the Arctic circulation," *Journal of Geophysical Research: Oceans*, vol. 94, no. C10, pp. 14485–14498, 1989.
- [31] J. M. Toole, M.-L. Timmermans, D. K. Perovich, R. A. Krishfield, A. Proshutinsky and J. A. Richter-Menge, "Influences of the ocean surface mixed layer and thermohaline stratification on Arctic Sea ice in the central Canada Basin," *Journal of Geophysical Research: Oceans*, vol. 115, no. C10, 2010.
- [32] K. I. Ohshima, Y. Fukamachi, G. D. Williams, S. Nihashi, F. Roquet, Y. Kitade, T. Tamura, D. Hirano, L. Herraiz-Borreguero, I. Field and others, "Antarctic Bottom Water production by intense sea-ice formation in the Cape Darnley polynya," *Nature Geoscience*, vol. 6, no. 3, pp. 235–240, 2013.
- [33] D. Budikova, "Role of Arctic sea ice in global atmospheric circulation: A review," *Global and Planetary Change*, vol. 68, no. 3, pp. 149–163, 2009.
- [34] T. Vihma, "Effects of Arctic sea ice decline on weather and climate: A review," *Surveys in Geophysics*, vol. 35, no. 5, pp. 1175–1214, 2014.
- [35] K. R. Arrigo, "Sea ice as a habitat for primary producers," in *Sea Ice, 3rd Edition*, pp. 352–369, John Wiley & Sons, 2017.
- [36] J. W. Deming and R. E. Collins, "Sea ice as a habitat for bacteria, archaea and

- viruses,” in *Sea Ice, 3rd Edition*, pp. 326–351, John Wiley & Sons, 2017.
- [37] R. A. Horner, “Ecology of sea ice microalgae,” in *Sea ice biota*, pp. 83–103, CRC Press Boca Raton, FL, 1985.
- [38] R. Gradinger, “Sea-ice algae: Major contributors to primary production and algal biomass in the Chukchi and Beaufort Seas during May/June 2002,” *Deep Sea Research Part II: Topical Studies in Oceanography*, vol. 56, no. 17, pp. 1201–1212, 2009.
- [39] P. Assmy, M. Fernández-Méndez, P. Duarte, A. Meyer, A. Randelhoff, C. Mundy, L. Olsen, H. Kauko, A. Bailey, M. Chierici, Melissa and others, “Leads in Arctic pack ice enable early phytoplankton blooms below snow-covered sea ice,” *Scientific Reports*, vol. 7, p. 40850, 2017.
- [40] C. A. Ribic, D. G. Ainley and W. R. Fraser, “Habitat selection by marine mammals in the marginal ice zone,” *Antarctic Science*, vol. 3, no. 2, pp. 181–186, 1991.
- [41] K. M. Kovacs, C. Lydersen, J. E. Overland and S. E. Moore, “Impacts of changing sea-ice conditions on Arctic marine mammals,” *Marine Biodiversity*, vol. 41, no. 1, pp. 181–194, 2011.
- [42] K. L. Laidre and E. V. Regehr, “Arctic marine mammals and sea ice,” in *Sea Ice, 3rd Edition*, pp. 516–533, John Wiley & Sons, 2017.
- [43] T. G. Smith and I. Stirling, “The breeding habitat of the ringed seal (*Phoca hispida*). The birth lair and associated structures,” *Canadian Journal of Zoology*, vol. 53, no. 9, pp. 1297–1305, 1975.
- [44] H. P. Huntington, S. Gearheard, L. K. Holm, G. Noongwook, M. Opie and J. Sanguya, “Sea ice is our beautiful garden: indigenous perspectives on sea ice in the Arctic,” in *Sea Ice, 3rd Edition*, pp. 583–599, John Wiley & Sons, 2017.
- [45] E. J. Stewart, S. Howell, D. Draper, J. Yackel and A. Tivy, “Sea ice in Canada’s Arctic: Implications for cruise tourism,” *Arctic*, pp. 370–380, 2007.
- [46] D. L. Gautier, K. J. Bird, R. R. Charpentier, A. Grantz, D. W. Houseknecht, T. R. Klett, T. E. Moore, J. K. Pitman, C. Schenk, J. H. Schuenemeyer, John H and others, “Assessment of undiscovered oil and gas in the Arctic,” *Science*, vol. 324, no. 5931, pp. 1175–1179, 2009.
- [47] F. Lasserre and S. Pelletier, “Polar super seaways? Maritime transport in the Arctic: an analysis of shipowners’ intentions,” *Journal of Transport Geography*, vol. 19, no. 6, pp. 1465–1473, 2011. Special section on Alternative Travel futures.

- [48] L. Pizzolato, S. E. L. Howell, C. Derksen, J. Dawson and L. Copland, "Changing sea ice conditions and marine transportation activity in Canadian Arctic waters between 1990 and 2012," *Climatic Change*, vol. 123, no. 2, pp. 161–173, 2014.
- [49] F. Lasserre and P.-L. Têtu, "Transportation in the melting Arctic: contrasting views of shipping and railway development," 2020.
- [50] S. R. Stephenson, L. C. Smith, L. W. Brigham and J. A. Agnew, "Projected 21st-century changes to Arctic marine access," *Climatic Change*, vol. 118, no. 3-4, pp. 885–899, 2013.
- [51] Y. Aksenov, E. Popova, A. Yool, A. J. G. Nurser, T. D. Williams, L. Bertino and J. Bergh, "On the future navigability of Arctic sea routes: High-resolution projections of the Arctic Ocean and sea ice," *Marine Policy*, vol. 75, pp. 300–317, 2017.
- [52] "https://www.pmel.noaa.gov/arctic-zone/detect/documents/AMSA_2009_Report_2nd_print.pdf," last accessed 1 September 2020.
- [53] W. F. Weeks, "On the history of research on sea ice," *Physics of ice-covered seas*, vol. 1, pp. 1–24, 1998.
- [54] F. Nansen, *In Northern Mists: Arctic Exploration in Early Times. Volume One*. Ballantyne & Company Ltd, 1911.
- [55] E. F. Weeks, *On sea ice*. University of Alaska Press, 2010.
- [56] G. Dieckmann and H. H. Hellmer, "The importance of sea ice: An overview," in *Sea Ice, 2nd Edition*, pp. 1–21, John Wiley & Sons, 2010.
- [57] J. Hutchings, N. Hughes, A. Orlich, S. MacFarlane, A. Cowen, L. Farmer and K. Faber, "Ice Watch: standardizing and expanding Arctic ship based sea ice observations," *White Paper Presented at Arctic Observing Summit*, 2016.
- [58] O. J. Hegelund, A. Everett, T. Cheeseman, P. Wagner, N. Hughes, M. Pierechod, K. Southerland, P. Robinson, J. Hutchings, A. Kærbech and others, "Extending the Ice Watch system as a citizen science project for the collection of In-Situ sea ice observations," in *EGU General Assembly Conference Abstracts*, p. 7126, 2020.
- [59] C. Haas, "Airborne electromagnetic sea ice thickness sounding in shallow, brackish water environments of the Caspian and Baltic Seas," in *Proceedings of OMAE2006 25th International Conference on Offshore Mechanics and Arctic Engineering, June 4-9, 2006, Hamburg, Germany*, 2006.
- [60] C. Haas, S. Hendricks, H. Eicken and A. Herber, "Synoptic airborne thickness surveys

- reveal state of Arctic sea ice cover,” *Geophysical Research Letters*, vol. 37, no. 9, 2010.
- [61] “<https://www.npolar.no/en/projects/n-ice2015/>,” last accessed 21 September 2020.
- [62] “<https://mosaic-expedition.org/>,” last accessed 10 September 2020.
- [63] G. Spreen and S. Kern, “Methods of satellite remote sensing of sea ice,” in *Sea Ice, 3rd Edition*, pp. 239–260, John Wiley & Sons, Ltd Chichester, UK, 2017.
- [64] J. Grahn, *Multi-frequency radar remote sensing of sea ice: Modelling and interpretation of polarimetric multi-frequency radar signatures of sea ice*. PhD thesis, UiT The Arctic University of Norway, 2018.
- [65] J. A. Richards, *Remote sensing with imaging radar*, vol. 1. Springer, 2009.
- [66] F. Ulaby and D. Long, *Microwave radar and radiometric remote sensing*. The University of Michigan Press, 2014.
- [67] S. Andersen, R. Tonboe, S. Kern, H. Schyberg, “Improved retrieval of sea ice total concentration from spaceborne passive microwave observations using numerical weather prediction model fields: An intercomparison of nine algorithms,” *Remote Sensing of Environment*, vol. 104, no. 4, pp. 374–392, 2006.
- [68] N. Ivanova, O. M. Johannessen, L. T. Pedersen and R. T. Tonboe, “Retrieval of Arctic sea ice parameters by satellite passive microwave sensors: A comparison of eleven sea ice concentration algorithms,” *IEEE Transactions on Geoscience and Remote Sensing*, vol. 52, no. 11, pp. 7233–7246, 2014.
- [69] Q. P. Remund and D. G. Long, “Sea ice extent mapping using Ku band scatterometer data,” *Journal of Geophysical Research: Oceans*, vol. 104, no. C5, pp. 11515–11527, 1999.
- [70] R. Belmonte Rivas, I. Ootosaka, A. Stoffelen and A. Verhoef, “A scatterometer record of sea ice extents and backscatter: 1992–2016,” *The Cryosphere*, vol. 12, no. 9, pp. 2941–2953, 2018.
- [71] W. N. Meier and J. Stroeve, “Comparison of sea-ice extent and ice-edge location estimates from passive microwave and enhanced-resolution scatterometer data,” *Annals of Glaciology*, vol. 48, pp. 65–70, 2008.
- [72] D. J. Cavalieri, P. Gloersen and W. J. Campbell, “Determination of sea ice parameters with the Nimbus 7 SMMR,” *Journal of Geophysical Research: Atmospheres*, vol. 89, no. D4, pp. 5355–5369, 1984.

- [73] T. Lavergne, S. Eastwood, Z. Teffah, H. Schyberg and L.-A. Breivik, "Sea ice motion from low-resolution satellite sensors: An alternative method and its validation in the Arctic," *Journal of Geophysical Research: Oceans*, vol. 115, no. C10, 2010.
- [74] S. Martin, R. Drucker, R. Kwok and B. Holt, "Estimation of the thin ice thickness and heat flux for the Chukchi Sea Alaskan coast polynya from Special Sensor Microwave/Imager data, 1990–2001," *Journal of Geophysical Research: Oceans*, vol. 109, no. C10, 2004.
- [75] S. Martin, R. Drucker, R. Kwok and B. Holt, "Improvements in the estimates of ice thickness and production in the Chukchi Sea polynyas derived from AMSR-E," *Geophysical Research Letters*, vol. 32, no. 5, 2005.
- [76] K. Nakamura, H. Wakabayashi, K. Naoki, F. Nishio and others, "Sea-ice thickness retrieval in the Sea of Okhotsk using dual-polarization SAR data," *Annals of Glaciology*, vol. 44, pp. 261–268, 2006.
- [77] N. T. Kurtz, T. Markus, D. J. Cavalieri, L. C. Sparling, W. B. Krabill, A. J. Gasiewski and J. G. Sonntag, "Estimation of sea ice thickness distributions through the combination of snow depth and satellite laser altimetry data," *Journal of Geophysical Research: Oceans*, vol. 114, no. C10, 2009.
- [78] H. J. Zwally, B. Schutz, W. Abdalati, J. Abshire, C. Bentley, A. Brenner, J. Bufton, J. Dezio, D. Hancock, D. Harding and others, "ICESat's laser measurements of polar ice, atmosphere, ocean, and land," *Journal of Geodynamics*, vol. 34, no. 3-4, pp. 405–445, 2002.
- [79] N. T. Kurtz, N. Galin and M. Studinger, "An improved CryoSat-2 sea ice freeboard retrieval algorithm through the use of waveform fitting," *The Cryosphere*, vol. 8, no. 4, pp. 1217–1237, 2014.
- [80] N. Longépé, P. Thibaut, R. Vadaine, J.-C. Poisson, A. Guillot, F. Boy, N. Picot and F. Borde, "Comparative evaluation of sea ice lead detection based on SAR imagery and altimeter data," *IEEE Transactions on Geoscience and Remote Sensing*, vol. 57, no. 6, pp. 4050–4061, 2019.
- [81] N. T. Kurtz, S. L. Farrell, M. Studinger, N. Galin, J. P. Harbeck, R. Lindsay, V. D. Onana, B. Panzer and J. G. Sonntag, "Sea ice thickness, freeboard, and snow depth products from Operation IceBridge airborne data," *The Cryosphere*, vol. 7, no. 4, pp. 1035–1056, 2013.
- [82] W. Dierking, "Sea Ice and Icebergs," in *Maritime Surveillance with Synthetic Aperture Radar*, Institution of Engineering and Technology, 2020.

- [83] N. Zakhvatkina, V. Smirnov and I. Bychkova, "Satellite SAR Data-based Sea Ice Classification: An Overview," *Geosciences*, vol. 9, no. 4, 2019.
- [84] "<https://www.canada.ca/en/environment-climate-change/services/ice-forecasts-observations/publications/interpreting-charts/chapter-1.html>," last accessed 10 September 2020.
- [85] D. G. Flett, "Operational use of SAR at the Canadian Ice Service: Present operations and a look to the future," *ESASP*, vol. 565, p. 20, 2004.
- [86] B. Scheuchl, D. Flett, R. Caves and I. Cumming, "Potential of RADARSAT-2 data for operational sea ice monitoring," *Canadian Journal of Remote Sensing*, vol. 30, no. 3, pp. 448–461, 2004.
- [87] S. Khaleghian, J. Lohse and T. Kræmer, "Synthetic-Aperture Radar (SAR) based Ice types/Ice edge dataset for deep learning analysis," 2020.
- [88] "cirfa.uit.no," last accessed 23 December 2020.
- [89] J. Schürmann, *Pattern classification: A unified view of statistical and neural approaches*. John Wiley & Sons, Inc., 1996.
- [90] S. Theodoridis and K. Koutroubas, *Pattern Recognition, Fourth Editions*. Academic Press, Inc., 4th ed., 2008.
- [91] "<https://scikit-learn.org/stable/tutorial/index.html>," last accessed 15 August 2020.
- [92] F. Pedregosa, G. Varoquaux, A. Gramfort, V. Michel, B. Thirion, O. Grisel, M. Blondel, P. Prettenhofer, R. Weiss, V. Dubourg, J. Vanderplas, A. Passos, D. Cournapeau, M. Brucher, M. Perrot and E. Duchesnay, "Scikit-learn: Machine Learning in Python," *Journal of Machine Learning Research*, vol. 12, pp. 2825–2830, 2011.
- [93] L. Buitinck, G. Louppe, M. Blondel, F. Pedregosa, A. Mueller, O. Grisel, V. Niculae, P. Prettenhofer, A. Gramfort, J. Grobler, R. Layton, J. VanderPlas, A. Joly, B. Holt and G. Varoquaux, "API design for machine learning software: experiences from the scikit-learn project," in *ECML PKDD Workshop: Languages for Data Mining and Machine Learning*, pp. 108–122, 2013.
- [94] K. Fukunaga, *Introduction to statistical pattern recognition*. Academic Press, 2nd ed., 1990.
- [95] J. Miao and L. Niu, "A survey on feature selection," *Procedia Computer Science*, vol. 91, pp. 919–926, 2016.

- [96] W. Sun and Q. Du, "Hyperspectral band selection: A review," *IEEE Geoscience and Remote Sensing Magazine*, vol. 7, no. 2, pp. 118–139, 2019.
- [97] S. Solorio-Fernández, J. A. Carrasco-Ochoa and J. Martínez-Trinidad, "A review of unsupervised feature selection methods," *Artificial Intelligence Review*, vol. 53, no. 2, pp. 907–948, 2020.
- [98] Y. Chauvin, "Generalization performance of overtrained back-propagation networks," in *European Association for Signal Processing Workshop*, pp. 45–55, Springer, 1990.
- [99] E. Parzen, "On Estimation of a Probability Density Function and Mode," *The Annals of Mathematical Statistics*, vol. 33, no. 3, pp. 1065–1076, 1962.
- [100] L. Breiman, "Random Forests," *Machine Learning*, pp. 5–32, 2001.
- [101] M. Dabboor, B. Montpetit, S. Howell and C. Haas, "Improving sea ice characterization in dry ice winter conditions using polarimetric parameters from C-and L-band SAR data," *Remote Sensing*, vol. 9, no. 12, p. 1270, 2017.
- [102] H. Han, S.-H. Hong, H.-C. Kim, T.-B. Chae and H.-J. Choi, "A study of the feasibility of using KOMPSAT-5 SAR data to map sea ice in the Chukchi Sea in late summer," *Remote Sensing Letters*, vol. 8, no. 5, pp. 468–477, 2017.
- [103] D. Murashkin, G. Spreen, M. Huntemann and W. Dierking, "Method for detection of leads from Sentinel-1 SAR images," *Annals of Glaciology*, vol. 59, no. 76pt2, pp. 124–136, 2018.
- [104] Y. Grandvalet, "Bagging equalizes influence," *Machine Learning*, vol. 55, no. 3, pp. 251–270, 2004.
- [105] "<https://scikit-learn.org/stable/modules/generated/sklearn.ensemble.RandomForestClassifier.html>," last accessed 22 August 2020.
- [106] S. Leigh, Z. Wang and D. Clausi, "Automated ice–water classification using dual polarization SAR satellite imagery," *IEEE Transactions on Geoscience and Remote Sensing*, vol. 52, no. 9, pp. 5529–5539, 2013.
- [107] N. Y. Zakhvatkina, V. Y. Alexandrov, O. M. Johannessen, S. Sandven and I. Y. Frolov, "Classification of Sea Ice Types in ENVISAT Synthetic Aperture Radar Images," *IEEE Transactions on Geoscience and Remote Sensing*, vol. 51, no. 5, pp. 2587–2600, 2013.
- [108] H. Liu, H. Guo and L. Zhang, "SVM-based sea ice classification using textural features and concentration from RADARSAT-2 dual-pol ScanSAR data," *IEEE Journal of Selected Topics in Applied Earth Observations and Remote Sensing*, vol. 8, no. 4,

- pp. 1601–1613, 2014.
- [109] R. Kwok, Y. Hara, R. G. Atkins, S. H. Yueh, R. T. Shin and J. A. Kong, “Application Of Neural Networks To Sea Ice Classification Using Polarimetric SAR Images,” in *[Proceedings] IGARSS’91 Remote Sensing: Global Monitoring for Earth Management*, vol. I, pp. 85–88, 1991.
- [110] Y. Hara, R. G. Atkins, R. T. Shin, Jin Au Kong, S. H. Yueh and R. Kwok, “Application of neural networks for sea ice classification in polarimetric SAR images,” *IEEE Transactions on Geoscience and Remote Sensing*, vol. 33, no. 3, pp. 740–748, 1995.
- [111] J. Karvonen, “Baltic sea ice SAR segmentation and classification using modified pulse-coupled neural networks,” *IEEE Transactions on Geoscience and Remote Sensing*, vol. 42, no. 7, pp. 1566–1574, 2004.
- [112] R. Ressel, A. Frost and S. Lehner, “A Neural Network-Based Classification for Sea Ice Types on X-Band SAR Images,” *IEEE Journal of Selected Topics in Applied Earth Observations and Remote Sensing*, vol. 8, no. 7, pp. 3672–3680, 2015.
- [113] “https://scikit-learn.org/stable/modules/neural_networks_supervised.html,” last accessed 23 August 2020.
- [114] D. E. Rumelhart, G. E. Hinton and R. J. Williams, “Learning representations by back-propagating errors,” *nature*, vol. 323, no. 6088, pp. 533–536, 1986.
- [115] Y. Xu and K. A. Scott, “Sea ice and open water classification of sar imagery using cnn-based transfer learning,” in *2017 IEEE International Geoscience and Remote Sensing Symposium (IGARSS)*, pp. 3262–3265, IEEE, 2017.
- [116] H. Boulze, A. Korosov and J. Brajard, “Classification of sea ice types in Sentinel-1 SAR data using convolutional neural networks,” *Remote Sensing*, vol. 12, no. 13, p. 2165, 2020.
- [117] R. Kruk, M. C. Fuller, A. S. Komarov, D. Isleifson and I. Jeffrey, “Proof of Concept for Sea Ice Stage of Development Classification Using Deep Learning,” *Remote Sensing*, vol. 12, no. 15, p. 2486, 2020.
- [118] D. Malmgren-Hansen, L. T. Pedersen, A. A. Nielsen, M. B. Kreiner, R. Saldo, H. Skriver, J. Lavelle, J. Buus-Hinkler and K. H. Krane, “A Convolutional Neural Network Architecture for Sentinel-1 and AMSR2 Data Fusion,” *IEEE Transactions on Geoscience and Remote Sensing*, 2020.
- [119] “<http://earthanalytics.eu/index.html>,” last accessed 23 August 2020.

- [120] J.S. Lee and E. Pottier, *Polarimetric radar imaging: from basics to applications*. CRC Press Taylor and Francis Group, 1st ed., 2009.
- [121] C. Oliver and S. Quegan, *Understanding synthetic aperture radar images*. SciTech Publishing, 2004.
- [122] A. J. Schweiger, “Changes in seasonal cloud cover over the Arctic seas from satellite and surface observations,” *Geophysical Research Letters*, vol. 31, no. 12, 2004.
- [123] C. Elachi and J. Van Zyl, *Introduction to the physics and techniques of remote sensing*, vol. 28. John Wiley & Sons, 2006.
- [124] S. Skrunes, *Characterization of Low Backscatter Regions in the Maritime Environment by Multipolarization C- and X-band Synthetic Aperture Radar Data*. PhD thesis, UiT The Arctic University of Norway, 2014.
- [125] J. C. Curlander and R. N. McDonough, *Synthetic aperture radar*, vol. 11. Wiley, New York, 1991.
- [126] J. van Zyl and Y. Kim, *Synthetic aperture radar polarimetry*, vol. 2. John Wiley & Sons, 2011.
- [127] “<https://sentinel.esa.int/web/sentinel/user-guides/sentinel-1-sar/acquisition-modes>,” last accessed 12 August 2020.
- [128] S. C. Liew, “<https://crisp.nus.edu.sg/~research/tutorial/rsmain.htm>,” last accessed 07 August 2020.
- [129] “<https://sentinel.esa.int/web/sentinel/user-guides/sentinel-1-sar/revisit-and-coverage>,” last accessed 10 August 2020.
- [130] W. Parker, “Discover the benefits of radar imaging: The Top 10 Considerations for Buying and Using Synthetic Aperture Radar Imagery,” *Earth Imaging Journal*, 2012.
- [131] IEEE, “IEEE standard letter designations for radar-frequency bands,” *IEEE Std 521-2002 (Revision of IEEE Std 521.-1984)*, 2003.
- [132] J. A. Bruder, J. Carlo, J. Gurney and J. Gorman, “IEEE standard for letter designations for radar-frequency bands,” *IEEE Aerospace & Electronic Systems Society*, pp. 1–3, 2003.
- [133] M. Drinkwater, J. Crawford and D. Cavalieri, “Multi-frequency, multi-polarization SAR and radiometer sea ice classification,” 1991.

- [134] L. Eriksson, K. Borenäs, W. Dierking, A. Berg, M. Santoro, P. Pemberton, H. Lindh and B. Karlson, "Evaluation of new spaceborne SAR sensors for sea-ice monitoring in the Baltic Sea," *Canadian Journal of Remote Sensing*, vol. 36, no. sup1, pp. S56–S73, 2010.
- [135] J. Karvonen, E. Rinne, H. Sallila and M. Mäkynen, "On Suitability of ALOS-2/PALSAR-2 Dual-Polarized SAR Data for Arctic Sea Ice Parameter Estimation," *IEEE Transactions on Geoscience and Remote Sensing*, 2020.
- [136] A. M. Johansson, C. Brekke, G. Spreen and J. King, "X-, C-, and L-band SAR signatures of newly formed sea ice in Arctic leads during winter and spring," *Remote Sensing of Environment*, vol. 204, pp. 162–180, 2018.
- [137] I. H. Woodhouse, *Introduction to microwave remote sensing*. CRC press, 2005.
- [138] R. K. Raney, "A perspective on compact polarimetry," *IEEE Geoscience and Remote Sensing Newsletters*, vol. 160, no. 160, pp. 12–18, 2011.
- [139] M.-A. M. Moen, S. N. Anfinsen, A. P. Doulgeris, A. H. H Renner. and S. Gerland, "Assessing polarimetric SAR sea-ice classifications using consecutive day images," *Annals of Glaciology*, vol. 56, no. 69, pp. 285–294, 2015.
- [140] W. Dierking, H. Skriver and P. Gudmandsen, "On the improvement of sea ice classification by means of radar polarimetry," *Remote Sensing in Transition*, pp. 203–209, 2004.
- [141] D. Massonnet and J.-C. Souyris, *Imaging with synthetic aperture radar*. CRC Press, 2008.
- [142] M. Espeseth, C. Brekke, C. E. Jones, B. Holt and A. Freeman, "The impact of system noise in polarimetric SAR imagery on oil spill observations," *IEEE Transactions on Geoscience and Remote Sensing*, vol. 58, no. 6, pp. 4194–4214, 2020.
- [143] I. G. Cumming and F. H. Wong, "Digital processing of synthetic aperture radar data: algorithms and implementation," 2005.
- [144] F. Carsey, *Microwave remote sensing of sea ice*. American Geophysical Union, 1992.
- [145] J. Karvonen, "Baltic sea ice concentration estimation using SENTINEL-1 SAR and AMSR2 microwave radiometer data," *IEEE Transactions on Geoscience and Remote Sensing*, vol. 55, no. 5, pp. 2871–2883, 2017.
- [146] W. Aldenhoff, C. Heuzé, L. Eriksson, "Comparison of ice/water classification in Fram Strait from C-and L-band SAR imagery," *Annals of Glaciology*, vol. 59, no. 76pt2,

- pp. 112–123, 2018.
- [147] J. W. Park, A. Korosov, M. Babiker, S. Sandven and J. S. Won, “Efficient thermal noise removal for Sentinel-1 TOPSAR cross-polarization channel,” *IEEE Transactions on Geoscience and Remote Sensing*, vol. 56, no. 3, pp. 1555–1565, 2018.
- [148] J. W. Park, J. S. Won, A. Korosov, M. Babiker and N. Miranda, “Textural noise correction for Sentinel-1 TOPSAR cross-polarization channel images,” *IEEE Transactions on Geoscience and Remote Sensing*, vol. 57, no. 6, pp. 4040–4049, 2019.
- [149] R. G. Onstott, “SAR and scatterometer signatures of sea ice,” in *The Remote Sensing of Sea Ice*, pp. 73–104, 1993.
- [150] M.-A. N. Moen, A. P. Doulgeris, S. N. Anfinson, A. H. H. Renner, N. Hughes, S. Gerland and T. Eltoft, “Comparison of feature based segmentation of full polarimetric SAR satellite sea ice images with manually drawn ice charts,” *The Cryosphere*, vol. 7, no. 6, pp. 1693–1705, 2013.
- [151] World Meteorological Organization, “WMO sea-ice nomenclature, Terminology, codes and illustrated glossary,” *Secretariat of the WMO, Geneva*, no. 259-TP145 (I-III), 1985.
- [152] D. O. Dammann, L. Eriksson, A. Mahoney, C. Stevens, J. Van der Sanden, H. Eicken, F. Meyer and C. Tweedie, “Mapping Arctic bottomfast sea ice using SAR interferometry,” *Remote Sensing*, vol. 10, no. 5, p. 720, 2018.
- [153] D. O. Dammann, L. Eriksson, A. Mahoney, H. Eicken and F. Meyer, “Mapping pan-Arctic landfast sea ice stability using Sentinel-1 interferometry,” *The Cryosphere*, vol. 13, no. 2, pp. 557–577, 2019.
- [154] R. Kwok, S. Nghiem, S. Yueh and D. Huynh, “Retrieval of thin ice thickness from multifrequency polarimetric SAR data,” *Remote sensing of environment*, vol. 51, no. 3, pp. 361–374, 1995.
- [155] W. Dierking, “Sea Ice Monitoring by Synthetic Aperture Radar,” *Oceanography*, vol. 26, no. 2, pp. 100–111, 2013.
- [156] D. Isleifson, B. Hwang, D. Barber, R. Scharien and L. Shafai, “C-band polarimetric backscattering signatures of newly formed sea ice during fall freeze-up,” *IEEE Transactions on Geoscience and Remote Sensing*, vol. 48, no. 8, pp. 3256–3267, 2010.
- [157] D. Isleifson, R. Galley, N. Firoozy, J. Landy and D. Barber, “Investigations into Frost Flower Physical Characteristics and the C-Band Scattering Response,” *Remote Sensing*, vol. 10, no. 7, p. 991, 2018.

- [158] B. Holt, "SAR imaging of the ocean surface," in *Synthetic Aperture Radar Marine User's Manual*, pp. 25–80, U.S. Department of Commerce, National Oceanic and Atmospheric Administration, 2004.
- [159] N. Zakhvatkina, A. Korosov, S. Muckenhuber, S. Sandven and M. Babiker, "Operational algorithm for ice–water classification on dual-polarized RADARSAT-2 images," *The Cryosphere*, vol. 11, no. 1, pp. 33–46, 2017.
- [160] B. Scheuchl, R. Caves, I. Cumming and G. Staples, "Automated sea ice classification using spaceborne polarimetric SAR data," in *IGARSS 2001. Scanning the Present and Resolving the Future. Proceedings. IEEE 2001 International Geoscience and Remote Sensing Symposium (Cat. No. 01CH37217)*, vol. 7, pp. 3117–3119, 2001.
- [161] T. Geldsetzer and J. J. Yackel, "Sea ice type and open water discrimination using dual co-polarized C-band SAR," *Canadian Journal of Remote Sensing*, vol. 35, no. 1, pp. 73–84, 2009.
- [162] H. Han, J. Im, M. Kim, S. Sim, J. Kim, D. Kim and S. Kang, "Retrieval of Melt Ponds on Arctic Multiyear Sea Ice in Summer from TerraSAR-X Dual-Polarization Data Using Machine Learning Approaches: A Case Study in the Chukchi Sea with Mid-Incidence Angle Data," *Remote Sensing*, vol. 8, no. 1, 2016.
- [163] R. Ressel and S. Singha, "Comparing Near Coincident Space Borne C and X Band Fully Polarimetric SAR Data for Arctic Sea Ice Classification," *Remote Sensing*, vol. 8, no. 3, 2016.
- [164] R. Ressel, S. Singha and S. Lehner, "Investigations into the X and C band Quad-Pol Features for Sea Ice Classification," in *Proceedings of EUSAR 2016: 11th European Conference on Synthetic Aperture Radar*, pp. 1–4, 2016.
- [165] R. M. Haralick, K. Shanmugan and I. Dinstein, "Textural features for image classification," *IEEE Transactions on Systems, Man and Cybernetics*, pp. 610–621, 1973.
- [166] D. G. Barber and E. LeDrew, "SAR Sea Ice Discrimination Using Texture Statistics: A Multivariate Approach," *Photogrammetric Engineering and Remote Sensing*, vol. 57, no. 4, pp. 385–395, 1991.
- [167] Q. A. Holmes, D. R. Nuesch and R. A. Shuchman, "Textural Analysis And Real-Time Classification of Sea-Ice Types Using Digital SAR Data," *IEEE Transactions on Geoscience and Remote Sensing*, vol. GE-22, no. 2, pp. 113–120, 1984.
- [168] M. E. Shokr, "Evaluation of second-order texture parameters for sea ice classification from radar images," *Journal of Geophysical Research: Oceans*, vol. 96, no. C6, pp. 10625–10640, 1991.

- [169] L.-K. Soh and C. Tsatsoulis, "Texture Analysis of SAR Sea Ice Imagery Using Gray Level Co-Occurance Matrices," *IEEE Transactions on Geoscience and Remote Sensing*, vol. 37, no. 2, pp. 780–795, 1999.
- [170] D. A. Clausi, "Comparison and fusion of co-occurrence, Gabor and MRF texture features for classification of SAR sea-ice imagery," *Atmosphere-Ocean*, vol. 39, no. 3, pp. 183–194, 2001.
- [171] D. A. Clausi, "An analysis of co-occurrence texture statistics as a function of grey level quantization," *Canadian Journal of remote sensing*, vol. 28, no. 1, pp. 45–62, 2002.
- [172] H. Deng and D. A. Clausi, "Unsupervised segmentation of synthetic aperture radar sea ice imagery using a novel Markov random field model," *IEEE Transactions on Geoscience and Remote Sensing*, vol. 43, no. 3, pp. 528–538, 2005.
- [173] M. Mäkynen and J. Karvonen, "Incidence Angle Dependence of First-Year Sea Ice Backscattering Coefficient in Sentinel-1 SAR Imagery Over the Kara Sea," *IEEE Transactions on Geoscience and Remote Sensing*, vol. 55, no. 11, pp. 6170–6181, 2017.
- [174] M. P. Mäkynen, A. T. Manninen, M. H. Similä, J. A. Karvonen and M. T. Hallikainen, "Incidence angle dependence of the statistical properties of C-band HH-polarization backscattering signatures of the Baltic Sea ice," *IEEE Transactions on Geoscience and Remote Sensing*, vol. 40, no. 12, pp. 2593–2605, 2002.
- [175] J. P. S. Gill, J. Yackel, T. Geldsetzer and M. C. Fuller, "Sensitivity of C-band synthetic aperture radar polarimetric parameters to snow thickness over landfast smooth first-year sea ice," *Remote Sensing of Environment*, vol. 166, pp. 34–49, 2015.
- [176] M. S. Mahmud, T. Geldsetzer, S. E. L. Howell, J. J. Yackel, V. Nandan and R. K. Scharien, "Incidence Angle Dependence of HH-Polarized C- and L-Band Wintertime Backscatter Over Arctic Sea Ice," *IEEE Transactions on Geoscience and Remote Sensing*, pp. 1–13, 2018.
- [177] J. Karvonen, "A sea ice concentration estimation algorithm utilizing radiometer and SAR data," *The Cryosphere*, vol. 8, no. 5, pp. 1639–1650, 2014.
- [178] F. Dinessen, "Operational multisensor sea ice concentration algorithm utilizing Sentinel-1 and AMSR2 data," *EGUGA*, p. 19037, 2017.

